DOE/BC/10842-5
(DE87001260)

FLOW IN POROUS MEDIA, PHASE BEHAVIOR AND ULTRALOW INTERFACIAL TENSIONS: MECHANISMS OF ENHANCED PETROLEUM RECOVERY

First Annual Report for the Period
October 1, 1985-September 30, 1986

By
H. T. Davis
L. E. Scriven

October 1987

Performed Under Contract No. AC19-85BC10842

University of Minnesota
Minneapolis, Minnesota

Bartlesville Project Office
U. S. DEPARTMENT OF ENERGY
Bartlesville, Oklahoma

DISCLAIMER

Printed in the United States of America. Available from:
National Technical Information Service
U.S. Department of Commerce
5285 Port Royal Road
Springfield, VA 22161

NTIS price codes
Paper copy: **A11**
Microfiche copy: **A01**

DOE/BC/10842-5
Distribution Category UC-122

FLOW IN POROUS MEDIA, PHASE BEHAVIOR AND ULTRALOW INTERFACIAL TENSIONS: MECHANISMS OF ENHANCED PETROLEUM RECOVERY

First Annual Report for the Period
October 1, 1985–September 30, 1986

By
H. T. Davis
L. E. Scriven

October 1987

Work Performed Under Contract No. AC19-85BC10842

Prepared for
U.S. Department of Energy
Assistant Secretary for Fossil Energy

Fred W. Burtch, Project Manager
Bartlesville Project Office
P.O. Box 1398
Bartlesville, OK 74005

Prepared by
University of Minnesota
Institute of Technology
Department of Chemical Engineering and Materials Science
Department of Chemistry
Minneapolis, MN 55455

FLOW IN POROUS MEDIA, PHASE BEHAVIOR
AND ULTRALOW INTERFACIAL TENSIONS:
MECHANISMS OF ENHANCED PETROLEUM RECOVERY

Department of Chemical Engineering and Materials Science
University of Minnesota

CONTENTS

Page No.

FLOW IN POROUS MEDIA, PHASE BEHAVIOR AND ULTRALOW INTERFACIAL TENSIONS: MECHANISMS OF ENHANCED PETROLEUM RECOVERY

Department of Chemical Engineering and Materials Science
University of Minnesota

ABSTRACT

A major program of university research, longer-ranged and more fundamental in approach than industrial research, into basic mechanisms of enhancing petroleum recovery and into underlying physics, chemistry, geology, applied mathematics, computation, and engineering science has been built at Minnesota. The 1985-86 outputs of the interdisciplinary team of investigators were again ideas, instruments, techniques, data, understanding and skilled people:

- 28 scientific and engineering publications in leading journals.
- Two Ph.D. theses, the author of one going to industry, the other to a university.
- Numerous presentations to scientific and technical meetings, and to industrial, governmental and university laboratories in the U.S., Europe and South America.
- Vigorous program of research visits to and from Minnesota.

This report summarizes the papers and theses that emerged during the period 1 Oct 1985 to 30 Sept 1986 and features fifteen major accomplishments of the program during that year. Abstracts of the 28 publications and 2 theses are reported and several major accomplishments are reported in greater detail. Further details of information transfer and personnel exchange with industrial, governmental and university laboratorires appear in Quarterly Reports available from the Department of Energy and are not reproduced here.

INTRODUCTION

This report summarizes the outputs that emerged from the Minnesota research program during the period 1 Oct. 1985 to 30 Sept. 1986. The goals of the program are ideas, instruments, techniques, data, understanding, and skilled people for enhancing the recovery of petroleum in the short term as well as in the longer term, and doing so especially by elucidating basic mechanisms. For then the uncertainties of process design, particularly in scale-up, control and optimization, are reduced, and innovative process development is promoted.

The original focus was surfactant-based chemical flooding, but the approaches taken were sufficiently fundamental that the research, longer-ranged than most industrial efforts, has become quite multidirectional. Many current outputs of the program are basic enough to pertain to pertroleum recovery more broadly and to other energy-related technologies as well.

Research Highlights

The emphasis of the research program is on understanding basic physical and chemical mechanisms with the goal of transforming this knowledge into the concepts and mathematical formulations needed for engineering process design and analysis. The research reported here can be discussed conveniently under three broad headings:

1. SCIENCE OF MICROSTRUCTURED FLUIDS AND APPLICATION TO THEIR PHASE BEHAVIOR, INTERFACIAL TENSION, AND RHEOLOGY. Leading examples of fluid microstructures are the surfactant-based micelles, microemulsions, liquid crystals, vesicles, etc. all of which are found in chemical flooding formulations. Interfaces and adsorbed layers or thin films on solids are fluid microstructures that aid and abet the wettability syndromes that govern capillary pressure and relative permeability behavior.

Microemulsions and their precursors. The aim of the Minnesota program has been to identify the microstructure of microemulsion in midrange compositions (oil and water present in comparable amounts) and to determine what role this microstructure plays in the ultralow tensions useful to enhanced oil recovery. It has long been generally accepted that at low water or oil content a microemulsion is a solution of sphere-like swollen micelles or inverted micelles. However, where ultralow tensions are observed between both coexisting oil-rich and water-rich phases the oil/water ratio is near unity and there has been considerable controversy concerning the microstructure there. The hypothesis put forward by Minnesota researchers at 1975 and 1976 Gordon Research Conferences was that microemulsion in midrange compositions is a bicontinuous fluid with oil-rich and water-rich regions separated by sheet-like zones of surfactant. The existence of bicontinuous microemulsions has now been confirmed by Minnesota researchers and several international groups elsewhere. The current state of understanding of microemulsions is presented in Section 1. There also the behavior of microemulsions is contrasted with that of molecular solutions in which the surfactant is replaced by mere amphiphiles such as monohydric alcohols. Many of the patterns originally associated with microemulsions are common to all hydrocarbon, brine and amphiphile. However, the lifetime or

persistence of microstructure distinguishes microemulsions.

New controlled environment, vitrification electron microscopy system. The most direct method for determining the microstructure of microemulsions and liquid crystalline dispersions is to freeze fluid samples and view them in the electron microscope. However, to avoid freezing to artifacts requires that freezing take place fast enough to vitrify the fluids, i.e., to suppress cyrstallization of solid phases. Such a system has now been constructed for viewing thin layers (2,000 — 3,000 A) of microstructured fluids. It is described in Section 2. The University of Minnesota has applied for a patent for the system. It controls the activities of the volatile components of the fluid to prevent composition change and plunges the sample in liquid ethane or propane which freezes it fast enough for vitrification. The controlled environment vitrification system has been used to study vesicle and liquid crystalline dispersions and is currently being applied to micellar solutions.

Mathematical modelling of bicontinuous structures. Surfactants in some microemulsions and cubic liquid crystals lie in sheet-like zones separating water-rich and oil-rich regions into separate sample spanning labyrinths. Any theory or model of the properties of these systems requires a quantitative description of their microstructures, which amounts to construction of dividing surfaces of prescribed curvature. The mathematical construction of families of such surfaces is presented in Section 3 and several examples are pictured. These constructs form the starting point of an on-going program to determine the surface forces and phase behavior of microemulsions and liquid crystals. Applications to X-ray scattering studies of microemulsions are given in D. M. Anderson's Ph.D. thesis (Publication 2) which was published June 1986. The constructs are also useful as cellular models for computing permeability and dispersion in porous media.

Self-diffusion in hydrocarbon, brine and surfactant solutions. The diffusivitities of the different molecules of colloidal dispersions and solutions provide information about fluid microstructures and their lifetimes. The old technique of radioactive tracers, chemical analysis, Taylor dispersion and the like are cumbersome and time consuming. Quasielectric light scattering, a newer technique, has an uncertain interpretation for concentrated solutions of scatterers. The spin echo, pulsed field gradient (SEPFG) nuclear magnetic resonance method on the other hand yields the self-diffusion coefficients of all the molecular constituents of a mixture unambiguously, accurately and relatively rapidly. We have applied this technique to hydrocarbon brine, and amphiphile mixtures. We have found that solutions of small ethoxylated alcohols with hydrocarbon and brine exhibit the same qualitative patterns of phase behavior, electrical conductivity and quasielastic light scattering as do microemulsions, indicating that these solutions are also microstructured (See Section 1.) However, the self-diffusion coefficients of all components of the solutions show that they diffuse as individual molecules (Publication 8). Thus, the microstructures in the small ethoxylated alcohol solutions are shorter-lived than those in microemulsions. With increasing alkane chain length the ethoxylated alcohol solutions become typical microemulsions. SEPFG NMR measurements have led to the discovery in these microemulsions of a temperature-driven transition from a bicontinuous microemulsion to a swollen micellar solution in a 50/50 oil-water microemulsion system. This system is presently being studied further.

2. SCIENCE OF POROUS MEDIA AND FLOW THEREIN AND OF CHAOTIC COMPOSITES. Porous media encompass sedimentary rocks, soil, other materials in nature and technology. A porous medium is a chaotic composite of solid and void, the void or porespace always containing one or more fluid phases. The science of porous media and flow therein is the science of disordered porespace morphology and the flow and transport dictated by this disorder. The thrust of the Minnesota program has been to introduce the concepts of modern statistical physics (in particular, percolation theory, effective medium theory, renormalization theory, and fractals) to achieve a unified theory of porous media and processes therein. During this report period further progress was made in the advancement of the theory of stability in frontal displacement, the statistical network theory of relative permeability in porous media, and the molecular theory of fluid-solid interactions and of transport in micropores. With the aid of the theory a mechanism based simulation of oil recovery processes is developed and applied to various two- and three-phase flooding situations. The theory is also used to test Stone's empirical correlation for three-phase relative permeabilities.

Wetting films in porous media. The augmented Young-Laplace equation is used to study the structure, distribution and stability of films and pendular structures of perfectly wetting fluids in axisymmetric pores (See Section 4). The elements of the theory are the interfacial tension and disjoining potential (or pressure). Both continuous and disconnected meniscus geometries have been considered. The results of these calcuations for single and multiple pore microscopic systems have been applied to macroscopic systems by the application of a statistical theory of multiphase transport in porous media developed by Heiba. The results indicate the existence of two transport mechanisms: a capillary jump mechanism by which the non-wetting fluid invades pores and a film drainage mechanism by which wetting films and pendular structures, remaining after the invasion of the non-wetting fluid, continue to drain. The difference between the two mechanisms is apparent at low wetting phase saturation in both the predictions of the statistical theory and in displacment experiments of perfectly wetting and intermediately wetting fluids in sintered teflon synthetic porous media.

Molecular theory of the ionic double-layer at a charged wall. The generalized van der Waals theory of inhomogeneous fluids has in recent years been a useful tool for studying molecular structure, stresses and thermodynamic potentials of fluids at solid walls. We have applied the theory to the double-layer problem of an electrolyte at a charged solid surface. The theory compares as well with Monte Carlo simulations on a model electrolyte as does the more classical Gouy-Chapman theory. However, the advantage of the van der Waals theory over the traditional Gouy-Chapman theory is that the solvent density and dielectric properties can be found self-consistently with the ionic distributions near the solid surface. Surface tensions, ion adsorption, double-layer electrical potential, and differential capacitance are predicted by the theory.

Adsorption, diffusion and flow of fluids in microporous media. A molecular theory has been developed which predicts density profiles, stresses and surface or disjoining forces, tracer diffusivity, and flow of fluids in micropores and thin films. The theory compares well with computer simulations (Section 6). In its simplest form it relates the local transport properties of inhomogeneous fluid to those of homogeneous fluid at a local average density. The choice of the local

average density is drawn from a rigorous formula for a one-dimensional fluid (Publication 11). This work complements our earlier work on wetting transitions and extends to thin thin-films and adsorbed layers and our earlier work on the spreading of thick thin-films.

3. SUPERCOMPUTER-SCALE THEORETICAL ANALYSES AND MATHEMATICAL MODELING. The Minnesota group has harnessed applied mathematics, numerical mathematics, and up-to-date scientific computers and computer software and is solving heretofore intractable problems. Modern finite element mathematics has emerged as the workhorse for the two-dimensional and three-dimensional physics and engineering involved. In many cases a supercomputer is needed. Late in 1981 Minnesota became the first university to install a supercomputer, a CRAY-1, to the great advantage of the research group. To this was added the CDC Cyber 205 supercomputer. The Cray-1 was recently replaced by a Cray-2. The group continues to pursue ever more reliable, cost-effective methods, whether on the CRAY-2, Cyber 205, or departmental VAX and Apollo midi-computers. Among the benefits of these facilities have been graduates skilled in matrix-handling methods, continuation schemes, Schwarz-Wenderoff approximation (for integral and intergrodifferential systems), stability analysis, efficient representation of boundary regions and in automatically adaptive discretizations for systems with sharp fronts or waves.

Adaptive, finite element simulation of frontal displacement. In a continuing investigation of frontal stability in immiscible displacement we have developed an efficient algorithm for the one-dimensional two-phase cases (Section VI). The algorithm incorporates the adaptive finite element method that has evolved from Benner's and Heiba's theses. A novel feature is the formulation of transient asymptotic boundary conditions for the semiinfinite frontal displacement problem. The code has been developed on the Cray-2 vectorization and multitasking. The accuracy and efficiency of the program has been tested against the analytic results Foleas and Yortsos obtained from their model. The asymptotic boundary condition has proven to be a valuable asset to the analysis.

Mechanism-based simulation of oil recovery. As a natural companion to development of a multiphase theory of capillary pressure and relative permeabilities, the thesis work of A. A. Heiba (Publication 13, 14) presents a one-dimensional simulator that closes the loop on computation of the local saturation and saturation-dependent properties. The simulator is based on an adapative finite element method, a predictor corrector algorithm for advancement in time. A special feature of the simulator is that mass is automatically conserved in the adaptive redistribution of elements. The properties are computed from the statistics of pore-filling sequences. Presently, the simulator is time consuming even on a supercomputer and so will be more useful in investigating issues of three phase displacement where few reliable data on capillary pressures on relative permeabilities exist, and in rational design of laboratory-scale experiments on three-phase flow. However, as computers become faster and with the expected continued simplification of the theory it could eventually form the basis of a practical simulator.

Molecular theory calculations and molecular simulations. In trying to understand the role of interfacial tensions, fluid-rock interactions, thin films and the like on fluid distribution and flow in porous media, we have developed a

molecular-level program in which theory and computer simulations (Monte Carlo and molecular dynamics) are closely coupled (Section 6). Theory is tested against molecular simulations which in turn suggest modifications or new directions for the theory. In connection with the theoretical work, we have developed finite element techniques for handling nonlinear integral equations, further development of the Schwarz-Wendroff method, asymptotic analysis of boundary regions and adaptive element placement being areas of special innovation. We are currently applying the molecular dynamics technique to surfactant solutions to try to understand at the molecular level the mechanisms of micellization, liquid crystallization, and microemulsion formation. The algorithm (Section 2) for construction of three-dimensionally distributed surfaces of prescribed mean curvature is unique, allowing construction for the first time several known three-dimensionally periodic surfaces, will be valuable in a variety of applications including surfactant solution microstructure, thin film and pendular structure distributions in porous media, and foam and emulsion structural representation.

1. MICROEMULSIONS AND THEIR PRECURSORS

Synopsis

Amphiphiles are generally defined with reference to water. An amphiphilic molecule possesses a hydrophilic (water soluble) moiety and a hydrophobic (water insoluble) moiety separable by a mathematical surface. In this paper the only hydrophobic moieties considered are those composed of hydrocarbon chains (as opposed, for example, to fluorocarbon chains). According to IUPAC [1], surfactants are substances which lower the surface tension of the medium in which they are dissolved and/or the interfacial tension with other phases. This definition is too broad as it would include substances such as benzene which lower the surface tension when dissolved in water but have none of the other properties expected of a surfactant. A generally accepted restriction of the definition is that surfactant molecules must be amphiphilic [2-4]. We adopt this restriction and, furthermore, share the view of Laughlin [5] that those properties associated with surfactancy (e.g., detergency, co-solubilization of oil and water, emulsification, foaming, and the like) are not common to all amphiphiles. He reserves the term "surfactant" for molecules which form association colloids such as micelles and liquid crystals. Thus, amphiphiles such as long-chained fatty acid salts (soaps), sodium alkyl sulfates and sodium alkyl sulfonates (detergents), and lecithins are clearly surfactants, whereas monohydric straight-chained alcohols and amines are mere amphiphiles. A special property of the association colloids formed by amphiphiles is that the amphiphiles associate into monolayer or sheet-like structures with the water soluble moieties on one side of the sheet and the water insoluble moieties on the other side (a bilayer is a pair of opposed monolayers). In the spirit of Laughlin, *we define surfactants as amphiphiles which form association colloids distinguished by sheet-like surfactant microstructure.*

By alcohol titration of an emulsion of oil and water stabilized by a surfactant, Schulman and coworkers obtained isotropic, transparent fluids [6-9]. Hoar and Schulman [6] described these fluids as what would in the current language of the field be called an aqueous solution of oil-swollen micelles and an oil solution of water-swollen inverted micelles. Noting that small spherical objects (of the order of 5 to 100 nm in diameter) were observed by chemical staining electron microscopy, Schulman, Stoeckenius and Prince [9] called these fluids "micro emulsions" and described them as "optically isotropic, fluid, transparent oil and water dispersions, consisting of uniform spherical droplets of either oil or water in the appropriate continuous phase."

In 1976, Scriven [10,11] put forward the idea that microemulsions containing comparable amounts of oil and water could be bicontinuous, with irregular sample-spanning water-rich regions separated by surfactant sheet-like zones from irregular sample- spanning oil-rich regions. As in two-component association colloids, the surfactant sheet-like zone admits a dividing surface on one side of which are the water-soluble moieties of the surfactant molecules and on the other side are the water-insoluble moieties. Thus, the surfactant sheet-like zone provides a topological ordering of the water-rich and oil-rich regions of the microemulsion, water on one side of the surfactant sheet and oil on the other. To include the possibility of such a microstructured fluid in the classification of

microemulsions we prefer the following definition: *A microemulsion is a thermodynamically stable, isotropic, topologically ordered microstructured phase containing at least surfactant, hydrocarbon and water.* With the interpretation that the topological order is that imposed by sheet-like surfactant zones, the above definition of microemulsion admits the possibility of dispersed droplet structures (swollen micellar or inverted micellar solutions) as well as bicontinuous ones. Often salt, alcohol, or a second surfactant is added to the surfactant-hydrocarbon-water mixture to obtain an isotropic microemulsion with the desired phase behavior. In many of the microemulsions of practical importance the surfactant and hydrocarbon materials are mixtures whose compositions are often not very well characterized.

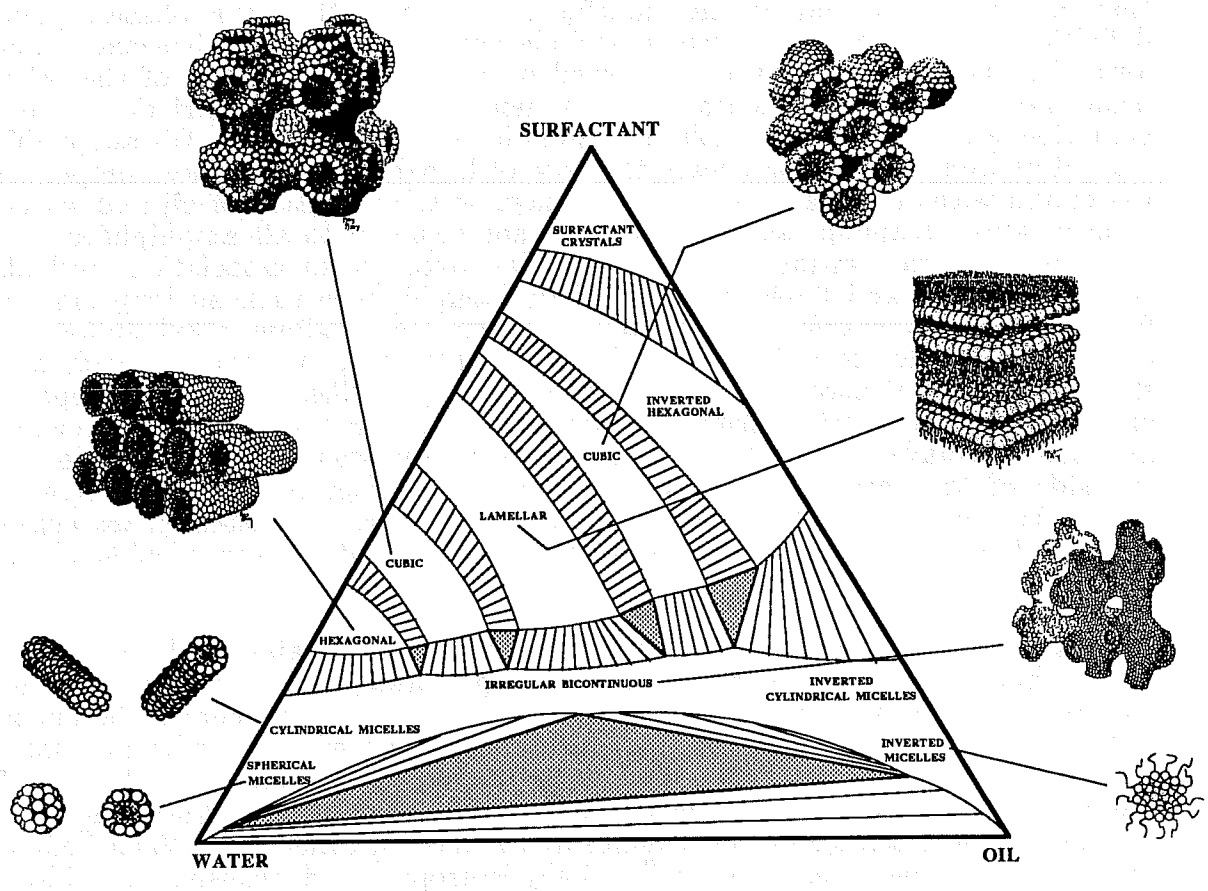

Figure 1. Schematic oil-water-surfactant phase diagram with microstructures depicted. Ref. 12.

In Figure 1, we present an idealized ternary phase diagram in which are illustrated fluid microstructures that have been identified in solutions of surfactants with water and/or oil [12-14]. The existence of solutions of spherical and cylindrical micelles or inverted micelles is generally accepted as are lyotropic liquid crystalline phases with lamellar, hexagonal and cubic symmetries. However, the detailed local shapes of the surfactant sheet-like zones, the role and importance of molecular fluctuations and bending and stretching motions of the sheet-like zones in micellar solutions and liquid crystals are issues not entirely

resolved and are the subjects of much current research. A convincing body of data now exists supporting the existence of bicontinuous microemulsions, but their detailed microstructure has not been established.

One of the goals of the research program at the University of Minnesota is to understand the relationship between molecular structure, fluid compositions and the properties of microemulsions. A logical step toward attaining this goal is to distinguish solutions of brine, hydrocarbon and mere amphiphile from microemulsions of brine, hydrocarbon and surfactant. To this end we have been carrying out a systematic study of the microstructure of a sequence of solutions of straight-chained ethoxylated alcohols with hydrocarbon and brine [15-22]. The sequence begins with propanol and includes $H(CH_2)_n (OCH_2CH_2)_mOH$ (denoted as C_nE_m) with n ranging from 3 to 12 and m from 0 to 7. We have made a concerted effort to investigate the low end of this sequence to try to capture the pre-surfactant trends and pre-microemulsion patterns of amphiphiles that do not qualify as surfactants. Our work is complementary to the extensive studies of microemulsions of C_nE_m carried out by Kahlweit and coworkers [23-27], Lindman and coworkers [28,29], and Shinoda and coworkers [30,31].

We report here the status of our studies of C_3E_0, C_4E_0, C_4E_1 and C_6E_2 — hydrocarbon-brine systems. Before giving these results, however, we present in the next section the established behavior of microemulsions with which we contrast that of these simple systems.

Patterns of Microemulsion Behavior

Because of their possible applications in enhancing oil recovery, the phase and interfacial behavior of microemulsions has received particular attention during the last decade. The special interest is to find the thermodynamic conditions for which a microemulsion phase has ultralow tensions against coexisting oil and water-rich phases. Under these conditions microemulsions injected into an oil reservoir will surround oil blobs trapped by capillary forces in the pores of the rock and will lower the overall tension sufficiently to mobilize the trapped blobs into a recoverable oil-bank.

For a given oil-water-surfactant system, the most frequently used method to adjust the phase splits and tensions in a microemulsion system is to add an alcohol and a salt, often NaCl. An example [32] of the phase behavior in a salinity scan of a low tension microemulsion system is shown in Fig. 2. The system is formed by mixing a given volume of brine solution with an equal volume of a mixture of alcohol, surfactant, and hydrocarbon. The type and amount of alcohol have been chosen so that in the three-phase region the microemulsion (middle phase) will have ultralow tension against both the oil-rich (top) and water-rich (bottom) phases. In the salinity scan the phase splits obey the $2\overline{3}2$ progression characteristic of low-tension microemulsions. Following Knickerbocker *et al.* [15,16], we denote by 2 a two-phase system in which the microemulsion is the lower, water-rich phase; by 3 a three-phase system in which the microemulsion is the middle phase and contains appreciable amounts of oil and water; and by $\overline{2}$ a two-phase system in which the microemulsion is the upper, oil-rich phase.

The pattern of interfacial tension behavior of a low-tension salinity scan is given in Fig. 3. The salinity at which the microemulsion interfacial tensions against the coexisting oil-rich phase and water-rich phase are equal, i.e., $\gamma_{om} = \gamma_{wm}$, was designated as "optimal" by Reed and Healy [33,34] because in this state the microemulsion is most favorable for coating and mobilizing capillary-trapped oil blobs. The ratio of the volumes of oil and water in the microemulsion-phase oil is approximately unity in the optimal microemulsion state shown in Fig. 3. Reed and Healy noted this and found that it is generally true for low tension microemulsions. Besides being a fascinating fact, the correlation of equal oil-water uptake with optimal tension lets one replace tension measurements by the easier volume uptake measurement in scanning candidate formulations for ultralow-tension microemulsions.

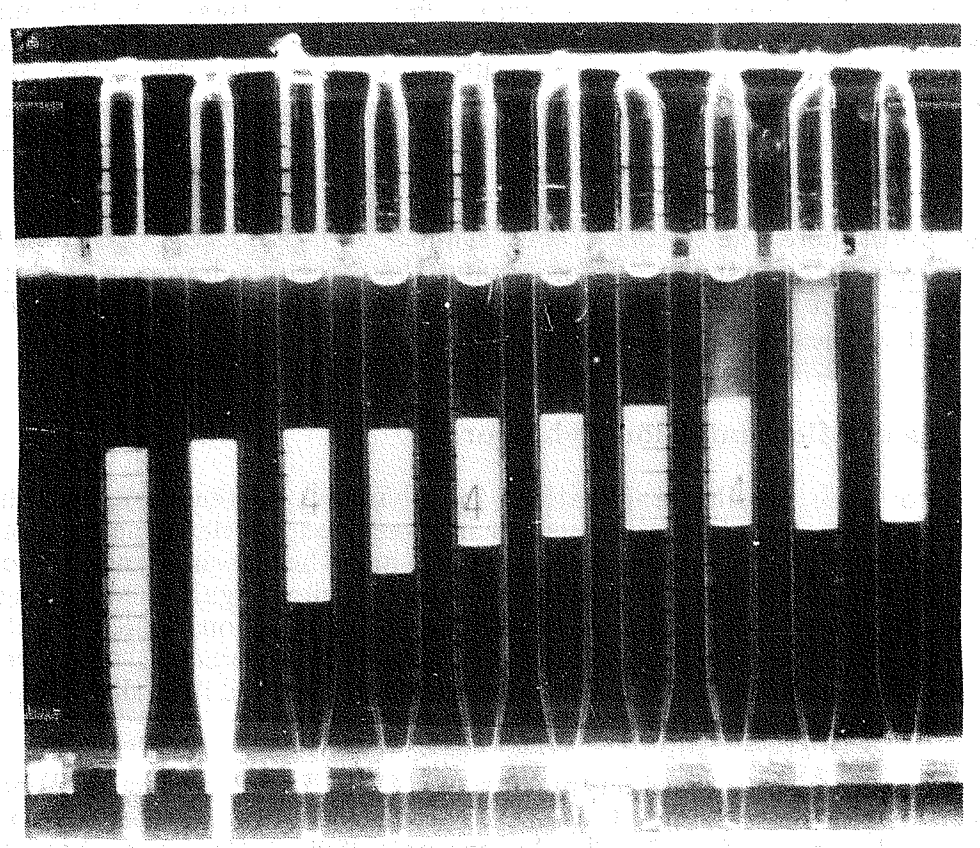

Figure 2. Salinity scan of a sodium sulfonate surfactant, isobutanol, n-hexadecane, and NaCl brine mixture. The surfactant is sodium 4-(1′-heptylnonyl) benzenesulfonate (SHBS). Mixtures were in the volume percent of about 5% surfactant plus alcohol, 45% hydrocarbon and 50% brine. The brine ranged in salinity from about 0.2 to 2 wt% NaCl. Ref. 32.

As illustrated by the example given above, the search for a surfactant formulation for enhancing oil recovery has generally involved the scanning of at least two field variables to find conditions under which the microemulsion will have ultralow tension against coexisting oil-rich and water-rich phases. A field

variable is defined as one which is the same in all phases in thermodynamic equilibrium. Common choices of field variables in microemulsion studies are the activity of added salt, alcohol or cosurfactant, temperature, pressure, hydrocarbon chain length, and chain length of the hydrocarbon moiety of the surfactant.

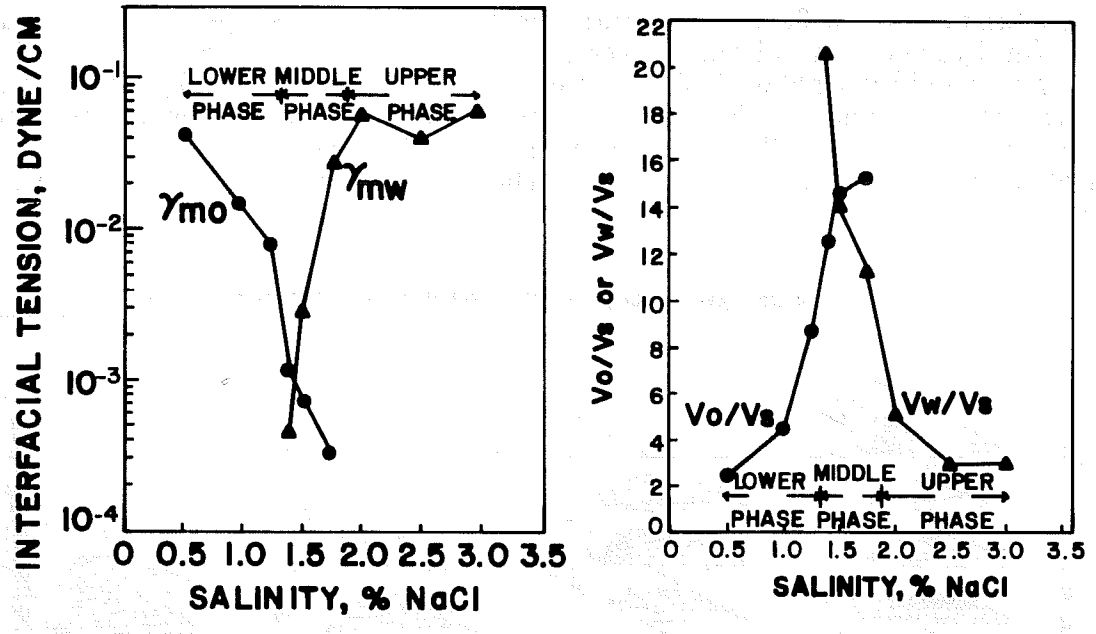

Figure 3. Interfacial tensions between microemulsion and oil-rich and water-rich phases. On the right is shown the ratio of volume of water or oil to volume of surfactant in the microemulsion phase. The system is a mixture of oil, NaCl brine, tertiary amyl alcohol, monoethanol amine salt of an alkylorthoxylene sulfonic acid. Composition is 4% surfactant and alcohol, 48% oil and 48% brine. Ref. 34.

The phase and tension behavior that has been observed can be summarized in terms of the generic patterns shown in Fig. 4. In Fig. 4, as Field Variable 1 increases from a low value, a middle or third phase appears, the 3-phase tie triangle springing from a critical endpoint tie line of the 2-phase system. As Field Variable 1 continues to increase, the middle phase progresses from water-rich to increasing oil-rich until the tie triangle collapses into a critical endpoint tie line of the 2-phase system. As one of the critical endpoints (CEP) is approached, the tension between middle phase and its near-critical partner of course approaches zero. As Field Variable 2 increases the two CEP's move together, i.e., the range of Field Variable 1 needed for a $\underline{2}$ to 3 to $\overline{2}$ scan is reduced. At sufficiently large Field Variable 2 the two CEP's collapse into a tricritical point (TCP). Since all three phases of the three-phase system become identical at the TCP, it follows that the tension at optimal salinities will decrease as Field Variable 2 is increased towards the TCP. Furthermore, as the three phases tend to become increasingly more alike it is reasonable to expect oil and water to be

equally welcome in the middle phase, i.e., to expect the oil-to-water ratio to tend towards unity as the TCP is approached. In the example shown in Fig. 2, Field Variable 1 is salinity (which should be converted to salt activity to be a proper field variable). Field Variable 2 is the alcohol which was added to advance the microemulsion towards the TCP and obtain ultra-low tension at optimal. The patterns represented in Fig. 2 have been verified for many field variables. For example, Bennett *et al.* [35] have observed the trends displayed in Fig. 4 with both a pure and a commercial alkylaryl sodium sulfonate surfactant with salinity as one field variable and carbon numbers as the other field variable (in hydrocarbon mixtures average carbon numbers have been found to function as field variables [36,37]. Kahlweit and coworkers [23-27] have demonstrated the patterns of Fig. 4 for ethoxylated alcohol-alkane-water mixtures with temperature and alkane carbon number as field variables. Kilpatrick *et al.* [19,20] have found them for alkane carbon number and ethoxylated alcohol homologous series.

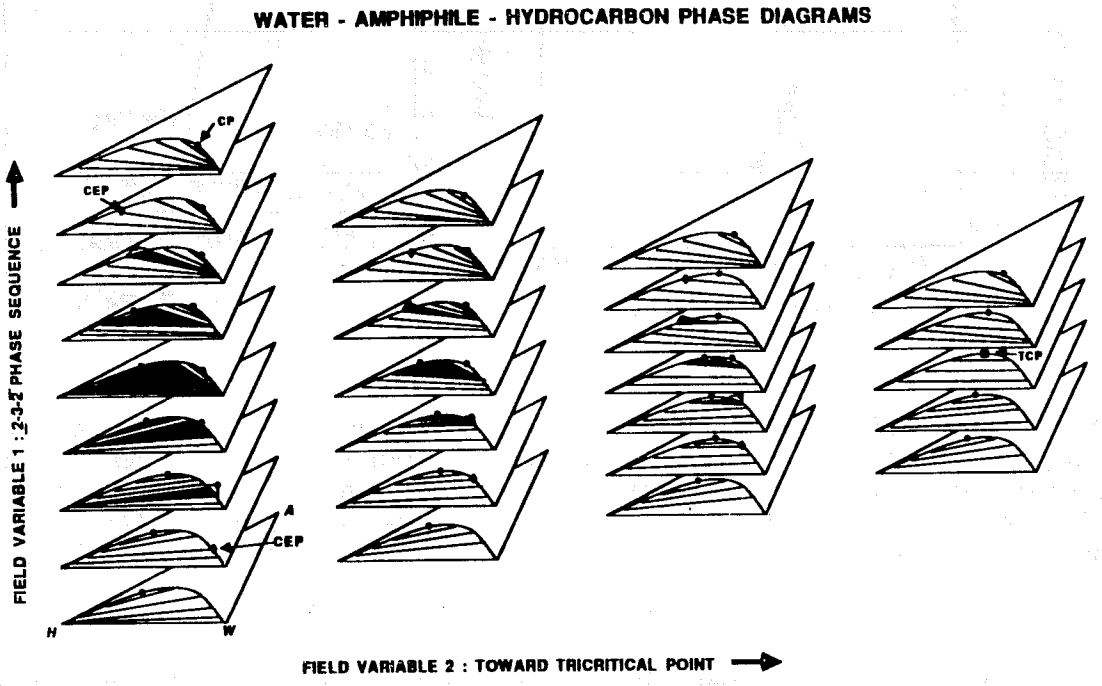

Figure 4. Generic progression of amphiphile, hydrocarbon, water ternary phase diagrams. Ref. 20.

To model microemulsion as an isotropic fluid with water-rich and oil-rich regions separated by sheet-like surfactant zones, Talmon and Prager [38,39] introduced the following statistical theory. They used the Voronoi polyhedral construction, Fig. 5, to randomly intersperse oil and water regions. They assumed that the surfactant lies entirely on the polyhedral faces separating the oil and water regions. The theory yields the purely entropic free energy density

$$f = ckT\left[\phi_0 ln\left(\frac{\omega c}{e}\phi_o\right) + \phi_w\, ln\left(\frac{\omega c}{e}\phi_w\right)\right], \tag{1}$$

where k is Boltzmann's constant, T the absolute temperature, ϕ_o and ϕ_w the oil and water volume fractions, c is the number density of Voronoi polyhedra, ω a volume parameter characteristic of the size scale of the microstructure of the microemulsion, and e the base of natural logarithms. The surfactant per unit volume c_s given by the formula

$$\begin{aligned} c_s &= 5.82\alpha_1 c^{1/3}\,\phi_o\phi_w - 17.52\alpha_2 c^{2/3}\,\phi_0\phi_w \\ &= [Ac^{1/3} - Bc^{2/3}]\phi_o\phi_w \ . \end{aligned} \tag{2}$$

In this expression, $5.82c^{1/3}\phi_0\phi_w$ is the mean area of oil-water boundary per unit volume and $17.52c^{2/3}\phi_0\phi_w$ is the mean edge length per unit volume of those Voronoi polyhedral faces that separate oil and water. The parameter α_1 gives the number of molecules per unit surfactant internal oil-water area.

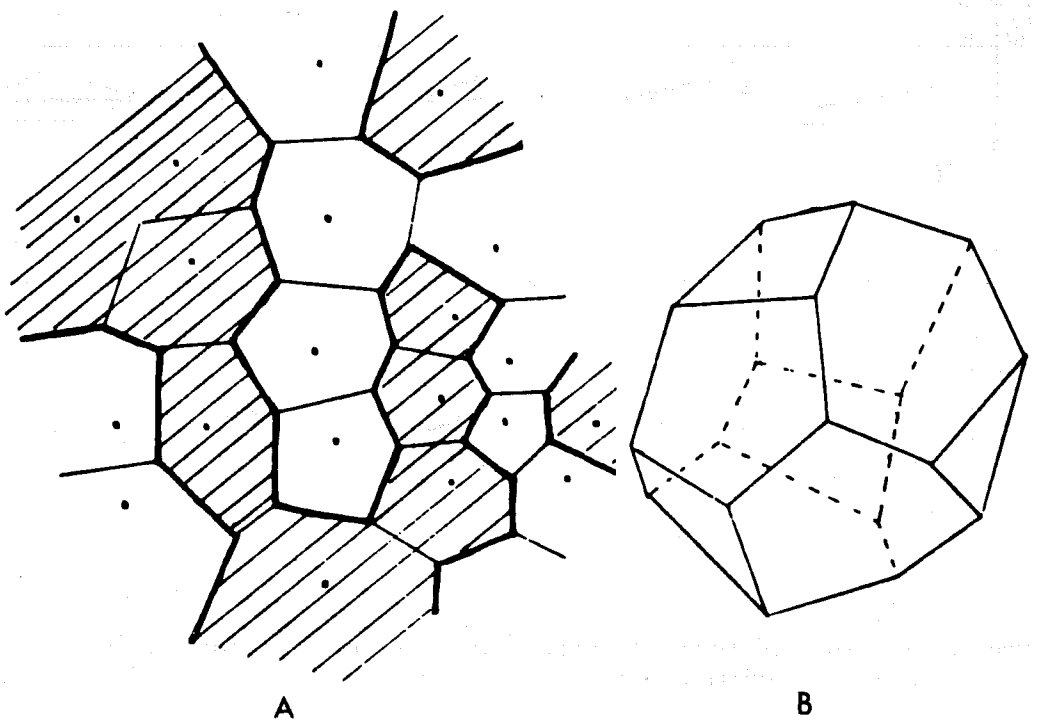

Figure 5. A Voronoi representation of a microemulsion. A) Two dimensional example. Shaded regions are occupied by oil-rich fluid, unshaded by water-rich material; heavy lines indicate the surfactant sheets. B) Typical Voronoi polyhedron. Ref. 38.

The amount of surfactant that can reside between oil and water regions

depends on the curvature of the surfaces dividing these regions. It is a mathematical artifact of the Voronoi tesselation that all the curvature lies along the polyhedral edges. Thus, the parameter α_2 represents the effect of curvature on the inventory of surfactant in the sheet-like surfactant zones.

In the Talmon-Prager theory $A = 5.82\alpha_1$ and $B = 17.5\alpha_2$ are adjustable parameters. Davis and Scriven [40] showed that the $2\bar{3}2$ phase sequence is predicted by the theory if it is assumed that $B = B_1 + B_2\,\phi_0$, where B_2 advances as field variable (see Fig. 6). If salinity is the field variable, the interpretation of Fig. 6 is that an increase in salinity increases the tendency of the sheet-like surfactant zones to curve into the water-rich regions.

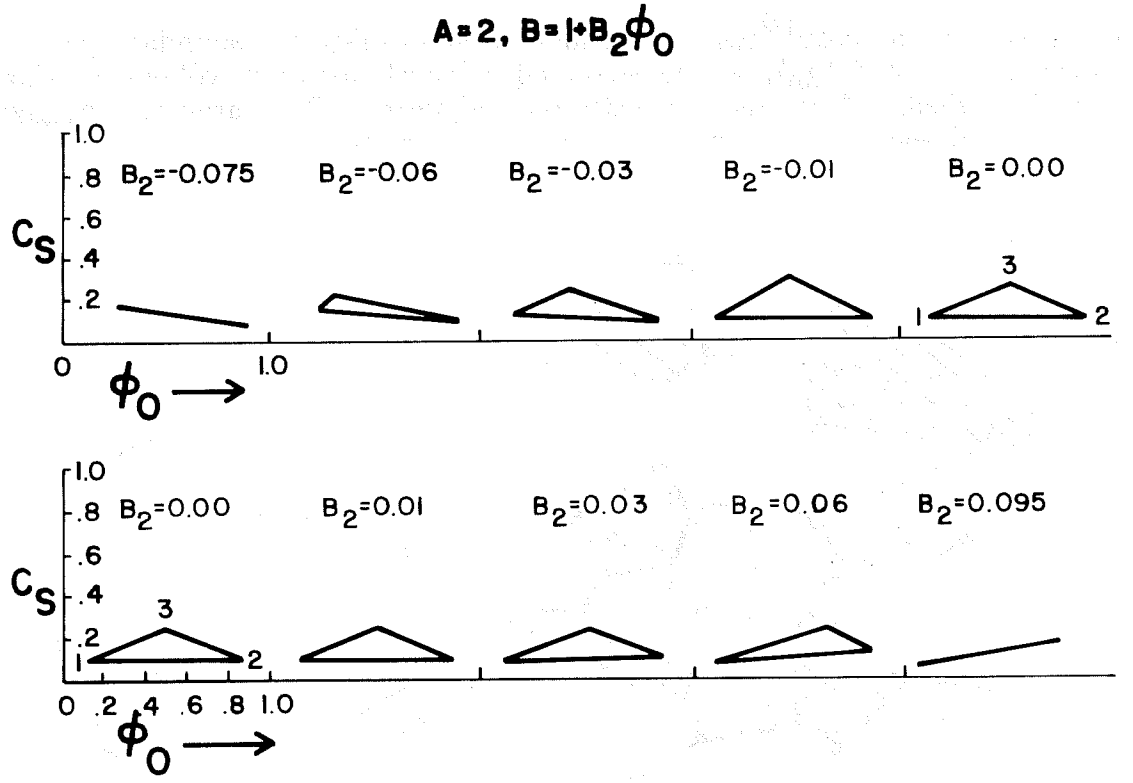

Figure 6. Sequence of ternary phase diagrams, opening and closing at critical end points (CEP), predicted by the Talmon-Prager model. Ref. 40.

Variations of the Talmon-Prager theory have been developed by de Gennes and coworkers [41] and by Widom [42]. de Gennes *et al.* [41] add to the theory the Schulman concept of zero internal film tension. In Widom's improvement of the theory, the characteristic size scale ω is obtained as a consequence of minimization of the free energy.

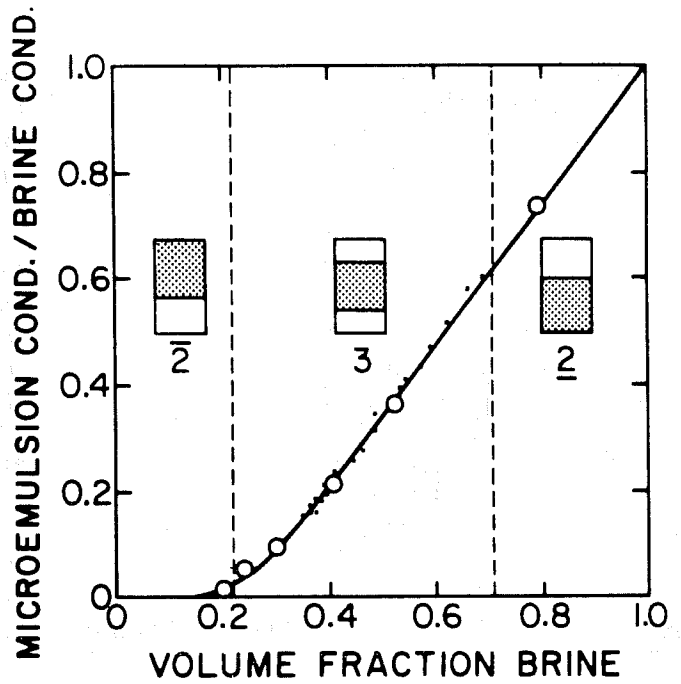

Figure 7. Conductivity versus volume fraction of brine in microemulsion phase. From a salinity scan of a Witco TRS 10-80 surfactant, tert-amyl alcohol (tAA), n-decane and NaCl brine. The surfactant is a commercial alkylaryl sodium sulfonate similar to SHBS. Ref. 32.

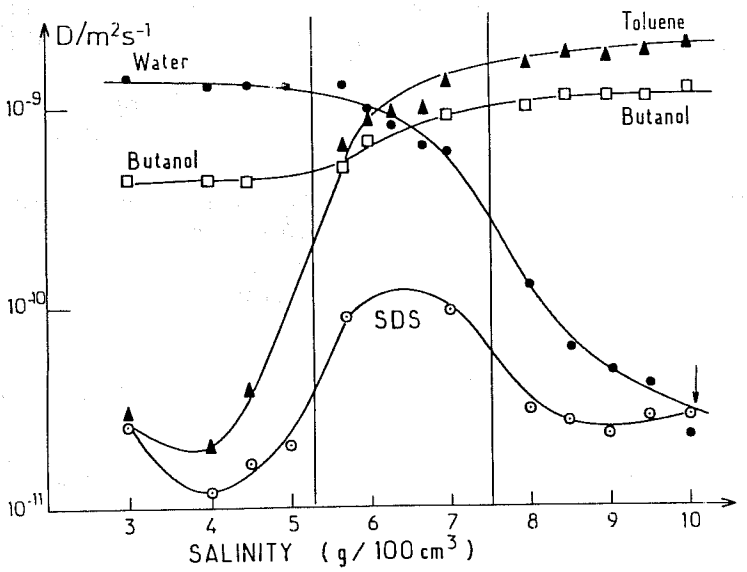

Figure 8. Diffusivities of components of SDS, butanol, toluene and NaCl brine mixture. Vertical lines denote 2̲3 and 3$\overline{2}$ phase transitions. Ref. 47.

If oil and water-rich regions are chaotically interspersed, it is a general prediction of percolation theory that there exists a volume fraction of water, ϕ_{wc} below which the oil-rich fluid is continuous, a volume fraction of oil, ϕ_{oc}, below which the water-rich fluid is continuous, and intermediate range of volume fractions in which the system is bicontinuous. The critical volume fractions are percolation thresholds, and, for the Voronoi tessellation, Monte Carlo simulations yield the estimate $\phi_{wc} = \phi_{oc} = 0.145$ [43]. The implication of the theory is that the electrical conductivity of a microemulsion should decrease dramatically as the water/oil ratio decreases to the value corresponding to percolation threshold. This expected behavior has been verified experimentally for many microemulsions [13,32,44-46]. In Fig. 7 we compare experimental conductivity results with those calculated in a Monte Carlo simulation [32,43] of a random oil-water interspersion on a Voronoi tessellation. Similar agreement has been obtained for several microemulsions. It should be noted that the percolation theory refers to the static interspersions. A microemulsion is a dynamic system and so the conductivity may be expected to have small but not zero value at the static percolation threshold. French researchers [45,46] have shown that dynamic effects are indeed present and have investigated these experimentally and explained them theoretically in terms of stirred percolation or mobile droplets.

Electrical conductivity cannot be used for probing the continuity of the oil-rich regions. However, self-diffusion provides such a probe and has indeed been pursued by several researchers using spin-echo pulsed-field gradient, NMR to measure the diffusivities of each component of a microemulsion. A good example of such a study is shown in Fig. 8.

The system is sodium dodecycl sulfate (SDS), butanol, brine and toluene. Similar studies have been independently reported by two groups [47,48]. The results indicate that at low salinity the oil and surfactant diffuse together as a swollen micelle and that at high salinity the water and surfactant diffuse together as a swollen inverted micelle. In the midrange we see a maximum in the surfactant diffusivity as would be expected of a bicontinuous microemulsion.

The data in Fig. 8 are consistent with the picture that as salinity is increased from a low there is a transition from a water-continuous swollen micellar solution to a bicontinuous microemulsion in an intermediate salinity range at the end of which there is a transition to an oil-continuous swollen inverted micellar solution.

At the 1986 conference on The Physics of Amphiphiles, Les Houches, France, R. Strey showed freeze-fracture electron micrographs that are convincing evidence that $C_{12}E_5$-octane-water microemulsions are also bicontinuous under certain conditions. Diffusivity evidence of bicontinuity in microemulsions involving $C_{12}E_5$ has also been presented. It appears then that bicontinuous microemulsions exist and that they are not restricted to ionic surfactant systems.

Viscosity is another special fingerprint of microemulsions [32,49]. A common pattern in a salinity scan is shown in Fig. 9. There are two peaks in between which there is a minimum. The minimum typically occurs at the optimal salinity, i.e., at the point of equal oil/water uptake in the microemulsion phase. In the several sodium sulfonate surfactant systems studied at Minnesota it appeared that the high salinity peak occurred near the percolation threshold as

corresponds to the percolation threshold at which oil becomes the discontinuous component.

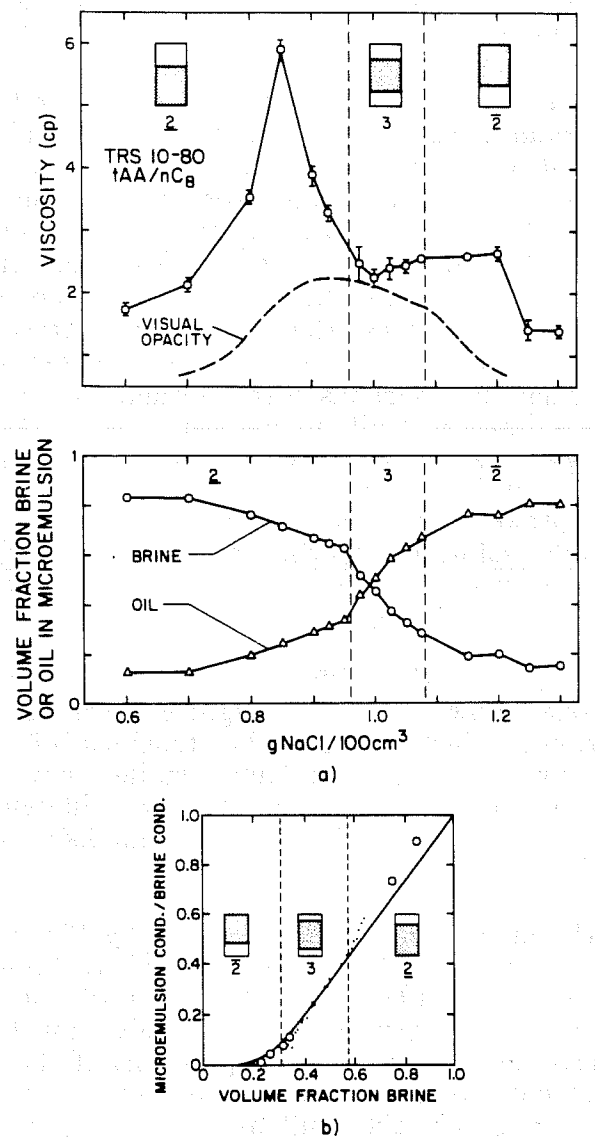

Figure 9. Microemulsion properties in a TRS 10-80/tAA/n-octane salinity scan. Ref. 32.

Near the viscosity peaks the microemulsion is somewhat nonNewtonian, shear thinning by a factor of about 2 to 5 at shear rates of 1000 sec^{-1}. Elsewhere the microemulsion is approximately Newtonian, although it is shear birefringent.

Alcohol-Brine-Hydrocarbon Solutions

The patterns of phase behavior shown in Fig. 4 have been observed for many monohydric alcohol solutions with brine and hydrocarbons [15,16,50,51]. Thus, the pattern is not specific to microemulsion systems, but rather is common to amphiphile, brine and hydrocarbon mixtures.

A natural question then is whether optimal tension and the state of equal water-to-oil uptake volumes coincide in alcohol, brine, and hydrocarbon solutions as they do in ultralow-tension microemulsions (Fig. 3). To answer the question, r researchers [17,18] in our laboratory studied the phase and tension behavior of solutions of brine and hydrocarbons with n-propanol and t-butanol. The results for n-propanol are summarized in Fig. 10. Similar results were obtained for the t-butanol solutions. In the figure γ_{ao} and γ_{aw} denote the tension of the alcohol-rich phase against the oil-rich and water-rich phases, respectively. V_o, V_w and V_a denote the volumes of oil, water and alcohol in the alcohol-rich phase. The hydrocarbons were normal alkanes. Thus, the field variables scanned are salinity and alkane carbon number. With decreasing carbon number the range of salinity needed to accomplish the $2\overline{3}2$ phase scan decreases, the optimal tension decreases and the salinities of optimal tension and equal oil/water uptake volumes approach one another. From this we conclude that, qualitatively, solutions of brine, oil and monohydric alcohols, which are amphiphiles but not surfactants, exhibit the same trends of phase *and* tension behavior as do microemulsion systems.

There are, however, quantitative differences. The volume uptake ratios near optimal salinity are one or two orders of magnitude smaller in alcohol systems than in microemulsions. Furthermore, the tensions of microemulsions at optimal are typically two orders of magnitude smaller than optimal tensions of the alcohol systems. We believe these quantitative differences arise from the microstructure of microemulsions and in fact distinguish them from solutions containing mere amphiphiles.

According to the thermodynamic theory implied by Fig. 4, ultralow tensions are achieved at optimal salinity by adjusting field variables to move in the direction of a tricritical point (TCP). In the light of the near-critical point interpretation, it is at first surprising that the ultralow tensions (0.01-0.001 dyn/cm) can be achieved even when the compositions of the oil-rich and water-rich phases differ markedly from that of the microemulsion phase. As pointed out in the preceding paragraph, these ultralow tensions are in contrast to the low tension of water-hydrocarbon-alcohol mixtures, even though the phase compositions in the alcohol system are closer to each other than in the microemulsion systems.

This quantitative difference can be understood in terms of the special microstructure of microemulsions. In the near-critical regime, the Talmon-Prager theory [39] predicts that the interfacial tension obeys the asymptotic formula

$$\gamma \sim 0.175 kT |\phi_w^2 - \phi_w^1|^3 / \xi^2 \qquad (3)$$

where T is temperature. k is Boltzmann's constant, ϕ_w^i is the volume fraction of water in phase i, and $\xi = \omega^{1/3}$ is a length scale characteristic of the microstructure of the solution.

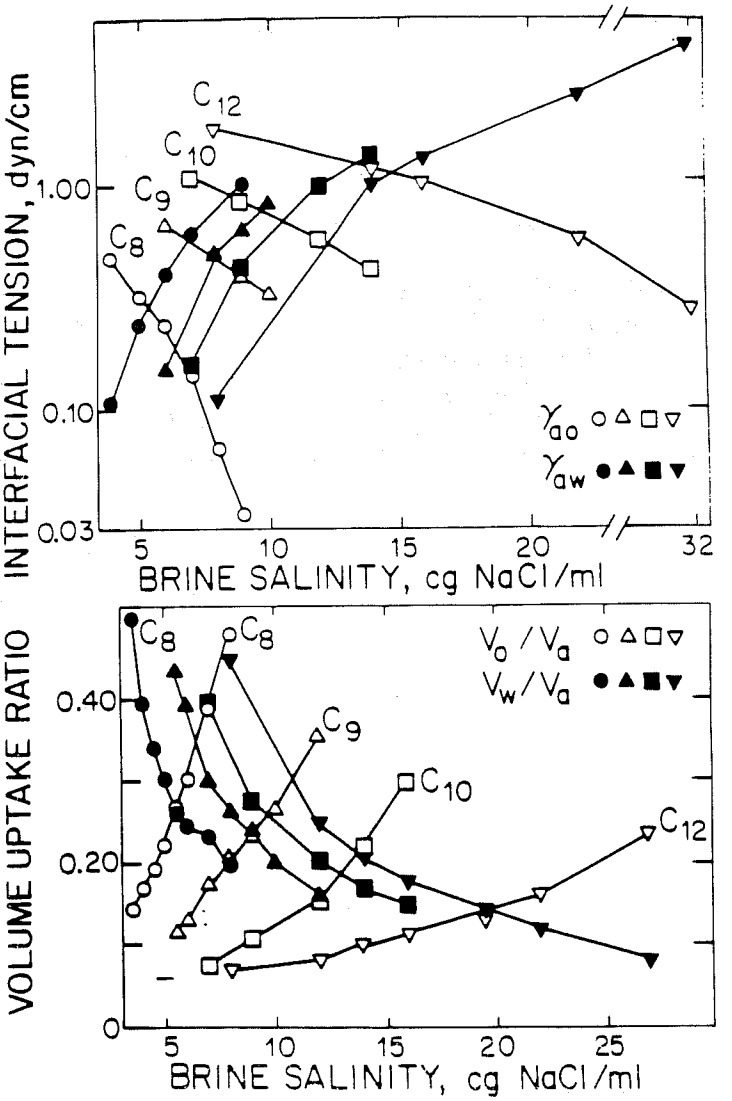

Figure 10. Salinity scans of interfacial tensions and volume uptake ratios versus brine salinity as a function of alkane chain length for mixtures of equal volumes of n-propanol hydrocarbon and brine. Ref. 18.

Typically in light scattering or small angle X-ray or neutron scattering experiments values of the order of 10 nm are deduced in microemulsions [44, 52]. On the other hand in molecular solutions of oil, water and alcohol there is no appreciable aggregation and so ξ is of the order of molecular sizes, say 1 nm. Thus, from Eq. (3) it follows that at the same distance from a critical point, as measured by the value of $(\phi_w^1 - \phi_w^2)$, the tension of a microemulsion system is

about two orders of magnitude smaller than that of a simple alcohol-water-oil system, in agreement the observed differences between alcohol and microemulsion systems.

That the values of the volume uptake of water and oil in microemulsion systems are one to two orders of magnitude higher than in alcohol systems is the result of the "packaging" ability of the sheet-like surfactant structures present in microemulsions but absent in alcohol solutions.

C_4E_1 and C_6E_2—Brine—Hydrocarbon Solutions

If n and m are sufficiently large, C_nE_m is known to be a full-fledged surfactant. We want to know to what degree do the amphiphiles C_4E_1 and C_6E_2 behave as surfactants. Let us first examine C_4E_1. Several properties of C_4E_1 in water and brine have been studied with the aim of discovering micellization tendencies. One of these is the leveling off of the surface tension at amphiphile concentrations above some critical value, as occurs at the critical micelle concentration (CMC) of a surfactant. This indeed happens as is shown in Fig. 11. The surface tension changes very little beyond a C_4E_1 mole fraction of about 0.02. Substituting 0.2M NaCl brine for water changes the results negligibly.

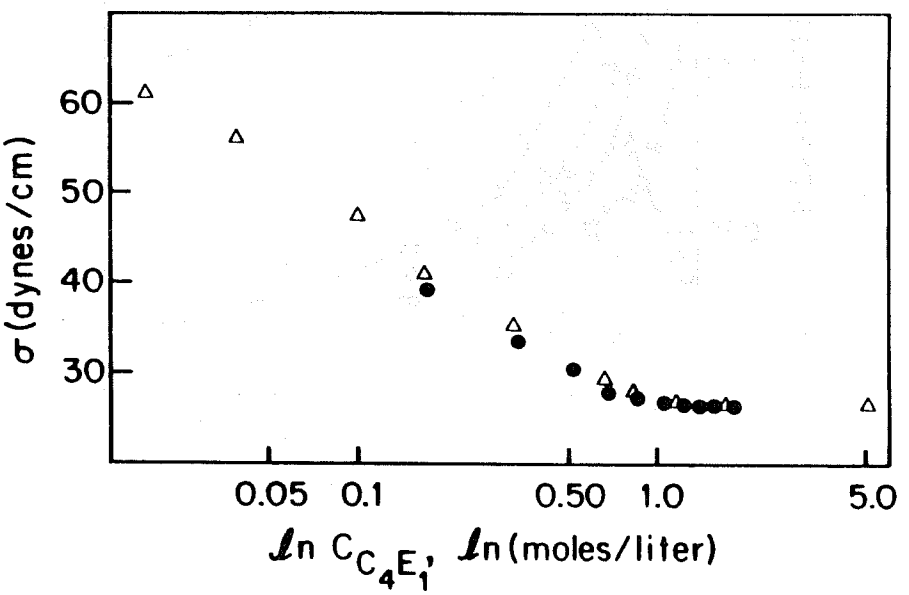

Figure 11. Surface tension of aqueous solution versus logarithm of molar concentration of C_4E_1 in water (open triangles) and 0.2M NaCl brine(filled circles) at 25 ° C. Ref. 21.

The ^{13}C NMR chemical shift is often used to estimate the CMC, at which concentration there is an abrupt change in the chemical shift. A fairly sharp change in the chemical shift is evident in the data shown in Fig. 12 at a C_4E_1 mole fraction of about 0.02. The water and brine results are indistinguishable within experimental error.

As is summarized in Table 1, several physical properties of aqueous solutions of C_4E_1 have been observed to change abruptly with C_4E_1 concentration at a mole fraction of about 0.02. Thus, on the basis of these properties it appears that there is significant molecular aggregation suddenly occurring when a critical mole fraction is reached, similarly to what happens in micellization.

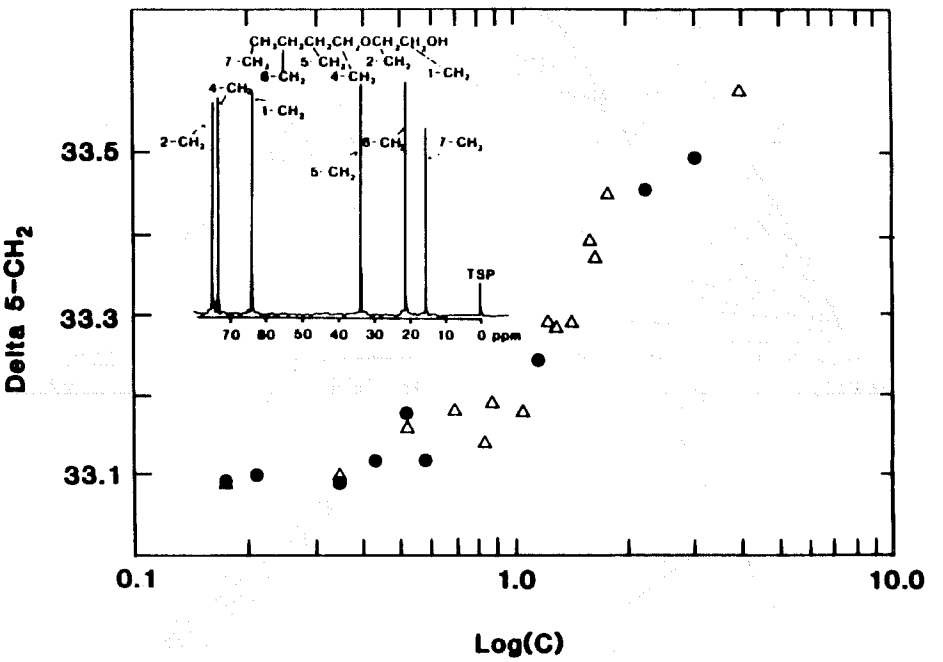

Figure 12. ^{13}C NMR chemical shift of 5-CH_2 carbon versus logarithm of molar concentration of C_4E_1 in water (open triangles) and 0.2 M NaCl brine (filled circles) solutions. Ref. 21.

Table 1. Physical properties changing abruptly at a C_4E_1 mole fraction of about 0.02 in water.

PROPERTY	TECHNIQUE	REFERENCE
Partial molar volume	Densitometry	Refs. 53, 54
Partial molar heat capacity	Microcalorimetry	Refs. 53, 54
Relaxation frequency	Ultrasonic absorption	Refs. 55
Diffusion coefficient	Quasielastic light scattering	Ref. 56
Raman spectra	Raman spectroscopy	Ref. 57
Partial molar refractive index	Refractometry	Ref. 21
Surface tension	Ring tensiometry	Ref. 21
Paramagnetic shielding	C^{13}NMR chemical shift	Ref. 21

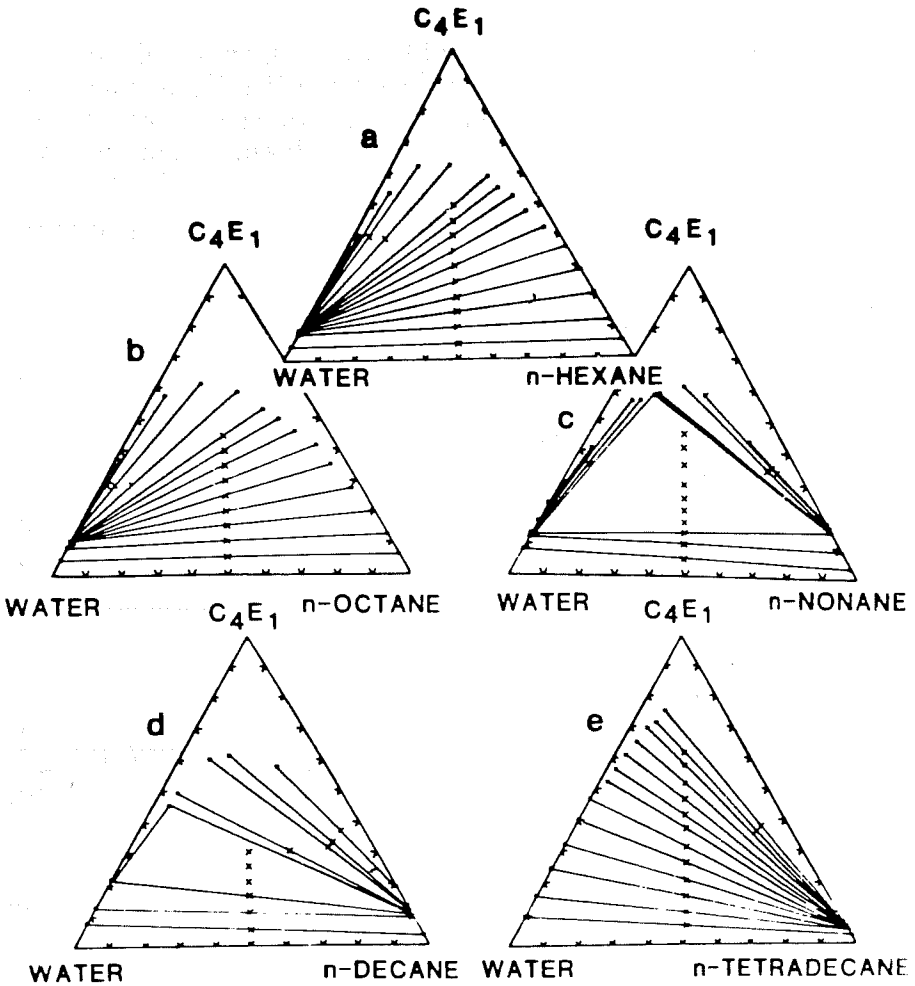

Figure 13. Ternary phase diagrams of C_4E_1, n-alkane, water solutions at 25 ° C. Compositions are in wt%, x's denote mixpoints, and ends of straight lines or vertices of triangles denote two or three phase compositions. Ref. 20.

Next consider the behavior of solutions of C_4E_1, water or brine, and hydrocarbons. Kahlweit *et al.* [25,26] have shown that C_4E_1-water-decane mixtures exhibit the $2\overline{3}2$ sequence as a function of temperature, the three-phase triangle opening at a water-rich critical endpoint (CEP) at about 23 ° C and closing at an oil-rich CEP at about 50 ° C. The trend with carbon number is shown in Fig. 13. The $2\overline{3}2$ phase sequence is again followed (with decreasing carbon number) except, of course, the discreteness of the carbon number variation does not allow a continuous scan through the CEP's.

We saw earlier that the electrical conductivity of a microemulsion passes through a percolation threshold if the water fraction drops to a sufficiently low value. In Fig. 14 the equivalent conductance is plotted versus weight percent brine along a composition path passing through the points 2,3,...,6 in Fig. 15. The equivalent conductance becomes very small below a brine fraction of about 2% by weight. This is qualitatively similar to microemulsion percolation behavior, although microemulsion percolation thresholds are usually about 10 or 15%.

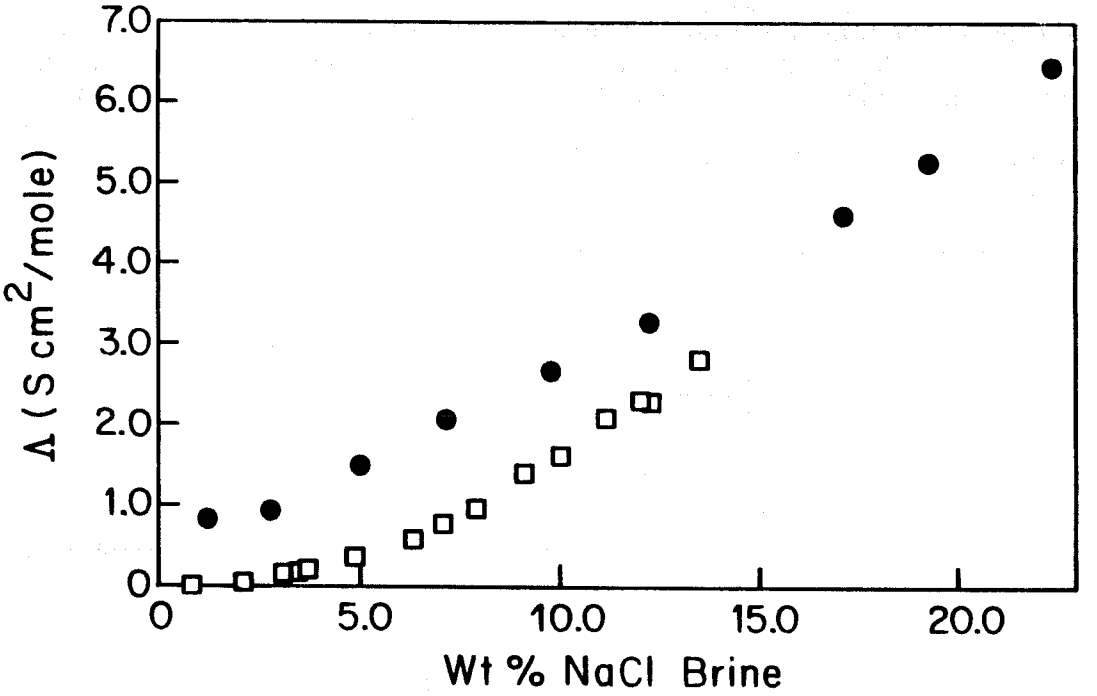

Figure 14. NaCl equivalent conductance of binary C_4E_1-brine (filled circles) and ternary C_4E_1-n-decane-brine mixtures (open squares). Ref. 21.

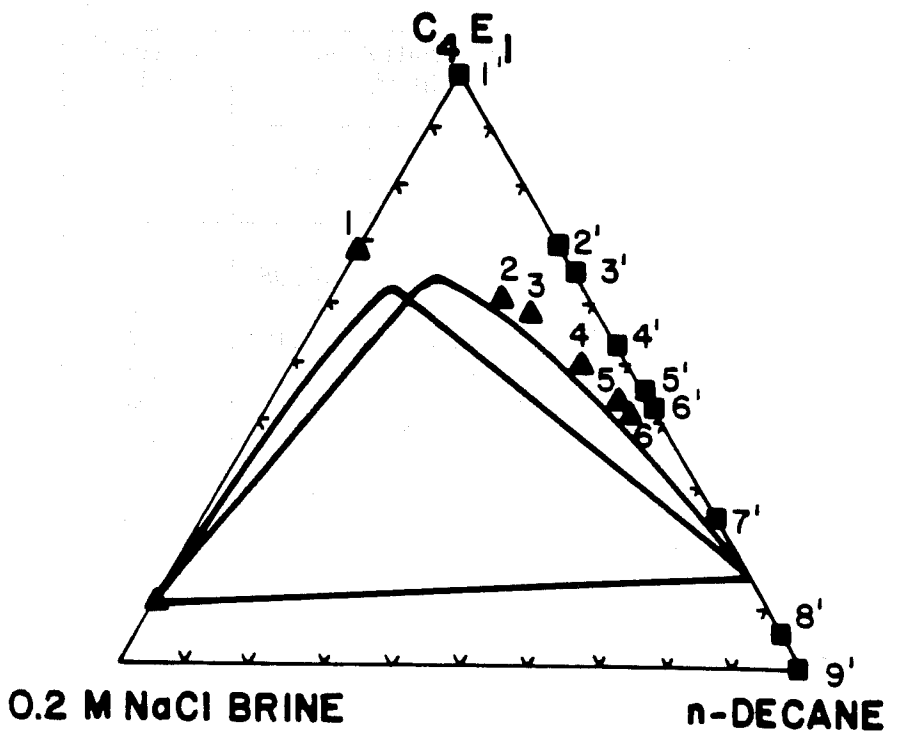

Figure 15. Pseudoternary phase diagram at 25 °C. Compositions are given in weight percent. Ref. 20.

Another characteristic property of microemulsions is that quasielastic light scattering (QLS) indicates large diffusive microdomains (of the order of 10nm) of refractive index heterogeneities, arising presumably from the microstructure of the fluid. In Table 2 are given diffusivities of the microdomains deduced by QLS for the compositions 1-6 shown in Fig. 15. They are quite low in view of the viscosities (Table 3) of the solution. The implication is that the microdomains are rather large compared to molecular dimensions.

Table 2. QLS results for 0.2M NaCl brine, C_4E_1, and normal decane mixtures. Ref. 21.

Solution #	D $Dx10^7$	R_H (A)
1	10	5.4
2	2.8	27
3	5.6	15
4	4.9	20
5	5.9	20
6	4.0	31

Table 3. Compositions and viscosities of 0.2M NaCl brine, C_4E_1 and normal decane mixtures. Refs. 21,22.

Solution #	Composition (Weight %)			Viscosity (cP)
	Brine	Decane	C_4E_1	
1	30.92	0	69.08	4.13
2	13.14	26.60	60.26	2.84
3	12.06	30.76	57.18	2.67
4	8.68	41.96	49.30	2.29
5	5.82	51.41	42.77	1.89
6	5.17	52.82	42.01	1.75
1′	0	0	100	2.83
2′	0	30.45	69.55	1.69
3′	0	35.02	64.97	1.67
4′	0	45.99	54.01	1.43
5′	0	53.96	46.04	1.28
6′	0	55.56	44.44	1.22
7′	0	74.97	25.03	1.02
8′	0	95.02	4.98	0.85
9′	0	100	0	0.84

If we assume that the domains obey the Stokes-Einstein law, then the radius R_H of a domain can be estimated from

$$R_H = \frac{kT}{6\pi\eta D} \quad , \tag{4}$$

where η is the viscosity and D is the diffusivity. The radius so-derived is large compared to the diameters of the fluid molecules, even in the decane-free case (#1).

If we were to stop at this point in the examination of the properties of the C_4E_1 solutions, it would be reasonable to designate C_4E_1 as a surfactant owing to (1) the implications of spontaneous aggregation implied by the measurements summarized in Table 1, (2) the patterns of ternary phase behavior, (3) the percolation threshold of the conductivity and (4) the microdomain sizes deduced from QLS. However, in a QLS experiment, scattering objects are tracked for microseconds only. In the micellar or swollen micellar (or inverted micellar) regimes of microemulsions, the self-diffusivities of the surfactant and the component dissolved in the micelle (or inverted micelle) are approximately the same and are similar to the QLS diffusivity. This is not the case for the C_4E_1 system. Self-diffusivities determined by spin echo, pulsed field gradient NMR (SEPFG NMR) are given in Table 4 for the composition path 1-6 and along the water-free path $1'$ - $9'$ shown in Fig. 15. The SEPFG NMR measurements were made for two diffusion times, 40 msec and 300 msec, and the results were the same to within the 1% error in the reproducibility of the experiments.

The Stokes radii for all the components are consistent with simple molecular diffusion. In fact the Stokes radius of C_4E_1 varys very little with solution composition, including the cases of pure C_4E_1 and its binary solutions with oil and water. Thus, the molecular association responsible for the results of Table 1 and the microdomains responsible for the light scattering have too short a life time or are too small in population to affect significantly the diffusive migration of the molecules of the solution. This is in sharp contrast to micellar solutions and microemulsions. On this basis then we judge that at $n = 4$ and $m = 1$, C_nE_m has not quite made it to the status of surfactant and is not quite capable of forming a microemulsion. Nevertheless, it does exhibit many of the patterns associated with surfactants and microemulsions.

A similar, but not as detailed analysis has been made for solutions of C_6E_2 with brine and dodecane. The QLS and SEPFG NMR results are given in Tables 5-7 for the composition paths labelled in Fig. 16. Again, although the QLS indicates microdomains larger than molecular sizes we see that, as in the case of the C_4E_1 solutions, these domains do not appreciately retard molecular diffusivity.

Table 4. SEPFG NMR results for 0.2M NaCl brine C_4E_1, and normal decane mixtures. Ref. 22.

	H_20		n-decane		C_4E_1	
Solution #	$Dx10^7$ (cm^2/sec)	R_H (A)	$Dx10^7$ (cm^2/sec)	R_H (A)	$Dx10^7$ (cm^2/sec)	R_H (A)
1	44	1.2	-	-	26	2.0
2	53	1.5	52	1.5	37	2.1
3	48	1.7	57	1.4	39	2.1
4	47	2.0	71	1.3	45	2.1
5	-	-	84	1.3	49	2.3
6	-	-	87	1.4	53	2.3
1′	--		-	-	39	2.0
2′	-	-	-	-	63	2.1
3′	-	-	-	-	65	2.0
4′	-	-	-	-	81	1.9
5′	-	-	-	-	83	2.0
6′	-	-	-	-	88	2.0
7′	-	-	-	-	110	1.9
8′	-	-	-	-	142	1.8
9′	-	-	159	-	-	-

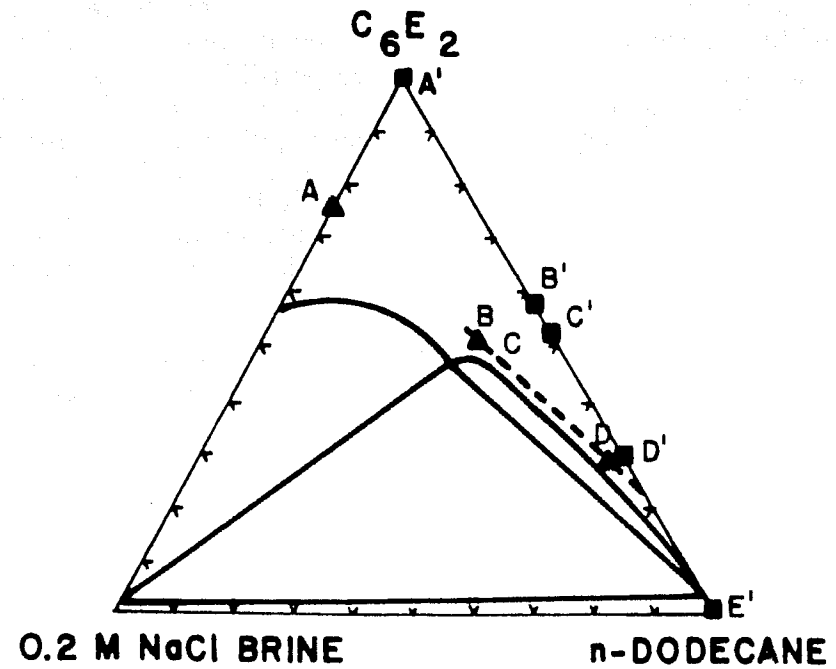

Figure 16. Pseudoternary phase diagram at 25 ° C. Compositions are given in weight percent. Ref. 20.

Table 5. Compositions and viscosities of 0.2M NaCl brine, C_6E_2 and normal dodecane mixtures. Ref. 21,22.

Solution #	Composition (Weight %)			Viscosity (cP)
	Brine	Dodecane	C_6E_2	
A	24.61	0	75.39	9.31
B	13.71	36.56	49.73	5.66
C	12.74	40.80	46.46	5.23
D	3.80	68.16	28.04	2.45
A′	0	0	100	6.8
B′	0	43.01	56.99	2.97
C′	0	47.28	52.72	2.76
D′	0	71.86	28.14	1.87
E′	0	100	0	1.34

Table 6. QLS results for 0.2M NaCl brine, C_6E_2 and normal dodecane mixtures. Ref. 21.

Solution #	D $Dx10^7$	R_H (A)
A	6.2	3.8
B	5.3	7.1
C	5.2	7.4
D	3.6	25.7

Table 7. SEPFG NMR results for 0.2M NaCl brine, C_6E_2 and normal dodecane mixtures. Ref. 22.

	H_20		Dodecane		C_6E_1	
Solution #	$Dx10^7$ (cm^2/sec)	R_H (A)	$Dx10^7$ (cm^2/sec)	R_H (A)	$Dx10^7$ (cm^2/sec)	R_H (A)
A	51	0.5	-	-	11.8	2.0
B	31	0.5	44	0.9	16.5	2.3
C	25	1.7	51	0.8	18.2	2.3
D	-	-	117	0.8	40	2.2
A′	-	-	-	-	15	2.1
B′	-	-	-	-	31	2.4
C′	-	-	-	-	35	2.3
D′	-	-	-	-	45	2.6

References

1. IUPAC Manual of Symbols and Terminology, Pure and Appl. Chem. *31*, No. 4, 577 (1972).
2. Shinoda, K., Nakagawa, T., Tamamushi, B. I., and Isemura, T., *Colloidal Surfactants. Some Physicochemical Properties* (Academic Press, New York 1963).
3. Rosen, M. J., *Surfactants and Interfacial Phenomene* (Wiley-Interscience, New York 1978).
4. Lindman, B. and Wennerstrom, H., Topics in Current Chemistry **87**, 3 (1980).
5. Laughlin, R. G.: *In advances in Lipid Crystals*, Vol. 3, ed. by G. H. Brown (Academic Press, New York 1978) p. 41.
6. Hoar, T. P., and Schulman, J. H., Nature **152**, 102 (1943).
7. Schulman, J. H., and Riley, D. P., J. Colloid Sci. **3**, 383 (1948).
8. Schulman, J. H., and Friend, J. A., J. Colloid Sci. **4**, 497 (1949).
9. Schulman, J. H., Stoeckenius, W., and Prince, L. M., J. Phys. Chem. **63**, 167 (1959).
10. Scriven, L. E., Nature **263**, 123 (1976).
11. Scriven, L. E.: In *Micellization, Solubilization and Microemulsions*, ed. by K. L. Mittal (Plenum, New York 1977) p. 877.
12. Composed by Michels, W. F., Ph.D. Thesis, University of Minnesota, 1987, using a schematic phase diagram published in Ref. 11, and combining cartoons of microstructures published in Ref. 13 and 14 with some newly drawn ones.
13. Hatfield, J. C., Ph.D. Thesis, University of Minnesota, 1978.
14. Brown, G. H., Doane, J. W., and Neff, V. D., *A Review of the Structure and Physical Properties of Liquid Crystals*, (CRC Press, Cleveland, Ohio 1971).
15. Knickerbocker, B. M., Pesheck, C. V., Scriven, L. E., and Davis, H. T., J. Phys. Chem. **83**, 1984 (1979).
16. Knickerbocker, B. M., Pesheck, C. V., Davis, H. T., and Scriven, L. E., J. Phys. Chem. **86**, 393 (1982).

17. Puig, J. E., Ph.D. Thesis, University of Minnesota, 1982.
18. Puig, J. E., Hemkeť, D. C., Gupta, A., Davis, H. T., and Scriven, L. E., J. Phys. Chem. **91**, 1137 (1987).
19. Kilpatrick, P. K., Ph.D. Thesis, University of Minnesota, 1983.
20. Kilpatrick, P. K., Gorman, C. A., Davis, H. T., Scriven, L. E., and Miller, W. G., J. Phys., Chem. **90**, 5292 (1986).
21. Kilpatrick, P. K., Davis, H. T., Scriven, L. E., and Miller, W. G., J. Colloid and Interface Sci. (to appear 1987).
22. Bodet, J. F., Davis, H. T., Scriven, L. E., and Miller, W. G., J. Colloid and Interface Sci. (submitted).
23. Kahlweit, M., Lessner, E., and Strey, R., J. Phys. Chem. **87**, 5032 (1983).
24. Kahlweit, M., Lessner, E., and Strey, R., J. Phys. Chem. **88**, 1937 (1984).
25. Kahlweit, M., Strey, R., and Haase, D., J. Phys. Chem. **89**, 163 (1985).
26. Kahlweit, M., Strey, R., Firman, P. and Haase, D., Langmuir **1**, 281 (1985).
27. Kahlweit, M., Strey, R., Firman, P., J. Phys. Chem., **90**, 671 (1986).
28. Nilsson, P. G., and Lindman, B., J. Phys. Chem. **88**, 4764 (1984).
29. Olsson, U., Shinoda, K. and Lindman, B., J. Phys. Chem. **90**, 4083 (1986).
30. Shinoda, K., and Saito, H., J. Colloid and Interface Sci. **26**, 70 (1968).
31. Shinoda, K., Prog. Colloid Polym. Sci. **68**, 3 (1983).
32. Bennett, K. E., Hatfield, J. C., Davis, H. T., Macosko, C. J. and Scriven, L. E.: In *Microemulsions*, ed. by I. D. Robb (Plenum, New York 1982), p. 65; K. E. Bennett, Ph.D. Thesis, University of Minnesota, 1985.
33. Reed, R. L., and Healy, R. N.: In *Improved Oil Recovery by Surfactant and Polymer Flooding*, ed. by D. O. Shah and R. S. Schechter (Academic Press, New York 1977). p. 383.
34. Healy, R. N., Reed, R. L., and Stenmark, D. C., Soc. Pet. Eng. J. **16**, 147 (1976).
35. Bennett, K. E., Phelps, C. H. K., Davis, H. T. ,and Scriven, L. E., Soc. Pet. Eng. J. **21**, 747 (1981).
36. Salager, J. L., Morgan, J. C., Schechter, R. S., Wade, W. H., and Vazquez, E., Soc. Pet. Eng. J. **19**, 107 (1979).
37. Salager, J. L., Bourrel, M., Schechter, R. S., and Wade, W. H., Soc. Pet. Eng. J. **19**, 271 (1979).
38. Talmon, Y. and Prager, S., J. Chem. Phys. **69**, 2984 (1978).
39. Talmon, Y. and Prager, S., J. Chem. Phys. **76**, 1535 (1982).
40. Davis, H. T., and Scriven, L. E., Soc. Pet. Eng. Reprint # 9278, 55th Annual Fall Technical Conference and Exhibition of the SPE of AIME, Dallas, TX, 1980.
41. de Gennes, P. G., and Taupin, C., J. Phys. Chem. **86**, 2294 (1982); J. Jouffroy, P. Levinson and P. G. de Gennes, J. Physique **43**, 1241 (1982).
42. Widom, B., J. Chem. Phys. **81**, 1030 (1984).
43. Jerauld, G. R., Scriven, L. E., and Davis, H. T., J. Phys. Chem. **17**, 3429 (1984).
44. Kaler, E. W., Bennett, K. E., Davis, H. T., and Scriven, L. E., J. Chem. Phys., **79**, 5673 (1983); J. Chem. Phys. **79**, 5685 (1983).
45. Lagues, M., Ober, R. and Taupin, C., J. Physique Lett. **39**, L487 (1978); M. Lagues, J. Physique Lett. **40**, L331 (1979).
46. Lagourette, B., Peyrelasse, J., Boned, C. and Clausse, M., Nature **281**, 60 (1979).
47. Guering, P. and Lindman, B., Langmuir **1**, 464 (1985); D. Dhatenay, P. Guering, W. Urbach, A. M. Cazabat, D. Langevin, J. Meunier, L. Leger, B. Lindman, 5th Int. Symp. on Surfactants in Solution, Bordeaux, France,

July, 1984.
48. Clarkson, M. T., Beaglehole, D. and Callaghan, P. T., Phys. Rev. Lett. **54**, 1722 (1985).
49. Papaioannou, A. T., Scriven, L. E., and Davis, H. T.: In *Proceedings of 5th International Symposium on Surfactants in Solution,* 1984, ed. by K. Mittal and P. Botherel.
50. Lang, J. C., and Widom, B., Physica A **81**A, 190 (1975); J. C. Lang, P. K. Lim and B. Widom, J. Phys. Chem, **80**, 1719 (1976).
51. Kahlweit, M. and Strey, R., Angew. Chem. Int. Ed: Engl. **24**, 654 (1985).
52. Chang, N. J., Billman, J. F., and Lickliden, R. A.: In *Statistical Thermodynamics of Micellar and Microemulsion Systems,*, ed. by S. H. Chen (Springer-Verlag 1986).
53. Roux, G., Perron, G., and Desnoyers, J. E., J. Phys. Chem. **82**, 966 (1978).
54. Roux, G., Perron, G, and Desnoyers, J. E., J. Soln. Chem. **7**, 639 (1978).
55. Nishikawa, S., Tanaka, M., and Mashima, M., J. Phys. Chem. **85**, 686 (1981).
56. Ito, N, Saito, K., Kato, T., and Fujiyama, T., Bull. Chem. Soc. Jpn. **54**, 991 (1981).
57. Ito, N., Fujiyama, T., and Udagawa, Y., Bull. Chem. Soc. Jpn. **56**, 379 (1983).

2. CONTROLLED ENVIRONMENT VITRIFICATION SYSTEM: ELECTRON MICROSCOPY OF SURFACTANT SYSTEMS

Synopsis

Cryofixation of liquid samples for electron microscopy is facilitated by the Controlled Environment Vitrification System (CEVS). The CEVS permits cryofixation of hydrated biological and colloidal dispersions and aggregates from a temperature and saturation controlled environment. Specimens prepared in uncontrolled laboratory atmosphere are subject to evaporation and temperature fluctuations that may introduces artifacts due to concentration, pH, ionic strength and temperature changes. Moreover, it is difficult to examine microstructure of systems when conditions of interest are at temperatures other than ambient (e.g. biological systems at *in-vivo* temperatures). The system described here ensures that a liquid or partially liquid specimen is maintained in its original state while it is being prepared prior to vitrification, and once prepared, vitrified with minimal alteration of its microstructure. A controlled environment is provided within a chamber where temperature and chemical activity of volatile components can be precisely controlled while the specimen is being prepared. The specimen is mounted on a plunger, and a synchronous shutter is opened almost simultaneously with the release of the plunger, so the specimen is propelled abruptly through the shutter opening into a cryogenic bath. We describe the system and its use, and illustrate the importance of the technique with TEM examples of vesicles and liposomes of surfactants where artifacts were avoided by using the CEVS. We also discuss applications to other techniques like SEM and freeze-fracture, and to novel "on the grid" experiments that make it possible to freeze successive instants of dynamical processes such as membrane fusion, chemical reactions, and phase transitions.

Introduction

Specimen preparation has long been recognized as the most complicated step in the electron microscopy (EM) of fluid, labile systems, like biological and colloidal dispersions and aggregates. While EM has the potential of providing high resolution images for study of morphology (size, shape, form), connectivity, topography and texture, and, with analytical techniques, chemical composition, the high vapor pressure, low viscosity (leading to motion), susceptibility to electron beam induced damage, and low contrast in organic systems have prevented sub-nanometer resolution. Since the pioneering days of Ruska, much effort has been directed towards developing techniques for viewing labile systems by transmission and scanning microscopy with minimal changes to the specimen. These techniques, known generally as "fixation," address the problems of lowering vapor pressure, preventing motion, reducing electron-beam induced damage, and, in conjunction with staining, enhancing contrast.

All fixation techniques may produce artifacts (i.e. changes in morphology, composition, or texture), and some fixation techniques produce phase changes that may introduce microstructure not present in the original sample. The microscopist must judiciously select the technique that reduces artifact formation and prevents phase change. While negative-staining and chemical fixation techniques may still find use, the current method of choice for fixing labile

systems is well recognized to be thermal, i.e. cryofixation. Cryofixation with vitrification (i.e. rapidly cooling a liquid without detectable crystallization into a highly viscous, low vapor pressure, glassy state) prevents phase separation, rearrangement, artifact formation due to crystal growth, and problems of electron optics associated with a crystalline matrix (e.g. bend contours, thickness fringes, moire fringes, and contrast reversal). Adrian et al.[1] (1984) were the first to demonstrate a practical method to vitrify thin specimens of water or aqueous dispersions for TEM. Fast cooling was achieved by plunging a thin layer of specimen on a holey-film-covered or a bare electron microscope grid into liquid ethane at its melting point. A detailed description of fast freezing techniques is given by Newbury *et al.*[2] Elder *et al.*[3] have discussed various plunge-cooling methods and necessary precautions to obtain high cooling rates. The thin-film vitrification technique has been applied to the TEM study of a large variety of samples by several researchers: Lepault *et al.*[4] (1983) (phages, catalase), Lepault[5](1984), Downing[6] (1984) (electron diffraction from DNA platelet crystals), Milligan *et at.*[7] (1984) (ribosomes, bladder membranes, gap junctions), Talmon[8] (1986) (natural and synthetic liposomes and vesicles), and Bellare *et al.*[9] (1986) (surfactant liposomes, vesicles and micelles).

Although fixation has received much attention by microscopists, preparation of the sample prior to fixation has generally been more casual. Sample preparation, i.e. steps that are taken from the time the sample leaves the test-tube (or the culture-plate, organism, etc.) to the time the sample is fixed, determines what microstructure is fixed. For example, vitrified-hydrated-unstained (VHU) samples are prepared for the bare grid TEM method by placing a small (typically 5 microliters) drop of liquid on a bare or holey-film coated grid. A thin layer of the liquid is formed by blotting away most of the liquid with absorbent media like filter paper. The sample is then thermally fixed by plunging into a cryogen like liquid ethane or freon. The assumption that microstructure of the specimen just prior to fixing is the same as that of the original sample is not always true. Liquid-containing samples, if prepared in uncontrolled laboratory atmosphere, are subject to evaporation and temperature changes. This can concentrate solutions and suspensions several fold, change pH, increase ionic strength, and affect electrolyte balance. Concentration and temperature changes can in turn change the microstructure of the specimen. When the sample is far away from a phase boundary concentration changes may have only minor effects such as increase in number density. However, if the sample is near a phase boundary, drastic microstructural changes can occur: previously nonexisting structures can be introduced (e.g. crystals of a salt may appear in a solution which is near its solubility limit, or vesicles and liposomes may appear in single-phase solutions of surfactants, as shown by Talmon[6](1986)), or structures may agglomerate or invert. Without adequate prior physico-chemical knowledge of the sample, it is impossible to tell if structures seen in microscopy are "real" or induced by phase-change, unless adequate precautions have been taken to prevent phase changes during sample preparation and fixation. Techniques which rely on evaporation to form thin films for cryofixation (Jaffe and Glaeser[10], 1984) should be evaluated in this context.

Moreover it is difficult to prepare specimens at conditions different from ambient temperature when the microstructure of the sample is desired under such conditions, e.g. biological systems at *in vivo* conditions, or thermotropic liquid crystals that have phase-boundaries at temperatures higher than ambient. Also, when preparing specimens which may be toxic, virulent,

infectious or poisonous, special precautions have to be taken to avoid personal harm. Jeng *et al.*[11] (1987) have discussed a system that permits sample preparation with cryofixation for such toxic systems. Our goal has been to develop the Controlled Environment Vitrification System (CEVS) that avoids inducing concentration, temperature and phase change artifacts (Bellare[12] 1986, and Bellare et al.[13] 1986). We describe here the latest CEVS system, how it is used, and results demonstrating the power of the system. We conclude with potential applications for SEM and freeze-fracture techniques. This account opens with a description of the CEVS and its use, gives a set of TEM micrographs that demonstrate the importance, power and potential of the system, and concludes with a discussion of the application of CEVS to SEM, freeze-fracture, and TEM of more complex systems.

Description of the CEVS

The CEVS (Fig. 1) consists of four sub-systems: an environmental chamber in which specimens are made, a cryogen reservoir in which specimens are frozen, an assembly to transfer them from the cryogen reservoir to a storage dewar without temperature rise or frost deposition, and an instrument cluster providing measurement and control of environmental chamber conditions.

The environmental chamber (Fig. 2) encloses a vertical shaft on which a specimen support plate (e.g. a TEM grid) can be mounted with tweezers. The shaft, 3mm in diameter, can slide axially in a phenolic bearing and can be locked with a pin at a position where a spring inside the bearing is compressed to provide downward force on the shaft. The CEVS tweezer (e.g., Dumont 3c) has a sliding o-ring around it to permit holding of a specimen support plate. The tweezer has a magnetic strip attached to it, and the tweezer can be easily clamped to the shaft which has a mating magnetic strip in a recessed housing, assuring precise repositioning; this allows viewing of the specimen with a long-working distance stereomicroscope mounted outside the chamber. Illumination of the specimen support plate at near normal incidence is achieved by directing a fiber-optic light source down one ocular of the microscope, and viewing monocularly through the other ocular.

The polycarbonate environmental chamber, 10cm wide, 10cm deep and 20cm high, is suspended over a base plate. A reservoir with a cup for the vitrifying cryogen (typically ethane at its melting point) can be reproducibly positioned under the environmental chamber in locating plates on the base plate. The cryogen reservoir (Fig. 3) has a receptacle in which a specimen transfer box (Fig. 3, O, made from a grid storage box) can be mounted under the cryogen. After the specimen has been cryofixed, it can be placed into one of the 4 slots of the transfer box. A cover with carrying handle (Fig. 3, P) is used to mount and remove the specimen transfer box from the cryogen reservoir for storage in a 5 liter liquid nitrogen dewar. The specimen transfer box is based on a similar device designed by Gatan, and it fits their model 626 cryotransfer system.

The environmental chamber has reservoirs for two liquids (water or organics) with wicks to saturate the gas inside the chamber. More reservoirs for additional fluids could be added easily. A nozzle is provided on the chamber to permit introduction of an inert gas, or to draw a partial vacuum to enable safe disposal of air that may be contaminated with a toxic specimen. A capacitance

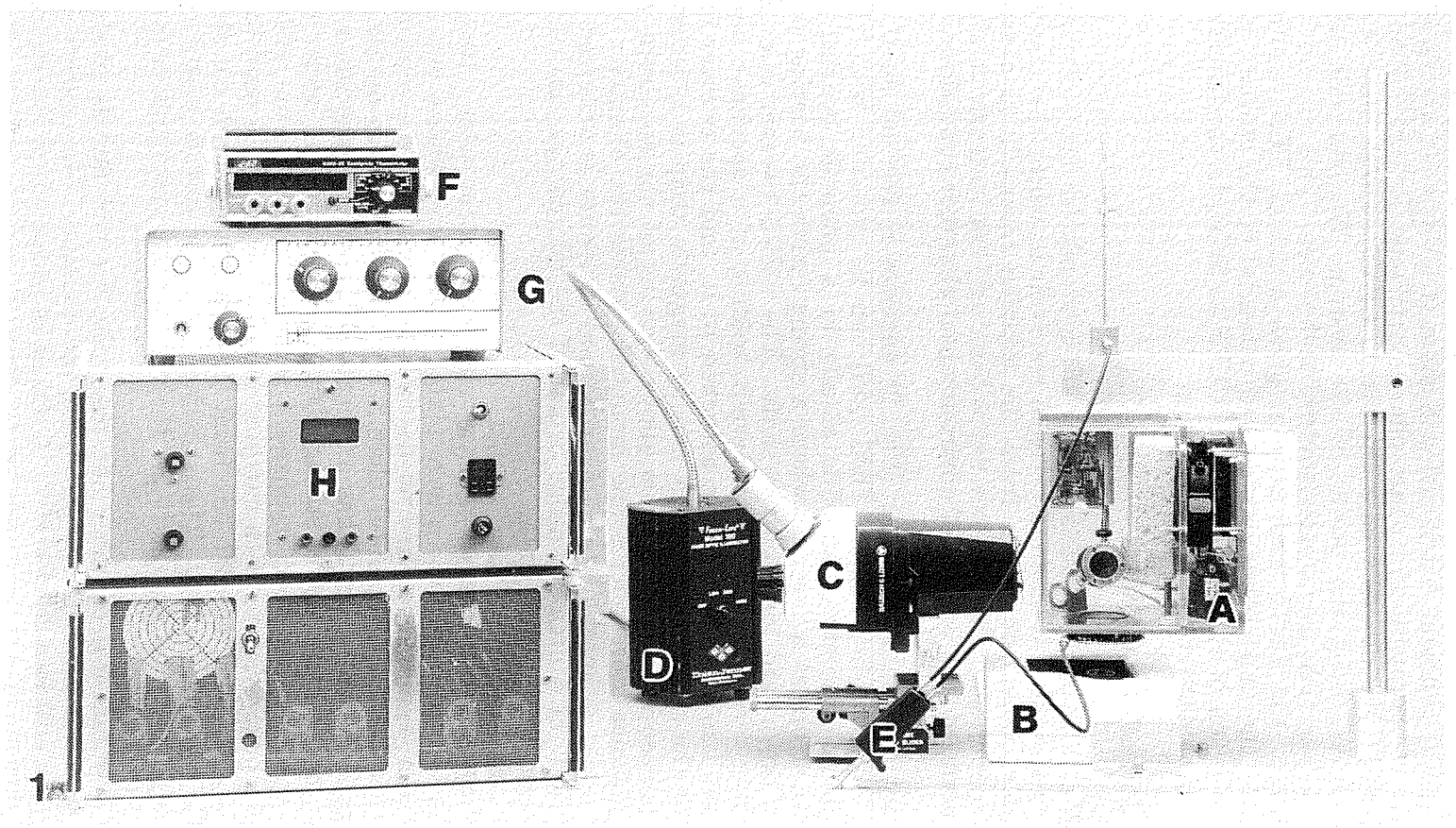

Figure 1. The Controlled Environment System with the environmental chamber (A), cryogen reservoir (B), stereomicroscope (C), illuminator (D), double cable release (E), and instrument cluster with digital thermometer (F), temperature controller (G), and humidity meter (H).

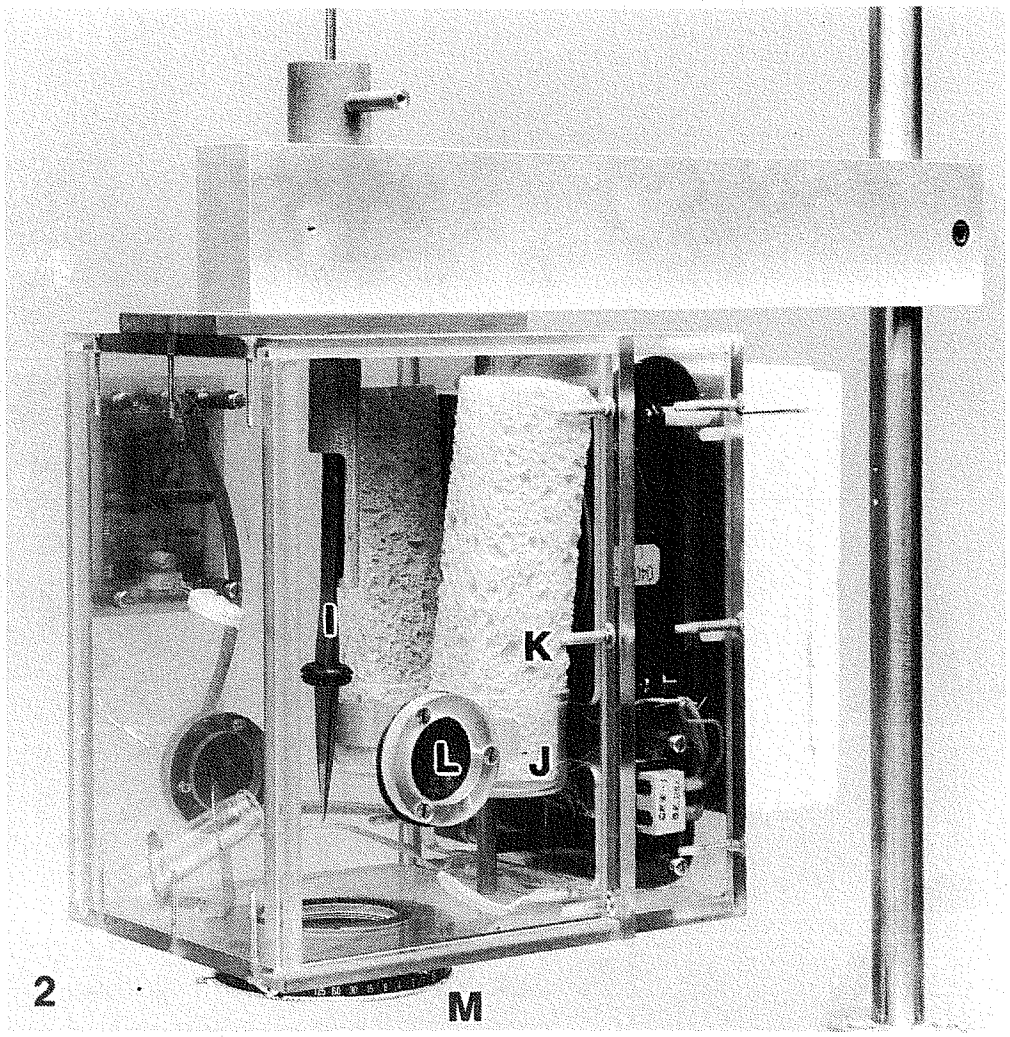

Figure 2. The environmental chamber (with insulation, used for operation from 80 to 90 ° C, removed for clarity) with tweezers (I) on the plunger shaft, saturating reservoirs (J) with wicks (K), port with split rubber septum (L), and shutter (M).

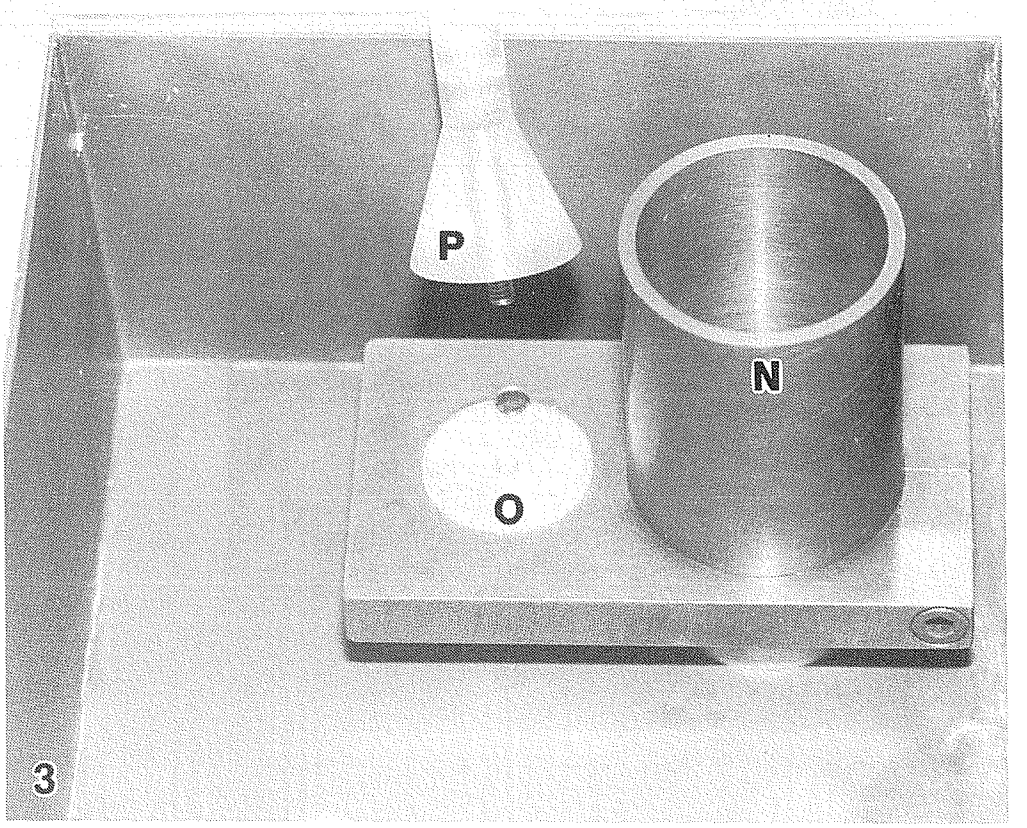

Figure 3. The cryogen reservoir with vitrifying medium cup (N), specimen transfer box (O), and specimen transfer cover (P).

A halogen-quartz lamp mounted inside the chamber is used as a compact source of heat, and a low-profile brushless fan provides forced convection (Figs. 4 and 5). Two thermistors are mounted near the specimen support plate; one is used to measure the temperature with a digital thermometer, the other to control the temperature with a proportional controller varying the power supplied to the lamp. A third thermistor may be placed in the saturating wicks to provide the wet-bulb temperature; this can be used to determine the chemical potential of a saturating component, if psychrometric data is available.

Stainless steel fins on the inside back face of the chamber are in thermal contact with an insulated reservoir mounted on the outside back face of the chamber. These fins are used to cool the chamber gas by circulating or statically placing a refrigerant (e.g. liquid nitrogen or dry-ice cooled acetone) in the reservoir. Thus the chamber gas temperature can be controlled from -5 ° C to +90 ° C, stable to better than 0.1 ° C.

The digital thermometer, temperature controller, humidity meter, and controls for the fan are mounted in an instrument cluster (Fig. 1). A multiconductor shielded cable from the CEVS carries signals to the instrument cluster.

The environmental chamber walls are assembled in a double C configuration: the top, bottom and front faces form one C, the two sides and back form the other C. The two assemblies slide together in grooves machined in the faces; thus the chamber can be opened to gain access to internal parts, and then sealed shut. A spring clip is provided in the chamber in which a stoppered 5 ml vial of sample can be placed prior to specimen preparation to allow equilibration to chamber conditions.

Three ports are provided on the chamber, one each on the left, right and bottom faces. The left and right openings are covered with split rubber septa and permit introduction of a pipette to remove a drop of sample from the bottle and place it on the grid, and to introduce and manipulate blotting media wrapped around a stainless steel strip (0.5 x 10 x 100 mm). The opening on the bottom face of the chamber is closed with a precision iris-type Prontor self-cocking camera lens shutter, set to "T" (for "time," so that the shutter remains open after firing).

When the sample is ready to be cryofixed, a pin holding the shaft is ejected with one leg of a photographic double cable release (Nikon AR-7). The other leg of the cable release fires the shutter, opening it just before the specimen support plate is forced through with spring-loaded impulse into the vitrifying medium. The plunge depth (i.e. depth below the surface of the vitrifying medium that the sample travels) can be adjusted (from 0 to 30 mm) by positioning a travel-stop on the shaft. Costello et al.[14] (1982) and Elder *et al.*[3] (1982) have discussed optimum conditions of the plunge depth for vitrification (which depends on the cryogen and any temperature gradients that may exist in it). The range provided in the CEVS covers the depth recommended. Thus the chamber is kept gas-tight and insulated until the specimen is plunged, maintaining environmental control and preventing phase-change and specimen pre-cooling.

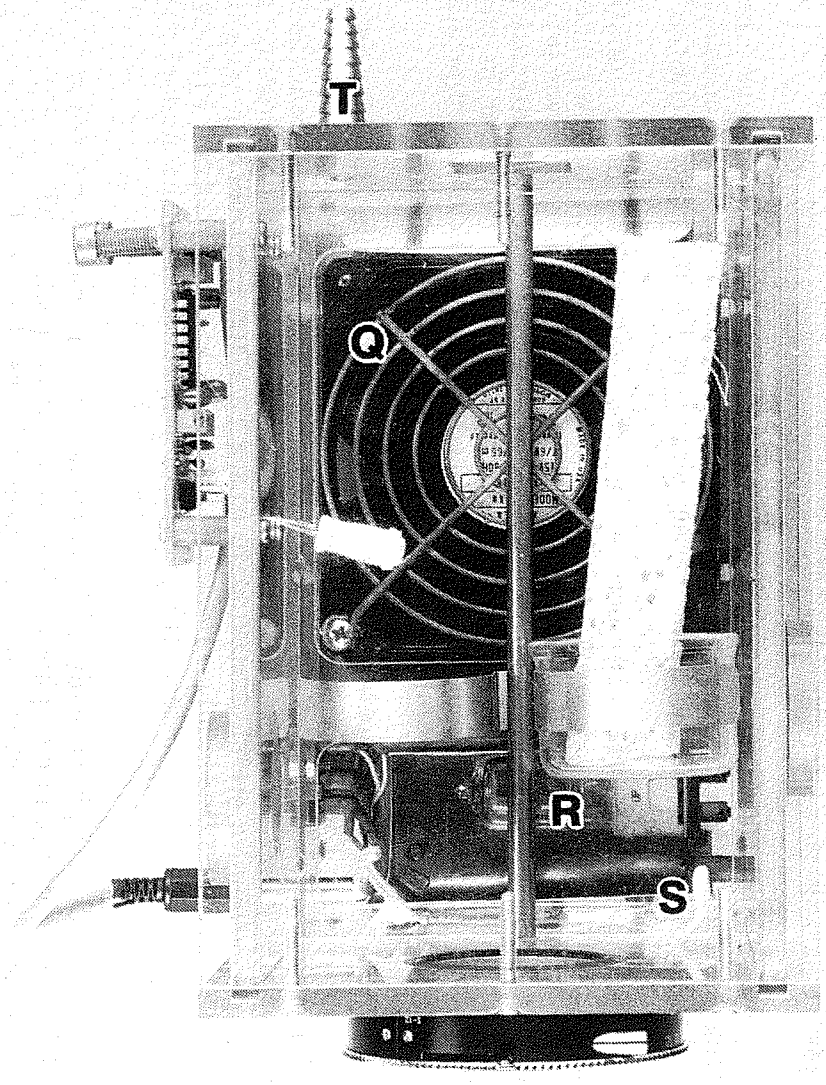

Figure 4. Front view of the environmental chamber (with one reservoir removed for clarity) showing the fan (Q), heater lamp (R), thermistors (S), humidity sensor, and gas inlet nozzle (T).

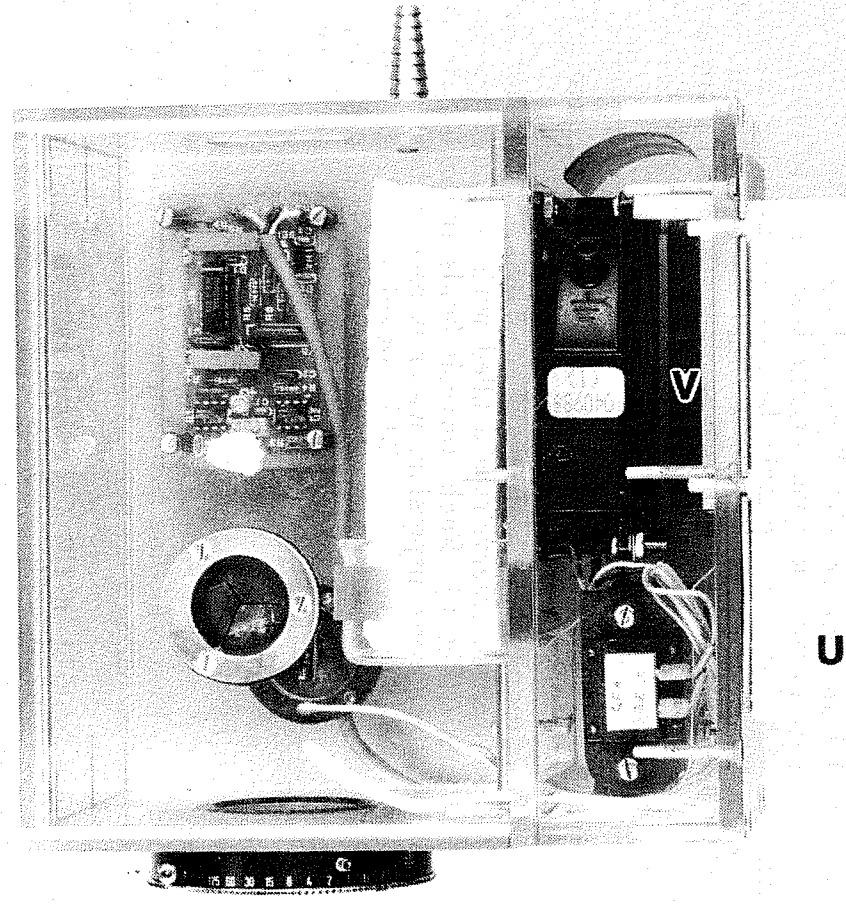

Figure 5. Side view of the environmental chamber showing the cooling reservoir (U) and cooling fins (V).

Sample Preparation with the CEVS

In this section we describe the procedure for preparing thermally fixed TEM specimens on bare or holey-carbon-film-coated grids with the CEVS. The following materials are required: bare (400 mesh) or holey-carbon-coated (200 mesh) grids, 90mm circles of paper (Whatman #1) or glass (Schleicher & Schuell #30) filter media, liquid nitrogen, ethane (99.0% cylinder size 3 with a single stage regulator is convenient; other cryogens can be used — e.g. freon, propane), a long surgical forceps, a pair of tweezers (e.g., Dumont 3c), and a 10 microliter repeating dispenser with pipette tips.

The sample preparation procedure is carried out with the CEVS inside a fume hood to prevent the fire hazard due to presence of ethane. Safety goggles or a face shield, and rubber or cotton gloves are also recommended because accidental skin contact with liquid ethane, unlike liquid nitrogen, can cause painful freeze-burns. However, ethane is superior to other commonly used cryogens for vitrifying the sample because in addition to the large difference between its melting point (-182 ° C) and its boiling point (-83 ° C), it forms a solid crust on the sample when it is placed in liquid nitrogen that protects the sample during transfer, and readily sublimes away when the sample is in the pre-pump chamber.

The following is a step-by-step description of specimen preparation:

0. The environmental chamber is opened by sliding the two sides backwards.
1. The saturating reservoirs are filled with the most volatile component(s) of the sample (Fig. 6). Each reservoir holds approximately 30 ml. If the sample is an aqueous dispersion, water is used in both reservoirs; if the sample contains both water and volatile organics, one reservoir is filled with water, the other with the organic liquid. Although this selection is adequate for most samples, complex systems near a phase boundary may require that chemical potentials of each of the sample components be matched in the liquid and vapor phase. This, in general, is difficult to achieve practically, but can be done by sequentially placing the sample itself (rather than pure components of the sample) in the chamber, allowing vapor-liquid equilibration, and then removing the sample. The goal is to be able to keep a sample in the chamber so that none of its components will evaporate into the vapor phase.
2. A grid is held in the CEVS tweezers by sliding the o-ring to clamp the tweezers closed. The tweezer is fixed onto the shaft with the magnetic clamp (Fig. 7).
3. The shaft is manually raised in its bearing until it locks after compressing the spring.
4. A 5 ml stoppered vial of sample is placed inside the chamber in the spring clamp.
5. The environmental chamber is closed by sliding the two sides forward. The shutter is closed by partially depressing the cable release.
5. If an inert atmosphere is desired inside the chamber, a stream of the desired gas is introduced into the chamber nozzle. If a hazardous sample is to be used, a vacuum aspirator can be turned on. The discharge of the aspirator can be disposed of with suitable precautions.
6. The fan inside the chamber is turned on.

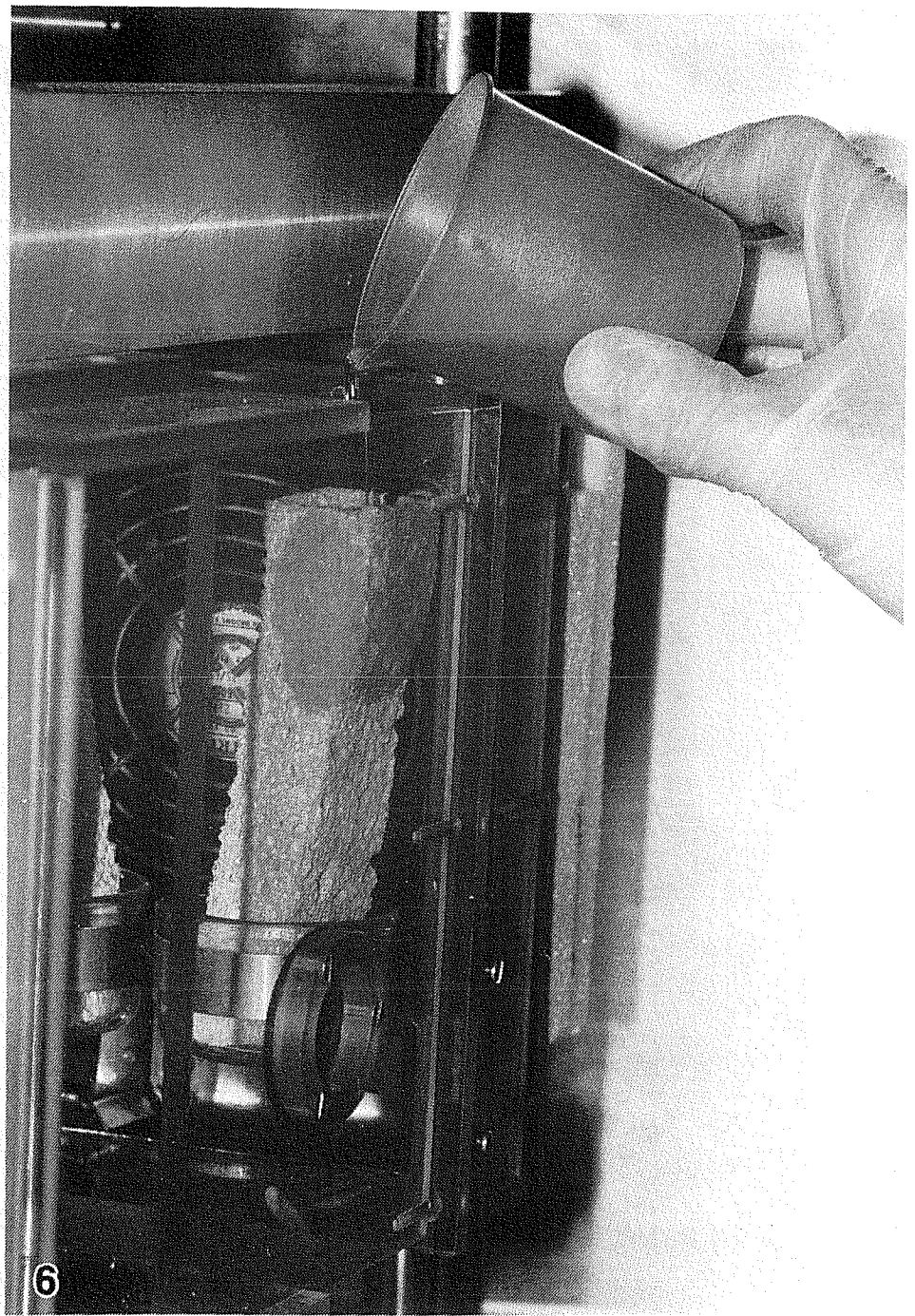

Figure 6. Sample preparation begins with filling the reservoir with the saturating fluid.

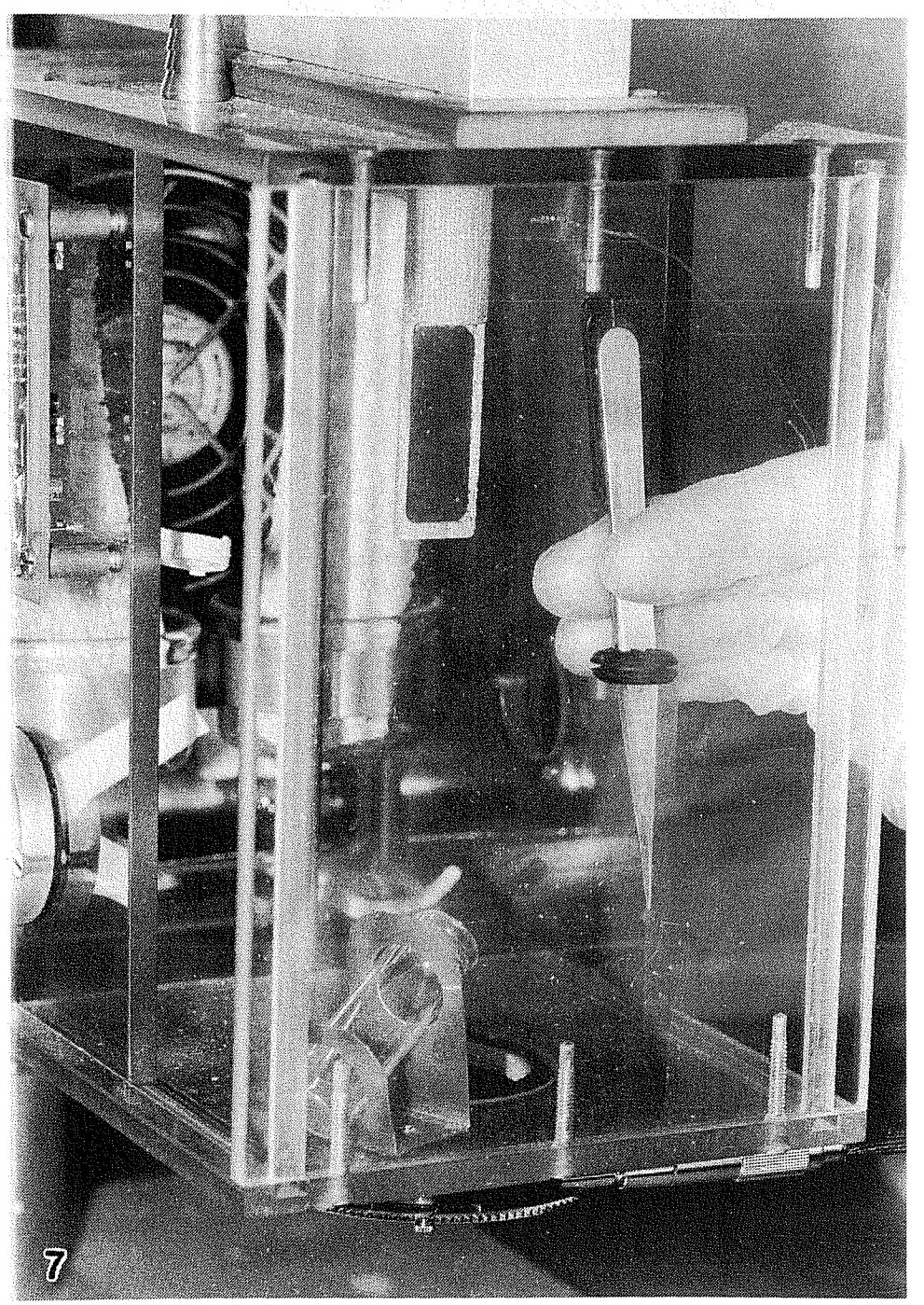

Figure 7. The CEVS tweezer with a grid is mounted on the magnetic clamp on the shaft.

7. The digital thermometer is turned on.
8. The temperature controller is turned on and the controller set point is set to the desired temperature.
9. If below ambient temperature is desired, the cooling reservoir on the back face of the chamber (Fig. 5) is filled with a refrigerant. Liquid nitrogen may be used for this as it usually is at hand; however water-ice-brine or dry-ice acetone provides longer operating times. The refrigerant may be circulated from a large auxiliary reservoir if extended operation without refilling is desired. Cooling will permit precise temperature control even for temperatures just above ambient temperature.
10. At this point the temperature and humidity can be monitored on the instrumentation cluster. If controlled humidity less than 100% is desired (e.g. for controlled intentional evaporation), salt solutions can be placed in the reservoirs instead of pure water. A chemistry handbook (e.g. Weast and Astle[15], 1981 or Perry, Green, and Maloney,[16] 1984) lists which salt and what temperature is required for a given humidity. Alternatively, the humidity meter output can be used to control a valve that mixes streams of saturated air and dry air (or other gas) that can be introduced into the chamber nozzle.
11. While the temperature and humidity stabilize (which takes about 20 minutes for 90 °C but only 5-10 minutes for 30 °C), the filter media is wrapped around stainless steel strip and inserted into the left port septum.
12. When the temperature and humidity have reached a steady state, liquid nitrogen is poured into the outer chamber of the cryogen reservoir. After the vigorous film boiling has subsided, ethane gas is directed into the cup inside the cryogen reservoir by means of a syringe needle connected to a Tygon tube leading from the ethane gas regulator (Fig. 8). The gas condenses into a liquid as heat is removed through the cup walls to the liquid nitrogen. The cup is filled to the brim with liquid ethane. The cryogen reservoir is covered with a styrofoam cover and the ethane is allowed to freeze on the walls of the cup.
13. The long forceps is inserted into the right port septum and the cover of the vial is removed and placed on the inside bottom face of the chamber. The forceps is withdrawn from the port.
14. The repeating dispenser volume is set to 5 microliters. A pipette tip is placed on the dispenser and inserted into the right port septum. The tip temperature is allowed to equilibrate with the chamber by waiting a few minutes.
15. Five microliters of sample are withdrawn into the pipette (Fig. 9) and placed on the front face of the grid (Fig. 10). Moving the tip around the face of the grid while depositing the sample helps in getting complete coverage of the grid. The pipette is withdrawn from the port septum.
16. With the filter medium present in the left port, the back face of the grid is wiped until the sample begins to wet the filter (Fig. 11). Similarly the front face of the grid is wiped (Fig. 12). The front and back wipes are repeated once or twice. this leaves a thin film, approximately 250 nm thick, on the grid. In general the number and duration of the wipes varies from sample to sample, and is determined by factors like interfacial tension, viscosity and grid-hole size. A few trials may be required before the right procedure is obtained. When working with a bare grid, the optical stereomicroscope can be used to view the specimen during blotting, and it is possible to determine when the film thickness is acceptable. Figure 13 shows successive stages in the blotting of a water film on a bare grid as photographed through the

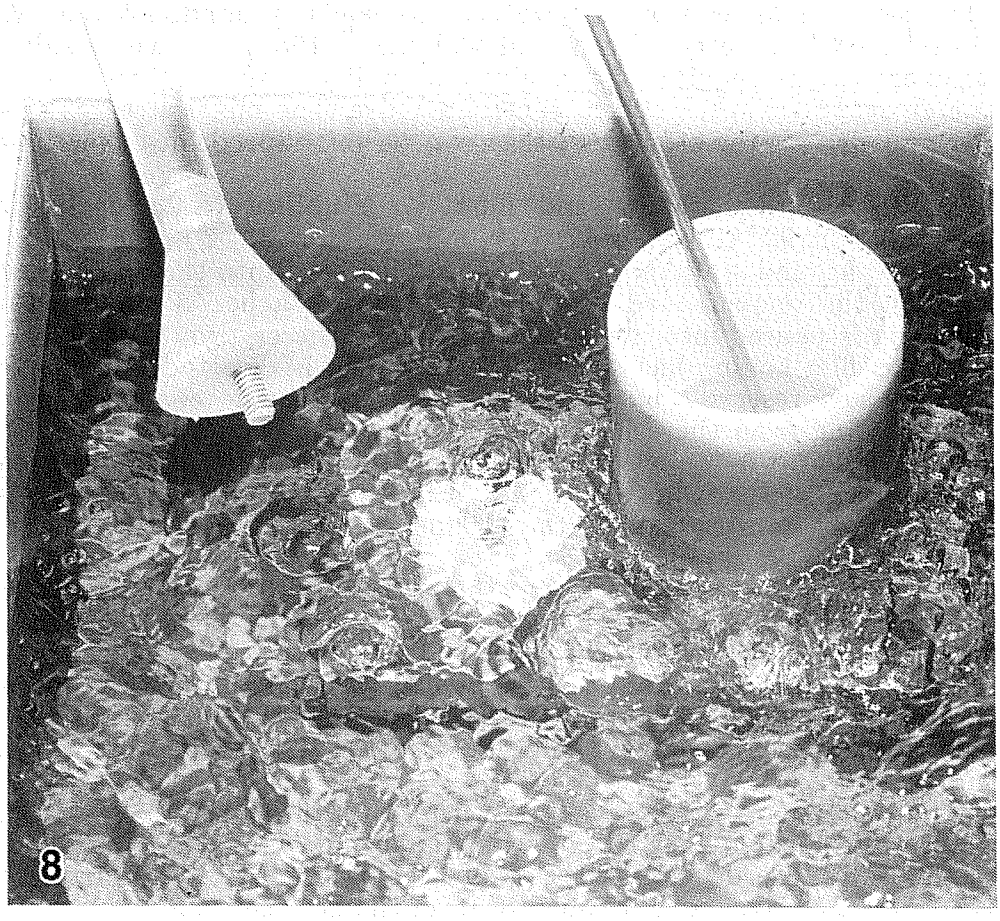

Figure 8. The cryogen reservoir is filled with liquid nitrogen, and ethane gas is liquified in the cup.

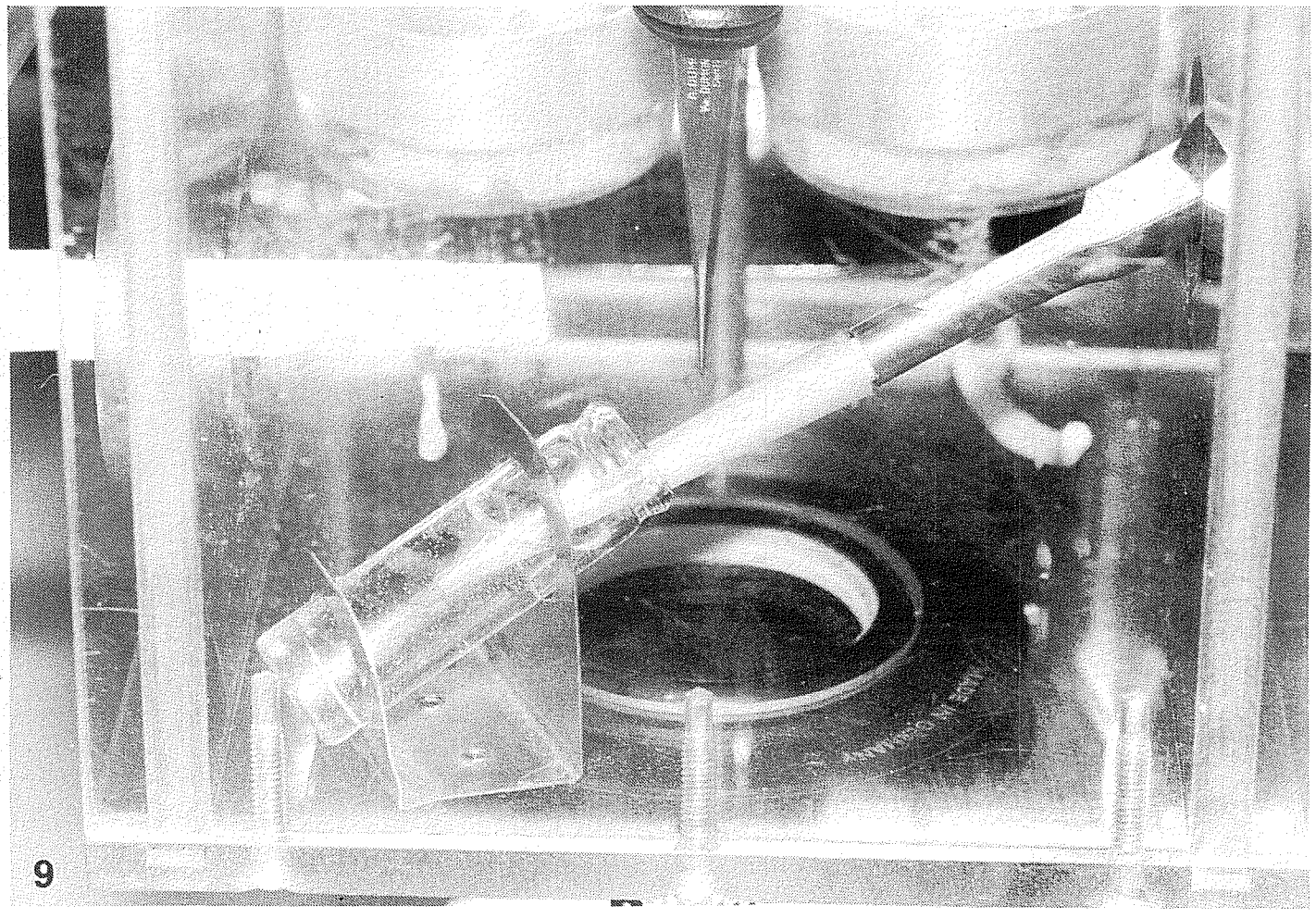

Figure 9. Five microliters of sample are withdrawn from a vial into a pipette inserted in the port of the environmental chamber.

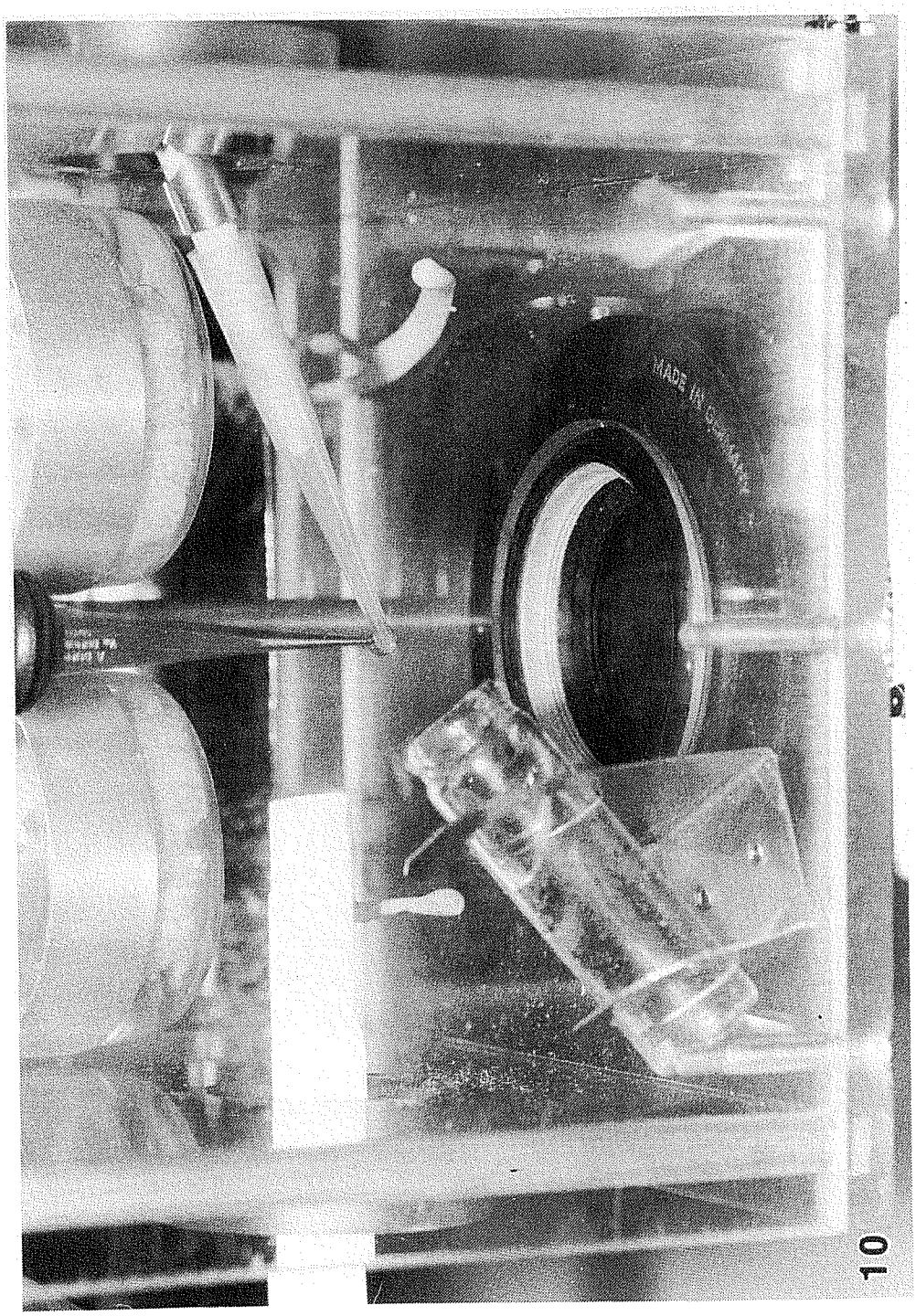

Figure 10. The sample is placed on the grid.

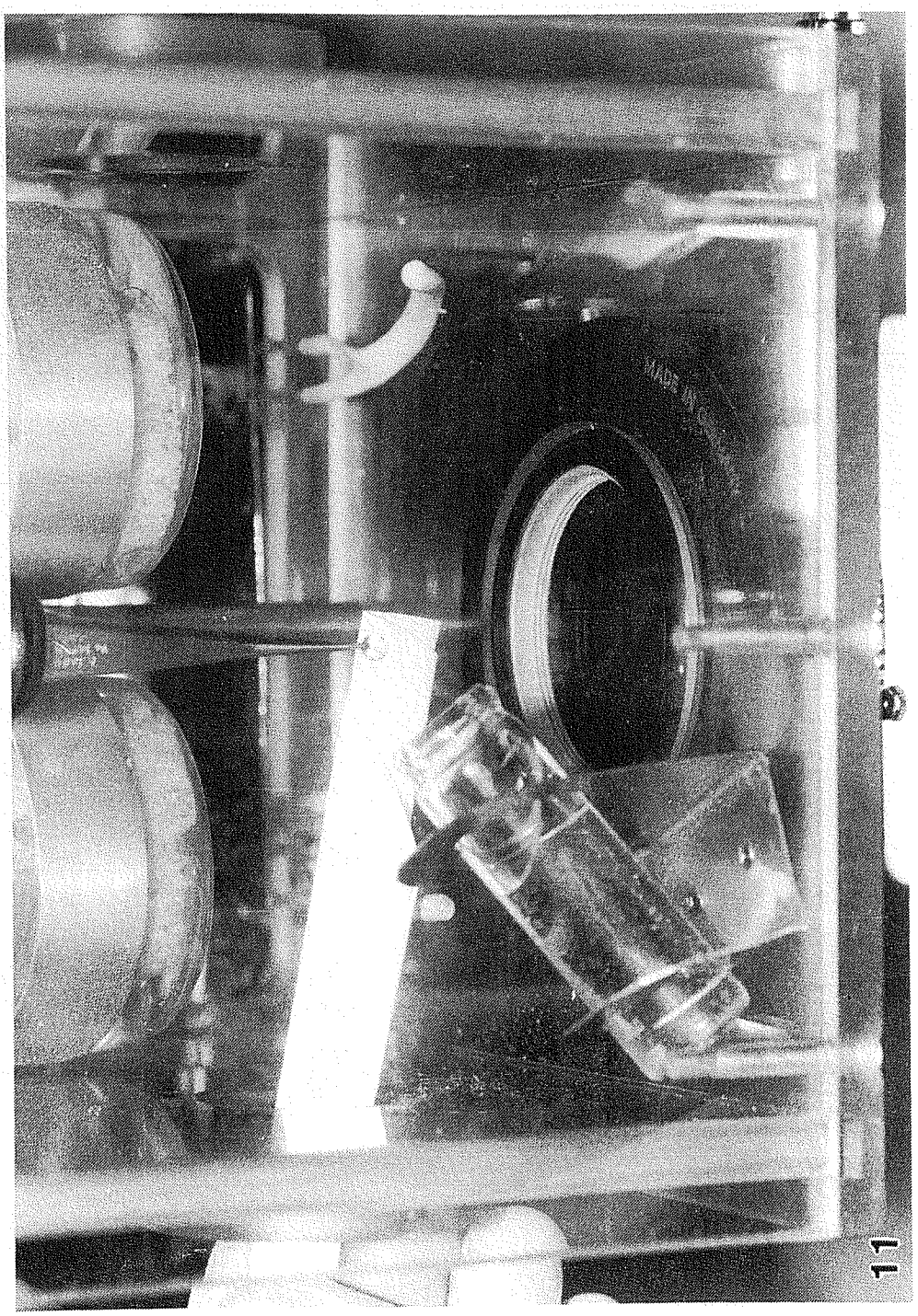

Figure 11. The sample drop on the grid is blotted with a filter paper from the back.

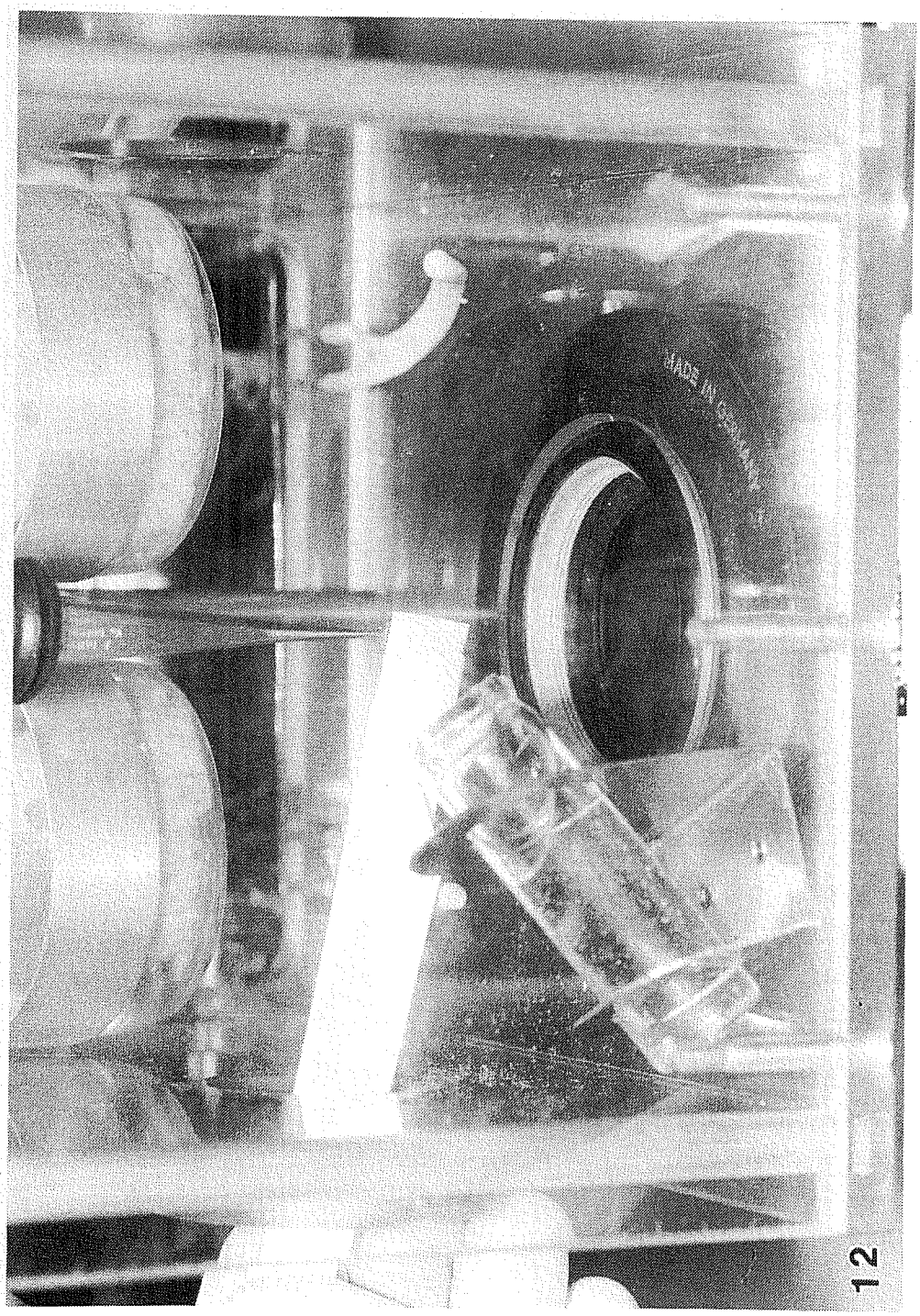

Figure 12. A thin film of sample is formed by blotting from the front.

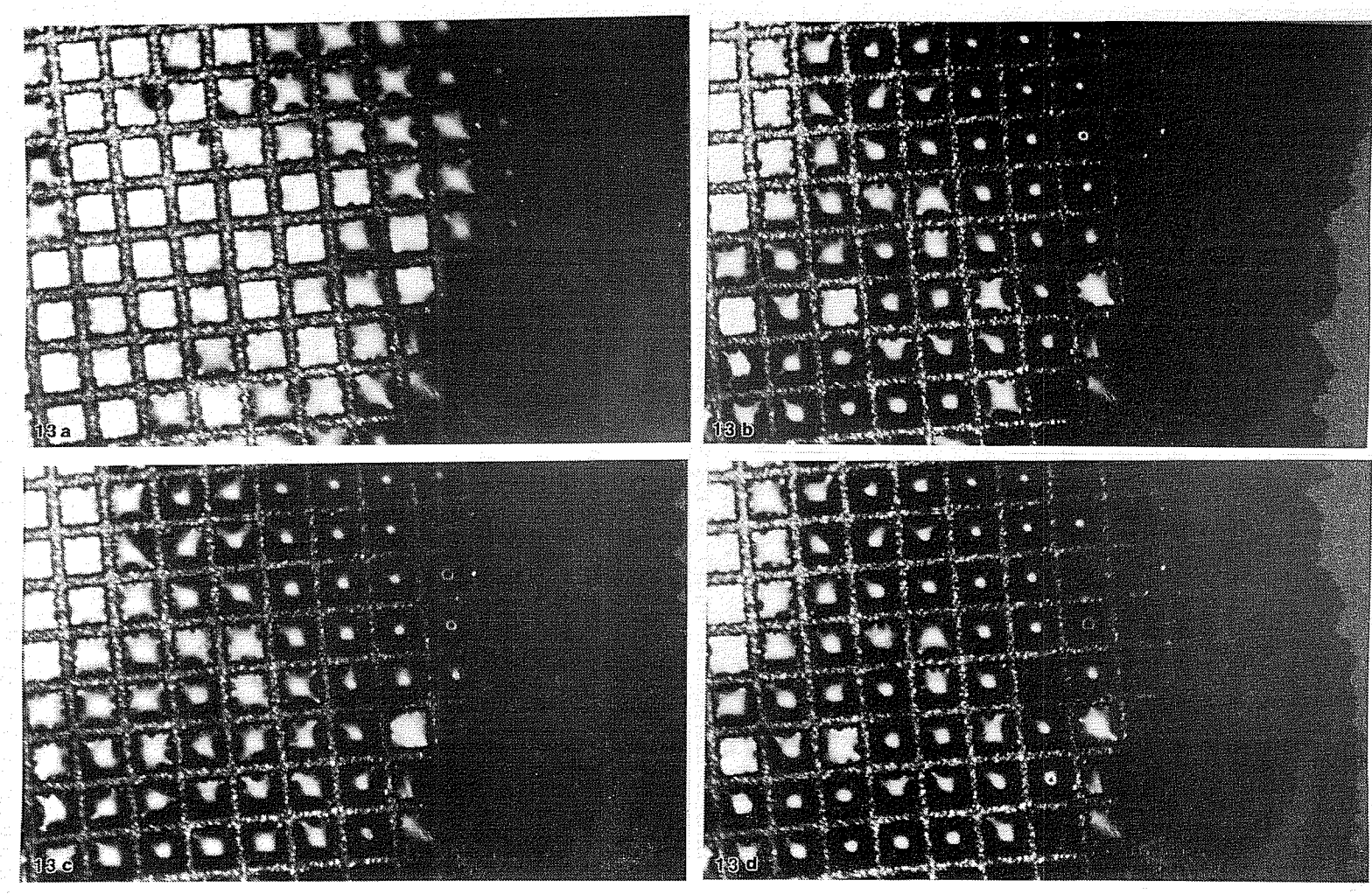

Figure 13. Successive stages (from (a) to (d)) in the blotting of a water drop on a bare grid as photographed through the optical microscope showing thin films that span the holes.

optical microscope. With a holey-carbon film the hole size is too small to resolve the liquid film spanning the holes.

17. The specimen is now ready to be cryofixed, but it may be kept in the chamber without evaporation or unintended temperature changes to allow relaxation from the shear imposed during blotting. Additional on-the grid experiments may be conducted at this stage, e.g. the sample can be heated to drive a chemical reaction, or cooled to induce a phase change. A chemical reagent may be placed on the grid to initiate a reaction, e.g. a gelling process, followed by further blotting to re-thin the specimen.
18. When the specimen is ready to be cryofixed the cryogen reservoir is placed under the environmental chamber against the locating plates and the styrofoam cover is removed.
19. The cable release is depressed: this opens the shutter and rapidly plunges the specimen into the liquid ethane (Fig. 14).
20. A pair of tweezers is introduced under the liquid ethane and inserted between the tines of the CEVS tweezers holding the specimen grid, and twisted slightly to force the specimen tweezers open and thus drop the specimen into the liquid ethane cup (Fig. 15).
21. The CEVS shaft is raised to lock it and the cryogen reservoir is removed from under the environmental chamber and placed on a work surface in the hood. The CEVS tweezers is detached from the shaft and the shutter is closed to permit the environmental chamber to equilibrate from the transient imposed by the plunging action.
22. The specimen grid is removed from the ethane with a pair of tweezers (Fig. 16) and rapidly moved through cold nitrogen vapor boiling from the reservoir and immersed in liquid nitrogen surrounding the ethane cup. It is then placed in a slot of the specimen transfer box under liquid nitrogen. After all the slots are filled with vitrified specimens, the transfer box may be covered by screwing on its cover.
23. The specimen transfer assembly is removed from the cryogen reservoir and is quickly placed into a liquid-nitrogen-containing dewar for transport to the electron microscope, or for further processing (e.g. freeze-substitution or fracture and replication) if desired. The specimen transfer cover and the liquid nitrogen that is carried in the slots of the specimen transfer box protect the specimen from frost deposition or temperature rise. The specimen can be cryotransfered into a cold stage and into the microscope following well established techniques (e.g. Perlov et al.,[17] 1982).

Additional samples can be prepared by replacing the CEVS tweezer with a new grid, replacing the filter medium, and allowing the chamber temperature and saturation to reach equilibrium. Cycle time depends on the operating temperature and is typically 5 to 15 minutes.

Sample Results

Surfactants are molecules having hydrophillic and hydrophobic ends. When dispersed in water, they form a variety of structures, e.g., vesicles (closed shells made of surfactant molecules arranged in a bilayer), liposomes (multilayered vesicles), micelles, and isotropic molecular solutions, depending on the type of surfactant, the temperature, the concentration and the presence of additional components like alcohols, oils, and salts. These structures are associated with thermodynamic phases.

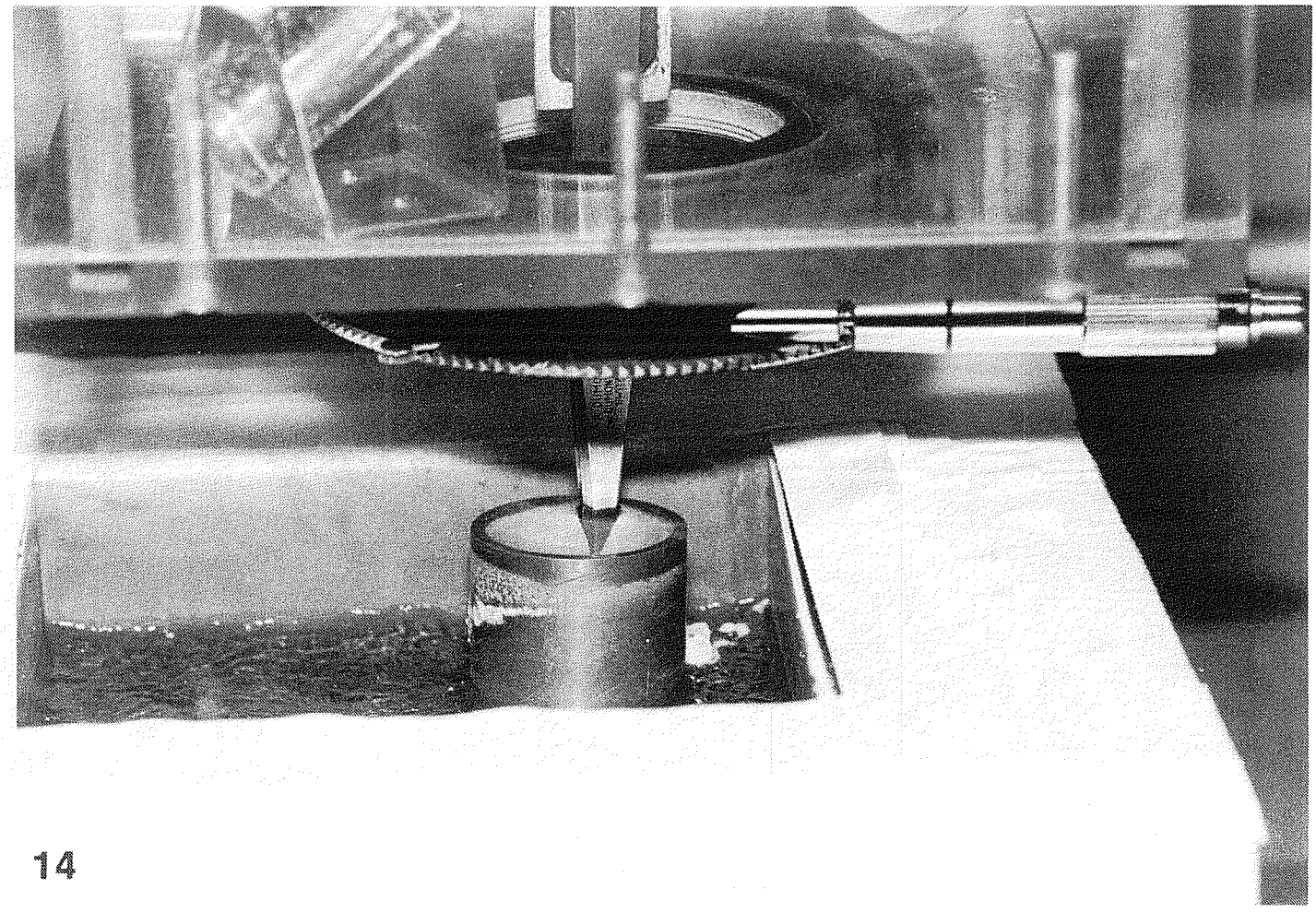

Figure 14. The sample is plunged into the ethane cup by triggering the spring loaded shaft; the shutter opens just before the specimen falls through.

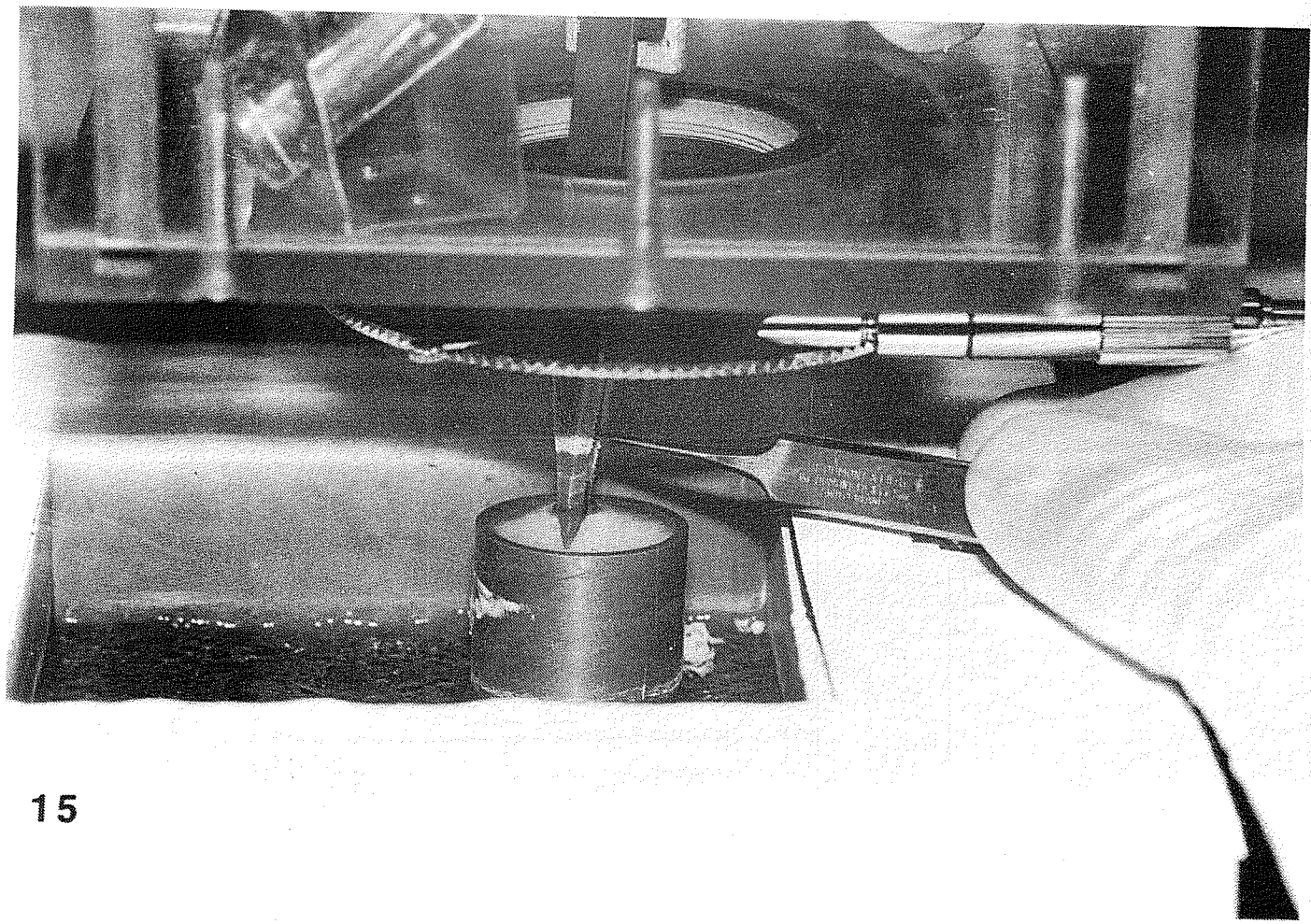

Figure 15. A tweezer is used to open the CEVS tweezer and thus drop the specimen into the ethane.

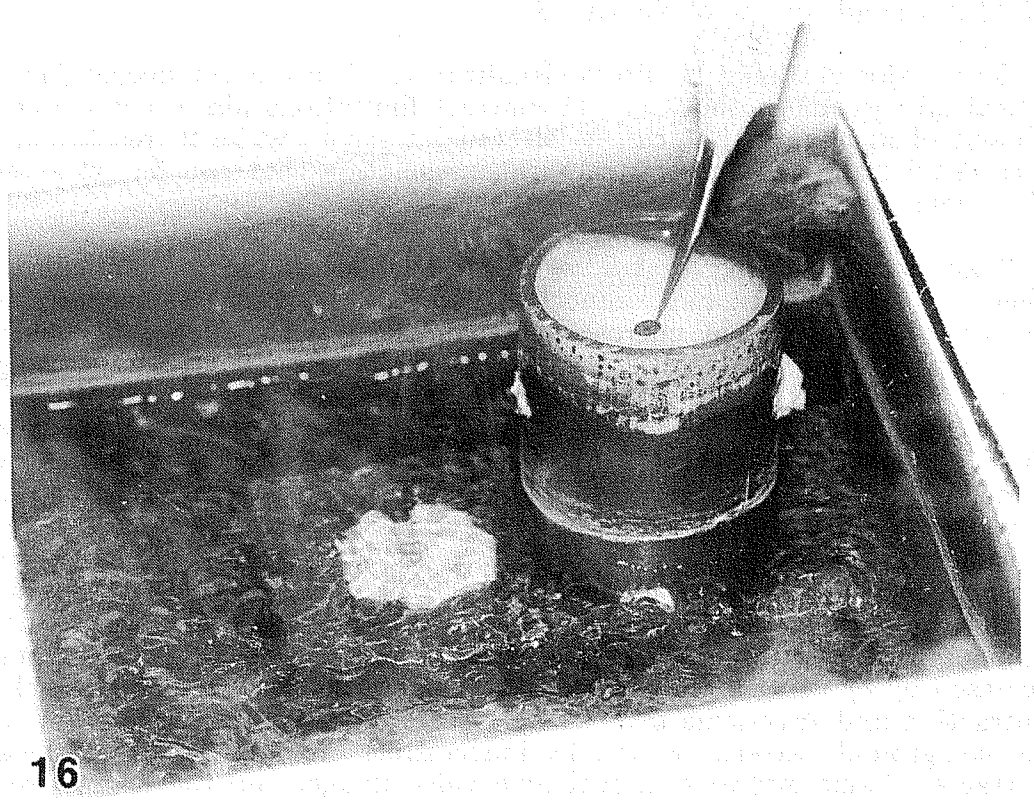

Figure 16. The vitrified specimen is removed from the ethane and tranferred into liquid nitrogen.

Surfactant dispersions are ideal test specimens to evaluate specimen preparation procedures because their phases have been, in many circumstances, well characterized by physico-chemical techniques like optical microscopy, light, x-ray and neutron scattering, rheology, and conductivity. Optical microscopy, and in particular, video- and computer-enhanced differential interference optical microscopy (Miller et al.,[18,19] 1987a, 1987b), of vesicles and liposomes provides a good comparison with electron microscopy because particles with diameters in the neighbourhood of a micron can be observed by both methods. Also, small variations in compositions or temperature can cause a drastic change in microstructure if the surfactant dispersion is near a phase boundary. Thus, if the results of electron microscopy do not agree with overwhelming data from other techniques, the integrity of the sample preparation technique can be questioned. We have used three surfactant dispersions to evaluate the performance and establish the advantage of the CEVS.

The major obstacles to direct visualization of surfactant microstructures by optical microscopy methods are 1) contrast limitations place a lower bound on the size of aggregate that can be slected for study, while 2) resolution limitations restrict the amount of structural information that can be extracted from microscopic observations.

Many surfactant aggregates, vesicles and microtubules in particular, are of inherently low contrast and cannot be distinguished from the background solution with orduinary light microscopy techniques. With video enhanced microscopy, contrast enhancement is obtained in three ways: 1) Optically, image contrast is boosted by the use of rectified differential interference contrast (DIC). This technique gives high contrast light or dark bands at regions in the sample where here are sharp refractive index gradients (such as surfactant aggregate-water interfaces). 2) Electronically, image contrast is increased through the use of a video camera instead of the human eye as the detection device. Unlike the human eye, a television camera is a linear device; it responds equally well to small diferences in intensity no matter what the background light level is. Thus a television camera linked to a DIC microscope (VEM) improves contrast by responding linearly to contrast at all light levels. 3) Digitally, image contrast is increased by by using a real-time digital image processor to perform background subtraction and gray-scale transformations. As a result of these manipulations the background pattern created by inaccessible dirt and lens imperfections is subtracted frame-by-frame in real-time video image, and the narrow region in gray-scale space occupied by the image (e.g., from gray level 120-140) is expanded to cover the full gray-scale of the display device (e.g., 0-255).

As a result of this contrast enhancement, small, isolated colloidal particles with diameters as small as 50 nm (such as unilamellar vesicles or polymer latex spheres) can be clearly and dynamically visualized. This is an important result, since it means that VEM can be used as a detection device in the study of colloidal microstructure; further microstructural details can be obtained by cryo-TEM. While there is no theoretical limit to the size of an isolated particle that can be detected by VEM (given sufficient contrast to distinguish the particle from the background), it is limited in resolution by the wave nature of light: the resolution limit of VEM is 100-250 nm. Higher resolution images can be obtained with cryo-TEM.

Materials

Sodium 4-(1'-heptylnonyl)benzene sulfonate (SHBS) was synthesized at the University of Texas and purified as described by Franses[20] (1979). Octyldodecyldimethylammonium bromide (ODDAB) was kindly provided by Dr. R. Zana of CNRS, Centre de Research sur les Macromolecules, Strasbourg. Dioctadecyldimethylammonium bromide (DODDAB) was kindly provided by Dr. D. F. Evans of the University of Minnesota, Minneapolis. The surfactants were dispersed in doubly distilled water further purified by dialysis. Liposomal dispersions were made by pouring water into weighed quantities of surfactants and gentle shaking by hand.

Methods

Vitrified-hydrated-unstained (VHU) specimens were made on holey-carbon-film-coated grids using the CEVS as described in the earlier section. Unless otherwise stated all specimens were made with the environmental chamber at 25 ° C and 100% relative humidity.

Specimens were examined in a JEOL 100CX analytical microscope, operating at 100 kV in the conventional TEM mode. The vitrified-hydrated-unstained specimens were mounted into a modified JEOL EM-SCH cooling holder using the cold stage transfer module described by Perlov etal.[17] (1982). The specimen holder temperature in all experiments was -168 ° C. Images were recorded on Kodak SO-163 film exposed for maximum rated speed, and developed for 12 minutes in full-strength Kodak D-19 developer.

Test Results

We have tested the CEVS with aqueous dispersions of ODDAB and DODDAB. A 2.0% solution of ODDAB, originally at 20 ° C was prepared for TEM. No vesicles are expected to be seen because at this concentration the surfactant forms aggregates smaller than 5 nm. Specimens prepared without environmental control (Fig. 17 a) have crossed a phase boundary (at about 2.5%, 20 ° C) due to evaporation and show vesicles; specimens prepared in the water-saturated environment of the CEVS show no evaporation-induced artifacts, demonstrating the importance of saturation that the CEVS achieves. Smaller aggregates may be present in the system, but cannot be resolved without further image processing.

DODDAB has a phase transition at about 30 ° C. Figure 18 a shows a 0.5% sonicated aqueous dispersion, originally at 20 ° C, examined by cryo-TEM. Large surfactant sheets and smaller lens-shaped structures are seen. Samples prepared at 50 ° C, using the CEVS, show (Fig. 18 b) vesicles and multilamelar liposomes, but no large sheets or lens-shaped structures. Preparing the specimen from 50 ° C would have been a difficult task without the CEVS.

These two test specimens conclusively demonstrate the importance of environmental control that the CEVS achieves during specimen preparation. We have also applied the technique to examine microstructures in SHBS at 90 ° C, where it had been previously believed that the solution was isotropic.

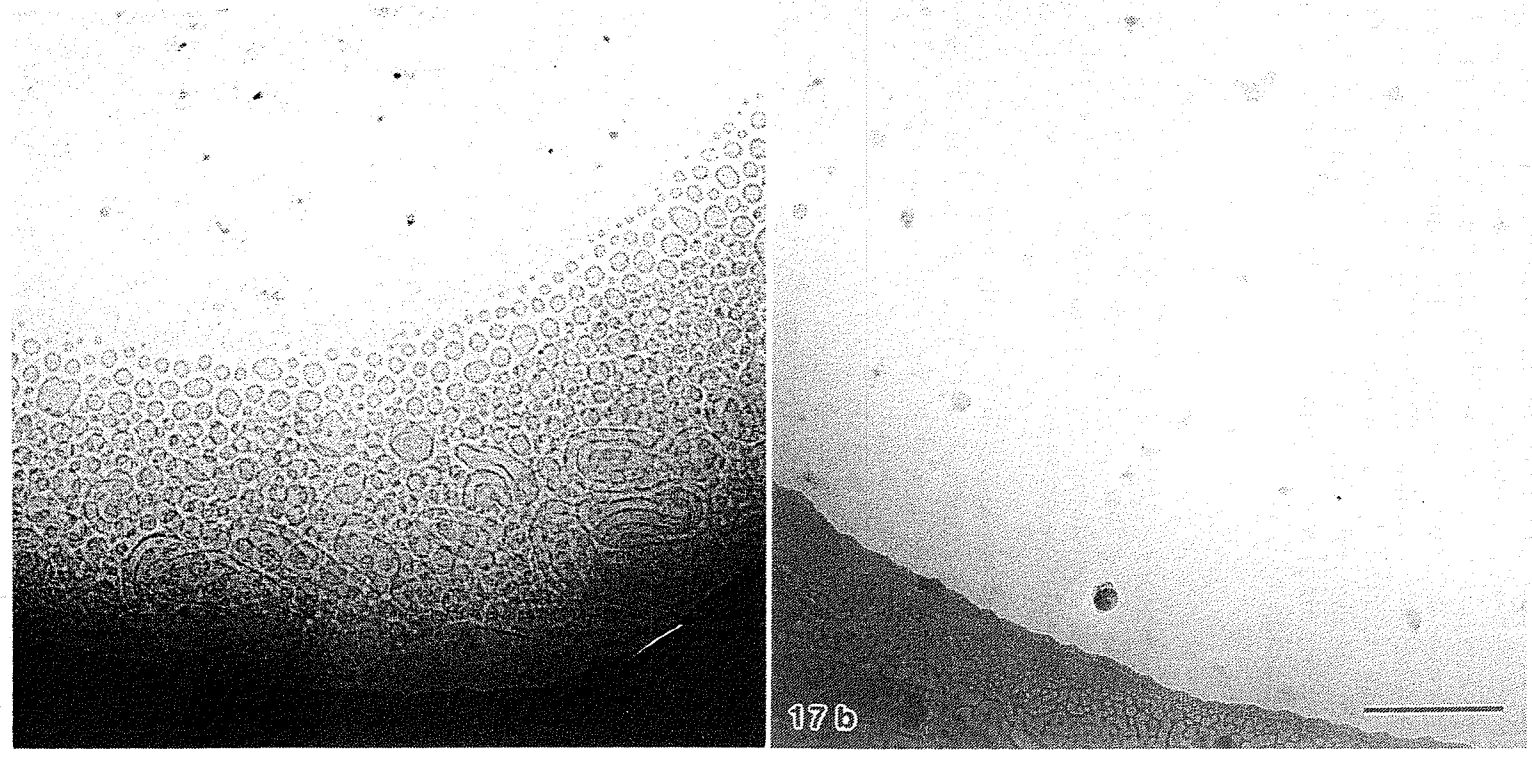

Figure 17. Vitrified-hydrated-unstained (VHU) specimens of 2.0% aqueous dispersion of octyldodecyldimethylammonium bromide (ODDDAB). (a) Prepared without environmenal saturation: note vesicles formed by evaporation (W); (b) Prepared with saturation using CEVS. No vesicles can be seen. Bar = 250 nm.

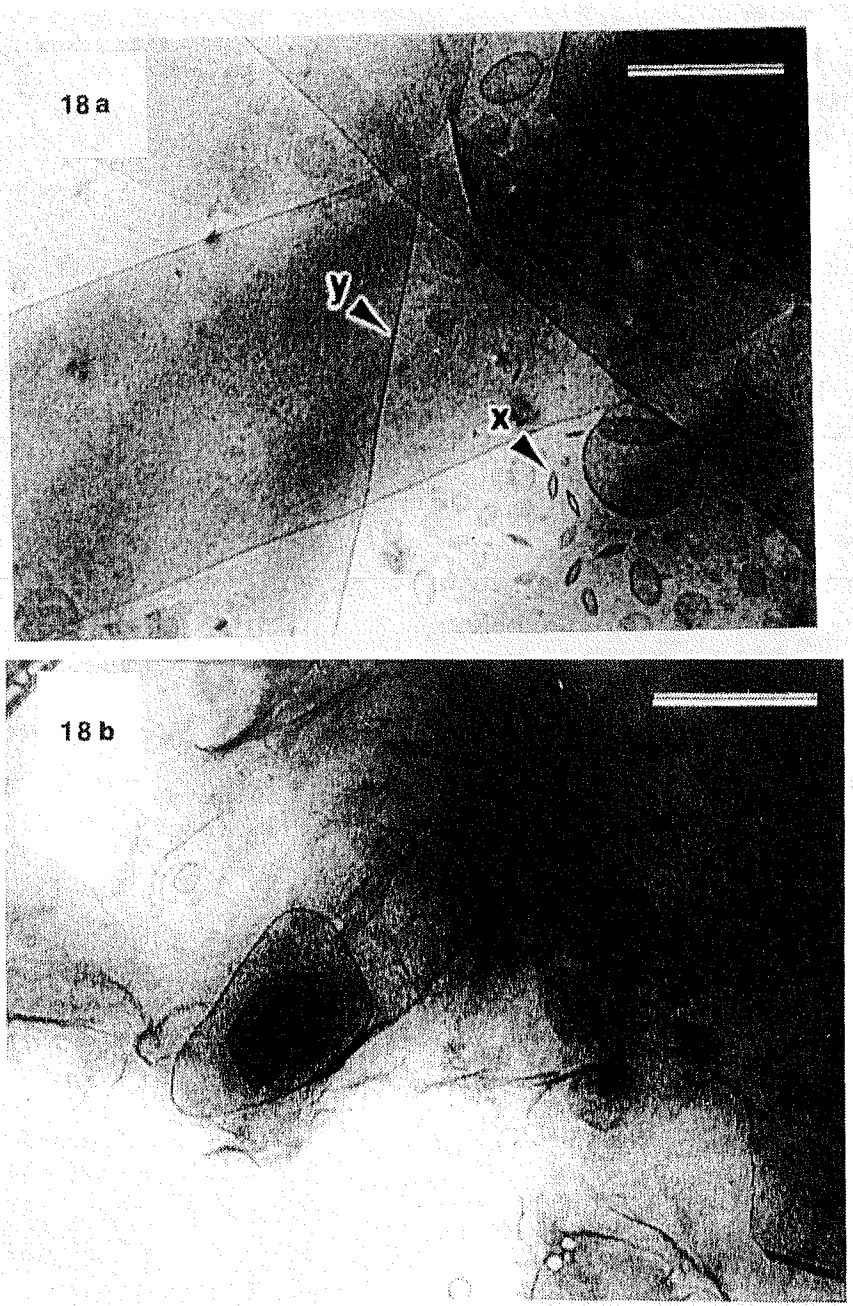

Figure 18. VHU specimens of 0.5% aqueous dispersion of dioctadecyidimethylam moninum bromide (DODDAB): (a) Sample prepared with CEVS from 20 ° C; (b) Prepared from 50 ° C. Note absence of lens shaped (X) and large sheets (Y) seen in (a). Bar = 250 nm.

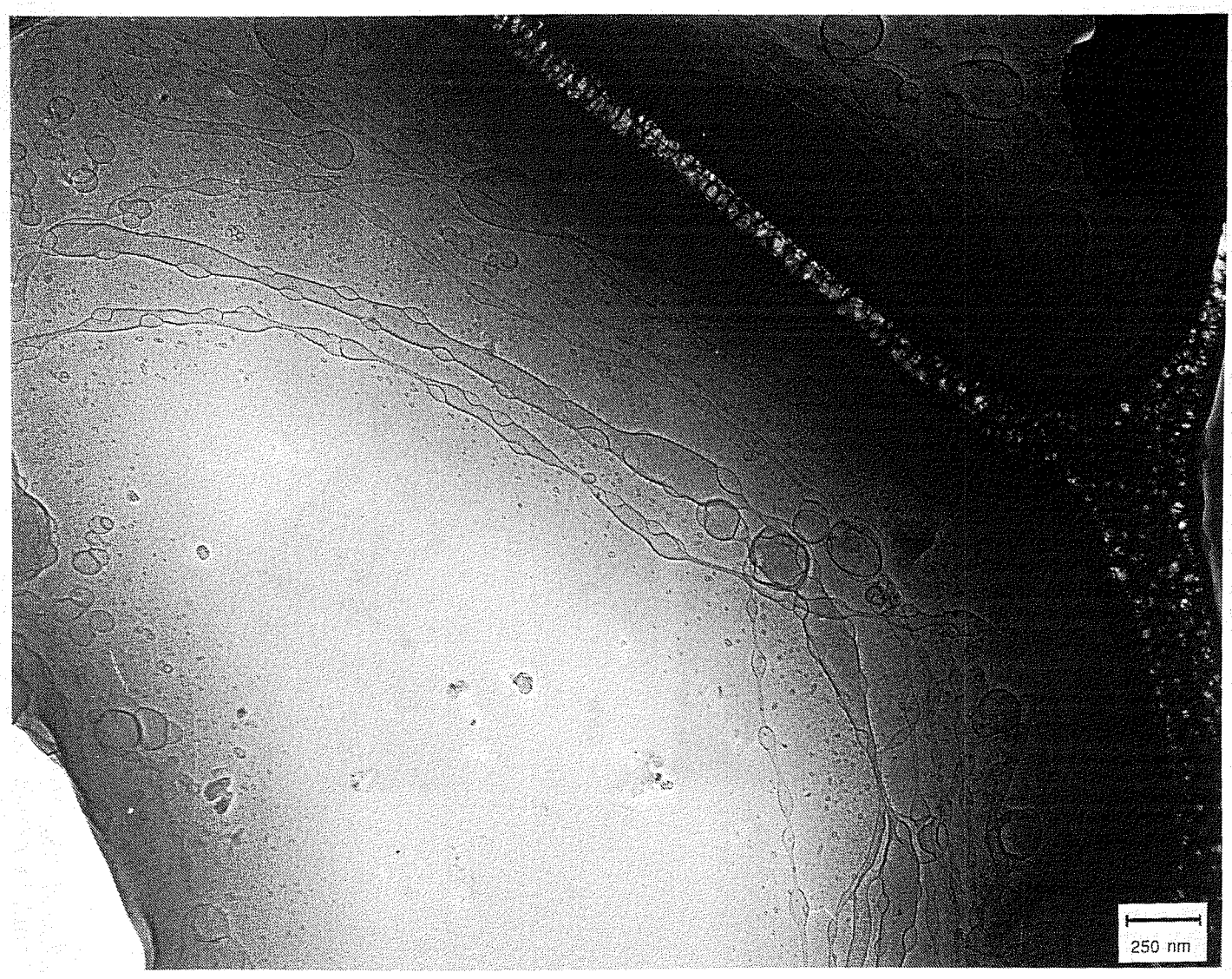

Figure 19. VHU specimen of 0.1% aqueous dispersion of sodium 4-(1'-heptylnonyl)benzene sulfonate (SHBS) prepared from 90 ° C showing liposomes and vesicles.

However, as Fig. 19 shows, vesicles and liposomes can be seen; these microstructures have been also observed by hot stage optical microscopy. We have also applied the CEVS to study the sol-gel processing of ceramics (Bellare et al.,[21] 1987).

Results

We now present and compare some video enhanced optical and cryo-transmission electron micrographs of microstructures formed by double-chained surfactants in water. A typical phase diagram for such a system is shown in Fig. 20. Our micrographs clearly demonstrate that aggregation in the "water + liquid crystal" region and in the isotropic, "micellar solution" phase is more complex than once thought.

SHBS: A diversity of structures.

A VEM picture of a six-month old 1.7 wt% SHBS sample (Fig. 21) shows the existence of polydisperse liquid crystalline aggregates with a wide diversity of structures. The large structures (points A,B, Fig. 21) show birefringence and the Maltese crosses characteristic of liquid crystalline liposomes when the VEM optics are switched to polarizing optics without moving the microscope slide. The undulations of individual layers within the birefringent liposomes (point B, Fig. 21) and the caged movement of smaller vesicles entrapped within larger vesicles (point C, Fig. 21) can be followed in real time. Of particular interest is the "unstructured" spherical region of diameter $\simeq$ 9 microns, point D, Fig. 21, which in real time shows a "sand storm" appearance associated with very small structures. A large number of other small structures which are beyond the resolution limit of the light microscope are also evident.

The cryo-TEM pictures of the same 1.7 wt% SHBS sample (Figs. 22-25) reveal the co-existence of vesicles within vesicles (Fig. 22), coiled tubules within vesicles (Fig. 23) and liposomes (Fig. 24) in which bilayer walls are visible in the clear field produced by vitrified ice: particularly interesting is Fig. 23, in which, incorporated inside the core of the larger vesicles, is an astonishing menagerie of coiled tubules, smaller vesicles and beaded tubes which appear to have been frozen in the process of transforming to small unilamellar vesicles. These intricate structures do not appear to be artifacts associated with sample preparation since the same structures are obtained when the thinned samples are held in the environmental chamber for 30 minutes before plunging into liquid ethane. Note that the large birefringent liposomal structures ($\simeq$ 5 microns) evident by polarizing microscopy and VEM are absent and probably located in the regions of the vitrified ice that are too thick for viewing.

Of particular interest for the comparison of cryo-TEM and VEM is the enclosed vesicle structure (point A, Fig. 22) of diameter 1.75 microns which contains a large number of small unilamellar vesicles. We believe that this structure is similar to the VEM structure of point D, Fig. 21. In fact, the sequence of structures point C, Fig. 21 (Diameter = 15 microns), point D, Fig. 21 (D = 9 microns), point A, Fig. 22 (D = 1.75 microns), point B, Fig. 24 (D = 0.01 microns) suggests that cyro-TEM and VEM visualize a continuity of self-similar structures (i.e., structures of similar topology but different sizes). We return to these structures later.

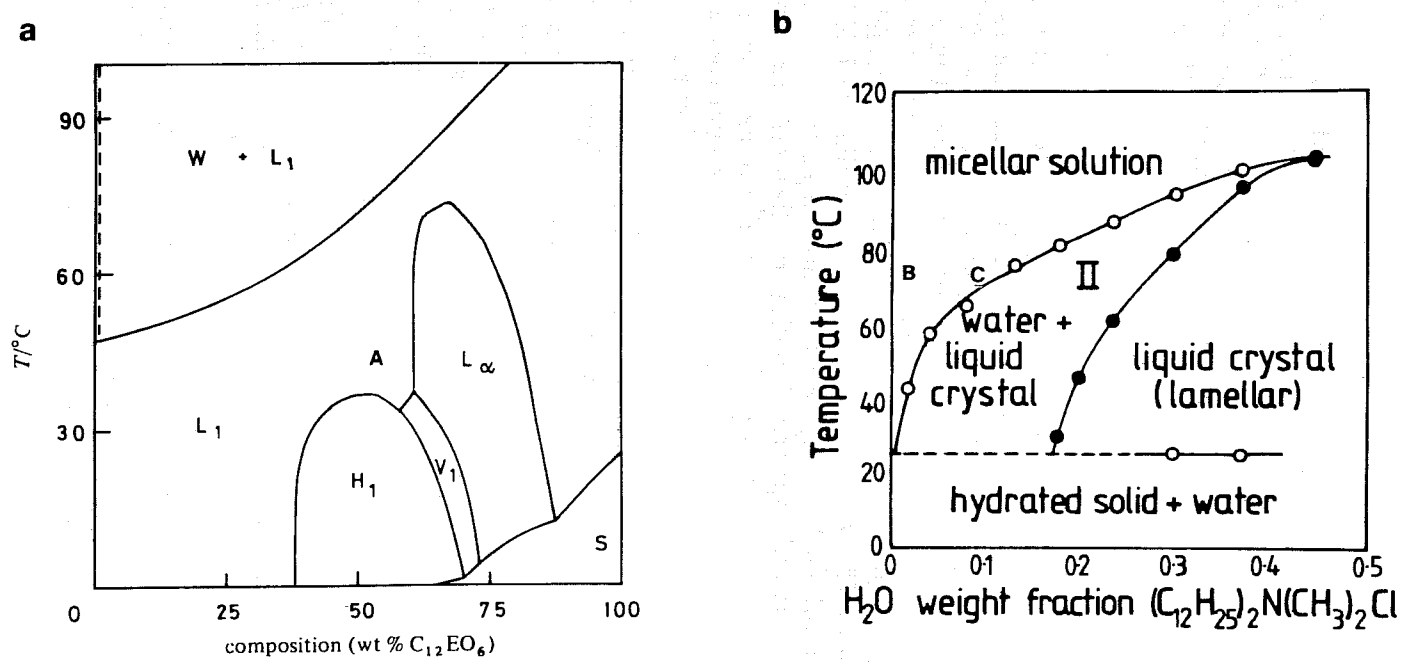

Figure 20. Phase diagram of didodecyldimethylammonium chloride (from Kunieda and Shinoda, 1978).

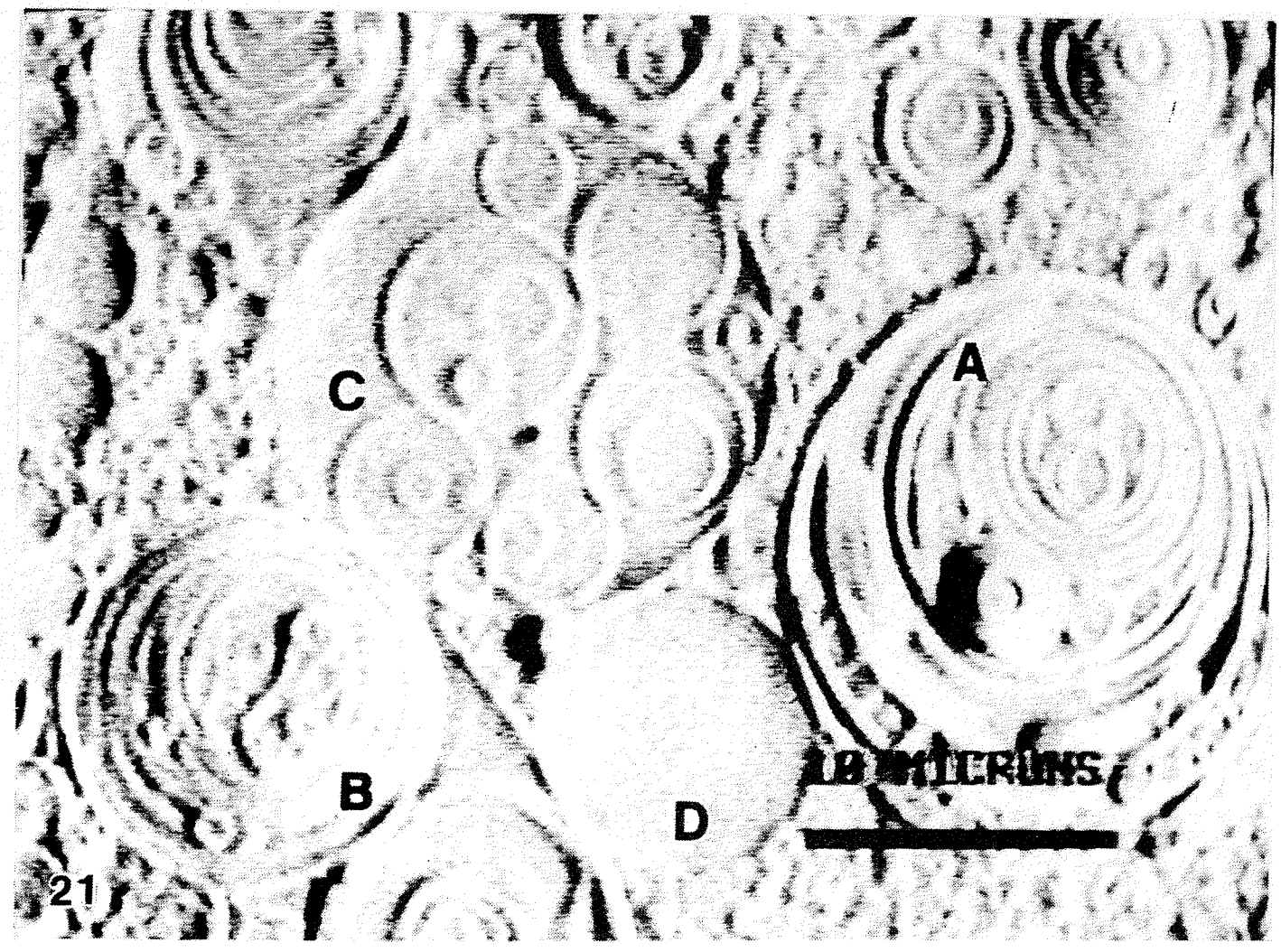

Figure 21. VEM micrograph of 1.7% SHBS. Bar = 0.01 mm. (A, B) Liposomes (birefringent under crossed polars). (C) Large vesicle containing entrapped smaller vesicles. (D) Vesicle with a "dust-storm" appearence in real-time, indicating that it is filled with small, unresolvable particles. Compare with Fig. 22.

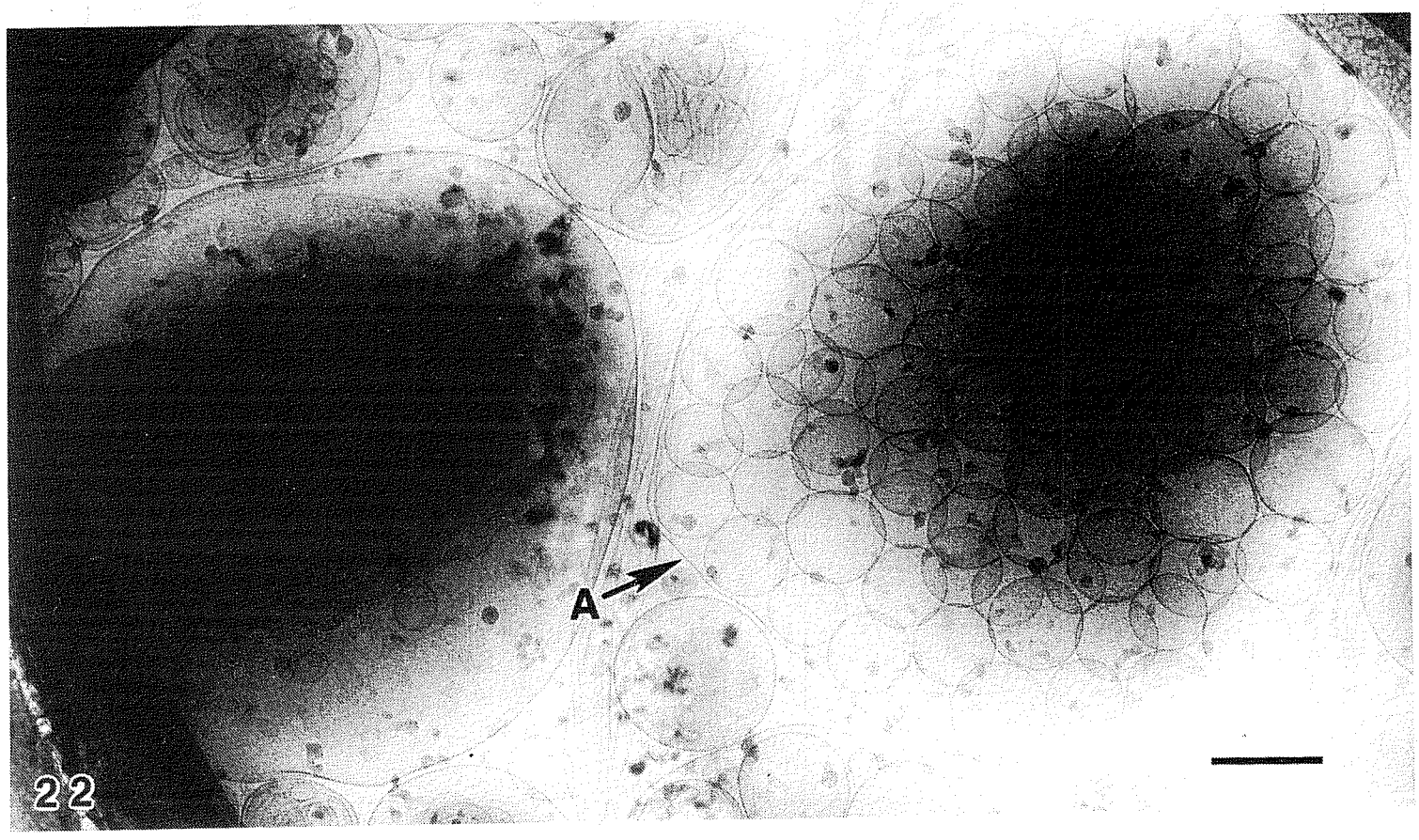

Figure 22. Vitrified hydrated unstained (VHU) cryo-TEM picture of a 1.7 wt % SHBS sample prepared with CEVS. Note large (1750 nm) single-walled vesicle (A) encapsulating many smaller vesicles. Bar = 250 nm.

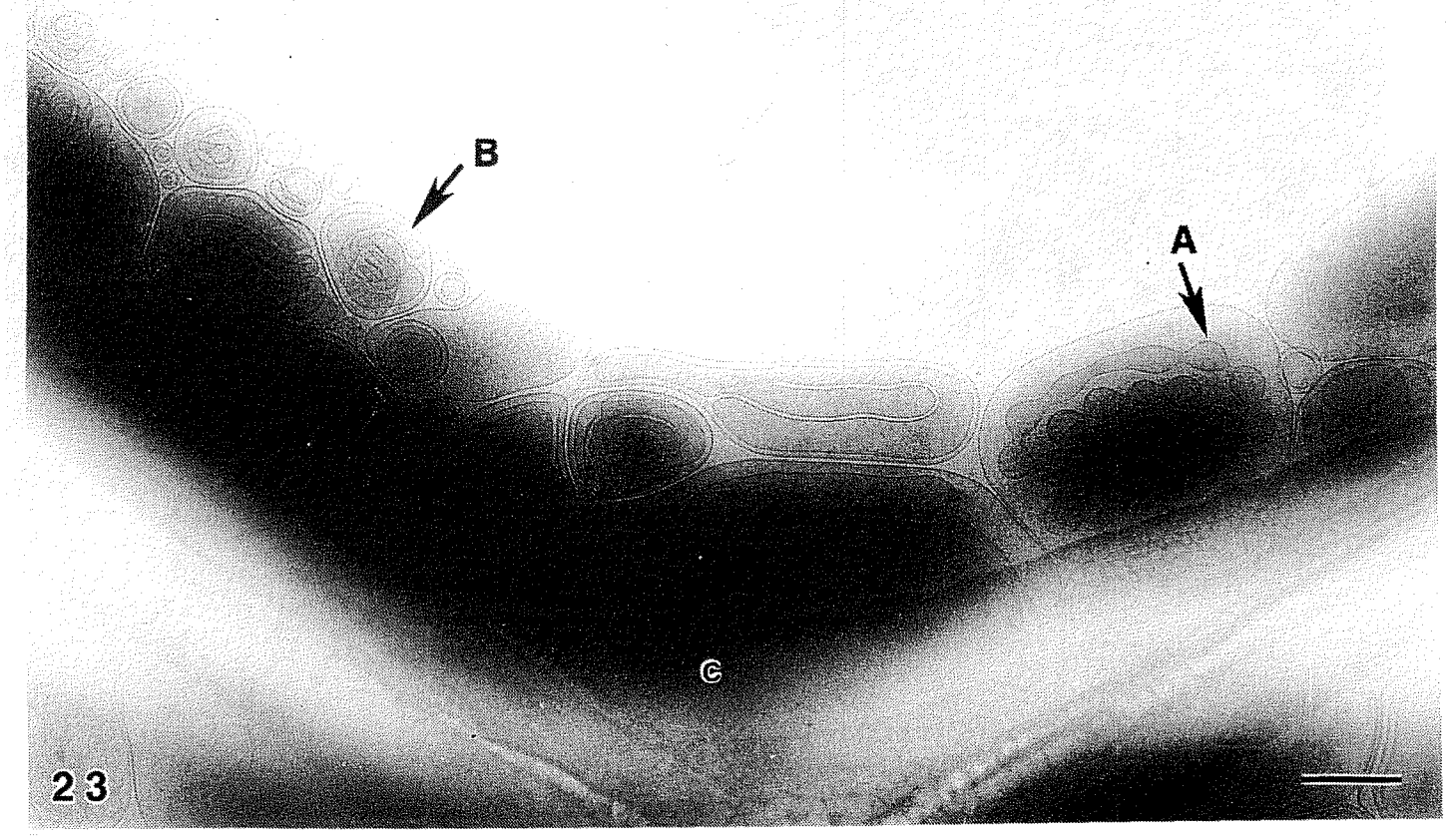

Figure 23. Electron micrograph of 1.7 wt % SHBS showing vesicle-encapsulated microtubules. (A) Microtubule in the process of budding off to form small vesicles; (B) coiled microtubule. Bar = 250 nm.

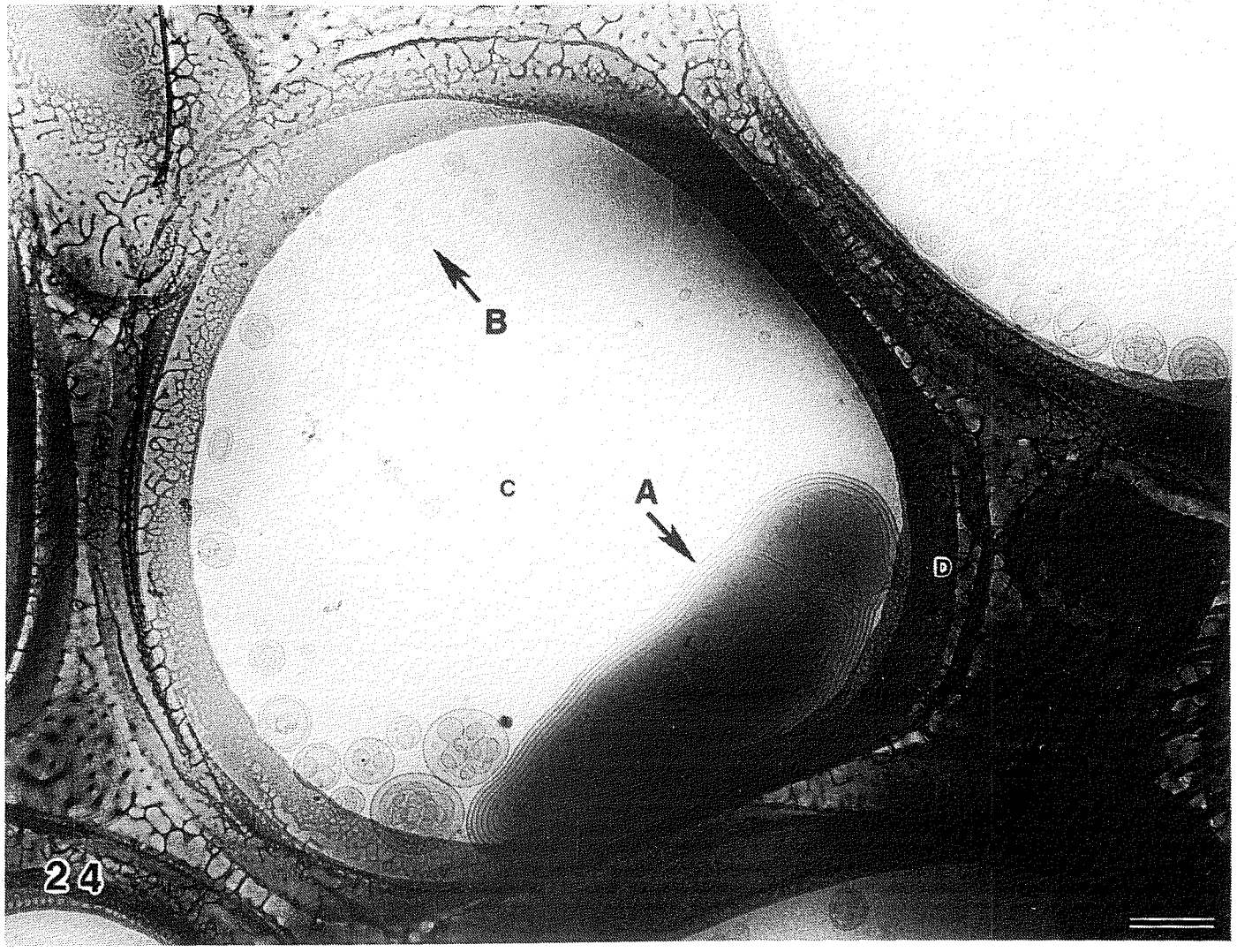

Figure 24. Vitrified solution of 1.7 wt % SHBS showing liposome with closely spaced bilayers (A) and small (10 nm) vesicles (B) in vitreous water (C) spanning holes in carbon film (D). Bar = 250 nm.

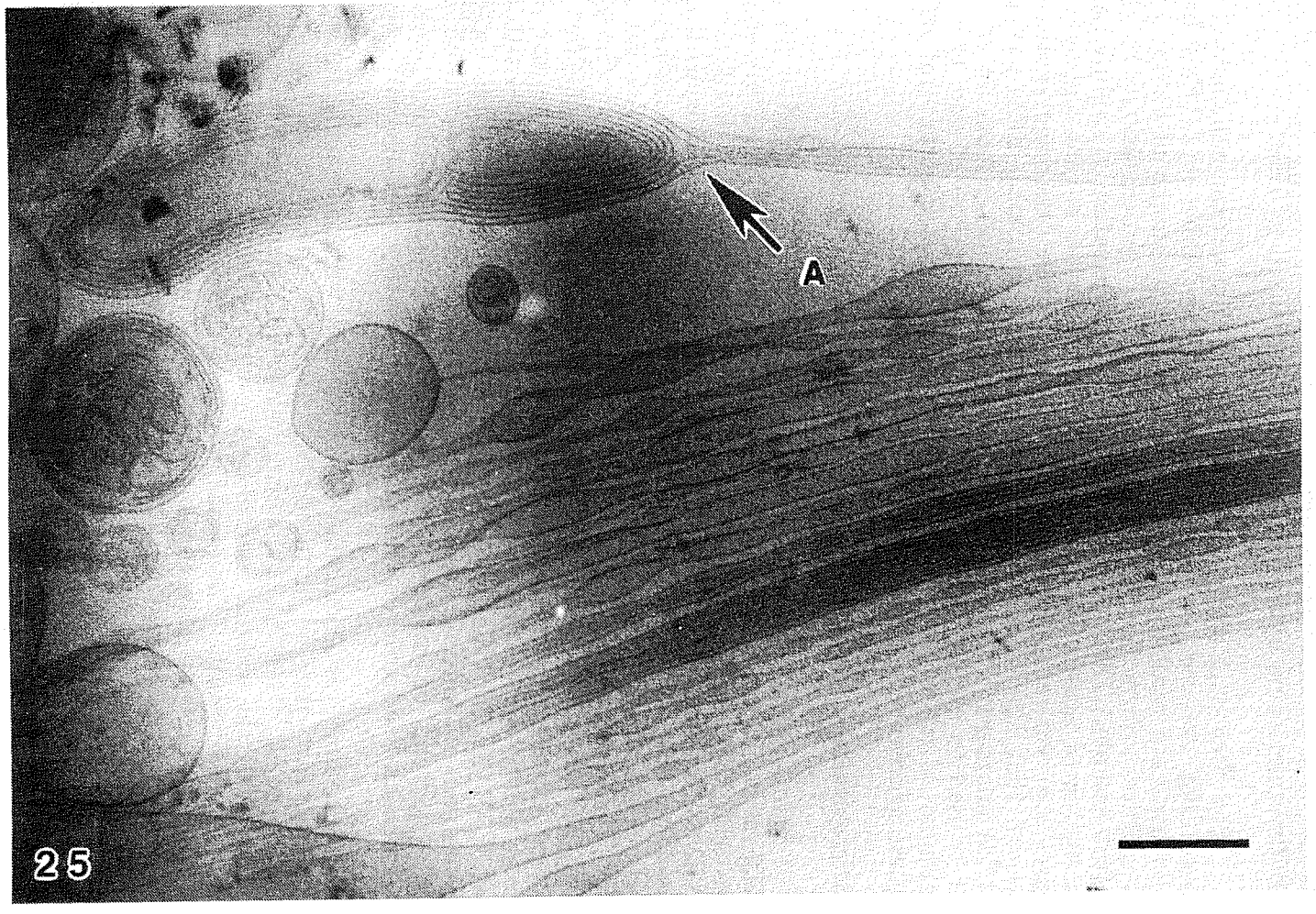

Figure 25. VHU cryo-TEM picture of 1.7 wt % SHBS showing existence of single- and multiple-walled tubules. Note liposome-tubule transition (A). Bar = 250 nm.

The collection of microtubules displayed in Fig. 25 demonstrate the existence of both single-walled and multiwalled microtubules. The multimicrotubule attached to the liposome structure (point A, Fig. 25) are reminiscent of larger, but similar vesicle-filament structures seen by VEM with didodecyldimethylammonium hydroxide partially neutralized by HBr.

The preceding observations allow some important conclusions to be drawn regarding the use of cryo-TEM and VEM. While cryo-TEM, because of its much higher resolving power, is clearly the technique of choice when detailed structural information is desired, it cannot be used exclusively to characterize a given sample. This is because the sample preparation procedure seems to cause a sorting of aggregates based on size. The result is that aggregates of certain sizes are over-represented in TEM pictures while other aggregates are excluded (recall that the large birefringent liposomes seen with VEM are absent in the TEM micrographs). Since VEM images all structures from 50 nm to 500 Cμm, it is used to initially characterize a solution in terms of size, type and relative number of aggregates present. Subsequent detailed structural information on these aggregates can be achieved using cryo-TEM.

Microstructure in isotropic phases: vesicles and micelles.

Didodecyldimethylammonium hydroxide and carboxylates form clear non-viscous solutions up to 0.5 M (Miller et al.[19], 1987b). In dilute solutions (0.001 to 0.001 M), only small particles beyond the resolution limit are detected by VEM. Examination of $2C_{12}N2C_1OAc$ by cryo-TEM establishes the presence of vesicles (Fig. 26(a)) which decrease in size upon concentration (Fig. 26(b)). Above 0.1 M, both cryo-TEM and VEM give pictures devoid of any structure.

The decreasing size of vesicle structure with concentration for $2C_{12}N2C_1OAc$ constitute a direct visualization of the conclusions drawn from fluorescence measurements. These conclusions were that the fraction of surfactant present as vesicles in the solution decrease from $\simeq 0.99$ at 0.001 M to $\simeq 0$ at 0.001 M and that the micelles were small (aggregation number 45) and remained of constant size across the vesicle-micelle transition range. This behavior can be rationalized by direct force measurements between bilayers which link head group forces directly to curvature and microstructure.

The same vesicle-micelle transformation with increasing surfactant concentration can also be induced in SHBS by addition of the cryptate C222 (Miller et al.,[19] 1987b). This macrocyclic compound forms large inclusion complexes with the sodium counterion thereby pulling it out from amongst the surfactant head group. The resulting electrostatic repulsion drives the head groups apart and induces more curvature which favors smaller aggregates. For a 0.5% SHBS solution containing C222 only small vesicles are visible (Fig. 27(a)). For a 2.0% SHBS solution with C222 (Fig. 27(b)) the electron microscope picture is devoid of any structure (it is impossible to decide where the residual graininess are micelles or noise). For comparison purposes ($\simeq$ 2%) SHBS without C222 is shown in Figs. 22-25.

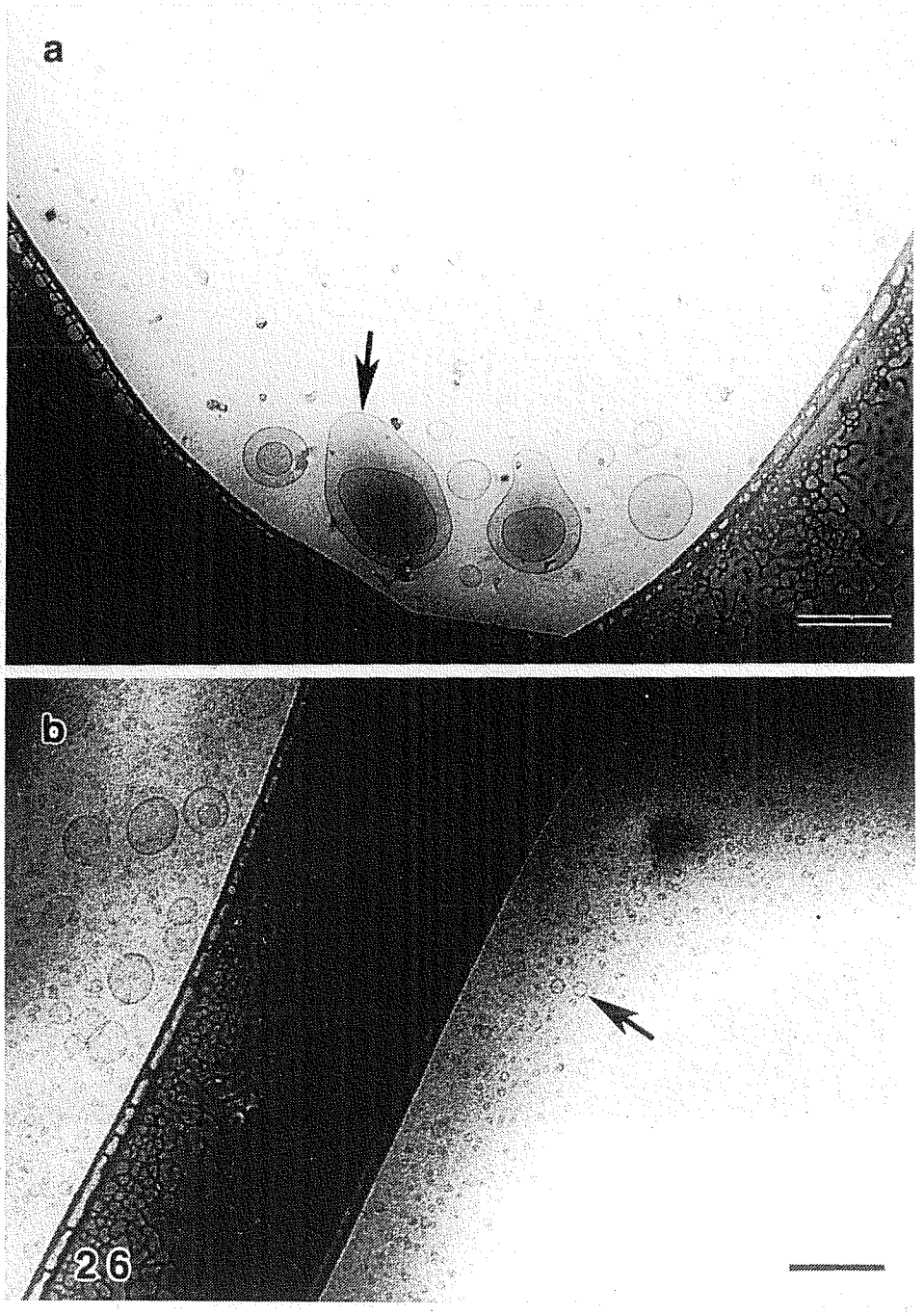

Figure 26. Aqueous dispersion of didodecyldimethylammonium acetate prepared with CEVS and examined with cyo-TEM. Bar = 250 nm. (a) Large single- and double-walled vesicles (arrow) at 0.5 wt %; (b) smaller single-walled vesicles at 1.0 wt %.

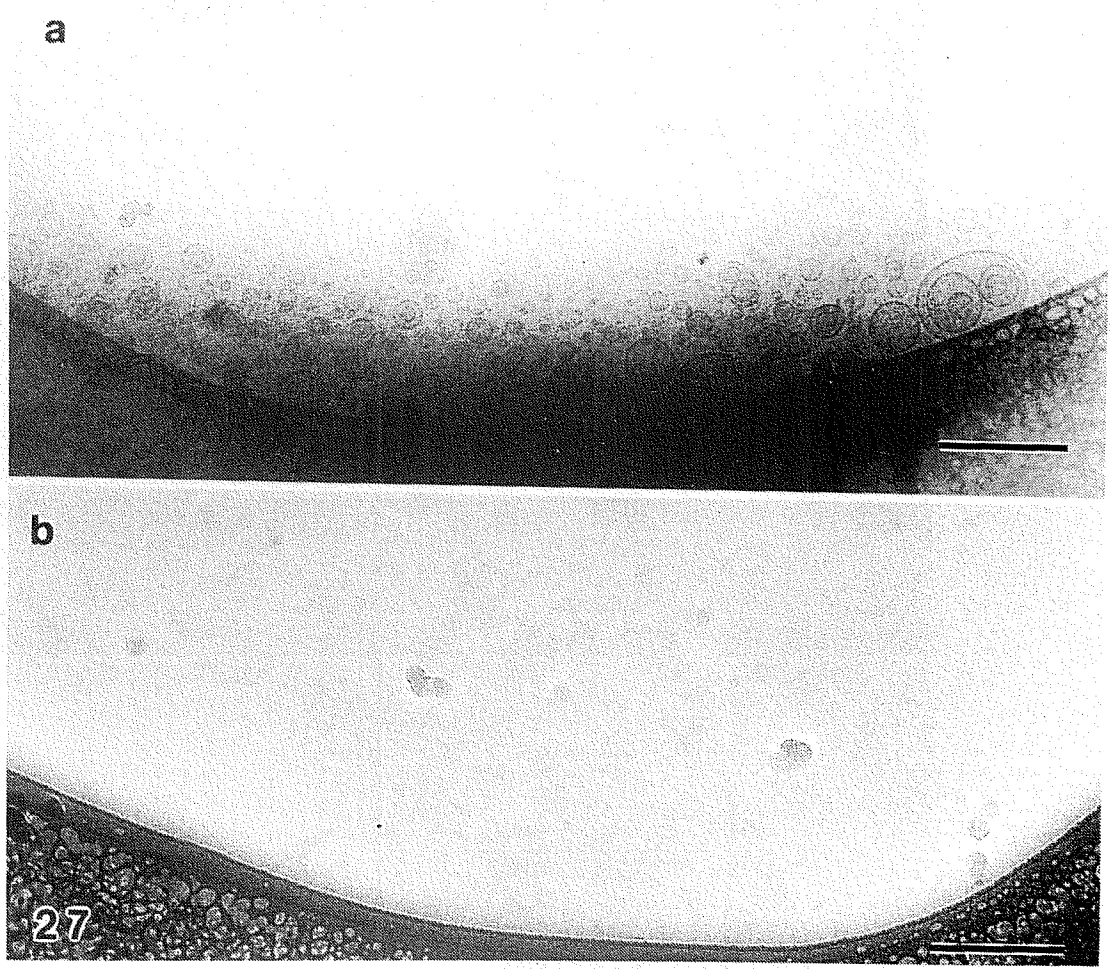

Figure 27. VHU cryo-TEM pictures of aqueous dispersions of SHBS plus the macrocyclic cryptate C222. C222 complexes the sodium counterion of SHBS which results in liposomes transforming to vesicles in dilute soluions and micelles in concentrated solution. (a) 0.5 wt % SHBS with a C222-to-surfactant ratio of 0.6. Note unilamellar vesicles with a few multilamellar liposomes. (b) 2% SHBS with a C222-to-surfactant ratio of 1.0. No microstructure is evident. Compare with Figures 23-26. Bar = 250 nm.

High temperature systems.

The chemical systems which display vesicle-micelle transitions described above involve unusual counterions (OH^-, Ac^-) or complexing agents. This can be understood in terms of a primitive model theory if these counterions behave as large "hydrated" hard-core spheres. Of more interest to our main theme is a system employing didecyldimethylammonium bromide ($2C_{10}N2C_1Br$) with the more familiar bromide counterion. At elevated temperatures, this system forms a clear isotropic "micellar" phase. Its microstructure, which has not been previously explored, varies continuously within a single phase region and surprisingly shows the same vesicle-to-micelle transition as the unusual counterions at lower temperatures. Thus if dilute $2C_{10}N2C_1Br$ is heated to 70 ° C in the CEVS chamber, and then plunged into liquid ethane, small vesicular structures (Fig. 28(b)) are seen. Upon concentration, only clear fields are seen in cryo-TEM pictures (Fig. 28(c)). Parallel to this, with VEM at 70 ° C very small structures are observed in dilute solution, no structures in concentrated solution. For comparison cryo-TEM (Fig. 28(a)) micrographs of $2C_{10}N2C_1Br$ at 25 ° C show multiwalled vesicles and liposomes. These observations provide a challenge to existing theories which can account for these phenomena only if postulated hard-core size depends on temperature. The power brought to bear by parallel use of these techniques is evident.

Discussion

The micrographs shown here demonstrate the ability of the CEVS to reduce artifacts arising from phase change induced by evaporation or temperature changes while preparing the specimen. The micrographs also illustrate the power of the system to permit sample preparation from temperatures different from ambient. Bellare et al.[21] (1987) have also demonstrated the capability of the CEVS in capturing instants of dynamical processes like sol-gel transformations.

In this account we have described the CEVS technique for preparing thin-film VHU specimens for TEM. However, the CEVS can be easily used to prepare specimens for SEM by using a 3 mm diameter flat copper plate as the specimen support. The CEVS can also be used for preparing specimens for freeze-fracture by making the specimen sandwich (between the copper planchettes) in the environmental chamber, and mounting it in the CEVS tweezers, as shown by Burns and Talmon[22](1987).

The controlled environment chamber can be used as a "mini-laboratory" to conduct dynamic experiments such as vesicle fusion, phase transitions, and chemical reactions on the grid. This permits freezing of successive instants of dynamical processes, which can then be studied by electron microscopy. Dynamical processes can be initiated, propagated and terminated by suitable combinations of parameters such as changes in temperature or saturation, on-the-grid mixing, or external irradiation e.g. ultraviolet light. Sol-gel processing for ceramics is being studied by this technique by applying, in succession, a drop of sol and a drop of catalyst onto the grid, blotting it, and then waiting for the reaction to proceed to the desired stage before cryofixing the specimen. Further processing steps, like drying and sintering can be conducted in the microsope with cold- and hot-stages.

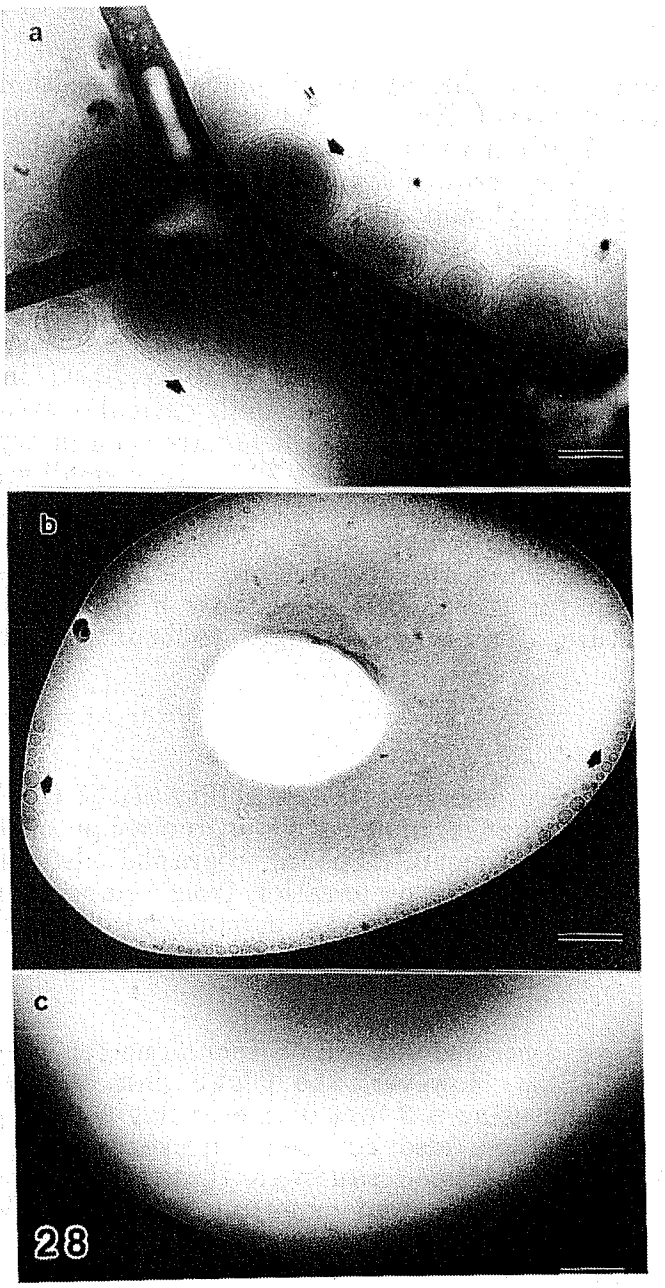

Figure 28. Didodecyldimethylammonium bromide prepared at 25 and 70 ° C with the CEVS: (a) 25 ° C and 1.5 wt % showing large liposomes; (b) 70 ° C and 0.4 wt % showing the transformation to vesicles in dilute solution; and (c) 70 ° C and 1,5 wt % giving a clear field with no visible aggregates. Whether the graininess in this electron micrograph represents micelles or noise is unresolved. Bar = 250 nm.

Construction plans for the system are available (Note 1). Ongoing work is directed towards adding a programmable temperature controller, electrical triggering of the plunging action, and a high-resolution long-working distance optical microscope for viewing the holey-carbon support. These modifications will permit interfacing the CEVS with a microprocessor to allow precise and repeatable timing control for accurately capturing desired instants of dynamical events. Auxiliary inputs, e.g. ultraviolet irradiation to initiate reactions and spectral techniques like fourier-transform infrared spectroscopy, may be used in conjunction with the microprocessor to ensure that the desired specimen conditions have been reached before cryofixation. The optical microscope will permit on-the-grid micromanipulation, e.g. deforming of vesicles, prior to vitrification. The success of the CEVS in reducing artifacts by preserving conditions very similar to the native state of the sample, and allowing "on the grid" experiments affords exciting new possibilities for membrane, virus, liquid crystal, micelle, microemulsion, polymer, and ceramic research.

References

1. Adrian, M., Dubochet, J., Lepault, J. and McDowall, A. W. Nature **308**, 32, (1984).
2. Newbury, D. E., Joy, D. C., Echlin, P., Fiori, C. E., and Goldstein, J. I. *Advanced Scanning Electron Microscopy and X-ray Microanalysis*, Plenum Press, New York, (1986)
3. Elder, H. Y., Gray, C. C., Jardine, A. G., Chapman, J. N., and Biddlecombe, W. H. J. Microscopy **126**, 45, (1982).
4. Lepault, J., Booy, F. F., and Dubochet, J. J. Microscopy **129**, 89, (1983).
5. Lepault, J., Proc. 41st EMSA Meet. ed. by G. W. Bailey, **426**, (1984).
6. Downing, K. H. , Ultramicroscopy **13**, 35, (1984).
7. Milligan, R. A., Brisson, A., and Unwin, P. N. T. J. Ultrastructural Res. **13** (1984).
8. Talmon, Y. J. Colloids and Surfaces, **19**, 237-248, (1986).
9. Bellare, J. R., Davis, H. T., Scriven, L. E., and Talmon, Y. Proc. XIth Int. Cong. on Electron Microscopy, Kyoto, 367-368, (1986b)
10. Jaffe, J. S. and Glaeser, R. M., Ultramicroscopy **13**, 373 (1984).
11. Jeng, T. W., Talmon, Y., and Chiu, W., J. Electron Microsc. Technique (submitted) (1987).
12. Bellare, J. Proc. 44th Annual Meeting of the EMSA, ed. by G. W. Bailey, 236-237, "A Controlled Environment System For Vitrification of Liquid TEM Samples." (1986a).
13. Bellare, J. R., Davis, H. T., Scriven, L. E., and Talmon, Y. Proc. XIth Int. Cong. on Electron Microscopy, Kyoto, 369-370, (1986c).
14. Costello, M. J., Fetter, R. and Corless, J. M., *Science of Biological Specimen Preparation* ed. by O. Johari, SEM Inc. AMF O'Hare (Chicago), IL 60666, U.S.A. 105-115,
15. Weast, R. C., and Astle, M. J. *CRC Handbook of Chemistry and Physics* 62nd edition, CRC Press, Inc., Boca Raton, Florida, p. E-1, (1981).
16. Perry, R. H., Green, D. W., and Maloney, J. O., (Editors) *Perrys Chemical Engineers' Handbook* 6th edition, McGraw Hill Book Company, New York, p. 3-63 to 3-73, (1984).
17. Perlov, G., Talmon, Y., and Falls, A. H. *Ultramicroscopy*, (1983).
18. Miller, D. D., Bellare, J. R., Evans, D. F., Talmon, Y., and Ninham, B. W. J. Phys. Chem. 91, 674-685, (1987a).
19. Miller, D. D., Evans, D. F., Warr, G. G., Bellare, J. R., and Ninham, B. W.

J. Colloid and Interface Science. (1987b)
20. Frances, Elias I., Ph.D. Thesis, University of Minnesota, 1979.
21. Bellare, J. R., Bailey, J. K., and Mecartney, M. 3rd International Conference on Ultrastructure Processing of Ceramics, Glasses and Composites, San Diego, Feb. 22-27, (1987).
22. Burns, J. L., and Talmon, Y. "Freeze-Fracture-Replication Using the Controlled Environment Vitrification System (CEVS), (1986).

3. PERIODIC SURFACES OF PRESCRIBED MEAN CURVATURE

Synopsis

While there are eighteen triply-periodic minimal surfaces that reportedly are free of self-intersections, to date there is no known example of a triply-periodic surface of constant, *nonzero* mean curvature that is embedded in $\mathbf{R}^3$. We compute and display five families of such surfaces, where every surface in a given family has the same space group, the same Euler characteristic per lattice-fundamental region, and the same dual pair of triply-periodic graphs that define the connectivity of the two labyrinthines subvolumes created by the infinitely-connected surface. Each family is comprised of two branches, corresponding to the two possible signs of the mean curvature, and a minimal surface. The branches have been tracked in mean curvature, and the surface areas and volume fractions recorded, with the relation $dA = 2HdV$ carefully checked to hold. The three families that contain the minimal surfaces P and D of Schwarz and the I-WP minimal surface of Schoen terminate at configurations that are close-packed spheres. However, one branch of the family that includes the F-RD minimal surface of Schoen, and both branches of the family that includes the Neovius surface C(P), contain self-intersection solutions and terminate at self-intersecting spheres. On approach to the sphere limit, whether self-intersection or close-packed, the gradual disappearance of small 'neck' or 'connector' regions between neighboring 'sphere-like' regions is in close analogy with the rotationally symmetric unduloids of Delauney. We give what we suspect are analytical values for the areas of the I-WP and F-RD minimal surfaces, and a possible limit on the magnitude of the mean curvature in such families is proposed and discussed. We also report that the I-WP and F-RD minimal surfaces each divide $\mathbf{R}^3$ into two subspaces of *unequal* volume fractions.

The numerical method is based on a new approach to the formulation of the Galerkin, or weak form, of the problem of prescribed — not necessarily constant — mean curvature. The Surface Divergence Theorem is applied directly to a vector-valued function that is the product of a scalar weighting function and a vector field chosen to enforce the boundary conditions. This formulation applied in the context of the finite element method provides a robust algorithm for the computation of a surface with: 1) mean curvature as a prescribed function of position, and 2) contact angle against an arbitrary bounding body as a prescribed function of position or of arc length. A parametrization scheme for triply-periodic surfaces is described that calls only for knowledge of the two 'skeletal' graphs; this is demonstrated by the computation of the triply-periodic minimal surface $S' - S''$ hypothesized by Schoen, who described only the skeletal graphs associated with the surface. The parametrization allows for easy calculation of the scattering function for various density profiles based on the solutions, as well as the areas and volume fractions. For the three minimal surfaces — P, D, and C(P) — whose areas and volume fractions are known analytically, the numerical results are in agreement with these values. Furthermore, we review the history of such surfaces, and clear up some inconsistencies in the literature over the D minimal surface.

Introduction

This research was stimulated by the need for mathematically well-characterized surfaces that divide space into two distinct, multiply-connected, intertwined subspaces — spatial structures that are called bicontinuous. Sponge, sandstone, apple, and many sinters are examples of relatively permanent though chaotic bicontinuous structures in the material realm. In these, one of the subspaces is occupied by a solid that is more or less deformable and the other, though it may be referred to as 'void', is occupied by a fluid. Certain lyotropic liquid crystalline states are probably also examples, one subspace being occupied by amphiphile molecules oriented and aggregated into sheet-like arrays that are ordered geometrically, the other subspace being occupied by solvent molecules; the characteristic scale of these structures is so small — 5 to 50 nm — that the issue of their bicontinuity has not been settled, however.[1–4] Related liquid crystalline states that contain two incompatible kinds of solvent molecules, e.g., hydrocarbon and water, present a further possibility in which one subspace is rich in the first solvent, the other in the second, and the surface between lies within a multiply-connected stratum rich in oriented surfactant molecules[1]. If two distinct surfaces dividing hydrocarbon-rich from surfactant-rich and surfactant-rich from water-rich are envisioned, this microstructure could be considered tricontinuous.

Certain equilibrium 'microemulsion' phases that contain comparable amounts of hydrocarbon and water as well as amphiphilic surfactant may be chaotic bicontinuous (or tricontinuous) structures, maintained in a permanent state of fluctuating disorder by thermal motions[1,5]; for they are fluid and give no indication of geometric order but there is some evidence of multiple continuity[6,7,8,9]. Here we concentrate on geometrically-ordered, bicontinuous structures. That these are indeed promising models for lyotropic liquid crystalline states known as 'cubic' or 'viscous isotropic' phases has been demonstrated in X-ray diffraction studies by Lindblom *et al.*[10], and Longeley and McIntosh[3]; see also Larsson[11]. However, the apparent matches of data with model could depend on the large number of parameters they used to define their structural models, which were based on approximations to the constant-mean-curvature surfaces of the type presented here.

Other possible areas of application of the periodic surfaces, or of disordered relatives of these, include structure of superconductors in the intermediate state[12], sintering kinetics[13], fluid flow through porous media[14], the topology of spacetime at the scale of Planck length[15], the structure of the prolamellar body in certain plastics[16], certain phase-segregated polymer blends[17], semiconductor based separations processes[18], shape-selective catalysts[19], and Fermi surfaces in electron band theory[20], see also Andersson[21].

The rest of this section provides some mathematical background and a brief historical review of the study of periodic minimal surfaces. In the next section we introduce the computational methods, for constructing a surface whose mean curvature is a prescribed function of position, and which meets a given body at a prescribed contact angle; elsewhere[22] the method is generalized to curves of prescribed space curvature lying in a known surface. In the Results section we present five new families of triply-periodic surfaces of constant mean curvature and record the areas and volumes of unit cells as we track in mean curvature; surfaces with prescribed nonconstant, smoothly varying mean curvature are also

computed.

Mathematical background

In 1865 the mathematician H. A. Schwarz published the first example of a minimal surface with full three-dimensional periodicity and free of self-intersections (or embedded in $\mathbf{R}^3$)[23,24], a surface now known as Schwarz's 'Diamond' surface (or 'D'). The designation[25] refers to the branching of the two congruent, intertwined but disjoint labyrinths lying on opposite sides of the infinitely-connected orientable surface. Each labyrinth contains in its interior a diamond-branched, symmetric graph of degree four, that is, a periodic array of nodes connected by edges in which four equivalent edges meet at the tetrahedral angle at each equivalent node (some authors, e.g. Mackay[26], give the name 'F' to this surface since it is of face-centered cubic symmetry). In Figure 1 are shown: (a) an extensive portion of this surface, together with the two graphs, (b) a lattice fundamental region (a lattice-fundamental, or L-F, region is the region that exactly fills space when the translational symmetries of the Bravais lattice are applied), and (c) a primitive patch bounded by straight lines lying in the surface (figure (c)) reproduced from Schwarz[24]. This primitive patch is the surface of minimal area that spans a circuit of four edges of a regular tetrahedron (it was also derived independently at about the same time by Riemann[27]. This was the first analytical solution to a general problem later named after Plateau, in which the surface of least area spanning a given closed loop is sought, representing the equilibrium configuration of a soap film spanning the frame. Schwarz's 1865 publication also mentioned that a periodic surface could be built up by rotating the patch through 180° rotational symmetry. Second, the surface is connected and free of self-intersections, even though it contains a network of edges of congruent regular tetrahedra and regular tetrahedra themselves cannot fill space without self-intersection.

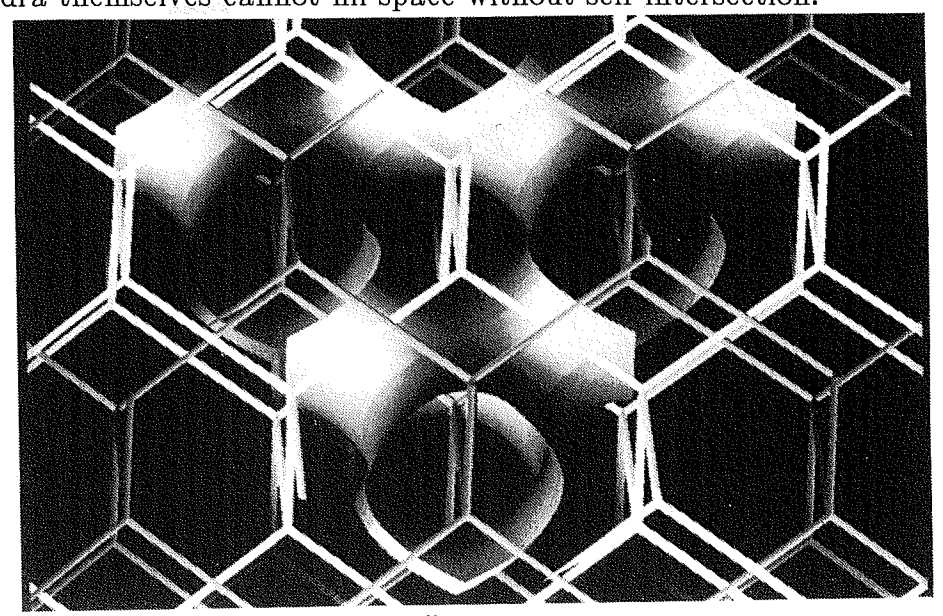

Figure 1a. The Schwarz 'D' or "Diamond minimal surface. Four lattice-fundamental regions are shown, making the Euler characteristic -16. The space group is F $\bar{4}$3m, that of diamond close-packed spheres. The two graphs thread the two labyrinths created by the space-dividing surface.

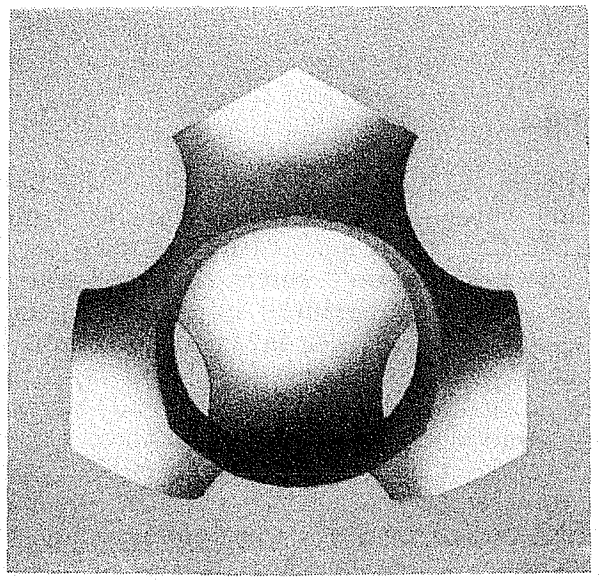

Figure 1b. A single lattice-fundamental region of the Schwarz D minimal surface, of Euler characteristic -4.

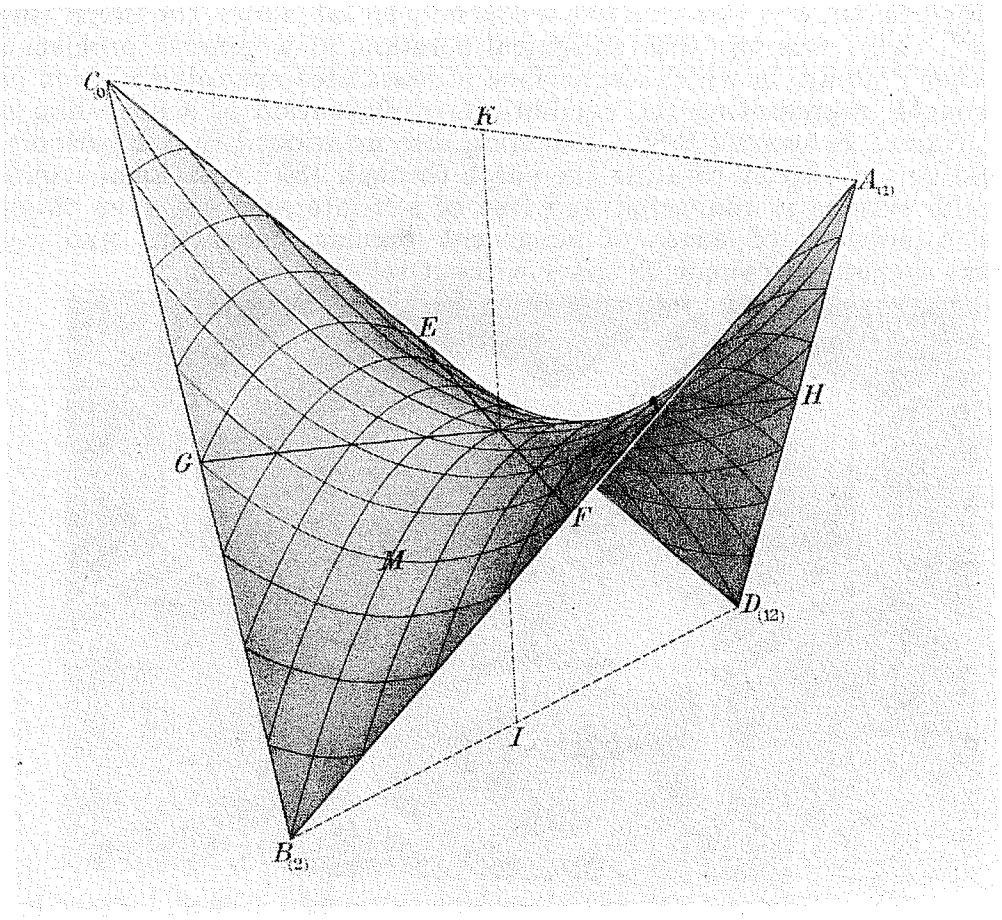

Figure 1c. A primitive patch of the D minimal surface bounded by straight lines that are axes of 180° rotational symmetry on the periodic surface (Figure reprinted from Schwarz[24]).

It can be shown that any solution to a Plateau problem must be a surface whose mean curvature H at each point is zero ($H = (1/2)[\kappa_1 + \kappa_2]$) , where κ_1 and κ_2 are the principal curvatures, reciprocals of the principal radii of curvature). A *minimal surface* is thus defined to be a surface of everywhere vanishing mean curvature[28] derived a partial differential equation for a surface of least area that is equivalent to the condition that $H = 0$). Each coordinate x_k of a minimal surface can be written as a harmonic function of certain surface coordinates[29]; see also Bonnet[30], i.e., $\partial^2 x_k/\partial u^2 + \partial^2 x_k/\partial v^2 = 0$. The reflection principle of harmonic functions then guarantees that a straight line lying in the surface is an axis of two-fold rotational symmetry Schwarz[24]. The maximum principle for harmonic functions requires that a minimal surface be wholly contained in the convex hull of its boundary curve. It can also be shown that, apart from the special case of a plane the Gaussian curvature K is negative except at isolated points where it may be zero[31,32] review these properties]. Mean and Gaussian curvature are the basic scalar invariants of the curvature dyadic, or second-rank tensors $\mathbf{b}(\mathbf{r})$, which describes the local state of surface curvature at points $\mathbf{r}$ on the surface. The curvature dyadic is the negative of the tangential gradient, or surface gradient ∇_s of the unit normal vector $\mathbf{n}$ to one side of the surface[33] (in the classical treatment of the differential geometry of a surface, this operator is suppressed). Thus:

$$\mathbf{b}(\mathbf{r}) = -\nabla_S \mathbf{n},\ H = 1/2\ \mathrm{tr}(\mathbf{b}) = -1/2\ \nabla_S \cdot \mathbf{n}\ . \qquad (1)$$

Excepting the plane, the integral Gaussian curvature (or 'total curvature') of a minimal surface is negative. Thus the integral Gaussian curvature of a periodic minimal surface must be infinite. By the Gauss-Bonnet theorem (the theorem for geodesic triangles is due to Gauss[34], and a more general form is due to Bonnet[35]; see also Darboux[36], $\iint_S K\, dA + \Sigma_i \int C_i \kappa_g ds = 2\pi\chi$, the Euler characteristic χ of such a surface is infinite. But the Euler characteristic of a lattice-fundamental regions is finite, and in the case of Schwarz's Diamond surface $\chi = -4$. The relation $\iint_S K da = 2\pi\chi$ holds for every lattice-fundamental surface patch treated here because each is bounded by geodesic curves $\kappa_g = 0$).

Schoen[25] has taken the relation $g = 1 - \chi/2$, which gives the genus g of a closed body in terms of its Euler characteristic, and applied it to a lattice-fundamental region of 17 of the 18 triply-periodic minimal surfaces known (the eighteenth surface was added in proof in a footnote, and not discussed in any detail); thus he listed the value 3 for the genus of a lattice-fundamental region of the D surface, and of its conjugate surface P (see below). However, the correct formula for the genus of a surface with r closed boundary loops (r holes) is $g = 1 - (\chi + r)/2$. The Euler characteristic of an nxnxn array of L-F region of the P surface is $-4n^3$, and the number of boundary loops is $6n^2$, so that the genus per L-F region of the infinite P surface is in fact:

$$g_{L-F} = \lim_{n \to \infty} [1 - (-4n^3 + 6n^2)/2]/n^3 = 2\ . \qquad (2)$$

In fact, the value listed by Schoen for the genus of a L-F region must in each of the 17 cases be diminished by one to give the correct value for the genus per L-F region. The correct value can be found from the Euler characteristic listed in this paper by dividing this value by -2. The genus of an orientable surface is

the maximal number of disjoint closed cuts which do not separate (disconnect) the surface. In the science of porous media, the average genus per unit volume of a dividing surface, whether periodic or not, provides a measure of the 'holeness' of the medium.[37,38]

Schwarz made his discovery with the aid of Weierstrass's integral representation of minimal surfaces in terms of the following triplet of harmonic functions of the complex variable u+iv, where the domain is a complicated Riemann surface:

$$x(u,v) = \kappa \, \mathrm{Re} \int_0^{u+iv} \frac{(1-\sigma^2)e^{i\theta}}{\sqrt{R(\sigma)}} \, d\sigma \tag{3}$$

$$y(u,v) = \kappa \, \mathrm{Re} \int_0^{u+iv} \frac{(1+\sigma^2)e^{i\theta}}{\sqrt{R(\sigma)}} \, d\sigma \tag{4}$$

$$z(u,v) = \kappa \, \mathrm{Re} \int_0^{u+iv} \frac{2\sigma e^{i\theta}}{\sqrt{R(\sigma)}} d\sigma \tag{5}$$

Schwarz was able to deduce that the diamond surface 'D' could be obtained by taking $R(\sigma)=1-14z\sigma^4+\sigma^8$, $\kappa = \sqrt{2}/K(1/2) = 0.8389222985...$, and $\Theta = 0$. The three conjugate harmonic functions, generated by taking $\Theta = \pi/2$, define the conjugate minimal surface to D also studied extensively by Schwarz[24]. This second surface is also periodic and free of self-intersections and is now known as Schwarz's 'Primitive' or 'P' Surface (see fig. 3a), because each of the two labyrinths created by the surface contains a symmetric graph of degree six (six edges meet at each node) with cubes). The Bravais lattice of P is simple cubic, and its space group is Pm3m (no. 221 in the Crystallographic Tables[40], Wyckoff notation 'n' with 48 equivalent positions; the Bravais lattice of D is face-centered cubic, and the space group is F 43m (no. 216), Wyckoff notation 'i' with 96 equivalent positions [see Schoen[25], and the Results section].

Neovius, a student of Schwarz, discovered another minimal surface periodic and embedded in three dimensions[40]. It is referred to simply as the 'Neovius Surface', or as 'C(P)'.[25] Schoen has introduced the concept of 'complementary' minimal surfaces, and his notation C(P) designates Neovius's Surface as the complement of Schwarz's P Surface. Two surfaces are said to be complementary if they contain the same straight lines and have the same space group. Despite these remarkable similarities, C(P) is considerably more complicated than P, the Euler characteristic of a lattice-fundamental region (which is also a unit cell) being -16 as opposed to -4 for P. The conjugate of Neovius's surface contains self-intersections[40] Neovius and Schwarz together discovered a total of five periodic minimal surfaces free of self-intersections, and no further examples were published until 1968. An example of a doubly-periodic minimal surface is Scherk's surface[41], also studied by Schwarz[24].

Schoen[25,42] has proven or hypothesized an additional thirteen triply-periodic embedded minimal surfaces. For one of these surfaces, which Schoen named the

'gyroid', an analytic solution with Weierstrass integrals was obtained. The surface is in fact related to both P and D by an 'associate transformation', in which the function $R(\sigma)$ and the Reimann surface in the Weierstrass representation are kept the same, and only Θ is changed. The Gauss map, which maps each point of the surface to a point on the unit sphere representing the normal to the surface, is invariant under the associate (or 'Bonnet') transformation, and since the algebraic area of the Gauss map yields the Euler characteristic, the Euler characteristic of a corresponding region of the 'gyroid' is the same as that of P and D.

The remaining twelve examples discussed in Schoen's note must be considered conjectures. In many cases physical models were built from plastic, or with soap films. Although analytic representations for these surfaces have not yet been found, Schoen's contribution to a subject which had seen little progress in over 75 years was substantial, and is carried further in this work. In this regard it should be recalled that even in the case of rotationally symmetric surfaces, the constant-mean-curvature solutions[43] do not admit closed-form analytic representations [see also Kenmotsu[44]].

Schoen's system of notation for periodic minimal surfaces will serve equally well for periodic surfaces of constant, but not necessarily zero, mean curvature. Each surface is named after the 'skeletal' graphs contained within the two labyrinthine regions into which $\mathbf{R}^3$ is partitioned by the surface. The two skeletal graphs are referred to as dual skeletal graphs and each has the same space group as the surface itself. If the surface contains straight lines, then these lines are two-fold rotation axes whose action is to interchange the two sides of the surface, and this implies that the two labyrinths — and therefore the two skeletal graphs — are congruent. The skeletal graph can then of course be called self-dual. The skeletal graphs of P, D, and C(P) are all self-dual, and hence these surfaces can be specified by the name of just one graph. In the cases of P and D, this graph is symmetric.[25,45] A graph is said to be symmetric if: 1) there exists a symmetry operation that is transitive on the edges that meet at a node; 2) there is a symmetry operation that is transitive on the nodes; 3) every vertex is joined to its z nearest neighbors (z is the degree of the graph); and 4) every vertex lines at the centroid of its z nearest neighbors. In the case of C(P) the graph is self-dual but not symmetric, having coordination symbol 12:4 [see Lines[46]] (this graph is constructed by connecting the centroid of each cube to the twelve edge-midpoints, in a simple packing of cubes). Schoen chose to name the Neovius surface by its complementary relation to P rather than by this skeletal graph.

In cases where the minimal surface does not contain straight lines, it is possible that the skeletal graph is not self-dual (although it may be, as in the gyroid, where the two graphs are identical except that one is left-handed and the other right-handed). In cases where it is not, Schoen has given hyphenated names indicating both skeletal graphs. The three such cases which will be pursued in this work are called F-RD, I-WP, and $S' - S''$. F refers to the face-centered cubic graph, which is a symmetric graph of degree 12 obtained by connecting nearest neighbors in a face-centered cubic lattice; its dual graph is not symmetric, and is named RD because it consists of all the edges of space-filling assembly of rhombic dodecahedra (each rhombic dodecahedron defines a lattice-fundamental region in the face-centered cubic lattice). Alternatively, the RD graph can be constructed by joining the centroids of nearest neighbor

polyhedra in a space-filling assembly of regular octahedra and regular tetrahedra, indicating clearly that the coordination symbol of the graph is 8:4. The I graph is the body-centered graph, a symmetric graph of degree 8 obtained by connecting all nearest neighbors of a body-centered cubic lattice; its dual graph is not symmetric, and is named WP because a unit cell resembles the string of a wrapped package. The WP graph is constructed by joining the face centers to the four edge-midpoints for each cube in a simple packing, so the coorindation symbol is 4:4 (the coordination symbol 4 is reserved for the symmetric graph of degree 4). The graph S′ is made by starting with parallel identical square tesselations, and joining corresponding edges in adjacent layers at their midpoints by edges which are perpendicular to the layers; its dual graph S″ starts with parallel identical square tessellations positioned halfway between the S′ layers and oriented 45° to the S′ squares, and edges perpendicular to the layers are erected at alternative vertices. Schoen's note[25] contains photographs of plastic models of F-RD and I-WP, but no visualizations of S′ — S″ are given.

Thirteen of the eighteen examples introduced or reviewed by Schoen contain plane lines of curvature, though many of these do not contain straight lines (including the important examples F-RD and I-WP). A plan line of curvature is a curve on a surface which lies in a plane and whose tangent at each point is parallel to one of the principle directions of the curvature dyadic. By Joachimsthal's theorem[30,47], the surface meets this plane at a constant angle, which in all the periodic surfaces treated here is $\pi/2$. In these thirteen cases Schoen has listed a 'kaleidescope' cell — one of the seven convex polyhedra proven by Coxeter[48] to be the only generators of discrete groups of reflections — which orthogonally bounds a primitive patch of surface. The periodic surface can be obtained by repeated mirror reflections through these kaleidescope cell (or 'Coxeter cell') faces. For example, Schwarz showed that a primitive patch of the D surface is orthogonally bounded by a certain tetrahedron named 'tetragonal disphenoid' by Coxeter. Thus D can be constructed by either solving a fixed-boundary problem and extending by repeated rotations, or by solving a free-boundary problem and extending by mirror reflections. The same is truce of P and C(P), while others such as F-RD and I-WP that are not self-dual can be generated only by repeated reflections of a surface patch meeting orthogonally the faces of a Coxeter cell. The lattice-fundamental region for each periodic surface in this paper is composed of an integral number of Coxeter cells, and because the boundary curves are plane lines of curvature and the surface meets this plane at an angle of $\pi/2$, the boundary curves are geodesics, as stated above.

Given fixed volume fractions, q and 1-q, of the two subvolumes into which a given convex body is to be divided by a surface of a fixed topological type, the dividing surface of minimum area a) has constant mean curvature, and meets the boundary of the body orthogonally. General existence proofs, in the context of geometric measure theory, can be found in Massari[49] and Giusti[50]. However, these proofs do not provide partitioning surfaces of prescribed topological type. Results regarding interior and boundary regularity have recently been extended from area-minimizing surfaces to surfaces of stationary area.[51,52] The problem of computing a surface of prescribed mean curvature and topological type is a fundamental one which is a natural generalization of the minimal surface problem, yet very little is known about the case of nonzero mean curvature. Nitsche[31] has reviewed the work on the problem of perturbing a minimal surface so as to have prescribed mean curvature, including the associated eigenvalue

problem; however, very few constructive results exist for the case of orthogonality boundary conditions. Schoen[25] has noted that the concept of dual skeletal graphs should apply to a constant-mean-curvature surface of the same topological type and space group as a periodic minimal surface. Recently the Weierstrass representation has been extended to surfaces of nonzero mean curvature[53], but to use his formulae to generate such a surface evidently requires its Gauss map, which in general is not known apriori. There has been no calculation of a triply-periodic embedded surface of constant, nonzero mean curvature reported in the literature.

In this paper we report such surfaces, that we have computed with a new finite element formulation. Rivas[54] has noted that finite difference techniques are not well-suited for handling contact angle boundary conditions. The finite element method has been shown to be an effective and versatile tool for the computation of minimal surfaces;[55,56], even when the surface does not admit singly-valued orthogonal projections onto planes. The method we have developed can produced surfaces of non-uniform, nonzero mean curvature that is a prescribed function of position, and we report triply-periodic examples of these as well. And the method can produce a finite surface, of prescribed mean curvature, whose contact angle against a given boundary is a prescribed function of position; the obvious application of this feature would be to fluid hydrostatics and hydrodynamics.

A rigorous mathematical existence proof for a periodic surface of small, nonzero constant mean curvature can be obtained with the methods of the theory of nonlinear elliptic differential equations. The resulting surface would be a perturbation of a known periodic minimal surface. But the intent of this paper is rather to exhibit numerical solutions that extend over wide ranges in mean curvature. The surprising fact that at the limits of these ranges simple close-packed sphere configurations are encountered might provide guidance to this seeking analytical representations of the solutions displayed.

Computational Method

In this section we introduce the computational method in the form used for the surfaces exhibited in the Results section, i.e., where the prescribed mean curvature of the computed surface is everywhere constant, and the boundary conditions are determined by two dual periodic graphs. We also give generalizations of the prescribed mean curvature of the computed surface is everywhere constant, and the boundary conditions are determined by two dual periodic graphs. We also give generalizations of the method for the computation for a surface of prescribed — not necessarily constant — mean curvature, with prescribed contact angle against a given surface. Generalization to the computation of space curves of prescribed curvature or geodesic curvature is available.[22]

Given a pair of dual period skeletal graphs, G′ and G″ with a certain space group, the first step is to identify the Coxeter (or of filling space by repeated applications of the mirror symmetries of the space group.[48] There are only seven possibilities for this cell, each of which is either a tetrahedron, a rectangular parallelopiped, or a right prism. Let $C_1,C_2,..,C_f$ be the faces of C.

This polyhedron C will contain at least a portion of one edge of each of the

graphs, since the group of reflection symmetries which exactly fills space when applied to C also generates G′(G″) when applied to the intersection of G′(G″) with C. Call the edge-portions $l_1,l_2,..,l_i \epsilon G' \cap C$ and $m_1,m_2,..,m_k \epsilon G'' \cap C$. If i or k > 1, then $f > 4$ and in this case C is divided into tetrahedra $\{T_{pq}$; the tetrahedron T_{pq} is exactly the convex hull of the segments l_p and m_q. If l_p and m_q are parallel then T_{pq} is not included. Let the faces of T_{pq} be T_{pqr}, r = 1, 2, 3, 4. Any face in the entire collection $\{T_{pqr}$ that is not part of any C_n is shared by exactly two tetrahedra.

The unit interval $0 \leq u \leq 1$ is divided into i subintervals $\{I_p\}$, and l_p is parametrized by a linear mapping from I_p;

$$\mathbf{r} = \mathbf{a}_p + \mathbf{b}_q u \quad , \quad u \ I_q \ . \tag{6}$$

similarly $0 \leq v \leq 1$ is divided into k subintervals $\{J_q\}$ and m_q parametrized by a linear mapping from J_q;

$$\mathbf{r} = \mathbf{a}_p + \mathbf{b}_q v \quad , \quad v \ J_q \ . \tag{7}$$

The entire tetrahedron T_{pq} is now parametrized by sending a spine[57] from each point on l_p to each point on m_q :

$$\mathbf{r}(u,v,w) = (\mathbf{a}_p + \mathbf{b}_p u)(1-w) + (\mathbf{a}_q + \mathbf{b}_q v) w =$$

$$= \mathbf{a}_{pq}(u,v) + \mathbf{b}_{pq}(u,v)w \ , \quad u \in I_p, \ v \in J_q, \ 0 \leq w \leq 1. \tag{8}$$

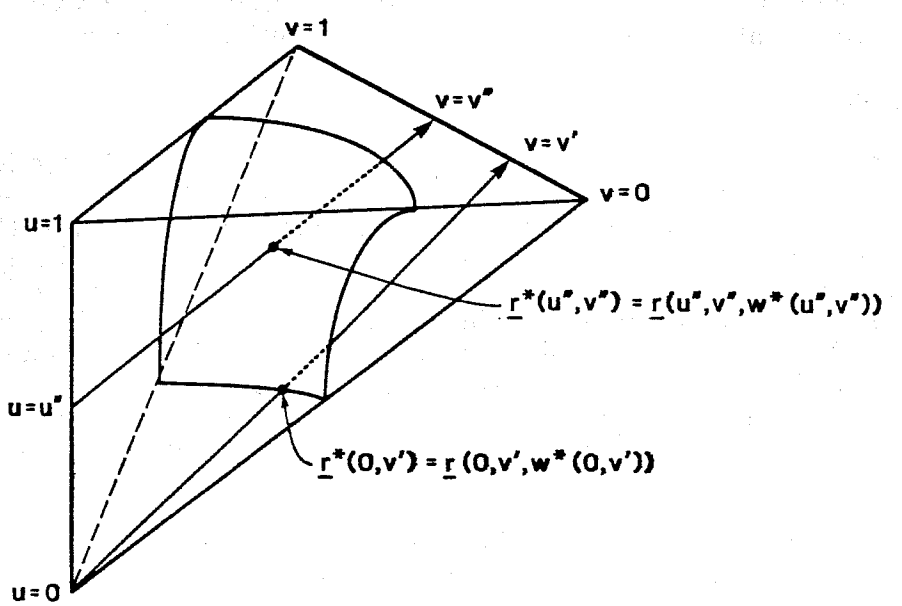

Figure 2. Parametrization of the primitive cell. One boundary spine and one interior spine are shown.

The (u,v) computational domain D consists of the union of the rectangles $R_{pq} = I_p x\ J_q$, one for each tetrahedron T_{pq}, with a pair of edges of two rectangles R_{pq} and $R_{p'q'}$ identified if T_{pq} and $T_{p'q'}$ share a face. In the cases of high symmetry examined in the next section, the identification of duplicated edges occurs automatically when the rectangles are assembled in the unit square. The parametrization of the surface patch S which spans C and is sufficient to generate the entire periodic surface by application of the group of reflections is defined by:

$$\mathbf{r}^*(u,v) = \mathbf{a}_{pq}(u,v) + \mathbf{b}_{pq}(u,v)\ w^*(u,v)\ . \tag{9}$$

The condition $0 < w^* < 1$ is necessary, though not sufficient, for the periodic surface to be free of self-intersections. The function $w^*(u,v)$ must be found to complete the characterization of the surface. Traditionally one solves the partial differential equation $\nabla_s \cdot \mathbf{n} = -2H$, which is a second order p.d.e. for $w^*(u,v)$. A finite difference or finite element solution for $w^*(u,v)$ is sought using basis functions $\phi_i(u,v)$ and finding coefficients α_i such that:

$$w^*(u,v) = \sum_{i=1}^{N} \alpha_i \phi_i(u,v)\ . \tag{10}$$

A common way of generating residual equations from which α_i's are determined is the Galerkin method, which yields:

$$\int\int_S \phi_j[\nabla_S \cdot \mathbf{n} + 2H]\ dA = 0\ ,\ \ j=1,\ldots,\ N. \tag{11}$$

It is advantageous to replace eqn. (5) by an equivalent expression with lower differentiability requirements on the basis functions, in which the boundary conditions are automatically satisfied. The appropriate integration by parts formula is the Surface Divergence Theorem (SDT)[33], which is an integral relation for a piecewise-differentiable vector-value function **f** defined on a surface:

$$\int\int_S \nabla_S \cdot \mathbf{F} dA = \int_{\partial S} \mathbf{m} \cdot \mathbf{F} ds - \int\int_S 2H\mathbf{n} \cdot \mathbf{F} dA\ ; \tag{12}$$

here **F** is an arbitrary C^1 vector-valued function defined on a surface S with normal **n** and area element dA, ∇_S is the surface divergence operator on S, H is the surface mean curvature, and ds and **m** are the differential arc length and outward pointing unit tangent along the boundary ∂S of the surface. The outward pointing tangent is defined to be orthogonal to both the surface normal **n** and the unit tangent **t** to the boundary curve ∂S;

$$\mathbf{m} = \mathbf{t} x \mathbf{n} = (d\mathbf{r}^*/ds) x \mathbf{n}\ ,\ \mathbf{r}^* \in \partial S\ . \tag{13}$$

However, if **F** is taken to be $\mathbf{n}\phi_j$, the result is equation (5), and so the SDT cannot be used to integrate (5) by parts since the SDT contains equation (5) as a special case.

The key to the present method is to choose the test functions $\mathbf{F}_j$ in terms of the fixed parametrization (2) and the weighting functions $\phi_j(u,v)$. An expedient choice for the test function $\mathbf{F}_j$ in the j^{th} residual equation equation is:

$$\mathbf{F}_j = \mathbf{M}\,\phi_j \tag{14}$$

where

$$\mathbf{M} = \partial\mathbf{r} \,/\, \partial w; \tag{15}$$

in the present case $\mathbf{M} = \mathbf{b}_{pq}$. The scalar multiplication by the weighting function ϕ_j is done so that weighted residuals result on application of the SDT. Since each spine is parametrized by w, the vector $\mathbf{M}$ is tangent to the spine given by (u,v,); in particular, if (u,v) is on the boundary of the computational domain, so that this spine rounds along some C_n, then $\mathbf{M}$ will lie in the plane of that face. The orthogonality boundary conditions for the desired surface are equivalent to the condition that $\mathbf{m}\cdot\mathbf{F}_j(= \mathbf{m}\cdot\mathbf{M}\phi_j) = 0$, and the orthogonality boundary conditions are enforced by simply striking the boundary term from each residual equation.

To carry out a computation H is prescribed and the surface operator ∇_S, the surface normal $\mathbf{n}$, and the area element data are expressed in terms of the solution (3) and its first partial derivatives. The Jacobian of the parametrization (2) is easily calculated to depend only on w:

$$\partial(x,y,z)/\partial(u,v,w)\ du\ dv\ dw = c_{pq}\ w(1-w)\ du\ dv\ dw\ , \tag{16}$$

where $c_{pq}=(\mathbf{b}_p x \mathbf{b}_q)\cdot(\mathbf{a}_q - \mathbf{a}_p)$. The transformation of course is singular along l_p and m_q, where $w = 0$ or 1, but the surface lies inside the C and does not intersect these segments. The surface normal is computed from the surface basis vectors $\mathbf{r}_u^* = \partial\mathbf{r}^*/\partial u$, and $\mathbf{r}_v^* = \partial\mathbf{r}^*/\partial v$, where in differentiating (3) we encounter the partials $\partial w^*/\partial u$ and $\partial w^*/\partial v$:

$$\mathbf{n} = \mathbf{r}_u^* \times \mathbf{r}_v^* / |\mathbf{r}_u^* \times \mathbf{r}_v^*| \ . \tag{17}$$

The surface operator is expressed in surface coordinates using a standard formula:

$$\nabla_S = \mathbf{s}_1\,\partial/\partial u + \mathbf{s}_2\,\partial/\partial v \tag{18}$$

$$= \frac{(G\mathbf{r}_u^* - F\mathbf{r}_v^*)}{EG - F^2}\partial/\partial u + \frac{(E\mathbf{r}_v^* - F\mathbf{r}_u^*)}{EG - F^2}\partial/\partial v \quad , \tag{19}$$

where $E = \mathbf{r}_u^*\cdot\mathbf{r}_u^*$, $F = \mathbf{r}_u^*\cdot\mathbf{r}_v^*$, and $G = r_v^*\cdot\mathbf{r}_v^*$ are the fundamental magnitudes of first order. The vectors $\mathbf{s}_1$ and $\mathbf{s}_2$ are the surface reciprocal basis vectors.

In the finite element method[58,59], the basis functions are of compact support -- that is, each ϕ_j is nonzero only on a small rectangle in D. Since the quantities that we want to calculate from the solutions, such as area, volume, and other surface or volume integrals such as the scattering function, do not call for explicit knowledge of the second or high partial derivatives, the most economical choice is bilinear basis functions, which are piecewise first differentiable. A method for estimating the Gaussian curvature from the solution is described later in this section.

The Galerkin-weighted residual equations are obtained by inserting the expression (3), (4), (8), (10) and (11) into the SDT (6), with the boundary term deleted:

$$0 = R_j = \int\int_S (\nabla_S \cdot \mathbf{F}_j + 2H\mathbf{n}\cdot\mathbf{F}_j)\, dA\ ,\ \ j=1,..,J\ . \tag{20}$$

The integrals are evaluated by numerical quadrature, with the local mean curvature H prescribed at each Gauss point. The equations can be solved for the α_i's by Newton iteration.

Mean curvature is a dimensional quantity, with dimensions of inverse length. One definition of a dimensionless measure is the product $H^* = H\cdot a$ of mean curvature times the lattice parameter. Thus the solutions presented can be scaled to any size lattice. Corresponding areas and volumes are found by multiplying the dimensionless quantities by a^2 and a^3, respectively.

A good initial estimate of the solution is necessary, and this often requires considerable trial-and-error. Techniques for generating an estimate for the first solution in a family have been given[22]; in the families treated here the minimal surface was found first, since the nonlinearities in the term containing H generally slow convergence. Once a single solution is available, first-order continuation[60] in parameter H^* can then used to examine a full range of constant mean curvature surfaces with the same space group and skeletal graphs as the known surface. In this continuation scheme, the change in the nodal values resulting from a small increment in H is predicted by solving for $\partial/\partial H$ in the matrix equation:

$$\partial R_j/\partial\alpha_k\ (\partial\alpha_k/\partial H) + (\partial R_j/\partial H)\ ,\ \ j = 1\ ,..,\ J\ . \tag{21}$$

where the inverse of the Jacobian matrix $[\partial R_j/\partial\alpha_k]$ is known from the final Newton iteration at the old value of H. The column vector on the right-hand side of (13) has already been calculated as one of the contributions (after multiplication by 2H; see eqn. (12)) in the residual R_j:

$$\partial R_j/\partial H = \int\int_S \mathbf{n}\cdot\mathbf{F}_j\ dA\ ,\ \ j = 1\ ,..,\ J\ . \tag{22}$$

For each surface of non-zero H^*, the sign convention for H^* reverses when the (orientable) surface is viewed from the other side. For the cases where the skeletal graph is self-dual, this corresponds to the two choices for the unit cell, one in which the centroid is a node of G′ and one where it is a node of G″.

Thus in these cases we need only substitute positive values for H^* in the computation, and use this transformation to display unit cells with H^* negative. In cases where G' and G'' are not congruent, both positive and negative values of H^* must be explicitly substituted.

It is a simple matter to compute the area of each computed surface, as well as the volume fractions of the two labyrinths created by the partitioning surface:

$$A(H) = \int\int_S dA = \int\int_D \sqrt{EG - F^2}\,dudv \ ,$$

$$V(H) = \int\int\int_{w<w^*} dV = \sum_{R_{pq}} \int\int \int_0^{w^*(u,v)} c_{pq} w(1-w)\,dw\,du\,dv$$

$$= \sum_p \sum_q c_{pq} \int J_q \int I_p (w^{*2}/2 - w^{*3}/3)\,du\,dv \ . \qquad (23)$$

This latter integral gives the volume in C lying on the same side of the surface as the skeletal graph G'. The relation:

$$dA = 2H\,dV \quad \text{or} \quad A'(H) = 2HV'(H) \qquad (24)$$

applies because each surface in a given family hits the faces of C orthogonally, and provides a check on the numerical accuracy of the constant-mean-curvature surfaces generated[31,34], derived a formula for the first variation of a surface which is easily reduced to (17) when H is constant; the authors do not know where (17) was first explicitly stated).

If H is specified as a function H(u,v) of the surface coordinates then this function is evaluated at each Gauss point P_m, where the value $H(P_m)$ is needed in those residual equations R_j satisfying $\phi_j(P_m)!=0$. Clearly a more rapidly-varying function will require a finer grid. If H is a specified function of spatial position H(r), then this is rewritten, via (2,3), as a function of u, v, and the solution $w^*(u,v)$. Examples of this are in the Results section. In principle it is possible to prescribe H as a function of position *and slope* by including in the prescribed function the values of $\partial w^*/\partial u$ and $\partial w^*/\partial v$ already calculated at the Gauss points, though this has not been tried. When H is prescribed as a function of position and/or slope, then the Jacobian matrix should include the dependence of this prescribed H on the nodal values; however, if this function is slowly-varying and the user is willing to sacrifice quadratic convergence, this contribution to the Jacobian can be neglected or approximated.

The method is easily generalized to allow specification of the contact angle γ between S and the surface ∂C of a known body C along $\partial S = S \cap \partial C$; the precise definition of this contact angle is the angle between the surface normal $\mathbf{n}$ and the normal $\mathbf{R}$ to ∂C, both taken at $\mathbf{r}^*(u,v) \in \partial S$. Since the surface ∇C is known, its normal $\mathbf{N}^*(u,v)$ presumably can be written (except perhaps on a set of measure zero) as a function of position in space, and ultimately of u,v, and

$w^*(u,v)$ using (2) and (3). In cases where C is a polyhedron, $\mathbf{N}$ is a constant independent of u and v along faces of the polyhedron.

The parametrization $\mathbf{r}(u,v,w)$ of C must always be defined in such a way that the spines whose (u,v) coordinates are on the boundary ∂D of the computation domain lie entirely on the boundary ∂C of the body C. By the work of Kistler and Scriven[61] it is known that the finite element method accommodates virtually any parametrization of the solution in terms of the coefficients, up to and including the representation of a surface by its intersections with predefined space curves selected as spines. In much of Kistler's work the spines were defined individually, with the basis function ϕ_i providing the interpolation between nodes. However the notion of a parametrization with spines also includes as special cases all of the traditional coordinate systems, normal perturbations to a known surface[22], and most importantly here, parametrizations that are interpolated between boundary z spines running along the surface of a given body, an example being the 'spine fields' concocted above to fill the Coxeter cells. Curved spines must be invoked if ∂C is itself curved, unless ∂C is a ruled surface (such as a generalized cylinder) in which case the generators could be taken as straight spines. The equations of this section have been developed in full generality of arbitrary spine parametrizations, and since the residual equations can be written immediately with low-order differentiability requirements on this parametrization, the method is quite general.

Recently[62] it has been noted that the generalized Coxeter cells of Bashkirov[63],which can have curved faces, could be used to determine orthogonality boundary conditions for periodic minimal surface (and so for constant mean curvature variants, we suggest). The generalization of the present method to curved spines provides one possible solution scheme to this approach.

Where curved spines must be invoked the w-dependence of $\mathbf{r}(u,v,w)$ will be more complicated than the linear dependence in (2). Nevertheless we still define $\mathbf{F}_j$ via equation (8), recognizing that $\mathbf{M}$ is now a function of u, v, *and* w^*. In addition to this tangent vector ∂C along the (u,v) spine, we define another vector $\mathbf{M}^\ddagger$also tangent to ∂C but orthogonal to the spine:

$$\mathbf{M}^\ddagger = \mathbf{M}\mathrm{x}\mathbf{N} \,, \tag{25}$$

and then

$$\mathbf{F}_j^\ddagger = \mathbf{M}_j^\ddagger \sigma \,; \tag{26}$$

we take $\mathbf{N}$ to be normalized so that $\mathbf{F}_j = \mathbf{N}\mathrm{x}\mathbf{N}_j^\ddagger$.

Combining this with equation (7), we have that:

$$\mathbf{F}_j \cdot \mathbf{m} = (\mathbf{N} \times \mathbf{F}_j^\ddagger) \cdot (\mathbf{t} \times \mathbf{n}) \quad . \tag{29}$$

By a simple vector identity this can be rewritten:

$$\mathbf{F}_j \cdot \mathbf{m} = (\mathbf{N}\cdot\mathbf{t})(\mathbf{F}_j^{\ddagger}\cdot\mathbf{n}) - (\mathbf{N}\cdot\mathbf{n})(\mathbf{N}\cdot\mathbf{n})(\mathbf{F}_j^{\ddagger}\cdot\mathbf{t})$$

$$= -\cos\gamma(\mathbf{F}_j^{\ddagger}\cdot\mathbf{t}) \tag{30}$$

where the contact angle γ is specified between the normalized vectors $\mathbf{n}$ and $\mathbf{N}$, and the dot product of the normal and tangent vectors $\mathbf{N}$ and $\mathbf{t}$ to ∂C is zero. Another simplification occurs when we notice that the differential arc length ds in the expression $\mathbf{t} = d\mathbf{r}^*/ds$ cancels with the ds in the integrand of line integral of the SDT:

$$\mathbf{F}_j \cdot \mathbf{m} ds = -\cos\gamma(\mathbf{F}_j^{\ddagger}\cdot d\mathbf{r}^*/ds)ds$$

$$= -\cos\gamma \mathbf{F}_j^{\ddagger}\cdot d\mathbf{r}^* \tag{31}$$

We specify the contact angle γ at each point of the boundary ∂S by inserting (18) into the SDT (6). In many cases the parametrization (Equations 8,9) and the boundary ∂D of the computational domain are such that the line integral can be performed analytically between nodes. For example, if C is a polyhedron parametrized as in the past section, then each $\mathbf{M}_j^{\ddagger}$ (and therefore $\mathbf{M}_j^{\ddagger}$) is independent of w, since only straight spines are needed; furthermore $\mathbf{r}^*$ is linear in u and v since the representation (Equations 8,9) with bilinear basis functions is piecewise linear along the polygonal boundary ∂D. Thus if the contact angle is to be everywhere constant, the integration over a boundary grid line is easily performed analytically, as is done in an example in the Results section. If the contact angle has a relatively simple analytic form as a function of u and v or of arc length s, again the analytic integration should be possible. One can imagine, on the other hand, situations where the contact angle prescription is sufficiently complicated (particularly a function of the spatial coordinates on ∂S) that the integration would have to be performed by numerical Gaussian quadrature.

In the expansion in bilinear basis functions, the Gaussian curvature is concentrated in the solid angles at nodes, where four surface elements meet. The following scheme is a sensible method of estimating K at each node, and gives an accurate value of the integral Gaussian curvature over any region comprised of a nontrivial number of elements.

The integral of the Gaussian curvature over an area of surface S is exactly the algebraic (or signed) area of the image on the unit sphere of the spherical map, which for every point on S assigns a point on the unit sphere corresponding to the direction of the normal on S. The area of the spherical image is taken to be negative if the orientation of a closed loop is reversed with respect to the orientation on S, and positive if the sense is preserved. If this rule is applied to a very small surface patch S, over which the Gaussian curvature is approximately constant, then a value approximation to the average pointwise Gaussian curvature is:

$$K \approx (\text{signed area of spherical image}) / (\text{area of S})$$

The normals to a surface defined with bilinear basis functions are most accurately calculated at the midpoints of elements; in this calculation only first-

partial derivatives are required. Thus if we are interested in the value of K at an interior node N_j, a simple calculation at the midpoints of each of the four elements meeting at N_j supplies four points on the unit sphere. Girard's theorem then provides a convenient means of evaluating the area of the spherical patch bounded by geodesics that form a circuit through these four points. By choosing geodesics to join consecutive points, we also insure that neighboring quadrilaterals join up exactly, without gaps or overlap; this is very important for the calculation of the total integral Gaussian curvature over a region of surface. To apply Girard's theorem we will need the angle between two geodesics g_1 and g_2, where g_1 passes through points on the unit sphere corresponding to the unit vectors $\mathbf{n}_i$ and $\mathbf{n}_j$, and g_2 passes through the endpoints of $\mathbf{n}_i$ and $\mathbf{n}_k$. But this angle is just the dihedral angle between the planes whose sections on the sphere are g_1 and g_2. The unit normal to the plane containing $\mathbf{n}_i$ and $\mathbf{n}_j$ is:

$$\mathbf{n}_{ij} = \mathbf{n}_i \times \mathbf{n}_j / | \mathbf{n}_i \times \mathbf{n}_j | , \tag{32}$$

and similarly for $\mathbf{n}_{ik}$. Then the angle $\bar{\omega}$ between g_1 and g_2 is given by:

$$\cos\bar{\omega} = \mathbf{n}_{ij} \cdot \mathbf{n}_{ik} . \tag{33}$$

After calculating the four angles of the geodesic quadrilateral, its area is given by Girard's theorem as the sum of the four angles, minus 2π. A convenient test for the sign of this integral Gaussian curvature is to check the sense of the loop $\mathbf{n}_1 \rightarrow \mathbf{n}_2 \rightarrow \mathbf{n}_3 \rightarrow \mathbf{n}_4$, by:

$$\text{sign } K = \text{sign } \{ [(\mathbf{n}_2 - \mathbf{n}_1) \times (\mathbf{n}_3 - \mathbf{n}_2)] \cdot \mathbf{n}_2 \} . \tag{34}$$

The resulting value of the integral Gaussian curvature is then divided by the area of the surface element, given by one term in equation (15).

To estimate K at a node that lies on the boundary of D, we have used a method based on Joachimsthal's theorem.[47] Whenever the boundary conditions require a fixed contact angle against a plane (or against any surface, such as a sphere, on which every point is an umbilic), then the curve of this intersection is a line of curvature. In the triply-periodic surfaces of this paper, whether of constant mean curvature or not, the boundary curves on the primitive patch S are thus plane lines of curvature. A scheme to estimate $| \kappa_1 |$, the magnitude of the curvature of this plane curve at a given point, is to circumscribe a circle about the triangle determined by three consecutive points centered about the given point. If a, b and c are the sides of this triangle and $s = (a + b + c)/2$, then the radius of curvature $R = 1/| \kappa_1 |$ is given by Heron's formula:

$$R = \frac{(abc)}{4\sqrt{s(s-a)(s-b)(s-c)}} . \tag{35}$$

There are then only two choices for the second principle curvature, because the sum of the curvatures equals $2H^*$. To distinguish between the two possibilities $\kappa_2 = 2H^* - | \kappa_1 |$ and $\kappa_2 = 2H^* + | \kappa_1 |$, the magnitude of κ_2 is estimated using the

above formula applied to the images of three points that begin at the given node and move directly into D.

P Family: Results

We now describe a family of triply-periodic embedded H-surfaces that each have space group Pm3m and divide space into two labyrinthine regions, which are threaded by two fixed dual symmetric P graphs of degree six. The solution for H = 0 is the Schwarz P minimal surface, and the limiting configuration on each of the two branches consists of simple cubic close-packed spheres. Except for these limiting configurations, the Euler characteristic of a unit cell of surface, which is also a lattice-fundamental region, is -4, and the number of boundary loops is r = 6.

The Coxeter cell C for each member of this family is a quadrirectangular tetrahedron, e.g., given by $0 \leq z \leq x < y \leq 1/2$. Among the edges of C are representative edge-portions of each of the two skeletal graphs G′ and G″:l_1 : $\{(0, u/2,0)\ 0 \leq u \leq 1\ \} \in G'$and m_1: $\{1/2, 1/2, v/2)\ ) \leq v \leq 1\ \} \in G''$. Thus the vector field **M** is simply **M**(u,v) = (1/2, 1/2-u/2, v/2). The generic residual equation is now determined, using the equations of the previous section. The constant c_{pq} in the Jacobian, Eqn. (9), is simply 1/4.

The computational domain is the unit square in u and v, and this was divided into a 15 x 15 mesh; i.e., 225 elements, and 16 x 16 = 256 nodes, so 256 basis functions and 256 residual equations. The Jacobian matrix was banded with a total bandwidth of 35. The first solution computed was the minimal surface, for which the initial estimate was an hyperbolic paraboloid. The nonlinear system of residual equations was solved by Newton iteration on a Cyber 124, each iteration using about 1 second cpu time. For nearly all the surfaces calculated, the mesh was an even mesh over the entire unit square. However, for the surfaces just near the close-packed spheres (CPS) limit, the nodes were evenly spaced in the u-direction but placed as follows in the v-direction: v = 0, 1/60, 1/30, 0.05, 0.075, 0.1, 0.15, 0.2, 0.3, 0.4, 0.5, 0.6, 0.7, 0.8, 0.9, and 1.0. In the case H* = 0 the straight lines on the surface should satisfy w = 1/2 on nodes where u = v, and this was satisfied to 13 digits (the accuracy of the Cyber 124 with single precision) for every such node; this remarkable accuracy was in fact observed for all three minimal surfaces treated containing straight lines, namely P, D, and C(P). Also for these surfaces, the volume fraction calculated was 1/2 to 13 significant figures.

The computer graphics were prepared using a Cray-1S with the graphics package MOVIE.BYU.[64] In this program, surfaces are represented by polygons. To meet this limitation, system at the University of Minnesota set an upper limit of 8,000 polygons. To meet this limitation, the 15 x 15 mesh was thinned to 8 x 8. A front clipping plane was used to reduce clutter, and to eliminate nodes of the skeletal graphs that would appear with the wrong coordination number, where the polygon limitation did not allow all of the edges coincident at these nodes to be included.

In the case of the P family, it was found best to exhibit an amount of surface that corresponds to 1 - 7/8 unit cells. There are two obvious choices possible for the unit cell; if a node of the G′ (lighter) skeletal graph is designated as

the origin, with the principle directions of the lattice coinciding with the coordinate directions, then the unit cube $\{('x, y, z) \mid -1/2 \; x, y, z \; 1/2\}$ centered at this origin could serve as the unit cell; alternatively the cube $\{ (x,y,z) \mid 0 \; x,y,z \; 1 \}$ centered at a node of the G″ (bolder) graph could be chosen. We have elected to exhibit both cells, which share the common octant $\{ (x,y,z) \mid 0 \; x,y,z \; 1/2 \}$. Thus we have a conception of both the 'solid' and the 'void' regions, as it were, as well as a common octant showing how these join. Another octant of surface, different from this shared octant, has been exploded and shaded differently; this is done not only to better define an octant of surface, but also because exploding this octant helps reveal the shared octant that would otherwise be obstructed.

Figures 3a through 3e are the resulting computer plots for five selected values of H*. Because the P skeletal graph is self-dual, a plot for any nonzero value of H* represents both the surface H = H* and H = -H*, the sign depending on which side of the surface one is viewing it from, or equivalently, which of the two unit cells described in the previous paragraph is the object of interest and which is part of the 'void'. The volume fraction V of that portion of a unit cell lying on the same side of the surface as the lighter skeletal graph is plotted versus H* in figure 3f; likewise the sign convention for H* is that we take the sign as seen from a node of the G′ skeletal graph. Figure 3g is a plot of A versus V, so that the slope dA/dV of the curve at any point is 2H*. In each graph the endpoints represent simple cubic close-packed spheres, where:

$$A = \pi, \text{ and } V = \pi/6 \text{ or } 1 - \pi/6, H^* = 2 \text{ or } -2 \; . \qquad (36)$$

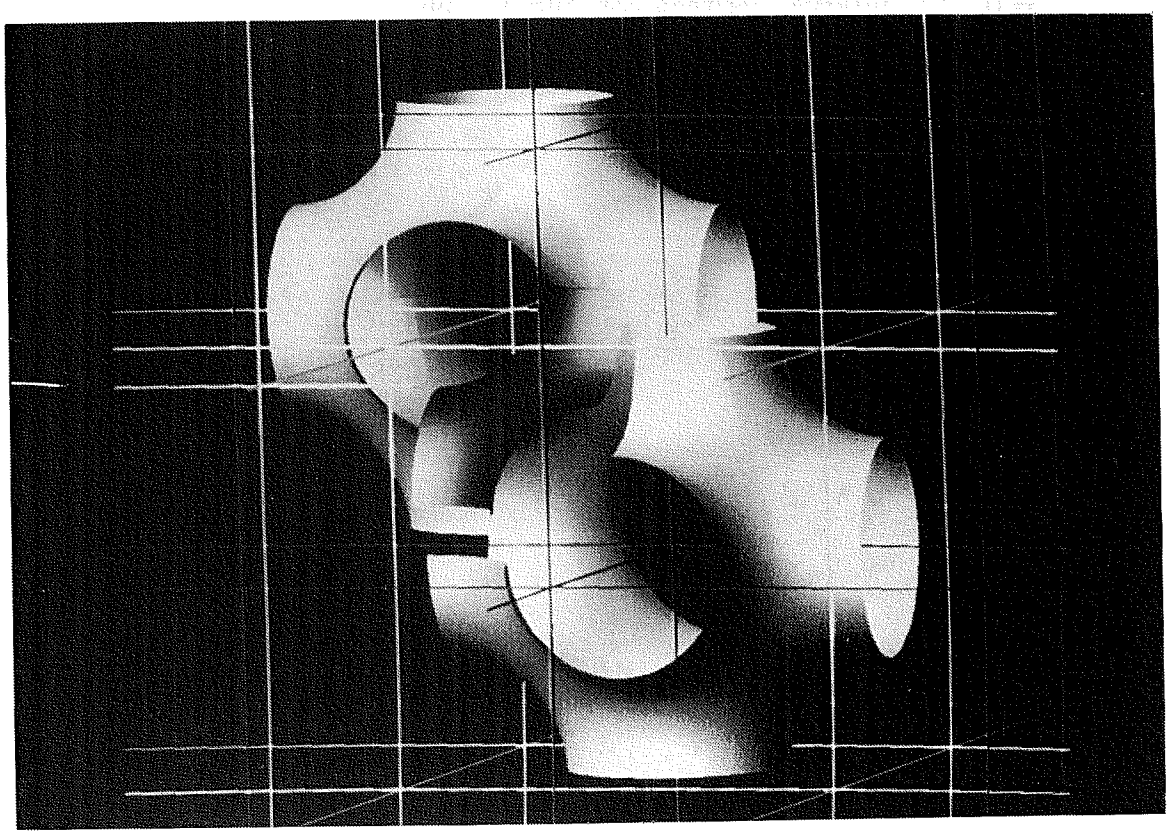

Figure 3a. The Schwarz P surface, the solution with H* = 0, space group Pm3m, Euler characteristic -4 per lattice-fundamental region.

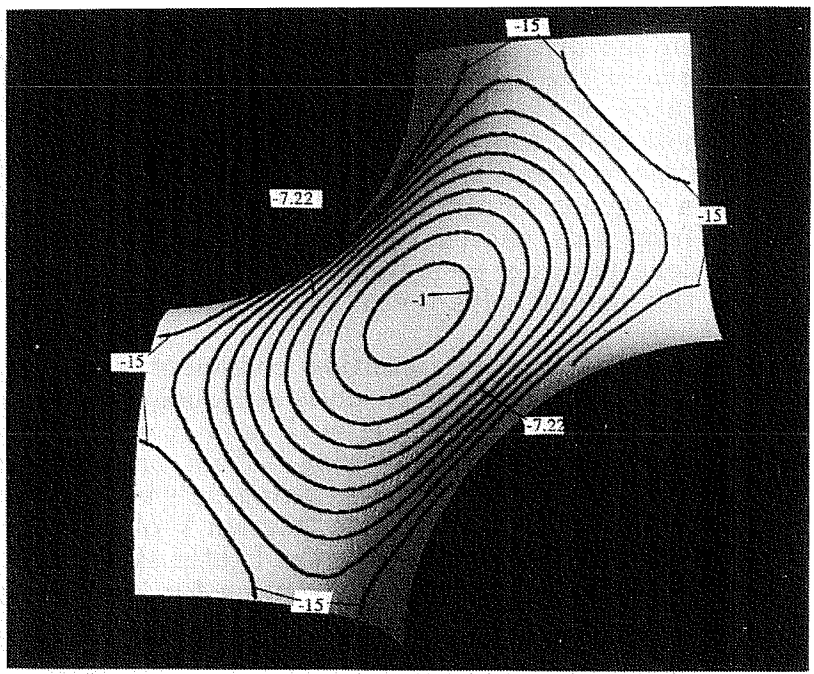

Figure 3a′. Contour plot of Gaussian curvature for the Schwarz P minimal surface, $H^* = 0$. The interval between contours is 1.56.

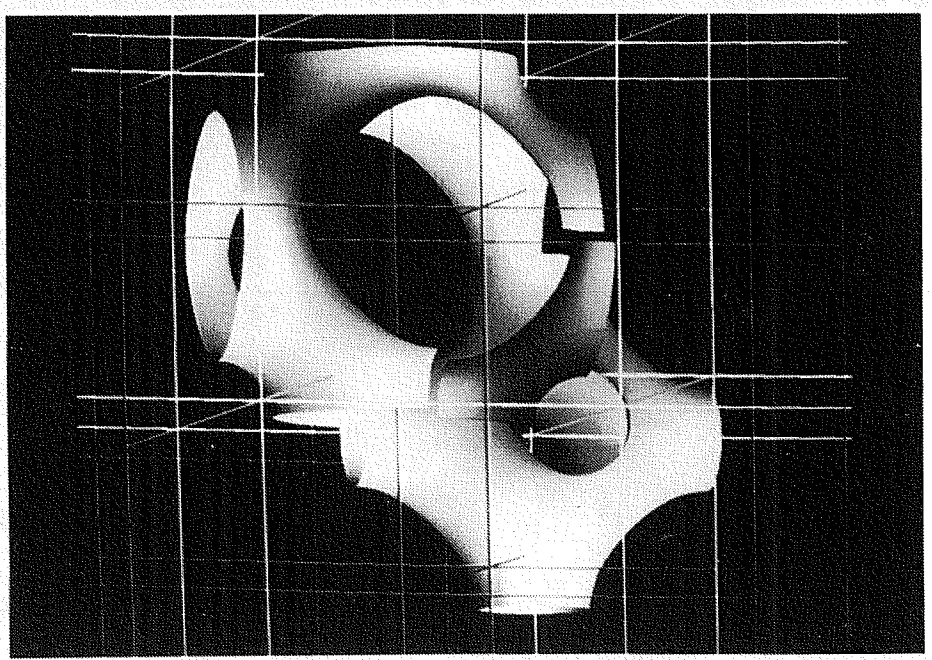

Figure 3b. The solution with $H^* = 1.0$, same space group and topological type as the Schwarz P minimal surface.

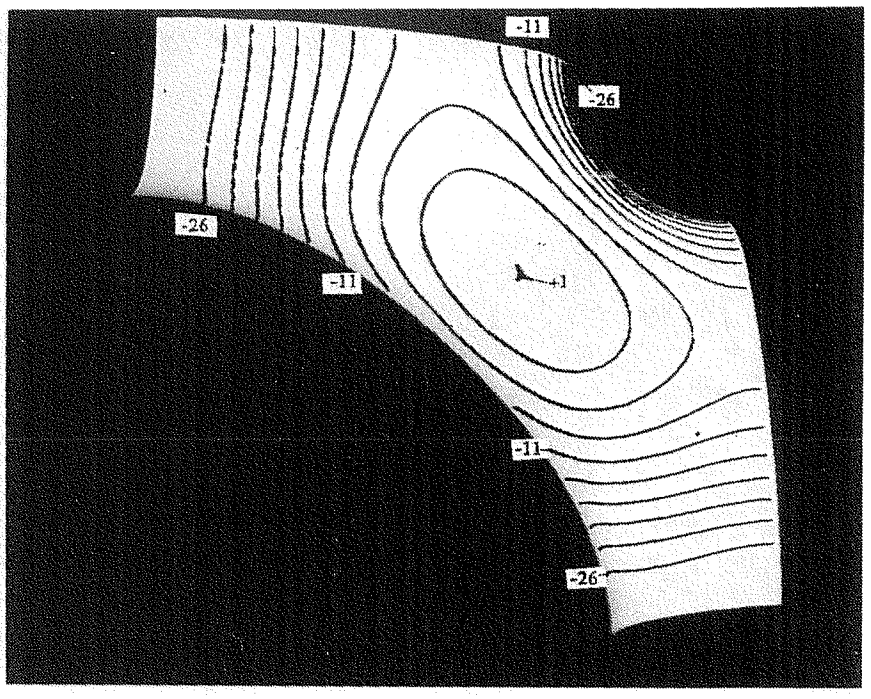

Figure 3b′. Contour plot of Gaussian curvature for an octant of the surface in figure 3b. Contour interval is 3.0.

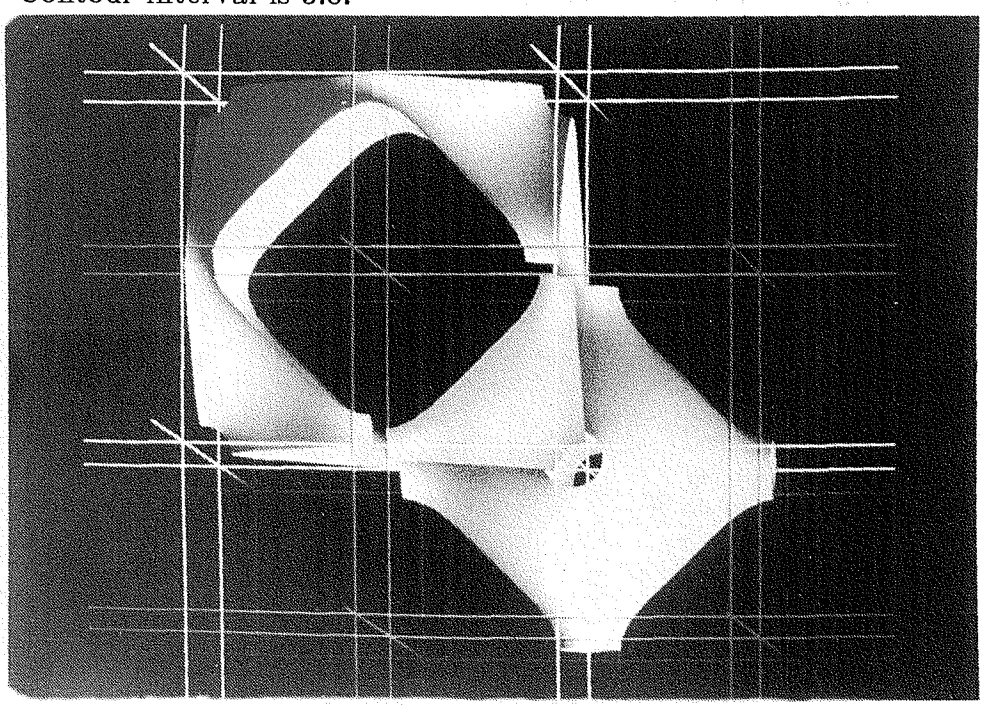

Figure 3c. The solution with $H^* = 1.7974$, same space group and topological type as the Schwarz minimal surface.

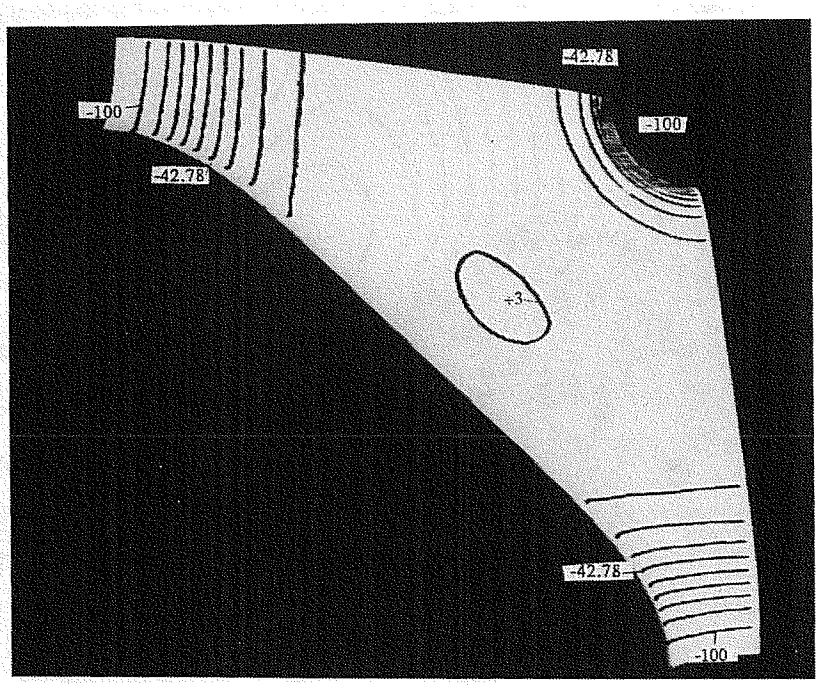

Figure 3c′. Contour plot of Gaussian curvature for an octant of the surface in figure 3c. Contour interval is 11.44.

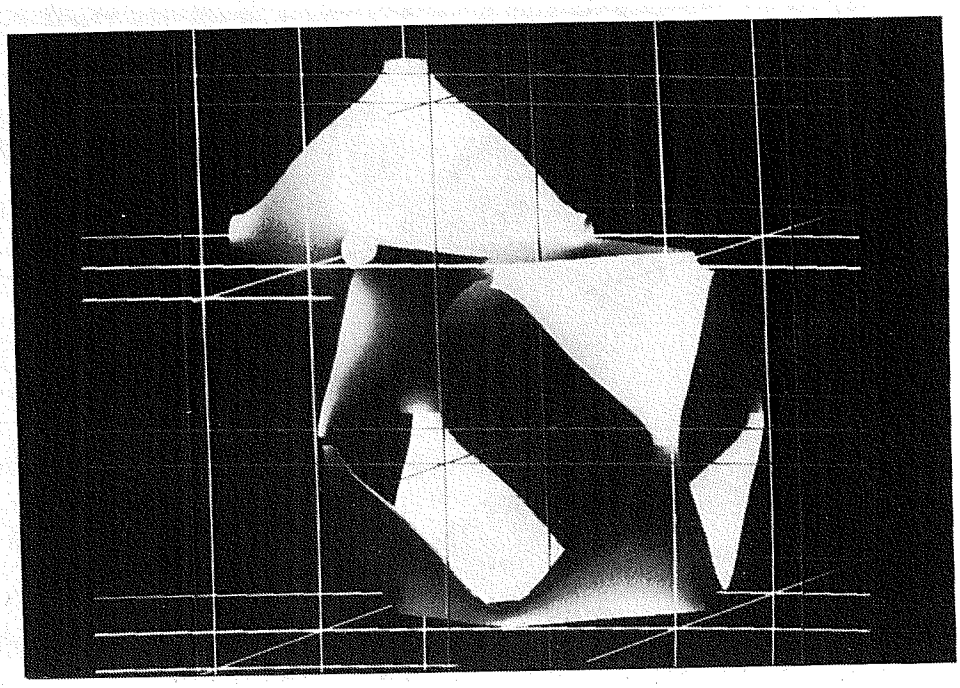

Figure 3d. Solution with $H^* = 2.0$, same space group and topological type as the Schwarz P minimal surface.

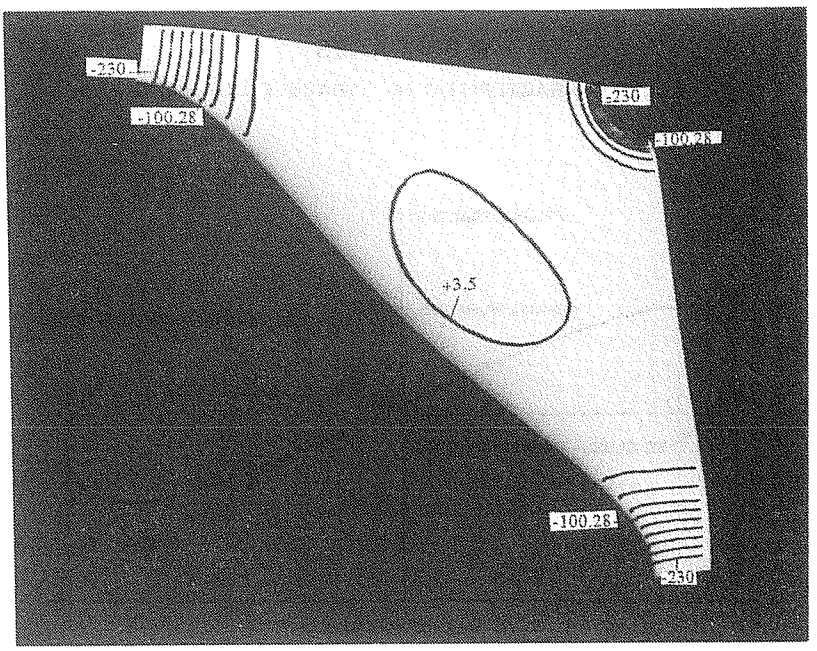

Figure 3d′. Contour plot of Gaussian curvature for an octant of the surface in figure 3d. Contour interval is 25.94.

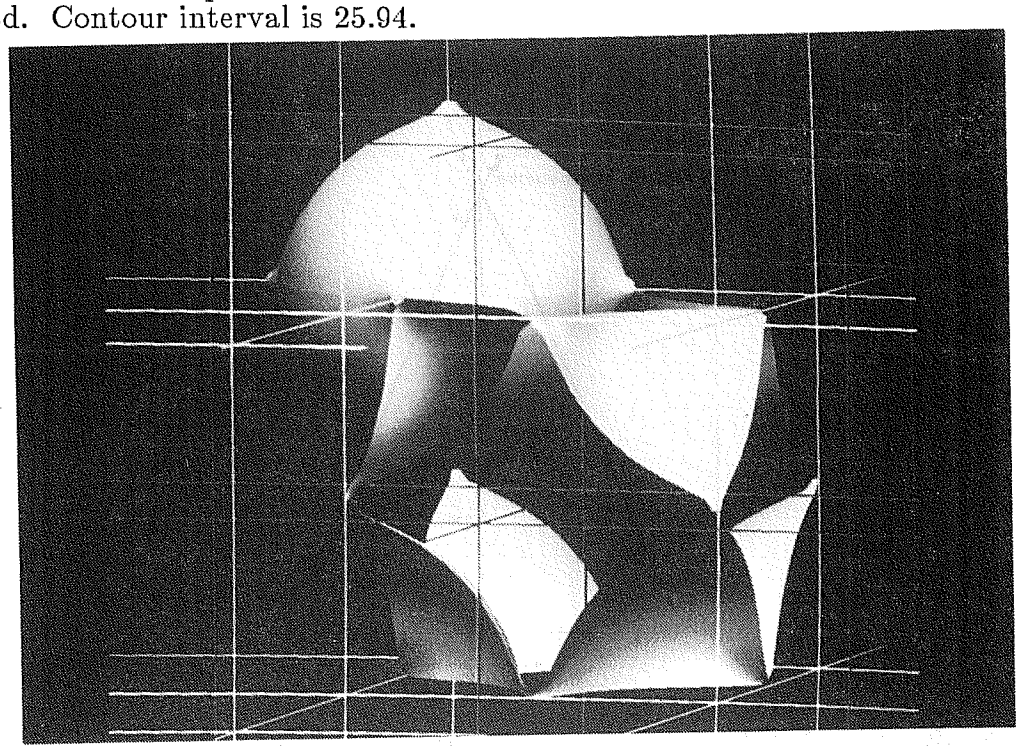

Figure 3e. Solution with $H^* = 2.133$, same space group and topological type as the Schwarz P minimal surface.

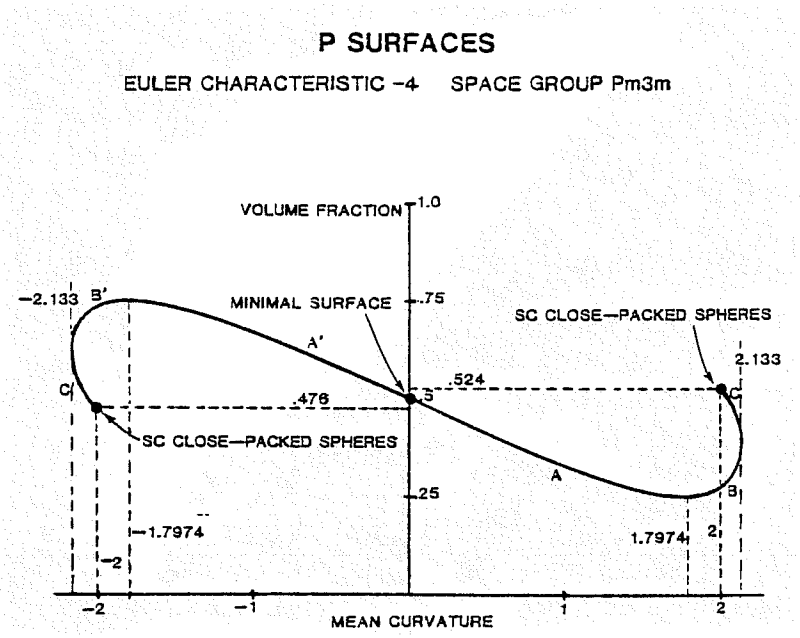

Figure 3f. Plot of volume fraction versus H* for the P family.

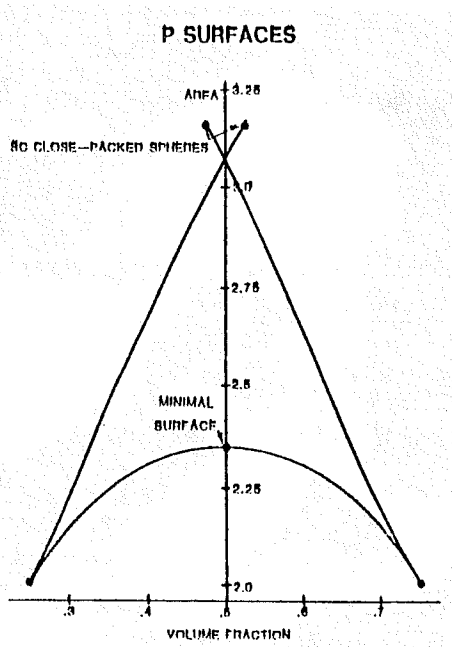

Figure 3g. Plot of area per unit cell versus volume fraction. The slope at each point is 2H*.

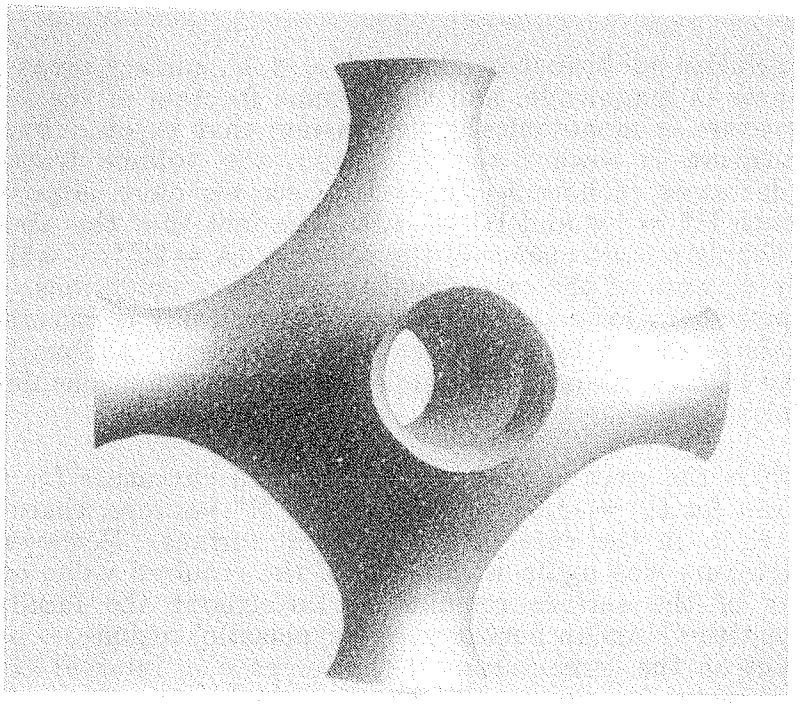

Figure 3h. A contact angle of 57.3° and a constant mean curvature of $H^* = 1.6$ have been perscribed.

The point $H^* = 0$ represents Schwarz's primitive minimal surface, the only case for which the two choices of unit cell are congruent by virtue of the fact that this minimal surface contains straight lines.

Throughout this paper we will continue to reserve the word 'branch' for a set of surfaces that constitute all of the H-surfaces attainable from a certain close-packing of spheres through a succession of H-surfaces having strictly the same sign of H. In the present family there are exactly two branches satisfying this definition, so that they can be called simply the positive-H branch and the negative-H branch. Each branch will be broken down into three 'subbranches' for discussion, those subbranches in the positive-H branch being called A, B, and C, and those in the negative-H branch being A'; B'; and C' in the self-dual cases and D, E, and F in the non-self-dual cases (I-WP and F-RD).

A contour plot indicating the distribution of Gaussian curvature over an octant of the minimal surface is shown in figure 3a'. The values of K at the nodes were computed by the method described in the previous Section. While it is true that there exists[24] a simple, closed-form analytic formula for K, the coordinates in that formula — those of the Weierstrass representation (1) — are not the curvilinear coordinates used in the present representation; thus, only in special cases can we determine what point on the computed surface corresponds to a value of K calculated with the analytic formula. Where it was possible to compare, the values of K computed compared very well with the analytical values, and the integral Gaussian curvature over the actant was within 1% of the value required by the Gauss-Bonnet theorem, namely $-\pi$ (the value $\Xi = -4$ for a unit cell corresponds to an integral Gaussian curvature of $2\pi(-4) = -8\pi$). The point at the center of the octant, which lies on an axis of three-fold symmetry, is the only point with $K = 0$ — there can be no points of strictly positive Gaussian curvature on a minimal surface.

On the solution subbranches labeled A and A', surface areas are decreasing as H^* increases in magnitude, and the volume fraction of the labyrinth of net positive curvature is monotonically decreasing; that is, on subbranch A where the net curvature is toward the G' graph, the volume fraction of this G 'labyrinth' decreases monotonically as H^* becomes more negative. Figure 3b represents both $H^* = 1.0$ and $H^* = -1.0$. The fact that the area is stationary at $H = 0$ is simply a consequence of the relation $dA = 2H^*dV$ which governs the entire family because of the orthogonality boundary conditions. The fact that the area is actually a local maximum within this family is discussed in the conclusion. Again it should be emphasized that the term 'minimal' surface refers to a property of area-minimization under boundary conditions determined by a fixed boundary curve.

Figure 3b′ is the contour plot of the Gaussian curvature for the surface $H^* = 1.0$, and also for $H^* = -1.0$. In the cases of H^* nonzero, there is no analytic formula for K as in the case of the minimal surface. However, the integral Gaussian curvature was again within 1% of the required value of $-\pi$: the Euler characteristic of the surface remains -4 throughout the family. Note that regions of positive Gaussian curvature — 'synclastic' regions — have grown out from the point on the three-fold axis; the increase in integral Gaussian curvature from this region is countered by the more highly negative values of K along the boundary of the octant.

The relation $dA = 2H^*dV$ implies a relation between the first nonzero coefficients H^* in the expansions of A and V about $H = 0$. While the first variation of the area is zero at $H = 0$, the coefficient of H^{*2} is nonzero:

$$A(H^*) = A(0) - cH^{*2} + \cdots \tag{37}$$

So $dA = 2cH^*dH^*$, which must equal $2H^*dV$, giving $dV = -cdH^*$, or:

$$V(H^*) = V(0) - cH^* + \cdots \tag{38}$$

The value of V(0) is of course 1/2, and the value of A(0) is also known in terms of complete elliptic integrals of the first kind:

$$A(0) = 3K(1/2)/K'(1/2) = 2.3451068 \cdots \tag{39}$$

The value of A(0) computed with a 15 x 15 mesh was 2.34547, which is within 0.015% of this analytic value. Concerning the question of the analytical value for c, we mention that there is a simple formula, using a quantity that appeared in the Introduction as a normalization constant in the Weierstrass representation of the P and D minimal surfaces, that yields a value within 0.01% of the observed value. Recall the constant $\kappa = \sqrt{2}/K(1/2) = 0.8389222985...$; if the representation is considered a dimensional equation, as is often conceptually useful, then this κ should be given units of inverse length. The observation is that the computed value of the constant c for the P family is, within the error of 0.03%, equal to $1/(2\kappa)^3 = 0.21171167...$, and furthermore, the dimensions of both c and $1/(2\kappa)^3$ are those of [length]^3. We suspect that this is indeed the exact value for the slope of the V-H^* curve in the P family.

The points labeled H_c^*, where A and A′ subbranches end and B and B′ begin, correspond to minima in area over the entire family. By the relation $dA = 2H^* dV$ these also appear as cusps, with the V-A curve approaching and leaving with asymptotic slope $2H^*$. The magnitude of H^* at these points is $H_c^* = 1.7974 + 0.0002$, and the area of a unit cell is $A = 2.0025 + 0.0005$; the volume fraction of the side of greater curvature is $V = 0.2488 + 0.0002$. The computer graphic representing these two points is shown in figure 3c.

It is seen from figure 3c that three of the boundary curves to an octant of surface are very close to being linear near their midpoints, giving the surface a describing the locus of points at which the Gaussian curvature vanishes, to these midpoints (figure 3c'). At some value of H^*, this contour Ψ separating the synclastic ($K > 0$) from the anticlastic ($K < 0$) regions makes tangential contact with each boundary curve, and does so at the midpoint of the curve by symmetry. Since Joachsimsthal's theorem guarantees that the three curves of lines of curvature, and since $K = 0$ at a point implies that one of the principle curvatures is zero, it is true that each curve is asymptotically linear at its midpoint, at that value of H^* was, within an error of about 0.15, equal to the value of H_c^* at which the minimum in area was recorded, for each branch where this was examined.

On subbranch B the magnitude of H^* is still increasing, but now the area is increasing with $|H^*|$, and the volume fraction of the labyrinth of net positive curvature is increasing. Figure 3d is a graphic of the solution on this subbranch with $H^* = 2.0$, and 3d' is the contour plot of K. At this value of H^*, the surface is largely synclastic, while the 'neck' regions of negative Gaussian curvature exhibit some values of K less than -200. The fact that H^* is increasing in magnitude means that the graph of A versus V in figure 3g is concave upward, although this is slight because the increase in H^* is only form 1.7974 to 2.1335 + 0.0005, the maximum value of H^* attained in this family. The endpoint of subbranch B(B′) corresponds to this maximum H^*, which appears as a turning point in figure 3f and as an inflection point in figure 3g. First-order continuation in H^* enabled us to get very close to this turning point, and the solution with $H^* = 2.133$ is figure 3e.

Past the turning point, on subbranch C or C′, the magnitude of H^* decreases from the maximum value of 2.1335 to the value 2 of the limiting CPS configuration. The curve in figure 3g is thus concave downward. Surfaces on this subbranch are very well described as spheres with small, nearly-unduloidal necks connecting nearest neighbors. On approach to the CPS limit, the necks become increasingly smaller in both average radius and length. Because the neck length is shrinking while the lattice parameter is remaining constant, the average radius of the sphere-like region in a cell must be increasing, and thus the area of a unit cell is increasing rather sharply as the C and C′ subbranches approach their CPS limits. The analogy with the pinching-off progression that occurs in the rotationally symmetric case is very close, and has been examined more closely.[22]

In figure 3h is shown a unit cube of surface with $H^* = 1.6$ which has been computed to make a contact angle of 57.3° with the cube faces, using the equations of the previous section for prescribing contact angles. Obviously this surface would not be smooth if continued periodically, but is is intended rather to demonstrate the generalized method.

D Family: Results

The starting point for this family is Schwarz's D minimal surface that is conjugate to the P minimal surface of the preceding family under the Weierstrass representation. The D minimal surface has been the object of investigation for many researchers in both the mathematical and the physical sciences, notably Schwarz[24], Riemann[27], Weierstrass[65], Schoen[25], Nitsche[31], Longeley and McIntosh[3], and Mackay[26], and we begin this discussion by clearing up certain inconsistencies in the literature. The space group of the minimal surface has been designated as Pn3m by some authors and F $\bar{4}$3 by others, resulting, for example, in differing values published for the normalized surface-to-volume ratio of a lattice-fundamental region of D.[26] This apparent conflict will be resolved in this subsection, and the results of these authors will be shown to be in perfect agreement except for a difference with respect to treatment of the orientability of the minimal surface. F $\bar{4}$3m is the space group of each of the two symmetric skeletal graphs of degree four, and of the diamond-cubic CPS limiting configuration, with a packing fraction of 0.3401. Pn3m is space group of the double-diamond packing found, for example, in cuprite[66], or ice VII.

A simpler example of the effect of orientability on the space group of a minimal surface is provided by the P minimal surface. We saw above that the space group of the P surface is Pm3m, when the surface is viewed as an oriented surface with two distinct sides facing two distinct skeletal graphs. However, the space group of the surface, considered as unoriented, with its two sides and two associated labyrinths equivalent, would be body-centered cubic, Im3m. This is because the point (1.2, 1/2, 1/2), for example, would be equivalent to the origin, since the two labyrinths in the case of H = 0 are congruent (this of course requires that H be identically zero, because of the change in sign of the mean curvature associated with crossing a surface). This has been pointed out by Fontell[2], in the context of a physical problem. It does not seem to have been mentioned in the literature but it is true that the hexagonal faces of the truncated octahedron that encloses a lattice-fundamental region of the body-centered Bravais lattice cut the minimal surface along straight lines lying in the surface. Thus in the case of the P minimal surface there is a perfect analogue to the lattice-fundamental region proposed for the D minimal surface by Schwarz (his Tafel 2), Nitsche (Abbildung 27), Longeley and McIntosh (figure 3), and Mackay (figure 1). This L-F region for D consists of six replicas of the minimal surface patch that spans a circuit of four edges of a regular tetrahedron; the twelve edges that lie on the boundary line also on the faces of a cube which determines both an L-F region and a unit cell. In the case of P, however, the truncated octahedron which determines an L-F region severs the surface into patches that meet only in point contacts.

This explains why the values of normalized surface-to-volume are different for Mackay and Schoen. The value of 1.9193 given by Mackay is for an L-F region which is only half that of Schoen in both volume and area. Therefore it should be less, by a factor of $2^{1/3}$, than Schoen's analytic value $A/V^{2/3}$ = 2.4176538..., or 1.91889309...

The volume determining the L-F region of the surface when considered oriented is composed of 24 replicas of the tetahedron known as the 'tetragonal disphenoid'. As noted by Schoen[25], this is the Coxeter cell C for a primitive patch of the D surface; note that this primitive patch is different than the one

in figure 1b, which is bounded by straight lines, and continued by rotations about these edges. The faces of C are isosceles triangles, and there are two right dihedral angles — these correspond under the conjugate transformation to the two right angles in the skew quadrilateral discussed above as lying in the P minimal surface. Giving the name U to the unit cell of Mackay cited above, the coordinates of the four vertices can be taken to be: P_1 (1/4, 1/4, 1/4), P_2 (-1/4,-1/4, -1/4), P_3 (1/4, 1/4, -3/4), and P_4 (3/4, -1/4, -1/4). The edge 1_1 connecting P_2 and P_3 is clearly parallel to a body diagonal of U, and in fact belongs to one of the skeletal graphs, say G′; a representative of the dual graph G″ is the edge m_1 connecting P_1 and P_4. Each face of this cell C is indeed a plane of mirror symmetry passing through a mid-plane of one of the six carpets T, and C contains a primitive patch S with a surface area amounting to exactly one-half of such a carpet. One can convert to the coordinates of the F $\bar{4}$3m unit cell by the transformation $(x',y',z') = 1/2(x + 1/4, \& + 1/4, z + 1/4)$.

Figures 4a through 4c are the graphics representing solutions for selected values of $H^* = Ha$, where the lattice parameter a is that of the F $\bar{4}$3m space group. Since the D skeletal graph is self-dual, the surfaces $H^* = h$ and $H^* = -h$ are identical except for interchange of the roles of the two skeletal graphs. Generally speaking the progression of solutions found above in the P family from the minimal surface, through a minimum in area at H_c^*, past a turning point in H^* and to a CPS limit, is observed again in the D family. One difference is that the value of H_c^* at the area minimum is greater than the value at the CPS limit in the D family, whereas it lies below the CPS value in the P family. This fact alone suggests that any link provided by the generalized Weierstrass representation[53] between the P and D families would be limited, or at least more complicated than a simple rescaling.

The residual equations were solved for a 15 x 15 mesh on the Cyber 124 for values of H^* less than 4. For values greater than this it was found necessary to increase the mesh to 20 x 20, and the equations were solved on a Cray-1S supercomputer. With a vectorized code, each iteration required approximately 0.18 seconds cpu time. A 20 x 20 mesh for a primitive patch is equivalent to 38,400 elements per unit cell.

In figure 1a we have exhibited four L-F regions of the minimal surface; thus the surface area is equal to that in an F $\bar{4}$3m unit cell, and the Euler characteristic is -16. The distribution of Gaussian curvature over a region made of six primitive patches is shown in 4a′. With the lattice parameter of the P minimal surface, and of the D minimal surface, set equal to unity, the values of K for these two conjugate surfaces do not agree, as they would if the two surfaces were as calculated in the Weierstrass representation. The constant κ = 0.8389222985... in equation (1) was chosen to make the edge-length of the regular tetrahedron discussed above equal to unity, and with this same constant the lattice parameter of the P minimal surface is 2κ, not 1. In order to see the equality of K at corresponding points of the P and D minimal surfaces it is necessary to rescale the values plotted in 3a' and 4a′ according to these dimensions. The value of a principle radius of curvature at the midpoint of a fundamental patch (as in figure 1c) of the D surface, estimated numerically by Mackay[26] at 0.29, can be evaluated analytically using Schwarz's formula for the Gaussian curvature, as $1/[8(2-\sqrt{3})K(7 - 4\sqrt{30}] = 0.296603823...$, where K is the complete elliptical integral of the first kind.

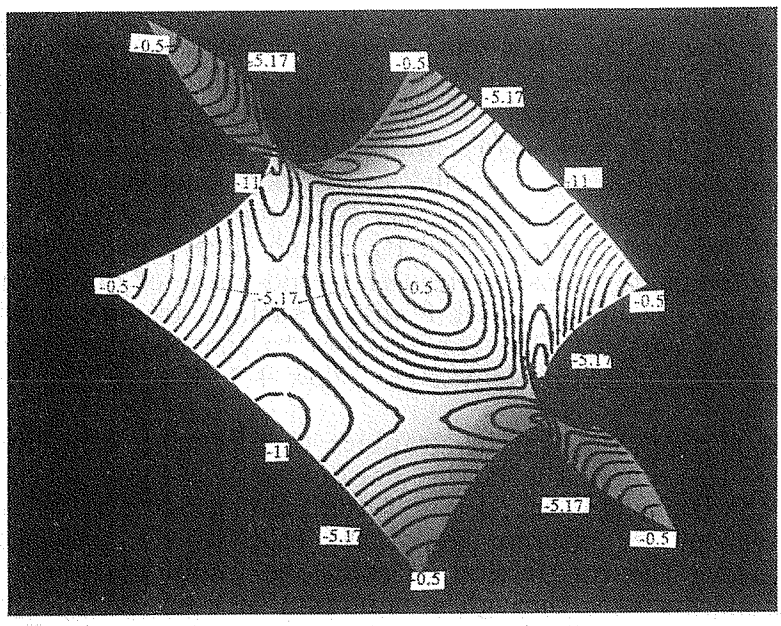

Figure 4a′. Contour plot of gaussian curvature for a portion of the Schwarz D minimal surface shown in figure 1a. The contour interval is 1.166.

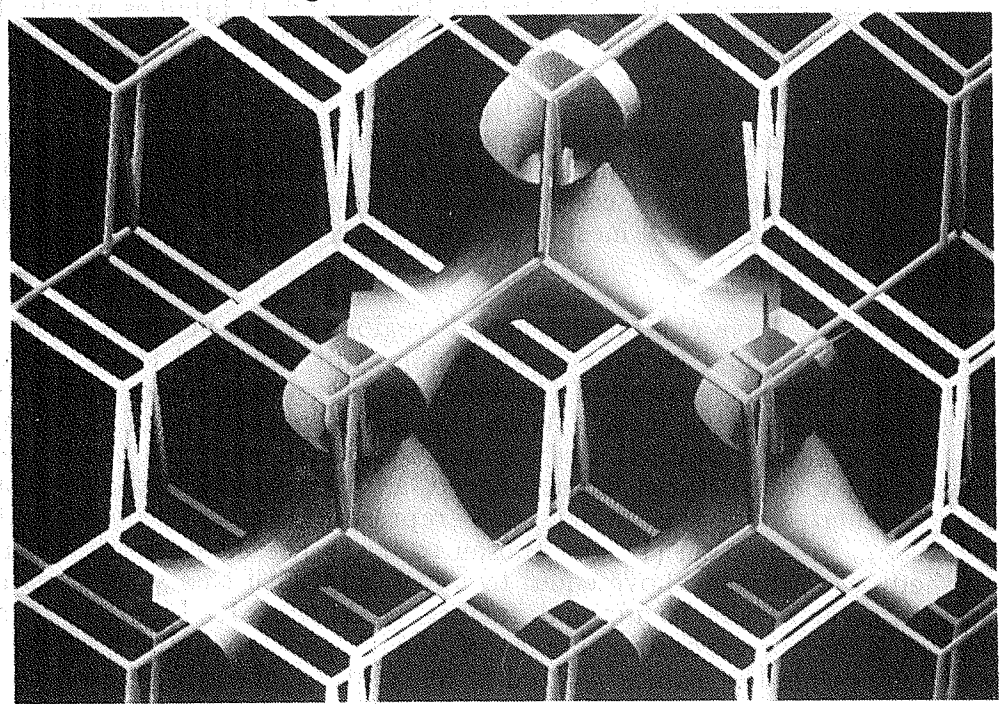

Figure 4b. Solution with $H^* = 3.8$, same space group and topological type is the Schwarz D minimal surface.

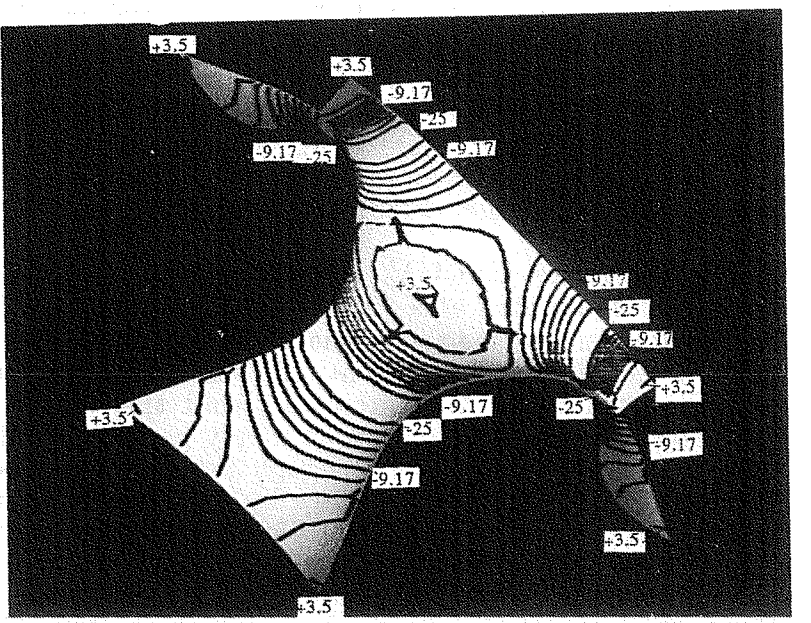

Figure 4b′. Contour plot of Gaussian curvature for a portion of the surface in figure 4b. Contour interval is 3.166.

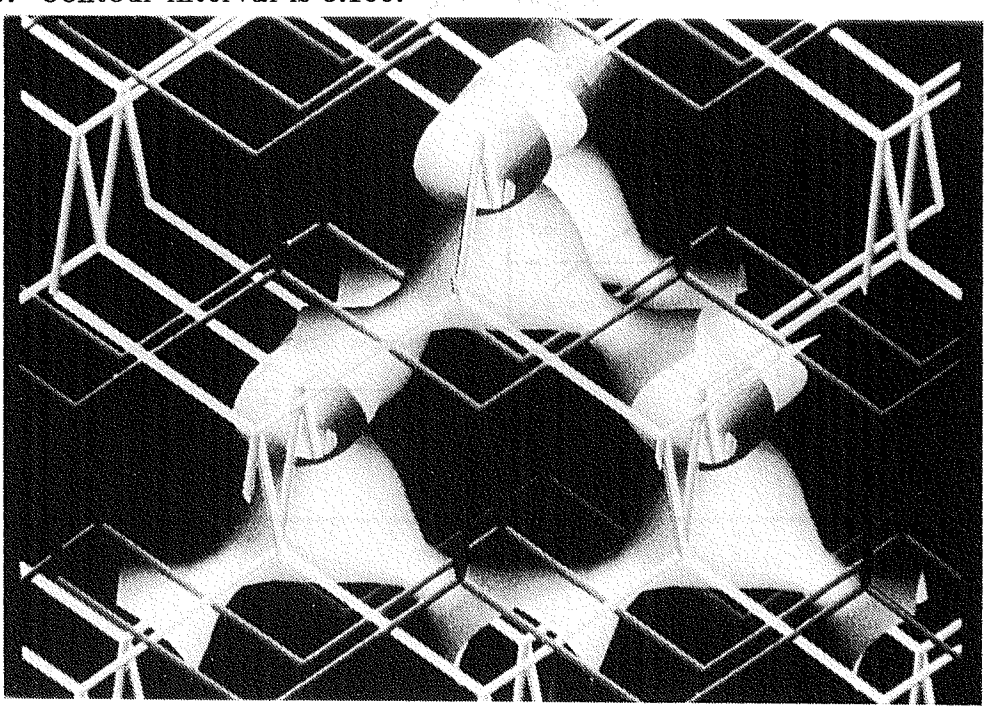

Figure 4c. Solution with $H^* = 4.836$, same space group and topological type is the Schwarz D minimal surface.

On subbranches A and P′, the area of the surface decreases as H* increases in magnitude, so that the area of the minimal surface is a local maximum, as in the P family. Also in analogy with the P family, the volume fraction of the labyrinth lying on the side of net positive curvature is decreasing as H* increases in magnitude (see figure 4d). The coefficient of H* in the expansion of V about H* = 0, which is of course the coefficient of H^{*2} in the series for the area, is, within the error of 0.03%, equal to exactly 2/3 times the value for the P family. As in the case of the constant c for the P family, we cannot now prove that this relation analytically. Figures 4b and 4b′ are for H* = ± 3.8.

At the end of subbranches A and A′, and beginning the subbranches B and B′, is the surface of minimum area at a value of $|H_c^*| = 4.836 \pm 0.001$, shown in figure 4c. The normalized surface-to-volume ratio for an L-F region at this minimum is 1.6527 ± 0.0005, which represents the smallest value for any surface in the five families treated here. It is interesting that this value, which is also lower than any value previously listed for a triply periodic minimal surface, occurs for a surface in the D family even though the P minimal surface has a value lower than that of the D minimal surface by 3%. In addition, the volume fraction ratio at this area minimum is 0.869195:0.130805, which represents the largest ratio of any surface (free of self-intersections) in the five families treated. This is not surprising since the packing fraction in the CPS limit is only 0.3401. Figure 4e is a plot of A versus V, in which the two minima in area appear as cusps.

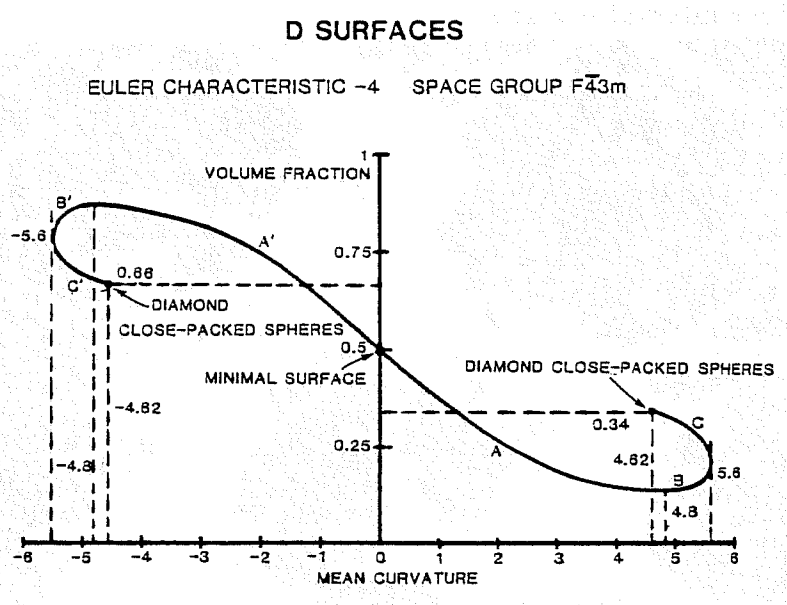

Figure 4d. Plot of volume fraction versus H* for the D family.

On subbranches B and B′ we find surfaces consisting of sphere-like regions lying inside the symmetry domains[25], with nearly-unduloidal necks piercing through each of the four faces of each symmetry domain and providing connections to the four neighboring sphere-like regions. The magnitude of H* then reaches a maximum of 5.6 ± 0.2, and past this turning point it begins to decrease, on subbranches C and C′. On C and C′ the area increases dramatically as the unduloidal necks pinch off, and H* decreases slowly to its value of $8\sqrt{3}$ corresponding to the diamond-cubic CPS limiting configuration.

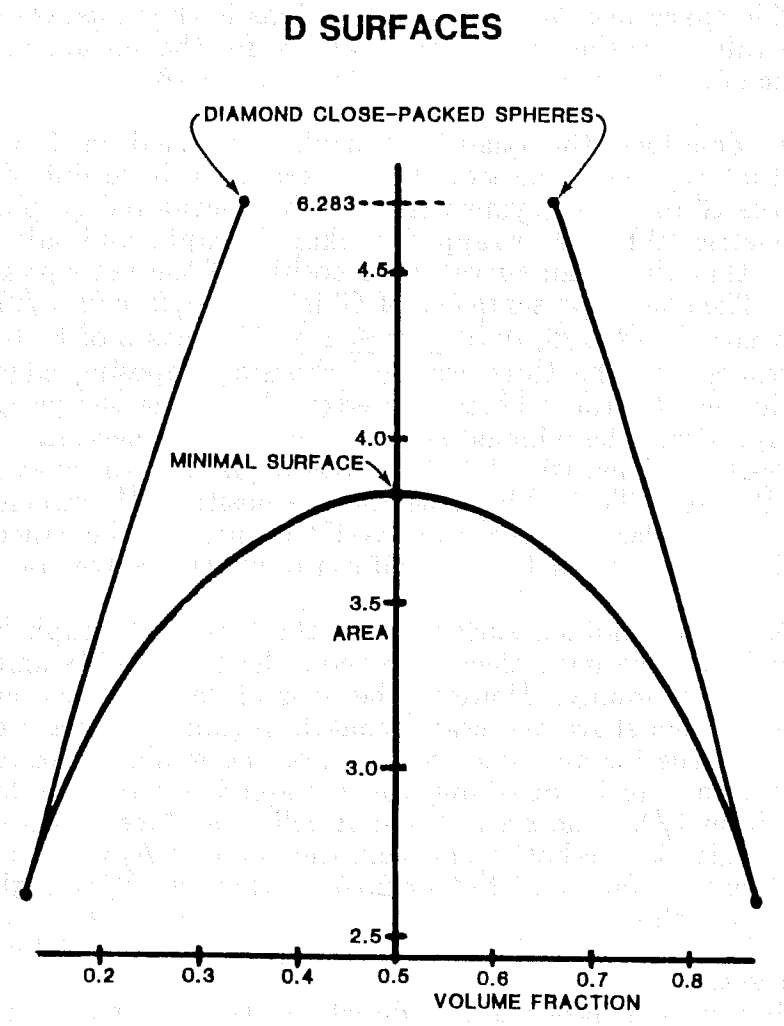

Figure 4e. Plot of area per unit cell versus volume fraction for the D family. The slope at each point is 2H*.

I-WP Family: Results

The minimal surface in this family was proposed by Schoen[25] as the conjugate to a self-intersecting minimal surface partly studied by Stessmann.[67] Schoen also built plastic models of the surface, and identified the space group as Im3m and the Coxeter cell as the quadrirectangular tetrahedron identical to that in the P family. Since the I graph is not self-dual — it and its dual WP were described in the Introduction — there cannot be straight lines lying in the minimal surface. This also means that the volume fractions of the two labyrinths need not be 1/2 (Mackay's[64] claim that all the known triply-periodic surfaces divide space into two congruent regions is thus mistaken). and Schoen did not give values for the volume fractions nor for the surface area. The Euler characteristic of an L-F region for any value of H* is -6.

We have described the quadrirectangular tetrahedron C above, but the edges of C that represent the two skeletal graphs will be different from the P case. We take G′ to be the symmetric 'I' or body-centered graph, and G″ to be the nonsymmetric 'WP', or "wrapped package" graph, and take the sign convention to be that the mean curvature is positive if the net curvature is toward the I graph. Then the representative of G′ is 1_1: $\{ (u/2, u/2, u/2) \mid 0 \leq u \leq 1\}$, and of G″ is m_1: $\{(v/2, 1/2, 0) \mid 0 \leq v \leq 1 \}$. The cases of P, I-WP, and C(P) in fact correspond to the three ways of choosing opposing edges of the quadrirectangular tetrahedron. These two edges determine the parametrisation in the usual way. From the minimal surface solution it is necessary to continue in both positive-H* and negative-H* directions explicitly, as opposed to the self-dual P and D cases. The subbranches on the positive-H* branch will be called A, B, and C, while those on the negative-H* branch will be called D, E, and F. The residual equations for a 15 x 15 uniform mesh were solved on a Cyber 124.

Figure 5a is the minimal surface, with the I skeletal graph bolder and the WP graph lighter. We have elected to show the same 1-7/8 unit cells as were displayed for the P family. However, because of the body-centered symmetry, the two cubes (which share an octant) contain regions of surface that are identical, and this is true for all values of H*. For the minimal surface, the volume fraction of the labyrinth containing the I graph is 0.53604 ± 0.0002, differing significantly from 1/2. The area of a unit cell of surface is 3.467 ± 0.003, and since an L-F region is one-half a unit cell, the value of $A/V^{2/3}$ for an L-F region is less than this by a factor of $2^{1/3}$, or 2.7521, which is 17.3% higher than the P value. Figure 5a′ shows the distribution of Gaussian curvature over an octant of unit cell. Each of the six 'corners' of this patch is an isolated point of zero Gaussian curvature.

Continuing in the positive H* direction, the volume fraction of the I labyrinth decreases along subbranch A (see figure 5d), and the area decreases. The constant c in formula (19) is 0.1385 ± 0.0005, and this constant applies for approach to H* = 0 from either above (subbranch A) or below (subbranch D).

Subbranch A ends at the value $H_c^* = 1.940 \pm 0.005$ which corresponds to a local minimum in area and a global minimum in volume fraction. Figures 5b and 5b′ are for H* = 2.0, and it is already evident at this value of H* that the solution is approaching the BCC-CPS limiting configuration. Subbranch B ends, and C begins at the turning point H* = 2.82 ± 0.01.

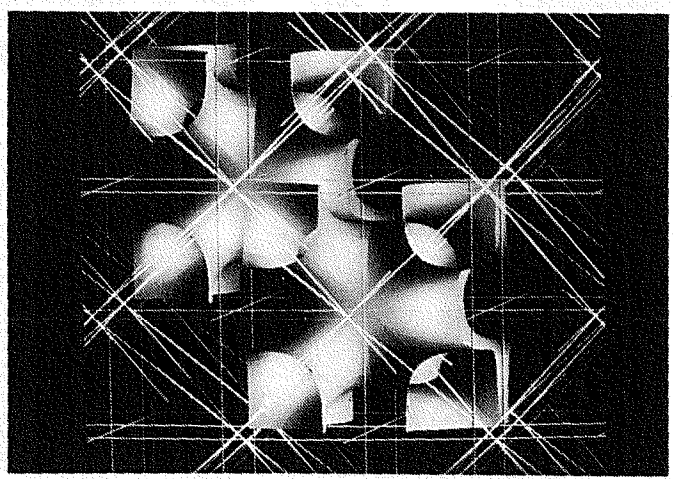

Figure 5a. The I-WP minimal surface, space group Im3m and Euler characteristic -6 per lattice-fundamental region. Fifteen octants are shown.

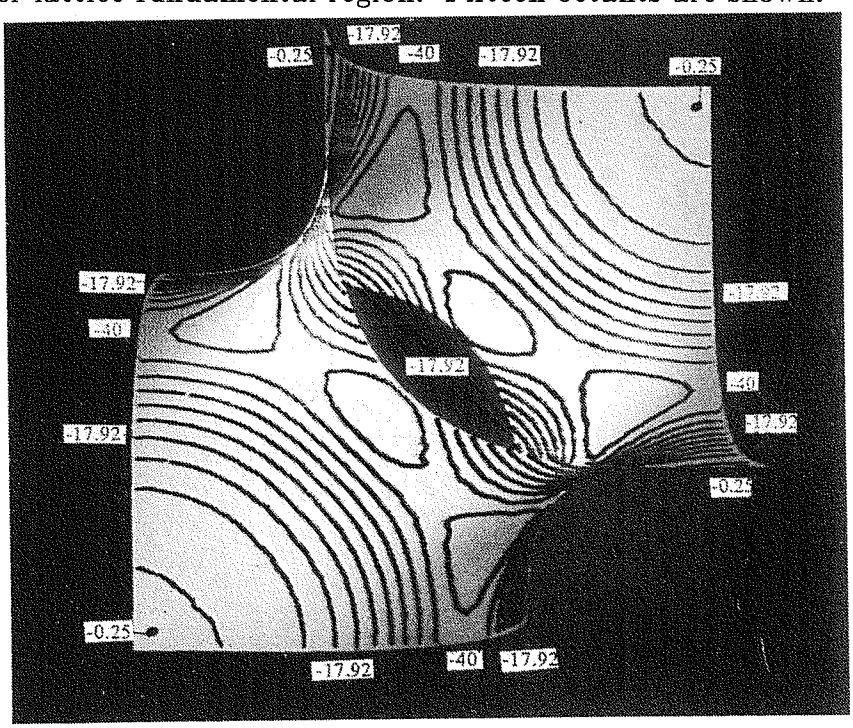

Figure 5a′. Contour plot of Gaussian curvature over an octant of the surface in figure 5a. Contour interval is 4.42.

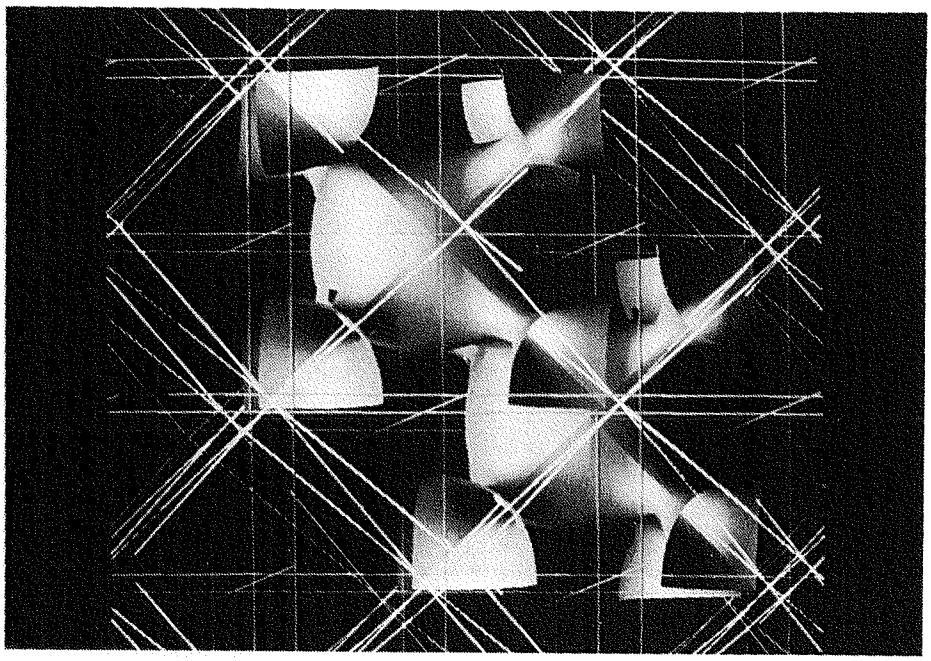

Figure 5b. Solution with $H^* = 2.0$, same space group and topological type as the I-WP minimal surface.

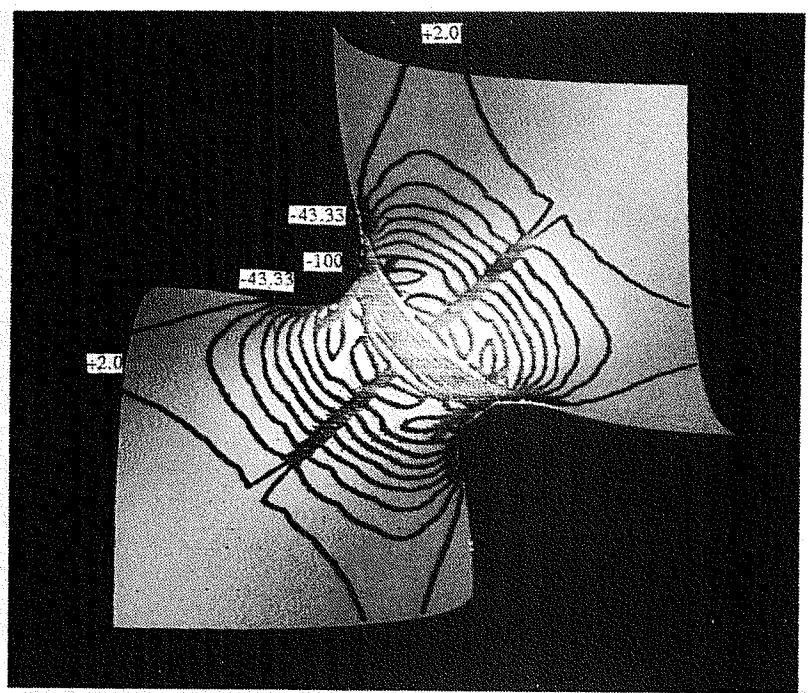

Figure 5b′. Contour plot of Gaussian curvature over an octant of the surface in figure 5b. Contour interval is 11.3.

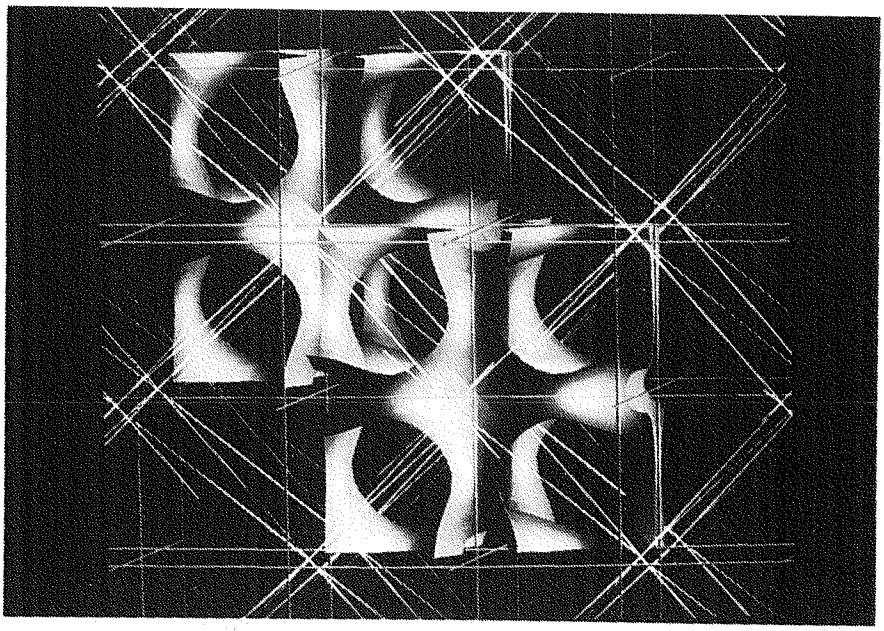

Figure 5c. Solution with H* = -3.55, same space group and topological type as the I-WP minimal surface.

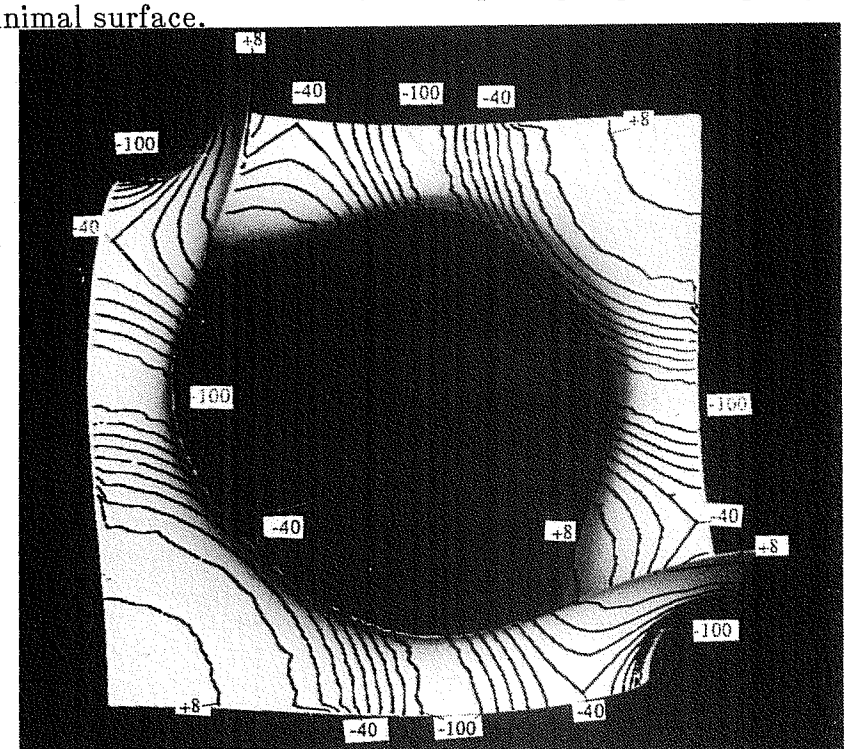

Figure 5c′. Contour plot of Gaussian curvature over an octant of the surface in figure 5c. Contour interval is 12.0.

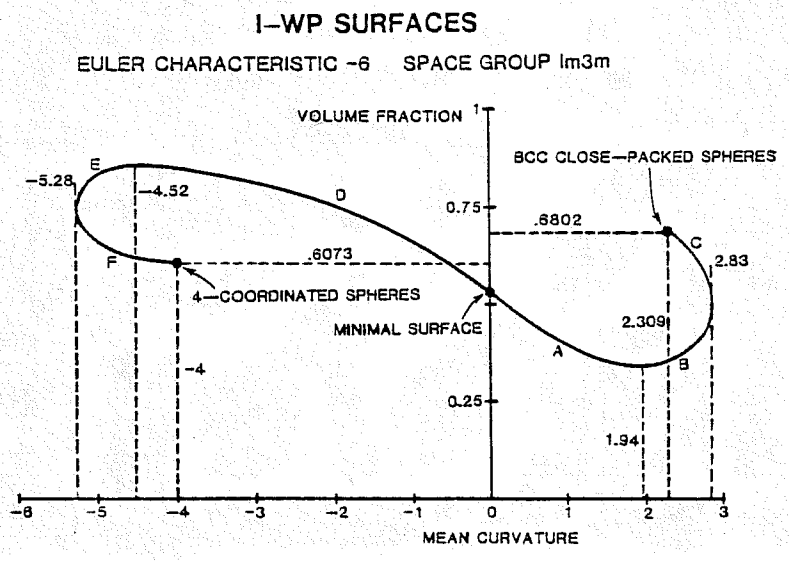

Figure 5d. Plot of volume fraction versus H* for the I=WP family.

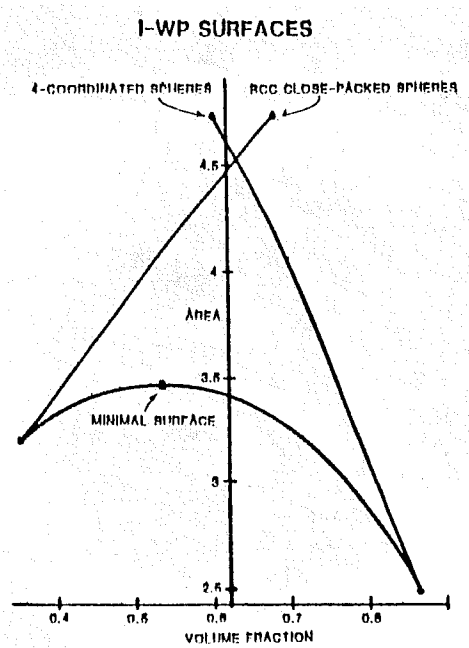

Figure 5e. Plot of area per unit cell versus volume fraction for the I-WP family. The slope at each point is 2H*.

Subbranch D, on which the volume fraction of the I labyrinth is monotonically increasing, extends all the way to the value $H_c^* = -4.52 \pm 0.05$ corresponding to the global minimum in area, and the global maximum in volume fraction. The volume fraction ratio at this maximum is 0.857:0.143 (see figure 5d), almost as high as the maximum ratio in the D family, which is remarkable because the volume fraction ratio at the CPS limit on this branch is 0.6073:0.3927. The value of $A/V^{2/3}$ for an L-F region of this surface is 1.96 ± 0.01. Figures 5c and 5c′ are for the global maximum in volume fraction. The volume fraction ratio at this maximum is 0.857:0.143 (see figure 5d), almost as high as the maximum ratio in the D family, which is remarkable because the volume fraction ratio at the CPS limit on this branch is 0.6073:0.3927. The value of $A/V^{2/3}$ for an L-F region of this surface is 1.96 ± 0.01. Figures 5c and 5c′ are for $H^* = -3.55$. Figure 5c″ shows a larger portion of the surface, without the skeletal graphs. Subbranch E ends at the turning point at $H^* = -5.28 \pm 0.05$. The CPS limit consists of spheres of radius 1/4 centered at each face-midpoint, and each edge-midpoint, of every unit cell. Figure 5d gives V versus H^*, and 5e is the plot of A versus V.

We suspect that the analytical value for the dimensionless area $A/V^{2/3}$ of an L-F region of the I-WP minimal surface is $3K(k)/K(k')$ with $k = \sqrt{13/32}$ (and so $k' = \sqrt{19/32}$). This value, 2.751347..., is approximately 0.013% lower than the value computed from the numerical solution; in the cases P and D of low Euler characteristic where the analytic value was known, the analytic value was approximately 0.01 to 0.015% lower than the computed value (note also that Mackay's value for the D surface, computed with a finite difference method, was about 0.02% high). The formula $A/V^{2/3} = 3K(k)/K(k')$ is due to Schoen[25], who adapted a result of Schwarz[24], and the work of Stessmann[67] shows that the formula applies to the I-WP minimal surface as well as the F-RD minimal surface. Stessmann's analysis was not complete enough to yield the modulus k, but by Schwarz's work it is known that $k^2 = (a_2 - a_3)/(a_1 - a_3)$ where $\{a_1, a_2, a_3\}$ are roots (in descending order) to a cubic polynominal that is not explicitly known for the I-WP surface, nor for the F-RD minimal surface. For the I-WP surface, the roots $\{1, 3/16, -1\}$ yield the value just given; for the F-RD minimal surface, we suspect the roots to be $\{14, -7 + 4\sqrt{3}, -7 - 4\sqrt{3}\}$. where the latter two roots are roots to the polynominal $s^2 + 14s + 1$ that occurs in Stessmann's analysis, and the three roots satisfy $a_1 + a_2 + a_3 = 0$. This has been discussed in more detail.[22]

F-RD Family: Results

As in the I-WP case, the minimal surface in this family was proposed by Schoen as the conjugate of a self-intersecting minimal surface studied by Stessmann (number V in Stessmann[67]; the conjugate to I-WP is number VI). Once again, the surface contains plane lines of curvature (corresponding to the straight edges that bound the patch of the conjugate surface) but no straight lines, and does not divide space 50:50. Schoen identified the space group as Fm3m and the Coxeter cell as a "trirectangular tetrahedron" (which is actually one-half of a tetragonal disphenoid), and incorrectly listed as genus of an L-F region as 6, meaning that its Euler characteristics is $\chi = 2 - 2 \cdot 6 = 10$, which is the correct value for χ. This L-F region is determined by a rhombic dodecahedron, and the edges of this space-filing assembly of rhombic dodecahedra comprise the nonsymmetric RD skeletal graph that is dual to the symmetric F graph.

The origin of the coordinate system will be taken to be a node of the F graph, and the other three vertices of a Coxeter cell are $P_2(0,1/4,1/4)$, $P_4(1/4,1/4,1/4)$. The segment P_1P_2 is one-half an edge of the F graph, and P_3P_4 is an edge of the RD graph, and as usual these two representative edges determine the parameterization.

We make the sign convention that the curvature is with respect to the F graph, and for $H^* \geq 0$ we will display one L-F region, composed of 48 cells C. However, for the surface from the negative-H^* branch that is exhibited, we have shown a portion of surface made from 72 copies of c. The F graph is shown in bold and the RD graph as lighter. The residual equations were solved on a Cyber 124 using a 15x15 uniform mesh, or in some cases on a Cray-1S using a 20x20 mesh; as in the I-WP case, no values for area or volume fraction have been published for the minimal surface to compare with.

The minimal surface in Figures 6a and 6a′ has volume fraction 0.5319 ± 0.0001. The area computed for a unit cell was 4.773 ± 0.001, giving a value of $A/V^{2/3}$ for an L-F region of 3.0065. This is in accord with the general trend of increasing values of $A/V^{2/3}$ as the Euler characteristic of the L-F region increases in magnitude. Figure 6a′ is the contour plot of K over a patch of surface corresponding to six Coxeter cells.

Subbranch A, on the positive-H^* branch, continues to a value of $H^* = 1.86 \pm 0.02$ corresponding to the global minimum in area of 4.639 ± 0.001 (for a value of $A/V^{2/3} = 2.922$). There is some doubt involved in calling this a global minimum since the minimum in area on the negative-H^* branch is very close to this, namely 4.6395 ± 0.001. The volume fraction of the F labyrinth at $H^* = 1.86$ is 0.489 ± 0.0002. The contour plot for $H^* = 1.86$ is shown in Figure 6b′. Since the FCC-CPS limit corresponds to $H^* = 2\sqrt{2}$, the value of H^* at this area minimum is considerably less than the CPS value.

Convergence is comparatively easy to achieve on the first portion of subbranch B, in contrast with the I-WP case. Figures 6c is for $H^* = 2.5$, and in 6c it is quite clear that the solution branch is approaching the limiting FCC (12-coordinated) sphere-pack. The volume fraction at $H^* = 2.5$ is 0.4691 ± 0.0002, and the area is almost exactly that of the minimal surface, being 4.779 ± 0.001. The volume fraction first exceeds 1/2 at $H^* = 2.67 \pm 0.02$.

Subbranch C begins at the turning point where H^* reaches the maximum of 2.92 ± 0.01. Using an unduloid as initial estimate, it was possible to converge to a solution on this subbranch corresponding to $H^* = 2.89914$. This value is simply 1.025 times the value of H^* at the limit, $2\sqrt{2}$, and an unduloid of mean curvature 2.05 was rescaled by $\sqrt{2}$ for the initial guess. The area of the solution was 5.997 ± 0.005 and the volume fraction 0.6303 ± 0.005.

Self-intersecting solutions occur on the negative-H^* branch. The edges of the RD skeletal graph are all of equal length, and one can easily imagine a limiting configuration consisting of close-packed spheres of radius $\sqrt{3}/8$, centered at each node of the RD graph whether 4- or 8-coordinated, but this is not found to be the limit. Rather, the branch seeks a limit which puts spheres of radius $\sqrt{3}/4$ at 8-coordinated nodes only, and self-intersections must occur since nearest-neighbor 8-coordinated nodes are only a distance $\sqrt{2}/2$ apart. As seen in Figure 6d ($H^* = 2.4$), for solutions on this branch before the point where

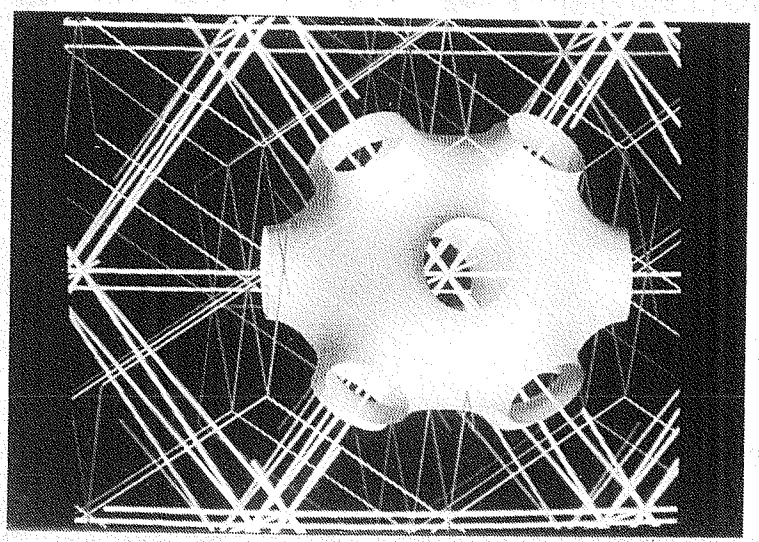

Figure 6a. The F-RD minimal surface. One lattice-fundamental region is shown. Space group is Fm3m and the Euler characteristic per lattice-fundamental region is -10. The twelve 'necks' are orthogonal to the twelve faces of the rhombic dodecahedron outlined by the lighter skeletal graph.

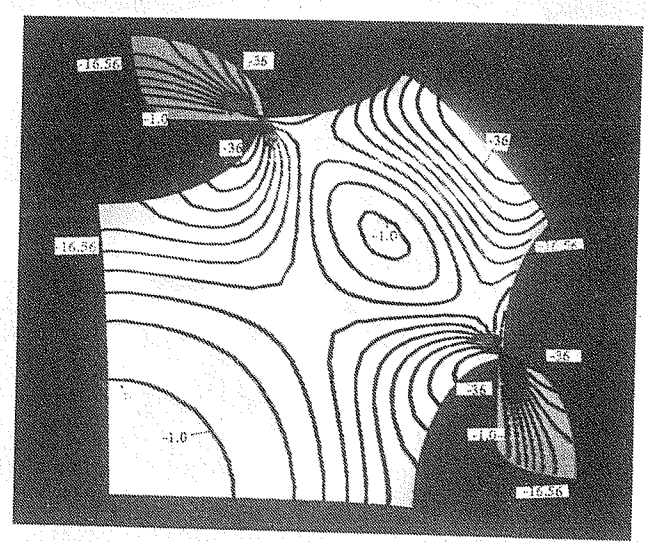

Figure 6a′. Contour plot of Gaussian curvature over a portion of the F-RD minimal surface. Contour interval is 3.889.

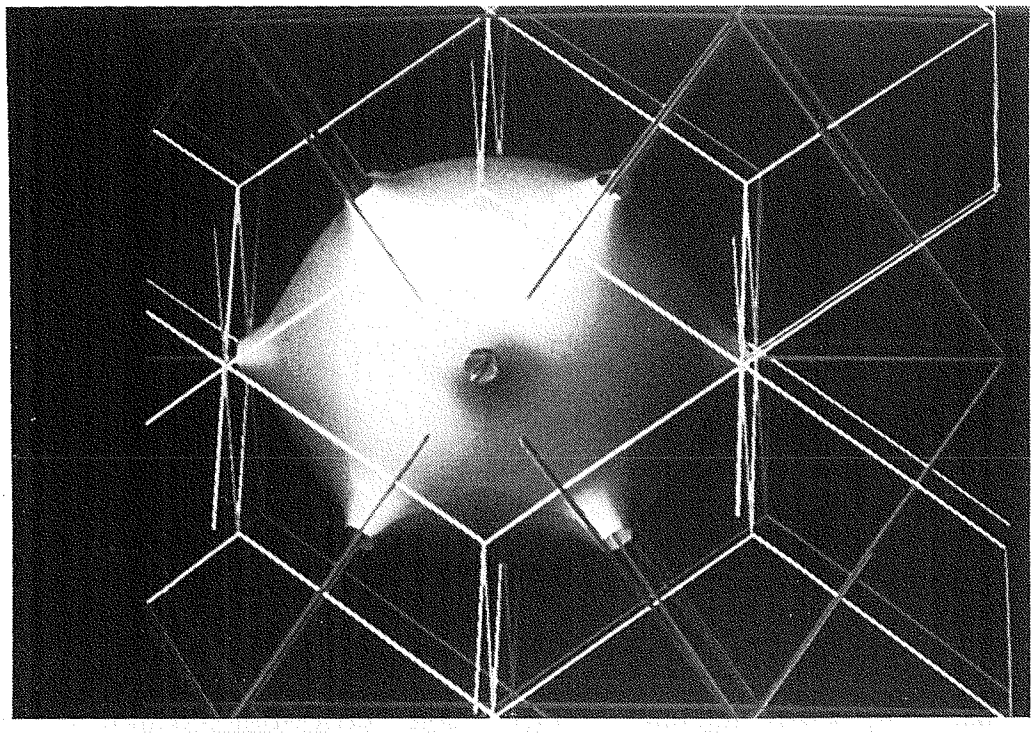

Figure 6b. Solution with $H^* = 2.5$, same space group and topological type as the F-RD minimal surface.

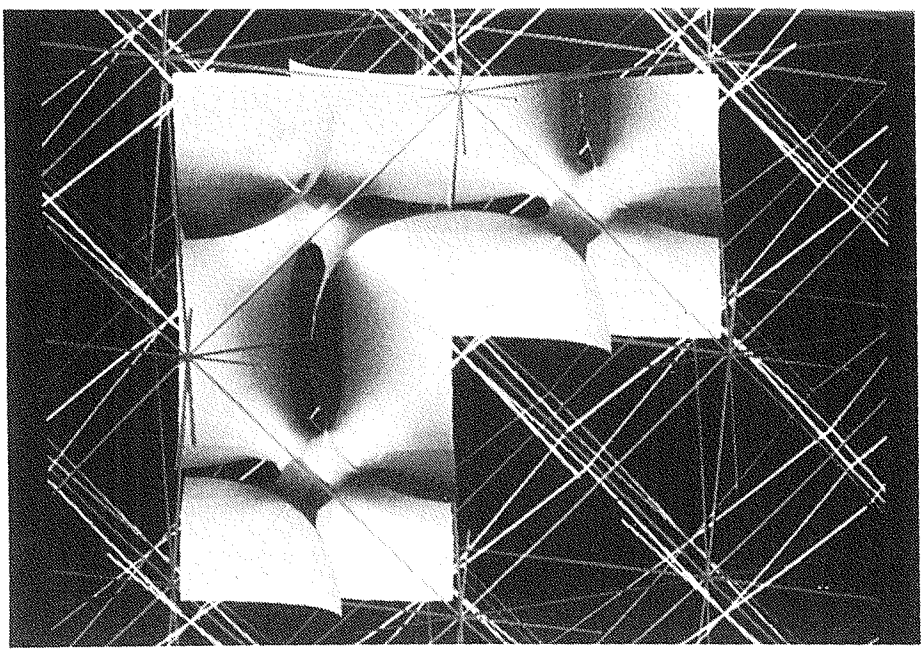

Figure 6c. Solution with $H^* = -2.4$, same space group and topological type as the F-RD minimal surface.

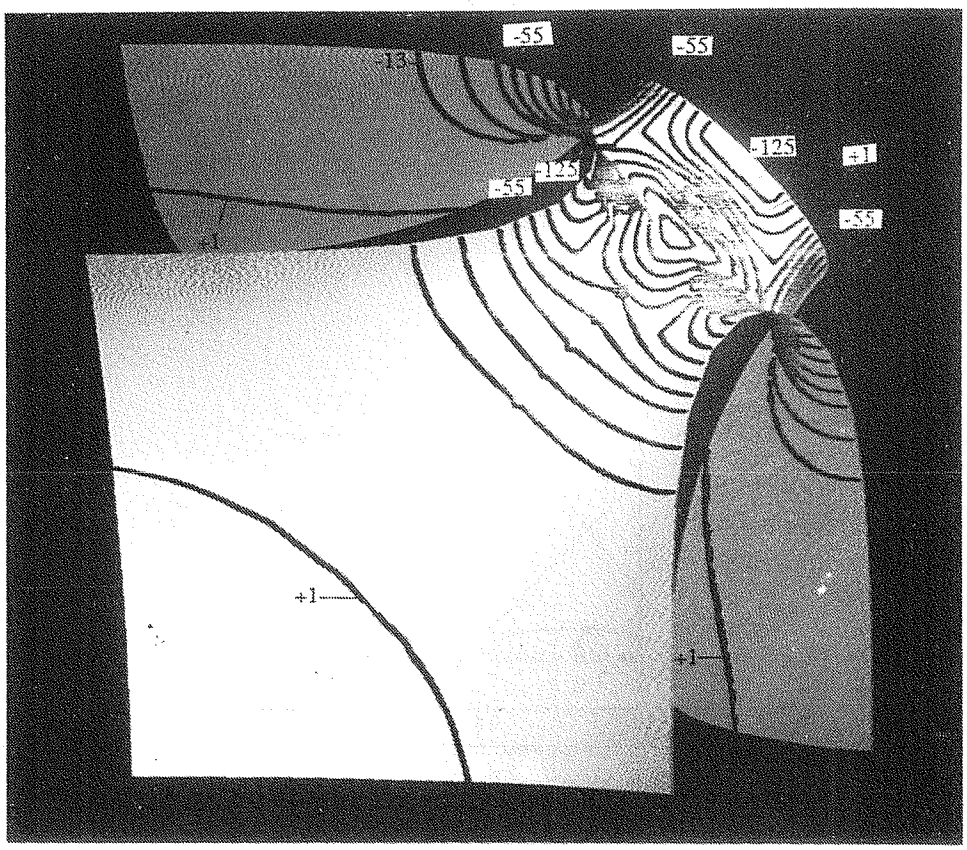

Figure 6c′. Contour plot of Gaussian curvature over a portion of the surface in figure 6c. Contour interval is 14.0.

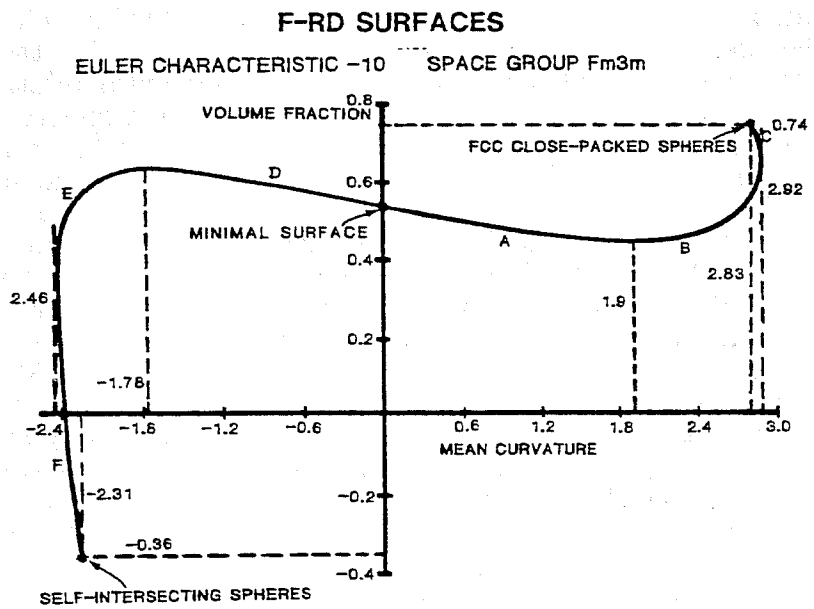

Figure 6d. Plot of area per unit cell versus H^* for the F-RD family.

self-intersections occur, the 4-coordinated nodes are centers of connector regions which join four neighboring sphere-like regions.

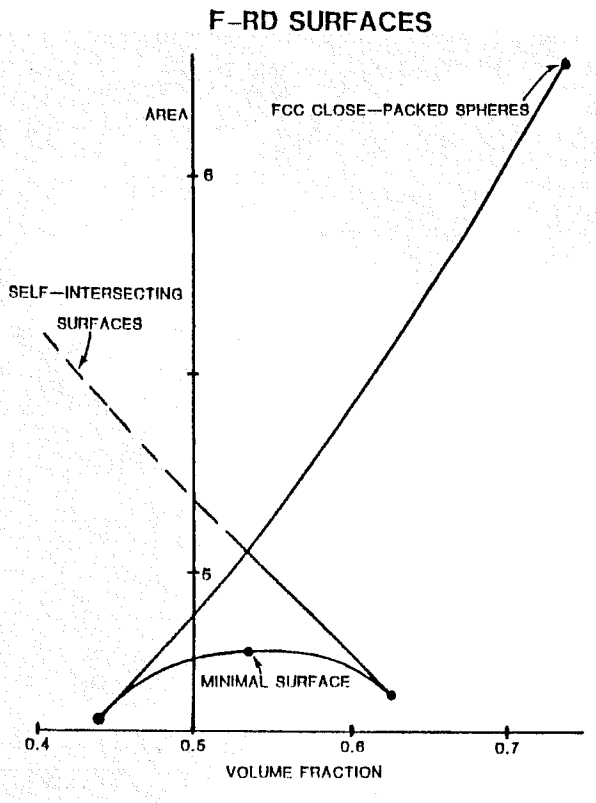

Figure 6e. Plot of area per unit cell versus volume fraction for the F-RD family. The slope at each point is 2H*.

We have stated that self-intersections are not examined closely in this study, but one important point must be made about the self-intersecting solutions on this branch. If the volume of overlap is counted *twice* in each case, one can complete the area-H*, volume-H*, and area-volume curves for this branch all the way to the limiting configuration with the fundamental relation $dA = 2H^* dV$ obeyed throughout. For the limiting configuration, the sphere radius of $\sqrt{3}/4$ gives a volume and area per sphere of $\pi\sqrt{3}/16$ and $3\pi/4$, respectively; since there are four spheres associated with each unit cell the equivalent volume fraction for the RD labyrinth is $\pi\sqrt{3}/4 = 1.360349...$and the area per unit cell is $3\pi = 9.42477....$ So we must assign a negative volume fraction to the F labyrinth, namely - .360349. Applying the mean value theorem between this endpoint — where $H^* = -4\sqrt{3} = -2.309...$ — and the solution for $H^* = 2.4$ where the area is found to be 5.0048 and the volume fraction of the F labyrinth is 0.54531 yields: $\Delta A/\Delta V = (3\pi\text{-}5.0048)/(-.360349 - .54531) = -4.8806 = 2H^*$, where $H^* = -2.4403$ is an acceptable intermediate value because the most negative value obtained on the path joining these solutions is -2.51 ± 0.02. In Figure 6e showing area versus volume fraction, this is seen as a nearly-linear portion of the curve ending at the limit just discussed, with the slope of the curve lying between 2 x -2.51 and 2 x -2.309. The maximum value for the volume fraction of the F labyrinth on this branch, namely $.6272 \pm 0.0002$, is achieved at $H^* = -1.76 \pm 0.02$, well before self-intersections occur.

We suspect that the exact analytical value for the dimensionless area $A/V^{2/3}$ of an L-F region of the F-RD minimal surface is $3K(k)/K(k')$ where $k^2 = 8\sqrt{3}/(21 + 4\sqrt{3})$. This value, 3.00534..., is approximately 0.05% lower than the value computed from the numerical solution; if this is indeed the correct value, the higher error in this case over that in the preceding cases would be

value, the higher error in this case over that in the preceding cases would be due to the higher magnitude of the Euler characteristic per L-F region. In the previous subsection the source of this value of k was discussed; a further discussion is available[22].

C(P) Family: Results

The minimal surface in this self-dual family is often called simply "Neovius' surface" after the pupil of Schwarz who discovered the surface and its Weierstrass representation.[40] As mentioned in the Background section, Schoen named the minimal surface C(P) to indicate that it is complementary to the P minimal surface, containing the same straight lines and having the same space group Pm3m. While the unit cell, which is also an L-F region, and the Coxeter cell are the same as for the P surface, the Euler characteristic per L-F region is -16 as opposed to -4 for the P family. The nonsymmetric, self-dual skeletal graph is constructed by connecting the centroid of every cube in a packing to the twelve edge-midpoints, so that the coordination symbol is 12:4; the two replicas of the graph are offset by (1/2,1/2,1/2).

The edges of the quadrirectangular tetrahedron C that represent the skeletal graphs G' and G" are l_1: $\{(u/2,u/2,0) \mid 0 \leq u \leq 1\}$ and m_1: $\{(v/2,1/2,v/2) \mid 0 \leq v \leq 1\}$. For the minimal surface, the straight line segment that lies in that part S of the surface contained in C is the locus of $u = 1-v$, $w = 1/2$, or in (x,y,z)-coordinates, $x = 1/4$, $y+z = 1/2$, exactly as for the P minimal surface in either coordinate system. However, the integral Gaussian curvature over this patch is four times as great in C(P), being $-2\pi/3$. To capture the regions of sharp curvature requires a fine mesh, and it was found necessary to use a 20x20 mesh in all cases. Even with this refinement, the accuracy in area and volume fraction values was much lower than that in the preceding cases; for example, the computed area of the minimal surface was higher than the analytic value by about 0.1%.

Figure 7a shows the minimal surface, corresponding to the cube $-1/2 \leq x,y \leq 1/2$, $0 \leq z \leq 1$; that is two neighboring unit cells have been bisected and two adjoining half-cells exhibited. This brings out the non-circular nature of the "holes" surrounding four-coordinated nodes. The area of a unit cell of the minimal surface, which is also the value of $A/V^{2/3}$ for an L-F region, is known analytically to be $3K(\sqrt{2}/3)\ /K(1/\sqrt{3}\ ) = 3.51048...$ [Neovius[40]; Schoen[25]].

On subbranch A the area, and the volume fraction of the labyrinth of positive curvature, decrease as always but only very slightly in this family (Figures 7c and 7d). By the time the subbranch ends, at the area minimum corresponding to $H_c^* = 0.60 \pm 0.02$, the area has decreased only by about 0.2%, and the volume fraction is 0.480 ± 0.001. Figure 7b shows the surface with $H^* = 1.05$.

On subbranches B and B′ a maximum $|H^*|$ of 1.48 ± 0.01 is reached, with the area increasing very rapidly past $H^* = 1.4$. As in the RD branch of the previous family, we must again count intersection volumes twice, so that the relation $dA = 2H^*\ dV$ is observed all the way to the limit point. When this is done we find that the endpoint of the B (B′) branch, where the value $H^* = 1.48$ is reached, corresponds to a volume fraction just less than unity, and the area is approximately 50% greater than that of the minimal surface.

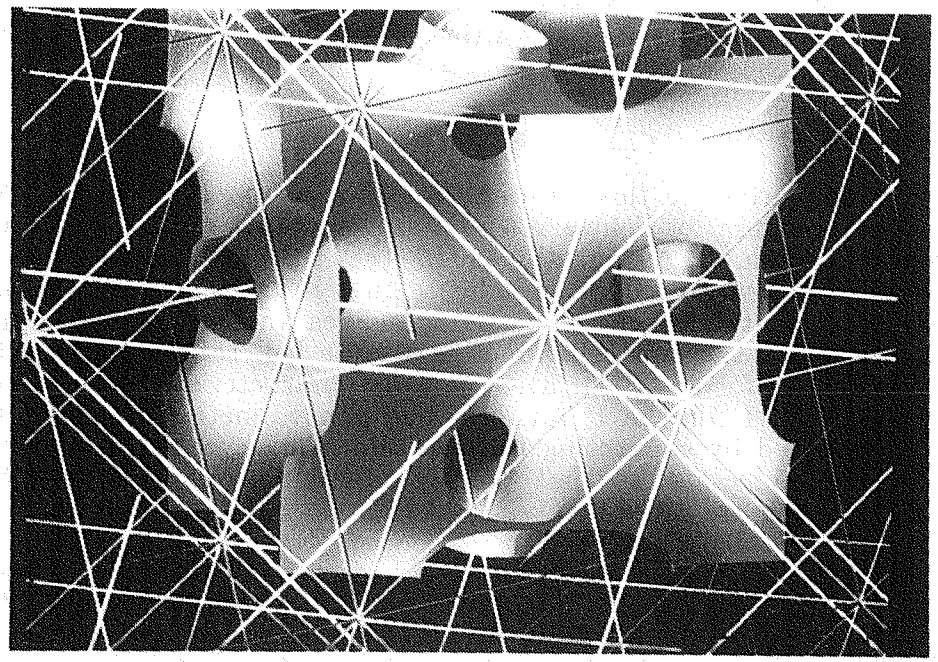

Figure 7a. The Neovius minimal surface C(P), space group Pm3m and Euler characteristic -16 per lattice-fundamental region. One unit cell is shown, which is also a lattice-fundamental region.

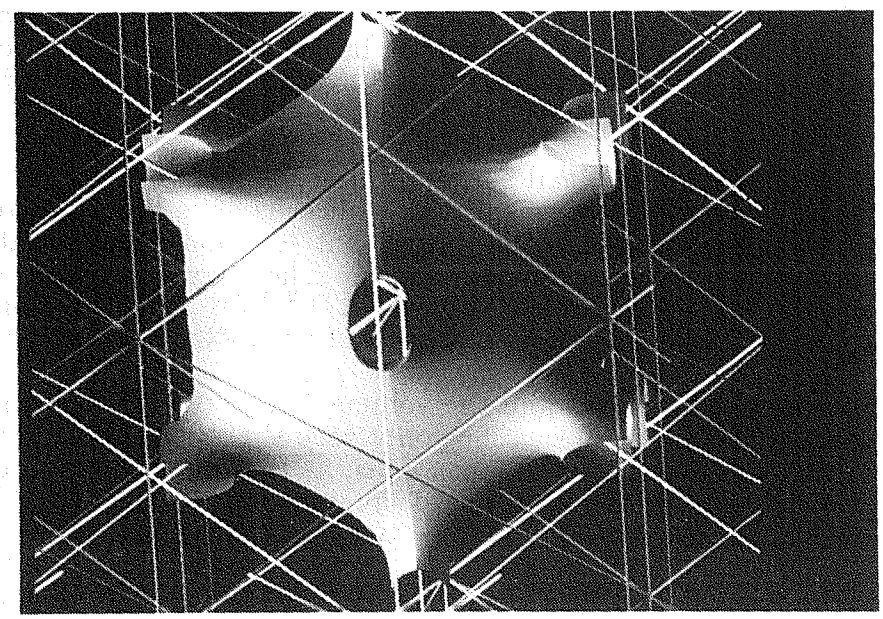

Figure 7b. Solution with $H^* = 1.05$, same space group and topological type as the Neovius surface.

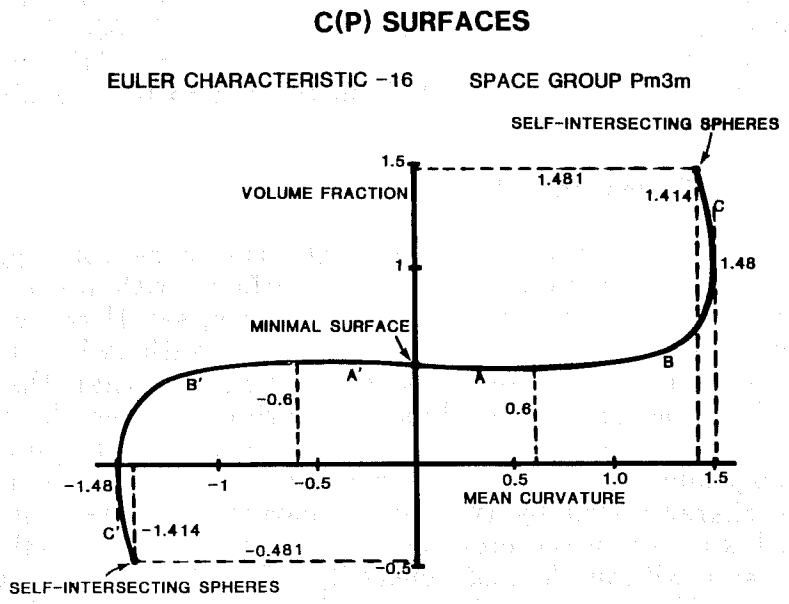

Figure 7c. Plot of volume fraction versus H* for the C(P) family. Errors are much higher than in the previous four families.

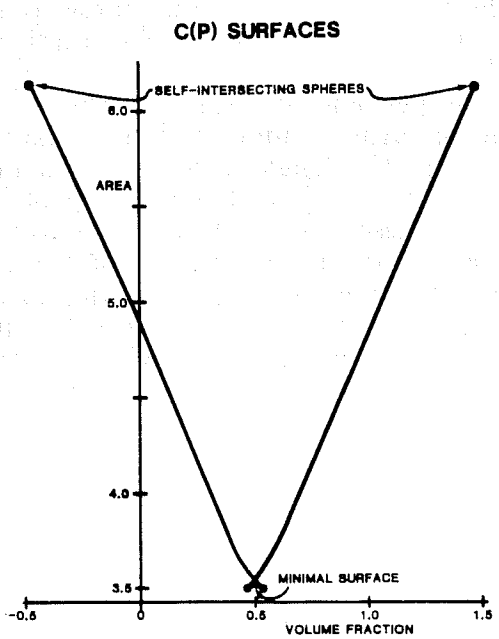

Figure 7d. Area per unit cell versus volume fraction for the C(P) family. The slope at each point is 2H*.

Subbranches C and C′ consist of self-intersecting solutions. The limiting configuration has $H^* = \sqrt{2}$, $A = 2\pi$, and "pseudo"-volume fraction 1.48096.... Taking a point on the subbranch B — $H^* = 1.35$, $A = 3.7555$, $V = 0.59273$ — and applying the mean-value theorem yields $\Delta A/\Delta V = 2.8458 = 2 \times 1.4229$, which is a good mean value for a path from $H^* = 1.35$ to a maximum of 1.48 and back to $\sqrt{2}$.

Generalized P Surfaces: Results

In this subsection we discuss surfaces with the same topological type as ("homeomorphic to") the Schwarz P minimal surface, with mean curvature a prescribed periodic function of one spatial coordinate, say $H = f(y)$; the period of f will coincide with the period of the surface, or with twice that distance. Such a surface with f nonconstant is of lower symmetry than the Pm3m surfaces treated above because of the loss of invariance under the interchanges $y \longleftrightarrow x$ and $y \longleftrightarrow z$. The space group will in fact be P4/m2/m2/m, number 123 in the Crystallographic tables, with 16 equivalent positions. This tetragonal space group is characterized by two lattice parameters, the unit cell having dimensions a x b x a. As in the previous cases, dimensional analysis shows that we can take $a = 1$ without loss of generality. The Coxeter cell C is a right prism the base of which is a right isosceles triangle; the mirror planes comprising the faces of the prism are $x = z$, $x = 0$, $z = 1/2$, $y = 0$ and $y = s$; the relation between s and the lattice parameter b is given next.

We give the name "six-armed cell" to the cell that is homeomorphic to a unit cell of the P minimal surface. If the length s of this six-armed cell is equal to the full period of the function f(y) (or any integral multiple of it) then the six-armed cell is also a unit cell and $b = s$. If in addition f(y) possesses mirror symmetry about the plane $y = b/2$, i.e., $f(y) = f(b - y)$, then this is a plane of mirror symmetry for the periodic surface. In these cases this mirror plane allows us to divide the six-armed (unit) cell into sixteen equivalent portions. However, in the cases where the length s of the six-armed cell is only half the period of f, the crystallographic unit cell is actually of length $b = 2s$ and is of Euler characteristic -8. In these cases each of the sixteen positions of the space group P4/m2/m2/m corresponds to one-eighth of the six-armed cell, while in the first case with $b = s$ the portion corresponding to a position of the space group is half that, one-sixteenth of the six-armed cell. In order to write a single code to handle all these cases, we chose to divide the six-armed cell into eight equivalent portions, ignoring the fact that in special cases these may be further bisected.

The parameterization used was:

$$\mathbf{r}(u,v,w) = \begin{cases} (2v,s,1/2)(1-w)+(0,s-2us,0)w & \text{if } 0 \le u \le 1/2 \\ (2v,s,1/2)(1-w)+(0,2us-s,2u-1)w & \text{if } 0 \le v \le 1/4, 1/2 \le u \le 3/4 \\ (1/2,3s/2-2vs,1/2)(1-w)+(0,2us-s,2u-1)w & \text{if } 1/4 \le 3/4, 1/2 \le u \le 3/4 \\ (2-2v,0,1/2)(1-w)+(0,2us-s,2u-1)w & \text{if } 3/4 \le v \le 1,\ 1/2 \le u \le 3/4\text{i}. \end{cases} \tag{40}$$

The computational domain was divided into 1401 elements, for 186 nodes. With this coarse grid, errors in area determinations were on the order of 0.5% (volume fractions errors were about 0.2%). With s set equal to unity, f was

chosen to be sinusoidal with period 2: $f(y) = \alpha \sin \pi(y - 1/2)$. Thus the unit cell is actually homeomorphic to two unit cells of the P surface, so that $b = 2$. The amplitude α was varied up to a value of 0.6, and the result for 0.6 is shown in Figure 8; two unit cells are shown side-by-side.

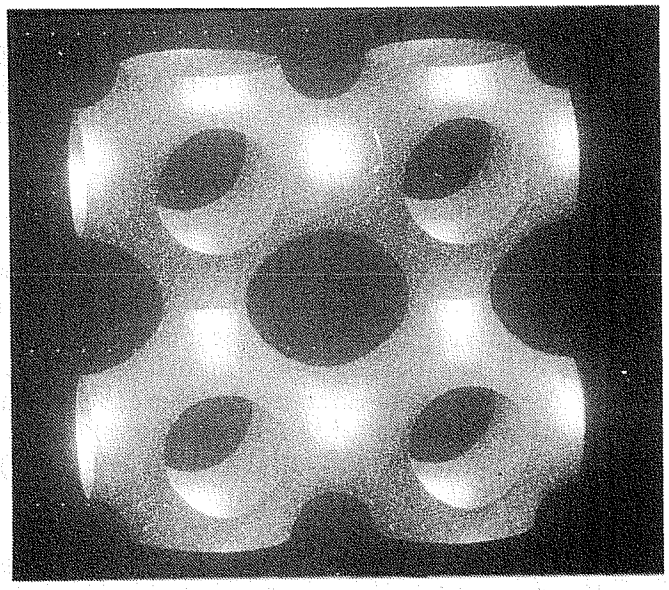

Figure 8. A periodic surface with the same topological type as the Schwarz P minimal surface, with sinusoidally-varying mean curvature in the vertical direction. Two unit cells are shown side-by-side.

With f identically zero, s was varied from 0.98 to 1.04, to investigate expansions of the area and volume fractions in s about $s = 1$. Strictly speaking, there is a (removable) singularity in the curve of area of a *unit cell* at $s = 1$ because of the change in symmetry from tetragonal to cubic (when f is constant), so we choose to report the area of a six-armed cell. It was found that to within 0.5%, the value of $A/V^{2/3}$ *remained constant* at the value 2.3451...of the Schwarz surface. The equivalence of the two labyrinths when H is identically zero guarantees that the volume fractions remain exactly at 1/2, at any value of s for which a solution exists; this held to within the error of 0.2% over the range examined.

We have computed surfaces with piecewise linear f, namely $f(y) = py + q$, $0 \leq y \leq s$, $f(y) = p(2s - y) + q$, $s \leq y \leq 2s$ with p and q small. Defining $H_{ave} = ps/2 + q$, we estimate the area per six-armed cell to be $A \sim (2.3451 - 2.117H_{ave}^2 - .023p^2)s^{2/3}$. For the case $s = 1$, we can give estimates for the volume fraction V of the labyrinth containing the origin and of the average radius R_0 (R_S) of the hole in the plane $y = 0$ ($y = s$): $V \sim 0.5 - 0.2117H_{ave}$, $R_0 \sim 0.25 + 0.095H_{ave} + 0.047p$, $R_S \sim 0.25 + 0.95H_{ave} - 0.047p$.

S′ — S″ Surface: Results

In this subsection we demonstrate, by means of an example, the

computation of a triply-periodic minimal surface from knowledge of only its two skeletal graphs. As mentioned in the Background Section, Schoen hypothesized a minimal surface that he named S′ − S″, for "large-square graph, small-square graph", and described the skeletal graphs S′ and S″, but did not provide pictures or any other data on the surface. Contrary to the cases of I-WP and F-RD that were also conceived by Schoen, S′ − S″ is not known to be related to any surface whose Weierstrass representation is skew pentagon, the five edges being normal to the five faces of the Coxeter cell C for S′ − S″ described below, and while Schoen proved that only eight such pentagonal modules could generate surfaces with discrete non-cubic symmetry groups, he did not elucidate these surfaces. The results in this subsection support, but of course do not prove, the existence of the minimal surface S′ − S″.

As noted by Schoen, the space group for S′ − S″ is tetragonal, P4/m 2/m 2/m, the same as that of the previous subsection, and again the Coxeter cell C is the isosceles right triangular prism with faces: $x = z$, $x = 0$, $z = 1/2$, $y = 0$ and $y = b/2$. The unit cell has been given dimensions 1xbx1, and no change of symmetry would occur for $b = 1$, as opposed to the case in the previous subsection. There are two edge-portions of each of the skeletal graphs G' $(= S'')$ among the nine edges of C; call these $l_1 : \{(1/2 - u, b/2, 1/2) \mid 0 \leq \{u \leq 1/2\}$, $1_2 : \{(0, b - bu, 1/2) \mid 1/2 \leq u \leq 1\} \in G'$ and $m_1 : \{(0, b/2 - v, 0) \mid 0 \leq v \leq 1/2\}$, m_2: $\{(v - 1/2, 0, v - 1/2) \mid 1/2 \leq v \leq 1\} \in G''$. The three pairs l_1m_1, l_1m_2, and l_2m_2 of opposing edge-portions determine spines that fill out C exactly, and the pair of parallel edge-portions 1_2 and m_1 does not contribute any spines, of course. The three rectangles in the u-v unit square corresponding to the three active pairs determine an L-shaped computational domain, with the square $\{(u, v) \mid 1/2 \leq u \leq 1, 0 \leq v \leq 1/2\}$ corresponding to the inactive pair l_2m_1 omitted. We have thus determined the parameterization, and the residual equations, without ever having seen any portion of the surface.

An initial estimate was formulated by inventing a "composite" distance from an arbitrary point to each skeletal graph (details in Anderson[22]), and the surface determined by the locus of points equidistant in this measure from the two graphs was used successfully for the surface with $H^* = 1.0075$ and $b = 0.936$. From this converged solution, b and H^* were incremented to smaller values simultaneously, with convergence becoming steadily easier, until a minimal surface with $b = 0.64$ was found. The area of such a unit cell was 2.0185; this area increased to 2.2640 when b was increased to 0.76, and within the error this represents a constant value of $A/V^{2/3}$ (equal to 2.718). We were not able to achieve convergence with $b = 0.80$, but his is not a proof that no minimal surface with $b \geq 0.80$ exists, of course. Figure 9a is a line drawing of a unit cell of the minimal surface with $b = 0.78$. Figure 9b is a line drawing of a unit cell with $b = 0.78$ and $H^* = 2.015$. The feature that best distinguishes S′ − S″ from the P minimal surface has to do with the connectivity between unit cells lying at the same value of y; to get from the centroid (0,0,0) of one unit cell to the centroid, say (1,0,0), of a neighboring unit cell while remaining within the labyrinth containing G′ requires a jig-jag path, say via the point (1/2, 0, 1/2). On the other hand the P minimal surface allows straight paths connecting nearest neighbor unit cells. The "holes" in the S′ − S″ unit cell centered about $y = 0$ are very similar to those in the surface C(P); in both cases, at each edge-midpoint of the cube a "throat" comes in orthogonally to the two adjacent cube faces, with throats from each of the four cells that share this edge-midpoint joining smoothly. In the C(P) surface, this situation is repeated at each of the

twelve edge-midpoints of the unit cell, whereas in $S' - S''$ it occurs only on the four edges parallel to the y-axis.

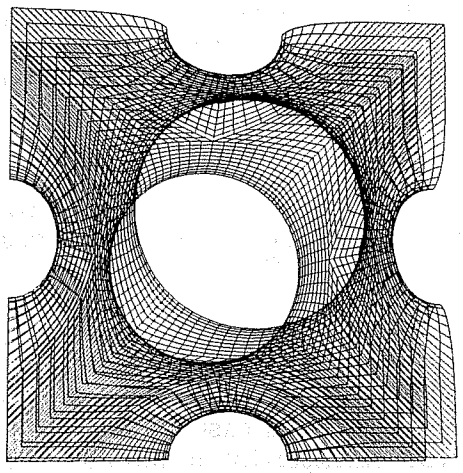

Figure 9a. Schoen's minimal surface $S' - S''$ with $b = 0.78$. One unit cell is shown, looking almost directly down the y-axis.

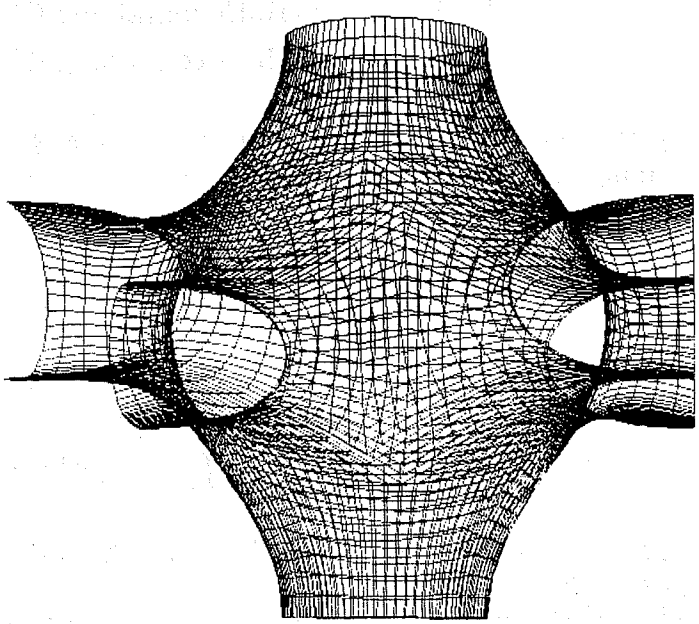

Figure 9b. Variant of the surface in figure 9a with $b = 0.936$ and $H^* = 1.0$. In this view the y-axis is vertical.

Scattering Function Calculations

At the time of this writing, the most immediate application for the surfaces discussed in this section is to provide models for viscous isotropic phase liquid crystals and certain phase-segregated polymer blends and block copolymers. In this subsection we show how to calculate diffraction peak intensities from a class of model structures based on these surfaces. The method applies to scattering density profiles (electron densities for X-ray scattering) determined by:

A) contrast between the two labyrinths ('bulk' scattering);
B) contrast between the surface — imagined as a thin layer — and two labyrinths of equal density ('film' scattering); or
C) a combination of A) and B).

Case C) involves three (electron) densities, one for each labyrinth and one for the surface layer. Because relative intensities are all that are usually measured, only *one parameter* is needed to allow for any combination of three densities. The scattering function calculated in case B) is what is frequently referred to as the *structure factor* of the surface; for a minimal surface characterized by a self-dual skeletal graph, this will correspond to a *different* space group than that of A) or C), or of case B) with nonzero mean curvature (see the 'D' family, above).

A model structure of type A0, based on a triply-periodic embedded surface S parametrized via the present method as $S:\{\mathbf{r}(u,v,w^*(u,v)) | (u,v)\epsilon D\}$, is in general described (for the purpose of relative intensities) by the following step-change density profile:

$$\rho_b(\mathbf{r}) = \begin{cases} 1 & \text{if } \mathbf{r} \in \text{"labyrinth containing } G' \\ 0 & \text{if } \mathbf{r} \in \text{"labyrinth containing } G'' \text{ .} \end{cases} \tag{41}$$

The portion of the volume inside the unit cell U for S that is part of the labyrinth containing the skeletal graph G' is exactly described by the condition $w<w^*$, and $w>w^*$ describes the G"-labyrinth, or:

$$\rho_b(\mathbf{r}(u,v,w(u,v)) = \begin{cases} 1 & \text{if} w<w^*(u,v) \\ 0 & \text{if} w>w^*(u,v)' \end{cases} \tag{42}$$

so that:

$$A_b(\mathbf{h}) = \int\int\int_U \rho_b(\mathbf{r}) e^{i\mathbf{hr}} d^3\mathbf{r} = \int\int\int_{U:w<w^*} e^{i\mathbf{hr}} d^3\mathbf{r} \quad . \tag{43}$$

In case B, *all* of the scattering contrast is from a high density region concentrated in a layer or 'film' about the surface. The singularity can be considered the limiting value of the project of the excess density and the layer thickness; that is, a region $[\mathbf{r}^* + s\mathbf{n}, \mathbf{r}^* \epsilon S, |s| \leq \tau/2)]$ of density $1/\tau$ in the limit as $\tau \downarrow 0$. The strength α can be assigned to the film contrast by multiplying the unit-strength singularity by α. The unit-strength singularity yields the structure factor A_f of the surface:

$$A_f(\mathbf{h}) = \lim_{\tau\downarrow 0}\iint'_{[\mathbf{r}=\mathbf{r}^*+s\mathbf{n},\mathbf{r}^*\epsilon S\cap U,|\,s\,|\,\leq\,\tau/2]}(1/\tau)e^{i\mathbf{h}\cdot\mathbf{r}} = \iint_{S\cap U}e^{i\mathbf{h}\cdot\mathbf{r}}dS \quad . \qquad (44)$$

at zero wave vector, a unit-strength singularity at the surface, taken over a unit cell of surface, yields the area of the surface.

The *amplitude* in case C) at a wave vector of **h** is the sum of the amplitudes of A_b and A_f from the bulk and film contrasts:

$$A(\mathbf{h}) = A_b(\mathbf{h}) + \alpha A_f(\mathbf{h}) \quad . \qquad (45)$$

The integration is over the unit cell U, and this region is produced by applying the mirror symmetries of the space group (but of course *not* the translational symmetries) to the Coexeter cell C. However, since the dependence on **h** is through the dot product $\mathbf{h}\cdot\mathbf{r}$ it is equivalent to apply the mirror symmetries of the space group to the vector **h** and integrate over just the Coxeter cell for each permutation of **h**, and then add the resulting partial amplitudes.

Because of the perfect periodicity of these profiles, the intensities will be nonzero only at a discrete set of wave vectors. The Miller indices (hkl) of the allowed reflections, as listed in the Tables of X-ray Crystallography for a given space group and Wyckoff position, determine the wave vectors for which intensities must be evaluated. The wave vector that corresponds to the reflection with Miller indices (hkl) is $\mathbf{h} = (2\pi h/a, 2\pi k/a, 2\pi l/a)$, where the lattice parameter a can be taken equal to unity here. The dot product $\mathbf{h}\cdot\mathbf{r}$ is then $2\pi(h,k,l)\cdot\mathbf{r}$ and by equation (2) $\mathbf{r}=\mathbf{a}(u,v) + \mathbf{b}(u,v)w$, so:

$$\mathbf{h}\cdot\mathbf{r} = 2\pi(h,k,l)\cdot[\mathbf{a}(u,v) + \mathbf{b}(u,v)w] = p(u,v) + q(u,v)w \quad . \qquad (46)$$

We need then to calculate the volume integral of $e^{i\mathbf{h}_j\cdot\mathbf{r}}$, where $\mathbf{h}_j$, j=1,...n are the permutations of **h** (with n typically 48), over the portion C_1 of C satisfying $w<w^*$, and the surface integral over the surface patch S_c inside C. As is well known, for a unit cell which is centro-symmetric ($\pi(\mathbf{r})=\pi(-\mathbf{r})$), the sine part of $e^{i\mathbf{h}_j\cdot\mathbf{r}}$ does not contributed to the amplitude, and this is true here in all cases for both amplitudes. We have shown in Section w that the Jacobian of the transformation from u-v-w to x-y-z coordinates is of the form cw(1-w) (see Eqn. (9)), so that:

$$A_b(\mathbf{h}) = \sum_{j=1}^{n}\iint_D\int_0^{w^*}\cos(\mathbf{h}_j\cdot\mathbf{r})cw(1-2)du\ dv\ dw \quad , \qquad (47)$$

where D is the computational domain for S_c as always.

The integration over the domain D is of course done one element at a time, and in all cases we have used four Gauss points per grain square. Therefore the functions p and q are approximately constant over the (small) region D_k of D belonging to a given Gauss point P_k, with values p_k and q_k respectively. The integral over D_k is then approximated by:

$$\iint_{Dk}\int_0^{w^*}\cos(\mathbf{h}_i\cdot\mathbf{r})cw(1-2)du\ dv\ dw = \cos(p_k = q_k w^* k)\sigma_k\Delta u\Delta v \quad . \qquad (48)$$

These terms are summed over the set of Gauss points, and then over $\mathbf{h}_j$,j=1...,n to yield the amplitudes A_b and A_f. When $\mathbf{h} = \mathbf{0}$, then p and q are zero for all (u,v), and the last formula reduces to that used for the determination of surface area. Thus for small wave vectors, say $|\mathbf{h}\cdot\mathbf{a}| < 1$, we should expect accuracies on the order of that seen in the area determinations, which are better than 0.05% for the P,D, I-WP and F-RD families. For larger values of h this accuracy decreases. For zero wave vector the bulk amplitude A_b yields the volume fraction of the G' labyrinth, so that the accuracies for small wave vectors are better than 0.01%.

Table 1 lists the two amplitudes for three members of the P family. For the minimal surface, the reflections that are forbidden in BCC symmetry are listed as zero amplitude, and in each case the computed amplitudes was less than 10^{-10}. For the I-WP family, there is no change in symmetry for H*=0, as seen in Table 2. The structure factor for the D minimal surface is shown in Table 3, and the last column in this table lists the values published by Mackay[26]; the results are in agreement.

When the amplitudes A_b and A_f have been calculated, the intensity I(**h**) is calculated as $I = [A_b+\alpha A_f]^2$. Thus a listing of the two amplitudes for each reflection permits easy calculation of the intensities for any number of choices of α; this simplicity is important in fitting the parameter α to experimental data.

A member of a family characterized by a self-dual graph can define a structure that has a different space group than that of each skeletal graph, by considering the region between the surfaces H* = h and H* = - h to be the region of unit density. We have seen that the transformation (u,v,w) $\longrightarrow$ (1-u, 1-v, 1-w) takes a surface S with H*= - h — positive with respect to the G′ graph — into its counterpart with the same curvature toward the G″ graph. This situation is easily represented in the present parametriziation by introducing the upper limit of integration w″(u,v) = 1 - w* (1-u,1-v), and $e^{i\mathbf{h}_j\cdot\mathbf{r}}$ is integrated over w∈ [w*,w″]; the condition w″>w* must of course be observed over the entire surface, and for the P and D families this hold s over the branches A and A′, and portions of B and B′. This represents, for example, an idealized density profile for a binary amphiphile-water cubic phase in which two equivalent but disjoint layrinths of water are separated by a continuous bilayer of amphiphile.[2,6] Table 4 shows the results of the calculation for the first eight allowed reflections for this case, based on the P surface with H* = 1.8.

Conclusion

A new approach to the computation of surfaces of prescribed mean curvature has been described and five new families of embedded, triply-period surfaces of constant mean curvature tracked between periodic limiting configurations of sphere packings. These five families include as members all of the embedded triply-periodic minimal surfaces that can be constructed from minimal surface patches spanning identical skew quadrilaterals, or from conjugates of such patches — for it was proven by Schoenfliess[69] [see also Schwarz[24], Stessmann[67]] that exactly six periodic minimal surfaces can be constructed from minimal surface patches spanning quadrilateral boundaries, and of these surfaces and their conjugates (which are bounded by four plane lines of

curvature), all but five are known to contain self-intersections. The representation of the surface in the new formulation allows for accurate calculation of scattering functions for a class of density profiles determined gy the solutions.

Many important questions and conjectures remain unresolved. It is not known whether these solutions are the only embedded H-surfaces for the five dual pairs of skeletal graphs studied, for example. An important issue is whether or not there exists a bound on the mean curvature attainable in such families; for all of the branches studied here, and for the family of unduloids with a fixed repeat distance,[22] the dimensionless mean curvature $H^{\#}=H\lambda$ is always less than π, where λ is the sphere diameter in the sphere-pack limit. It is possible that there exists an upper bound on $H^{\#}$ lower than π that depends on the coordination number, or the Euler characteristic. And for the P, D, I, WP, F, and RD branches, the islands R^{+} regions at a critical mean curvature that is the same (to within an error in H^* of about 0.15) as the value H^*_c corresponding to the local minimum in surface area. And we have given what we suspect to be analytical values for the areas of the I-WP and F-RD minimal surfaces, and for the first nonzero coefficient in both the area and volume expansions about $H^* = 0$ in the P family.

The fact that a local maximum in area occurs at $H^* = 0$ in each family is not predicted by any known theorem. Schwarz[24] showed that under the orthogonality boundary conditions the second variation of the area is negative for a minimal surface bounded by the planes of a tetrahedron, but this only means that *some* normal perturbation which preserves the orthogonality boundary conditions decreases the area, and does not say anything specifically about those perturbations with constant mean curvature.

The I-WP and F-RD minimal surfaces have been shown to provide two counterexamples to a conjecture that has previously been made:[78] "A triply-periodic minimal surface disconnects R^3 into two regions with asymptotically the same volume". The volume fraction of the labyrinth containing the symmetric skeletal graph is 0.5360 ± 0.0002 for the I-WP minimal surface and 0.5319 ± 0.0001 for F-RD.

In all of the solution branches investigated, we have observed qualitatively similar behavior: surface areas first decrease moving away from the minimal surface until a minimum in area is reached at some H^*_c, which also corresponds to the point of most unequal volume fractions; then, past H^*_c a turning point in H^* occurs at some H^*_{max}, and past H^*_{max} areas increase dramatically until a limiting configuration is reached consisting of identical spheres, either close-packed or self-intersecting. Table 5 records some of the significant parameters observed on the branches examined. The branches are listed according to the coordination number in the sphere-pack limit; if two branches have the same coordination, the symmetric graph is listed first. Some trends are indicated by the table, namely that for branches with higher coordination number in the sphere limit, we observe: 1) lower values of $H^{\#}_{max}$, 2) lower values of $|V(0)-V(H^*_c)|$, 3) lower values for the slope $dV/dH^{\#}|_{H^{\#}=0}$ of the V-$H^{\#}$ curve at $H^{\#} = 0$; and 4) higher values of $A(H_c)/V(H_c)^{2/3}$ per lattice-fundamental region.

A heuristic argument can be given as to the source of the trends in Table 5. Near the CPS limit on a given branch, the solution patch inside a single Coxeter cell is well-approximated by a patch of an unduloid, and in fact we have

successfully used unduloids as initial estimates for solutions near the CPS limits of the P and F branches. In the case of unduloids it can be shown[22] that $H^{\#}$ increases monontonically from $H^{\#}=2$ at the sphere limit to the limiting value of $H^{\#}=\pi$ at the cylinder limit. However in each of the branches treated here, $H^{\#}$ increases from 2 on moving away from the sphere limit but must eventually start to decrease and head toward the value $H^{\#}=0$ of the minimal surface. It is not unexpected that a higher coordination number would impose greater constraints on a brach of solutions, so tht the family of unduloids with its coordination of two would reach the highest value of $H^{\#}_{max}$ while those branches with coordination numbers of twelve never go higher than $H^{\#} = 2.1$. In short, we are imposing constraints on the solutions, by fixing a higher coordination number, that tend to limit excursions in the mean curvature, in volume fraction ratios, and in surface areas.

Table 1. Amplitudes for three P surfaces.

	$H^* = 0$		$H^* = -1.8$		$H^* = 2$ (CPS)	
(hkl)	A_b	A_f	A_b	A_f	A_b	A_f
(000)	0.5	2.345107	0.751.23	2.00264	0.52360	3.14159
(100)	0.16696	0	0.13022	-0.58291	0.15915	0
(110)	-1.66E-05	-0.44936	-0.04747	-0.20807	0.00392	-0.68158
(111)	-0.06057	0	-0.00837	0.57051	-0.04261	-0.43061
(200)	-1.41E-05	-0.54494	-0.01823	-0.15113	-0.03979	0
(210)	-0.0147	0	-0.01027	0.19855	-0.02041	0.30209
(211)	-1.29E-05	0.45618	0.02748	-0.13002	-0.00079	0-40312
(220)	-1.57E-05	-0.04256	0.00263	0.22521	0.01822	0.18147
(221)	0.01863	0	-0.00758	-0.30676	0.01768	0
(300)	-0.01849	0	0.00477	0.01301	0.01768	0
(310)	-7.36E-05	0.09885	0.00185	0.05618	0.01311	-0.15432
(311)	0.01583	0	-0.00608	-0.12509	0.00672	-0.25285
(222)	-3.13E-06	-0.40418	-0.01295	0.36989	0.00028	-0.28684
(320)	-0.00633	0	0.01065	-0.07833	-0.00501	-0.26224
(321)	-1.24E-05	-0.21779	-0.00703	-0.09816	-0.00853	-0.19387

Table 2. Amplitues for three I-WP surfaces.

	$H^* = -3.55$		$H^* = 0$		$H^* = 2.0$	
(hkl)	A_b	A_f	A_b	A_f	A_b	A_f
(000)	0.8477232	2.60518	0.5360401	3.466965	0.3521078	3.197987
(110)	0.04481	-0.67059	0.10465	-0.30988	0.11261	0.10664
(200)	-0.08244	0.89956	-0.09021	-0.52743	-0.01901	-0.97923
(211)	0.00172	0.12524	-0.02475	-0.12206	-0.02093	-0.43372
(220)	-0.03122	-0.07605	0.00983	-0.28466	-0.00459	-0.12859
(310)	0.02583	-0.10469	-0.00127	0.68039	-0.02468	0.2102
(222)	0.00489	-0.51241	-0.00108	0.50945	-0.01796	0.06465
(321)	-0.00203	0.17153	0.00344	-0.03437	0.00541	0.24275

Table 3. Amplitudes for D minimal surface (H = 0). Mackay's figures included for comparison.

(hkl)	A_b (this work)	A_f (this work)	A_f (Mackay)
(000)	0.5000	1.91928	1.9193
(111)	0	0	0
(200)	0	0	0
(220)	-2.000E-08	0.4780	0.4775
(311)	0	0	0
(222)	-2.400E-08	0.4840	0.4866
(400)	-1.400E-08	-0.2610	

Table 4. Amplitudes for P surface with $H^* = 1.8$, bilayer arrangement.

	$H^* = 1.8$
(hkl)	A_b (Bilayer)
(000)	0.50246
(110)	-0.09614
(200)	-0.03845
(211)	0.05381
(220)	0.00669
(310)	0.04401
(222)	-0.2352
(321)	-0.01289

Table 5. Parameters indicating excursion in mean curvature, volume fraction and surface area.

Branch	Coordination	$H^{\#}$max	$\lvert V(0)-V(H_c)\rvert$	$dV/dH^{\#}\lvert H^{\#}=0$	$A(H_c)/[V(H_c)]^{2/3}$
D	4	242	0.369	0.327	1.653
WP	4	264	0.357	0.277	1.960
P	6	2.13	0.250	0.212	2.002
I	8	2.45	0.117	0.160	2.530
RD	8	(2.18)	0.095	0.083	2.922
F	12	2.07	0.093	0.102	2.922
C(P)	12	(2.09)	0.020	0.032	3.503

References

1. Scriven, L.E. 1976 Nature **263**, 123-125.
2. Fontell, K. 1981 Mol. Cryst. Liq. Cryst. **63**, 59-82.
3. Longeley, W. and McIntosh, J. 1983 Nature, **303**, 612-614.
4. Bull, T. and Lindman, B. 1974 Mol Cryst. Liq. Crystal **28**, 155-160.
5. Scriven, L.E. 1977 "Equilibrium Bicontinuous Structures", *Micellization, Solubilization and Microemulsions*, ed. Mittal, K.L., Vol. 2 Plenum Press, NY, 877-893.
6. Lindman, B. and Stilbs, P. 1982 "Characterization of Microemulsion Structure Using Multicomponent Self-diffusion Data", *Surfactants in Solution*, eds. Mittal, K.L. and Lindman, B., L-103, 1651-1662.

7. Auvray, L., Cotton, J., Ober, R. and Taupin, C. 1984 J. Phys. Chem. **88**, 4586-4589.
8. Clarkson, M.T., Beaglehole, D. and Callaghan, P. T., Phys. Rev. Lett. **54**, (15) 1722-1724 (1985).
9. Kaler, E.W., Bennett, K.E., Davis, H.T. and Scriven, L.E. 1983 J. Chem. Phys. **79**, 5673-5684.
10. Lindblom, G., Larsson, K., Fontell, K. and Forsen, S. 1979 J. Am. Chem. Soc. **101** (19) 5465-5470.
11. Larsson, K., 1983, Nature **304**, 664.
12. Shal'nikov, A. 1941 Zhurnal Eksperimental noi i teoretischeskoi fiziki **11**, 202-210.
13. Hench, L.L. and Ulrich, D.R. eds. 1984, *Ultrastructure Processing of Ceramics, Glasses, and Composites,*, Wiley Interscience Pub., N.Y.
14. Zick, A.A. and Homsy, G.M. 1982 J. Fluid Mech. **115** 13-26.
15. Wheeler, J.A. 1957 Ann. Phys. **2** 604-614; also Misner, C. W. and Wheeler, J. A. 1957 Ann. Phys. **2** 525-603.
16. Gunning, B.E.S. 1965 Protoplasma **60**, 111-130.
17. Thomas, E.L., Alward, D. B., Kinning, D. J., Martin, D. C., Handlin, Jr, D. L., and Fetters, L. J. 1986 Macromolecules (submitted).
18. Faulkner, L.R. 1984, "Chemical Microstructures on Electrodes", Chemical and Engineering News, Feb. 27, 1984, 28-45.
19. Haggin, J. 1982, "Shape Selectivity Key to Designed Catalysts", Chemical and Engineering News, Dec. 13, 1982, pl 9.
20. Pippard, A.B. 1954 Adv. in Electronics **6** 1; also Proc. Roy. Soc. **A224**, 273.
21. Andersson, A. 1983 Angewandte Chemie **22** (2), 69-170.
22. Anderson, D.M. 1986 "Studies in the Microstructure of Microemulsion", Ph.D. Thesis, University of Minnesota.
23. Schwarz, H.A. 1865 Monatsberichte der Koniglichen Akademie der Wissenscaften zu Berlin, Jahrgang 1865, 149-153.
24. Schwarz, H.A. 1890 *Gesammelte Mathematische Abhandlungen,* Verlag-Springer.
25. Schoen, A.H. 1970 "Infinite Periodic Minimal Surfaces without Self-intersections", NASA Technical Note TD-5541.
26. Mackay, A.L. 1985 Nature **314**, 604-606; also Physica **131B**, 300-306.
27. Riemann, B. 1892 *Gesammelte Mathematische Werke,* 2 vols., B.G. Teubner, Leipzig.
28. Lagrange, J.L. 1761 Miscellanea Taurinensia **2**, 173-195; *Oeuvres de Lagrange,* Vol. 1, Gauthier-Villas, Paris, 335-362.
29. Weierstrass, K. 1866 Monatsber. Berlin Akad.
30. Bonnet, O. 1853 C.R. Acad. Sci. Paris. **37**, 529-532.
31. Nitsche, J.C.C. 1975, *Vorlesungen uber Minimalflachen,* Springer-Verlag, Berlin.
32. Lawson, H.B. 1980 *Lectures on Minimal Submanifolds.* Vol. 1, Publish or Perish, Inc., Berkeley, CA.
33. Weatherburn, C.E. 1927 *Differential Geometry of Three Dimensions,* Cambridge University Press, Vol. 1.
34. Gauss, C.F. 1827, *Werke.*
35. Bonnet, O. 1848 J. Ecole Polytechnique, **19** 1-146.
36. Darboux, G. 1894, *Lecons sur la theorie generale des surfaces et les applications geometriques du calcul infitesimal,* Vol. III, ch. VI, Gauthier-Villars, Paris.
37. Rhines, F.N. 1958 "A new veiwpoint on sintering", Trans. MPA (1058)

Plansee pub. 91-101.
38. Pathak, P. 1981, "Porous media: structure, strength and transport", Ph.D. thesis, University of Minnesota.
39. *International Tables for X-ray Crystallographyzf, 1952, The Kynoch Press, Birmingham.*
40. *Neovius, E. 1883 Bestimmung Zweier Speciellen Periodischen Minimalflachen,* J.C. Frenckell and Sons, Helingfors.
41. Scherk, H.F. 1835 J.R. Agnew Math. **13**, 185-208.
42. Schoen, A.H. 1968 Not. Amer. Math. Soc. **15**, 727; also **16**, 519.
43. Delauney, C. 1841, J. Math. Pures. Appl. Ser. 1 **6**, 309-320.
44. Kenmotsu, K. 1980 Tohoku Math. Journ. **32**, 147-153.
45. Schoen, A.H. 1967 Not. Amer. Math. Soc. **14**, 661.
46. Lines, L. 1965, *Solid Geometry*, Dover Publications.
47. Joachimtsthal, F. 1846 J.R. Angew. Math. **30** 347-350.
48. Coxeter, H.S.M. 1963, *Regular Polytopes,* MacMillan, NY.
49. Massari, U. Arch. Rat. Mech. Anal. **55**, 357-382 (1974).
50. Giusti, E. *Minimal surfaces and functions of bounded variation,* Birkhauser, Bonston — Basel — Stuttgart 1984.
51. Gruter, M., Hildebrandt, S. and Nitsche, J.C.C. 1981, Manuscr. Math., **35**, 387-410.
52. Gruter, M., S. Hildebrandt, and J. C. C. Nitsche Acta Math. **156**, 119-152 (1986).
53. Kenmotsu, K. 1978 "Generalized Weierstrass Formula for Surfaces of Prescribed Mean Curvature", *Minimal Submanifolds and Geodesics,* Kaigai Publications, Tokyo, 73-76.
54. Rivas, A.P. 1972 "Meniscus computations: shpaes of some technologically important liquid surfaces", M.S. Thesis, University of Minnesota.
55. Hinata, M., Shimasaki, M. and Kiyono, T. 1974 Math. of Computation **28** (125), 45-60.
56. Wagner, H.J. 1977 Computing **19** 35-58.
57. Kistler, S. F., Ph.D. Thesis, University of Minnesota 1983.
58. Courant, R. 1943 Bull. Am. Math. Soc. **49**, 1-23.
59. Turner, M.R., Clough, R. W., Martin, H. C., and Topp, L. J. 1956 J. Amer. Sci. **23** 805-823.
60. Silliman, W.J. 1979 "Viscous film flows with contact lines", Ph.D. thesis, University of Minnesota, Minneapolis.
61. Kistler, S. F. and Scriven, L.E. 1983 *Computational Analysis of Polymer Processing*, eds. Pearson, J.R.A. and Richardson, S.G., Applied Science Publishers Ltd., Barking, Essex, England. Chapter 8.
62. Hyde, S.T. 1986, "Infinite minimal surfaces and crystal structures", Ph.D. thesis, Monash University.
63. Bashkirov, N.M. 1959 Soviet Physics, Crystallography, **4** 442-447.
64. Christiansen, H.N., Stepheson, M. B., Nay, B. J., Ervin, D. G., and Hales, R. F. 1981 NCGA '81 Conf. Proc., June 1981, 275-282.
65. Weierstrass, K. 1903 *Mathematische Werke*, 3 vols., Mayer and Muller, Berlin.
66. Bragg, Sir L., Claringbull, G.F. and Taylore, W.H. 1965 Crystal
67. Stessmann, B. 1934 Math. Zeit. **33** 417-442.
68. Hyde, S.T., Andersson, S., Ericsson, B., and Larsson, K. 1984 Z. Krist. **168**, 213-219.
69. Schoenfliess, A. 1891 C.R. Acad. Sci. Paris **112**, 478-480; also 515-518.
70. Meeks, W. 1978, "Lectures on Plateau's Problem", Escola de Geometria Differencial, Universidade Federal do Ceara.

4. EQUILIBRIUM THIN FILMS ON ROUGH SURFACES: TWO-PHASE TRANSPORT IN IDEALIZED PORES

Synopsis

The structure and stability of perfectly wetting fluid menisci in axisymmetric pores have been investigated using the augmented Young-Laplace equation as solved by the Galerkin/finite-element method. Both continuous and disconnected menisci geometries have been considered. The results of these calculations for single and multiple pore microscopic systems have been applied to macroscopic systems by the application of a statistical theory of multiphase transport in porous media. The results indicate the existence of two transport mechanisms: a capillary jump mechanism by which the non-wetting fluid invades pores, and a film drainage mechanism by which wetting films and pendular structures, remaining after the invasion of the non-wetting fluid, continue to drain. The difference between the two mechanisms is apparent at low wetting phase saturation in both the predictions of the statistical theory and in displacement experiments of perfectly wetting and intermediately wetting fluids in sintered teflon synthetic porous media.

Introduction

In an earlier paper[1], we used the augmented Young-Laplace (AYL) equation[2–4] to calculate menisci shapes on two types of idealized surface roughness and to model film drainage processes in porous media. In this paper, we introduce an idealized pore model, calculate menisci shapes and stabilities for perfectly wetting fluids in these idealized pores, and apply a statistical theory[5] to a population of these pores to model the capillary pressure behavior of a displacement process in a porous medium. In Section 2, the AYL equation, the idealized pore model, and the statistical theory of displacement are all introduced. In Section 3, the Galerkin/finite element formulation of the AYL equation is developed from an energy principle. In Section 4, computational results for film profiles and stability are presented, and the implications of the menisci configurations (in the form of a microscopic capillary pressure curves) for macroscopic properties of a porous medium are interpreted through the use of the statistical theory. The predictions of the model for perfectly wetting and intermediately wetting fluids are compared to experimental data from displacement processes in uniformly wet porous media and shed light on the different mechanisms for two-phase transport in porous media.

Theory

Where menisci lie far from any third phase the pressure drop across the meniscus is governed by the Young-Laplace equation. When the meniscus separates a thin film from a bulk phase it is the augmented Young-Laplace equation that controls the pressure drop.

The Young Laplace equation,

$$2H\sigma = \Delta p \tag{1}$$

describes the shape of the meniscus between bulk fluid phases, where H is the mean curvature, σ is the interfacial tension, and Δp is the capillary pressure (pressure difference between the bulk phases). If one phase becomes colloidal in one dimension due to the presence of a third phase (either solid or liquid), the Young-Laplace equation must be augmented by a disjoining pressure contribution, to yield

$$2H\sigma + \Pi(h) = \Delta p \ , \tag{2}$$

where Π is the disjoining pressure, a function of the film thickness, h. Equation (2) is called the augmented Young-Laplace (AYL) equation. For the current work, we use the following form of the disjoining pressure:

$$\Pi(h) = \frac{A}{h^3} \tag{3}$$

where A is the Hamaker constant, which depends on the molecular interactions between the two fluid phases and the solid. The inverse cube dependence of the disjoining pressure on film thickness is commonly used to describe the disjoining pressure in films of non-polar fluids thinner than 20nm.

The idealized pore model consists of an axisymmetric sinusoidal pore. The aspect ratio, or ratio of pore body radius to pore throat radius, and the ratio of pore length to pore throat radius are the only two inputs to the pore geometry model. In the limiting case in which the aspect ratio is one, a model pore is simply a cylindrical tube. Everett and Haynes[6] have considered capillary condensation in cylindrical tubes in the absence of disjoining interactions. For the axisymmetric geometry, two types of meniscus shapes have been investigated (see Figure 1). They are classified as bicontinuous, continuous in both the wetting and nonwetting phase, and discrete clusters of the non-wetting phase. Two expressions for the mean curvature are required for these geometries, one in spherical coordinates and one in cylindrical coordinates:

$$2H = \begin{cases} \dfrac{1}{f(1+f_z^2)^{1/2}} - \dfrac{f_{zz}}{(1+f_z^2)^{3/2}} & \text{(cylindrical)} \\ \dfrac{f^2 + 2f_\theta^2 - ff_{\theta\theta}}{(f^2+f_\theta^2)^{3/2}} & \text{(spherical)} \end{cases} \tag{4}$$

where f is the position of the meniscus.

Statistical Theory of Displacement

For a given meniscus configuration of a wetting fluid in an idealized pore, we can calculate the wetting fluid volume in that pore. The statistical theory is

needed to average these microscopic or pore properties over an assemblage or population of pores. The theory, developed by Heiba et al. (5), supposes that for the non-wetting phase to displace the wetting phase from a pore (pore initially filled with the wetting fluid), two conditions must be satisfied. First, the capillary pressure must be high enough to force the advancing meniscus through the constriction at the pore throat. Assuming that the advancing meniscus takes the shape of a hemispherical cap, we can write the allowability (or enterability) criterion for a pore in terms of the pore throat radius, the interfacial tension, the contact angle, and the capillary pressure

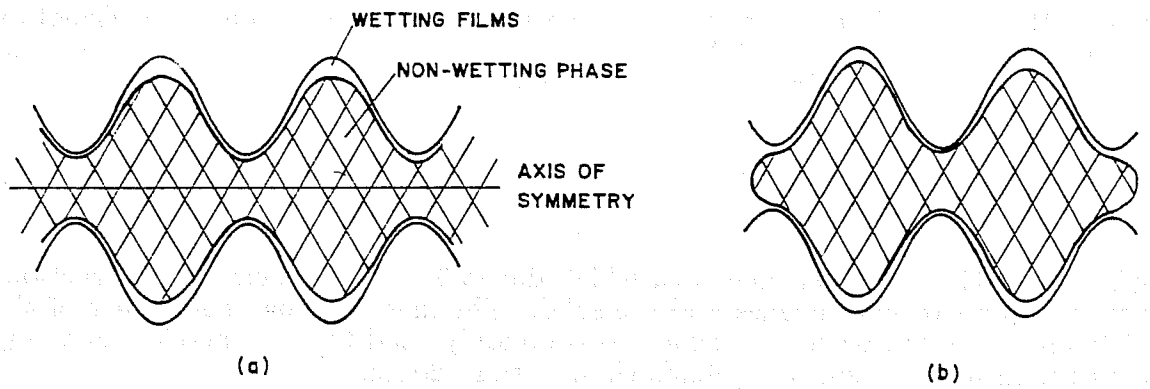

Figure 1. Meniscus geometries for (a) bicontinuous and (b) discrete configurations configurations in idealized axisymmetric pores.

$$\Delta p > \frac{2\sigma\cos\theta}{r} \tag{5}$$

where θ is the contact angle.

The second condition is the result of topological constraints imposed by the network nature of the porespace. At any point during the invasion of the non-wetting fluid, an individual phase can be occupied only if it is accessible to the invaded phase. For example, at high wetting phase saturations at the beginning of the drainage process, some of the larger pores that are allowed to the non-wetting phase at a given capillary pressure may be isolated from that phase by clusters of disallowed but accessible smaller pores occupied by the wetting fluid. Thus, a pore can be invaded only if it is part of the accessible fraction of allowed pores. Below a certain limit of allowable pores called the percolation threshold, none of the pores are accessible, i.e., a percolating or sample spanning cluster of pores must be allowable for any of the pores to be accessible. The percolation threshold, as a volume fraction of the pore space, is determined solely by the geometry and topology of the pore space and it is independent of the displaced and displacing fluids.

A Bethe lattice model (uniformly coordinated network with no reconnections) was used to specify the accessible fraction of pores as a function of the fraction of pores allowed to the non-wetting phase. The Bethe lattice model is particularly convenient because it yields an analytic form for the accessibility[7]

$$X^A(Q) = \begin{cases} Q[1 - (Q^*/Q)^{(2z-2)/(z-2)}] & Q \geq X_c \\ 0 & Q < X_c \end{cases} \tag{6}$$

where Q is the fraction of pores allowed to the advancing phase, X^A is the fraction of pores accessible to the advancing phase, X_c is the fraction of bonds required to form a percolating cluster, and z is the coordination number of the network. Here Q^* is the root of the following equation:

$$Q^*(1 - Q^*)^{z-2} - Q(1 - Q)^{z-2} = 0 \tag{7}$$

For a Bethe lattice, the percolating fraction is[7]

$$X_c = 1/(z - 1) \tag{8}$$

The non-wetting phase saturation, S_n, (volume fraction of porespace) is[5]

$$S_n(\Delta p, A, \sigma) = \frac{X^A(Q)\int_{r^*}^{\infty} p(r)s_n(\Delta p, A, \sigma, r)v_p(r)dr}{Q\int_0^{\infty} p(r)v_p(r)dr} \tag{9}$$

where r^* is the the smallest pore throat radius that satisfies Equation (5), Q is defined by

$$Q \equiv \int_{r^*}^{\infty} p(r)dr \ , \tag{10}$$

s_n is the microscopic non-wetting phase saturation in an individual pore, v_p is pore volume, and p(r) is the pore-size distribution.

Numerical Methods

The Galerkin/finite element formulation of the microscopic problem consists of three steps: (i) AYL equation is written in dimensionless form, (ii) the unknown mensiscus configuration is expanded in finite element basis functions, and (iii) the dimensionless form of the nonlinear AYL equation is written in weighted residual form. In addition a finite element basis set, a discretization scheme, and an iterative method to solve the nonlinear set of algebraic equations must be specified. For the current problem, we have selected linear basis functions,

both uniform and adaptive discretization[8] schemes, and a Newton-iterative method with a first-order adaptive continuation routine. The Newton iteration method is chosen because it results in rapid (quadratic) convergence. The first-order adaptive continuation scheme used in conjunction with Newton iteration, allows us to trace out solution branches in parameter space and locate turning points and other bifurcations. An adaptive step-sizing routine for the continuation scheme keeps the method within the tube of convergence surrounding the solution branch.

Equation (2) is reduced to dimensionless form through the specification of a characteristic length scale, L. We choose the pore throat radius to be the characteristic length and write the dimensionless form of the AYL equation as

$$2H^* + \frac{A^*}{h^{*3}} = \Delta p^* \tag{11}$$

where the dimensionless quantities are as follows:

$$\begin{aligned} H^* &= HL \quad A^* = A/L^2\sigma \\ h^* &= h/L \quad \Delta p^* = \Delta pL/\sigma \end{aligned} \tag{12}$$

For the remainder of Section 3, as a notational convenience we have suppressed the asterisks on the dimensionless quantities; all quantities are understood to be dimensionless.

The Galerkin/finite element forms of the AYL equation in the two coordinate systems are:

$$r_i = \begin{cases} \int\{ [f^{-1}(1 + f_z^2)^{-1/2} - (\Delta p - \Pi)] \phi^i + f_z\phi_z^i(1 + f_z^2)^{1/2}\}dz \\ \int\{[(2 - f_\theta^2 f^2)(f^2 + f_\theta^2)^{-1/2} - (\Delta p - \Pi)]\phi^i + f_\theta f^{-1}\phi_\theta^i(f^2 + f_\theta^2)^{-1/2}\}\sin\theta d\theta \end{cases} \tag{13}$$

where $f = \sum_i f_i\phi^i$ and $\{\phi_i\}$ is the set of finite element basis functions. The $\{f_i\}$ is the set of nodal values for the position of the meniscus, i.e., the the set of unknowns for the problem. A schematic of the domain and discretizations for the three problem geometries is presented in Figure 2.

It is more useful, however, to restate the AYL problem in terms of an energy principle. Such a formulation allows us to do stability analysis for the equilibrium menisci configurations. Following the approach of Huh[9], Brown and Scriven[10], and Marmur[11] for static fluid interfaces and Brown and Scriven[12] and Benner[13] for rotating drops, we define a mechanical energy functional, E, which has the following representation in cylindrical and spherical coordinates.

The quantities $\int U_{\alpha\beta\gamma}dz$ and $\int U'_{\alpha\beta\gamma}\sin\theta\, d\theta$ represent the solid-fluid interaction energy of a pore occupied by two-phases relative to that of a phase occupied by one-phase (wetting fluid). Expanding the meniscus position in the finite element

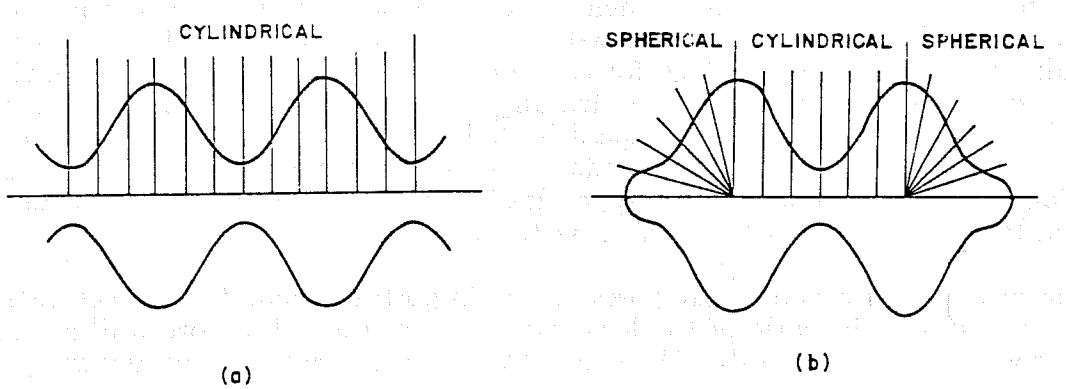

Figure 2. Schematic of the discretization scheme for the two menisci configurations.

$$E = \begin{cases} \int\{f(1+f_z^2)^{1/2} - f^2\Delta p/2 + U_{\alpha\beta\gamma}\}dz \\ \int\{f(f^2+f_\theta^2)^{1/2} - f^3\Delta p/3 + U'_{\alpha\beta\gamma}\}\sin\theta d\theta \end{cases} \tag{14}$$

basis functions and minimizing the functional with repect to the unknown coefficients of the expansion, we find that for $r_i' \equiv \partial E/\partial f_i$,

$$r_i' = \begin{cases} \int \{ [(1+f_z^2)^{1/2} + (\Pi - \Delta p)f]\phi_i + ff_z\phi^i(1+f_z^2)^{-1/2}\}dz \\ \int\{[(2f^2+f_\theta^2)(f^2+f_\theta^2)^{-1/2} + f^2(\Pi-\Delta p)]\phi^i + ff_\theta(f^2+f_\theta^2)^{-1/2}\phi_\theta^i\}\sin\theta d\theta \end{cases} \tag{15}$$

Stability is investigated by examining the eigenvalues of the Jacobian matrix, **J**

$$J_{ik} = \frac{\partial^2 E}{\partial f_i \partial f_k} \quad . \tag{16}$$

This approach to stability analysis highlights the utility of the finite element method. The Jacobian matrix is calculated as part of Newton's method to provide updated values for the unknowns (and solutions) based on a local linearization of the residual equations, and it also serves to provide stability information for these solutions.

Results and Discussion

Shape and Stability of Menisci in Idealized Pores

We have solved Equation (15) for two pore geometries and for several menisci configurations. In general, 40 quadratic elements were used to resolve the meniscus 'head' in spherical coordinates, and 25 quadratic elements were used per half-wavelength of a pore (e.g. for the dumbell shaped blob in Figure 2b, the number of elements is 40 + 25 = 65 leading to 131 equations). Convergence of the solution, as defined by the inequalities $\|r'\| < 10^{-8}$ for the residual vector and $\| \delta f \| < 10^{-8}$ for the solution update vector, was typically achieved in four iterations. All of the film profiles appearing in this paper were calculated at a reduced Hamaker constant value of $A^* = 10^{-4}$.

For axisymmetric sinusoidal pores, more important than the aspect ratio and pore length is the ratio of the local mean curvature of the pore wall at the pore throat and the pore body. We define the curvature ratio, κ, as follows:

$$\kappa \equiv H_{throat}/H_{body}.$$

We have studied menisci configurations in pores with aspect ratio four and with $\kappa > 1$ (pore wavelength, $\lambda = 20$ pore radii) and $\kappa < 1$ ($\lambda = 5$). In addition, we have examined the bicontinuous two-phase geometry and the discrete non-wetting phase geometry for up to four pore volumes for each of the two pore geometries. The results show that qualitatively different sequences of events lead to loss of stability, i.e. different transport mechanisms are at work for the two pore geometries. First, we consider the bicontinuous menisci solutions in these two pore geometries. The solution branches for the $\lambda = 5$ case are presented in Figure 3. The wetting phase saturation, S_w, is defined as the volume fraction of the porespace occupied by the wetting phase. The high wetting phase saturation branches (B, C, and D) all emanate from a cylindrical meniscus solution. The cylindrical mensicus is unstable with respect to Rayleigh disturbances, i.e. pinch-off points in the menisci profiles. In Figure 4, we show the development of pinch-off in these unstable menisci profiles.

Branch A represents a stable thin-film branch. Figure 5 shows a sequence of profiles that depict pronounced thickening of wetting layers in the pore body with small changes in the corresponding thicknesses at the pore throat. For the $\lambda = 5$ pore, $\kappa < 1$ and the mean curvature in the pore wall at the pore body is greater than at the pore throat. The films thicken first in the pore body as a consequence of the higher pore-wall curvature in that region.

Stability is lost at Point 1 on Branch A (Figure 3) with respect to a non-constant volume disturbance. The instability indicates that continued thickening of the wetting layer leads to a lower energy configuration. At Point 2, a second unstable mode appears in the solution and leads to choke-off at the pore throat with the wetting phase disconnecting the non-wetting phase. The sequence of profiles corresponding to the unstable region of branch A is depicted in Figure 6.

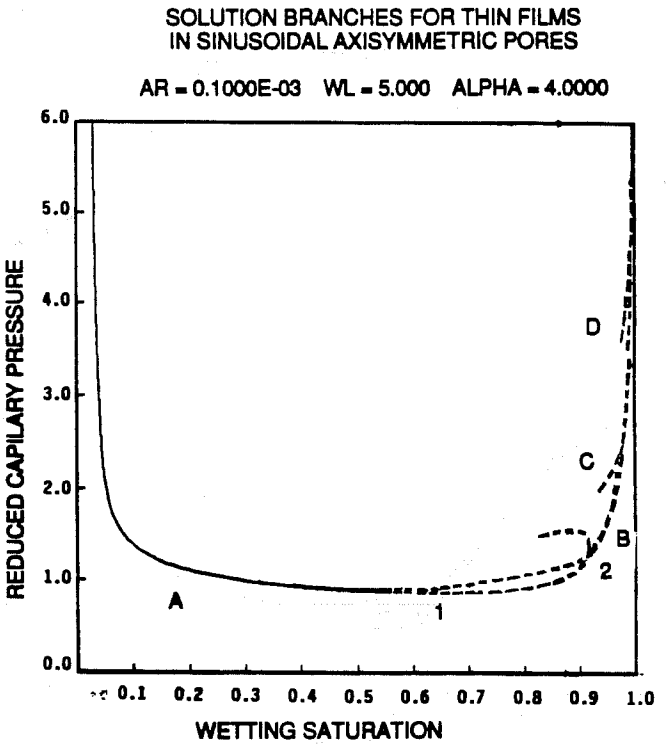

Figure 3. Solution branches for a bicontinuous meniscus in an axisymmetric pore with an aspect ratio of four and a pore length of five (unstable regions indicated by dashed curves).

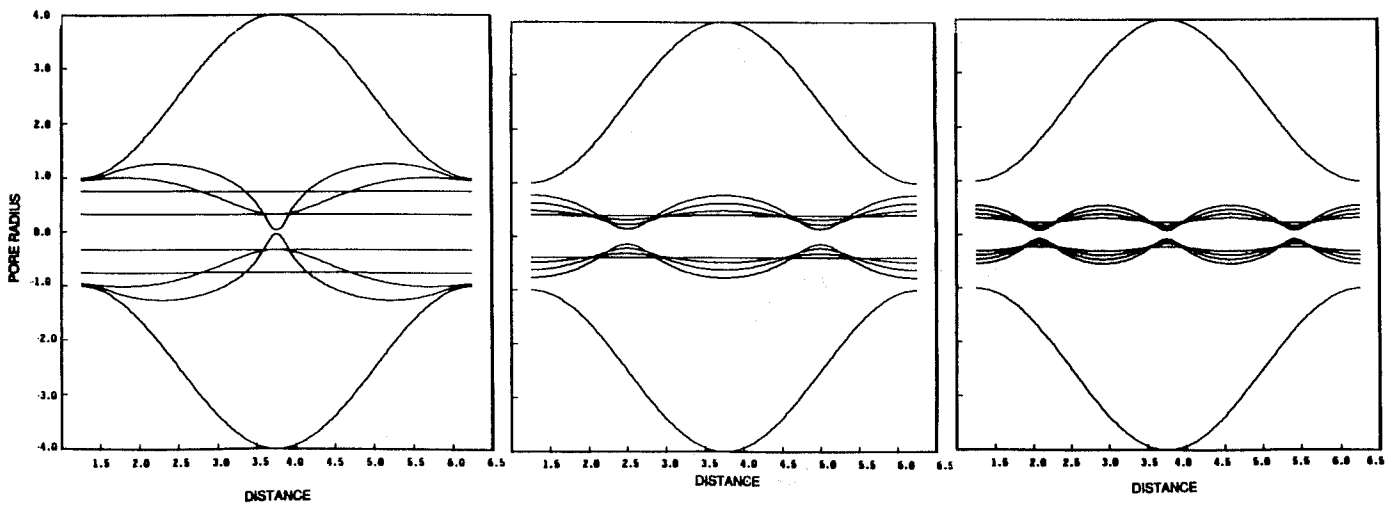

Figure 4. Unstable unduloidal variations in continuous menisci for (a) branch B, (b) branch C, and (c) branch D.

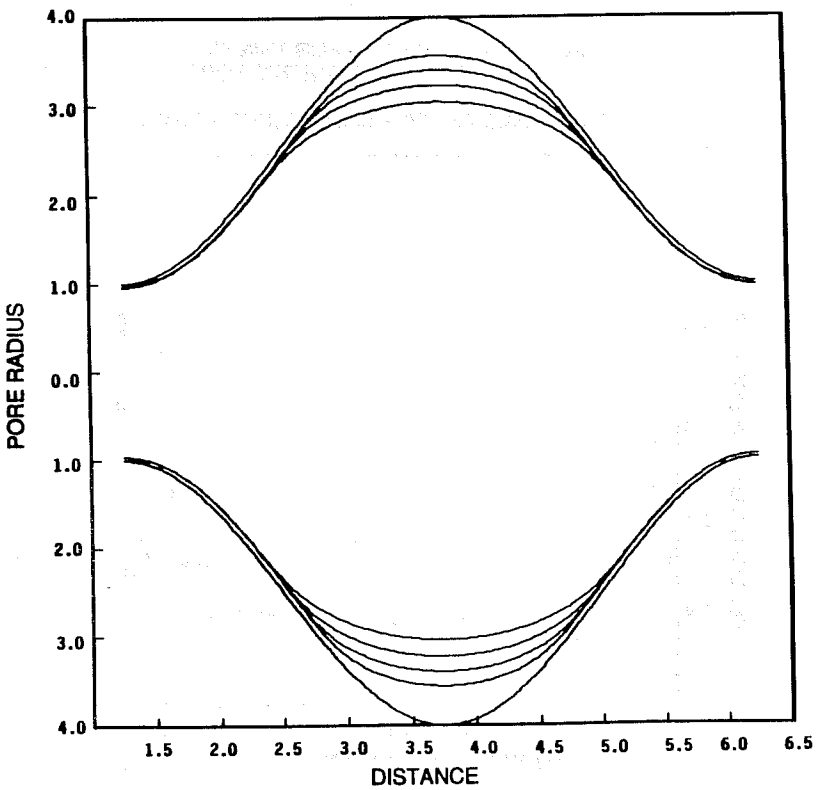

Figure 5. Menisci configurations corresponding to the stable portion of branch A in Figure 3.

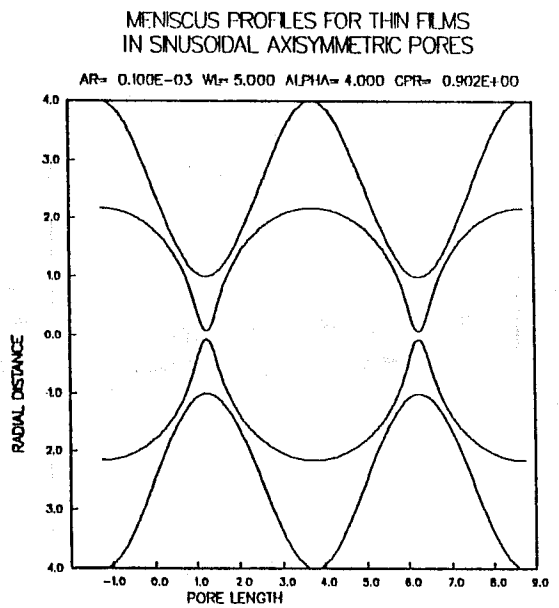

Figure 6. Unstable meniscus from branch A showing pinch-off developing at the pore throat.

In Figure 7, we present the solution branches corresponding to Branches A and B in Figure 3 for the $\lambda = 20$ pore geometry. It is immediately obvious that there are significant differences between these two figures. For the $\lambda = 20$ pore, a large gap exists between $S_w \sim 0.1$ and $S_w \sim 0.9$ in which no bicontinuous solutions exist. This result is quite different from the result for the $\lambda = 5$ pore in which Branches A and B form an almost continuous curve between $S_w = 0$ and $S_w = 1$.

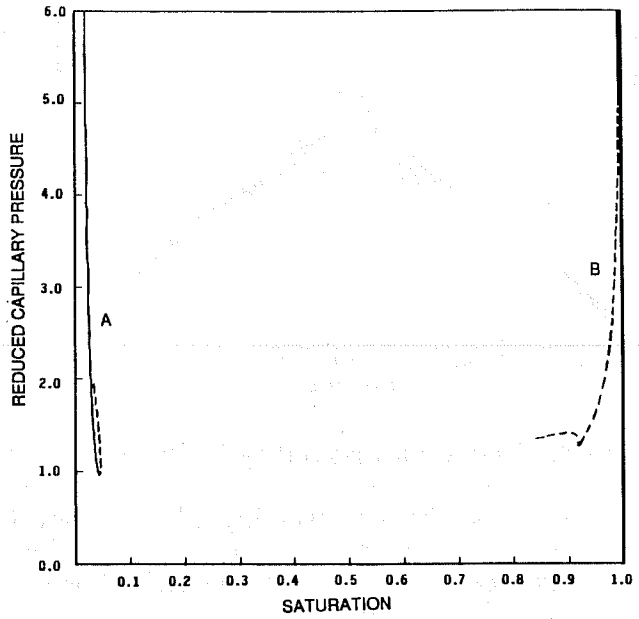

Figure 7. Solution branches for a bicontinuous meniscus in an axisymmetric pore with an aspect ratio of four and $\lambda = 20$ (unstable regions indicated by dashed curves).

The gap results from the increased curvature ratio for the $\lambda = 20$ pore. The wetting layers thicken primarily in the pore throats and the menisci become unstable with respect to the choke-off instability at branch A (in Figure 7). It is because the films thicken in the throats first that the instability is reached at a much lower wetting fluid saturation and the large gap is created. The onset and development of the choke-off instability is traced in Figure 8. These profiles are very similar to those calculated by Gauglitz[10] for a similar geometry using idealized flow equations.

The discontinuous or discrete non-wetting phase solutions to Equation (15) illustrate similar behavior, but in a somewhat different form. Solution branches for the two pore geometries are presented in Figures 9 and 10. In each case, two solution branches are plotted. The most obvious difference between the two is that the $\lambda = 5$ branches are continuous, whereas the $\lambda = 20$ branches are not. The discontinuity between branches for the $\lambda = 20$ geometry is again due to the choke-off instability.

The branches of discrete solutions for the $\lambda = 5$ geometry (Figure 9) represent symmetric expansions of blobs of non-wetting fluid about a pore body (Branch A) and a pore throat (Branch B). Examples of these profiles are shown in Figure 11. The maxima in these curves represents the capillary pressure required

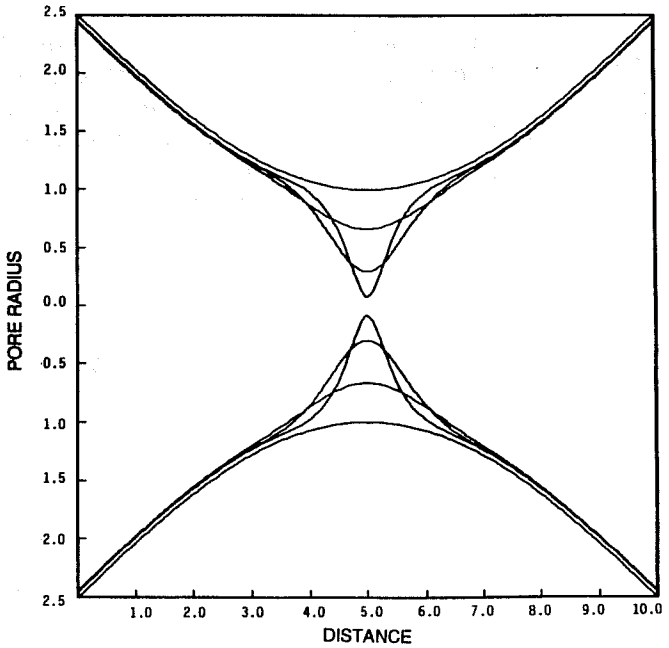

Figure 8. Choke off instability in Branch A.

to push the 'head' meniscus of the non-wetting phase front through the constriction at the pore throat. Advancing beyond the pore throat, the meniscus becomes unstable and advances rapidly into the neighboring pore in what is commonly referred to as a Haines jump. The decrease in capillary pressure for the advancing meniscus reflects the increase in the radius of curvature as it occupies the next pore (see Figure 12).

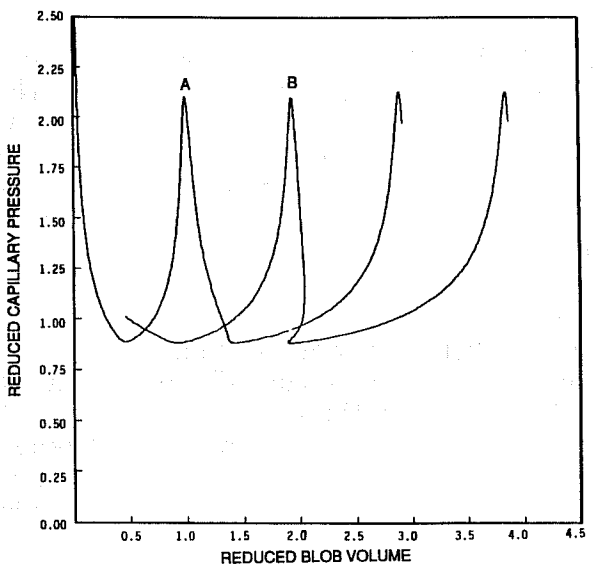

Figure 9. Branches of discrete solutions; $\lambda = 5$.

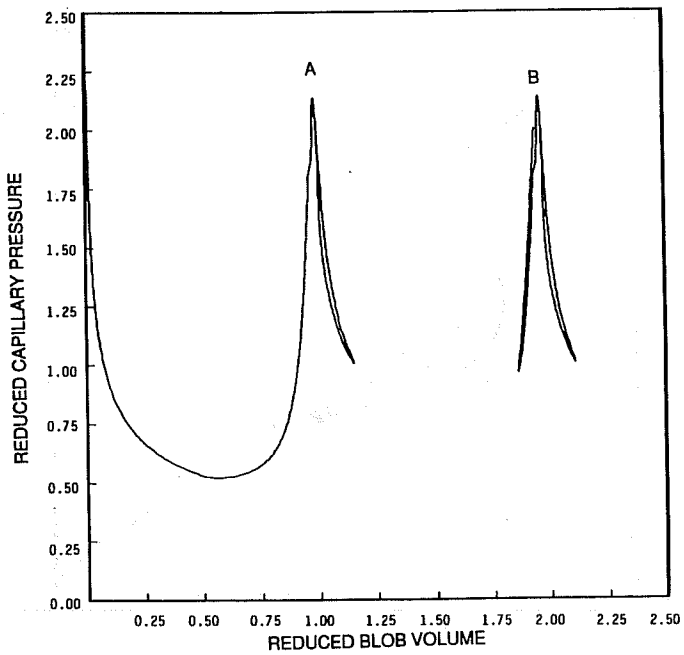

Figure 10. Branches of discrete solutions; $\lambda = 20$.

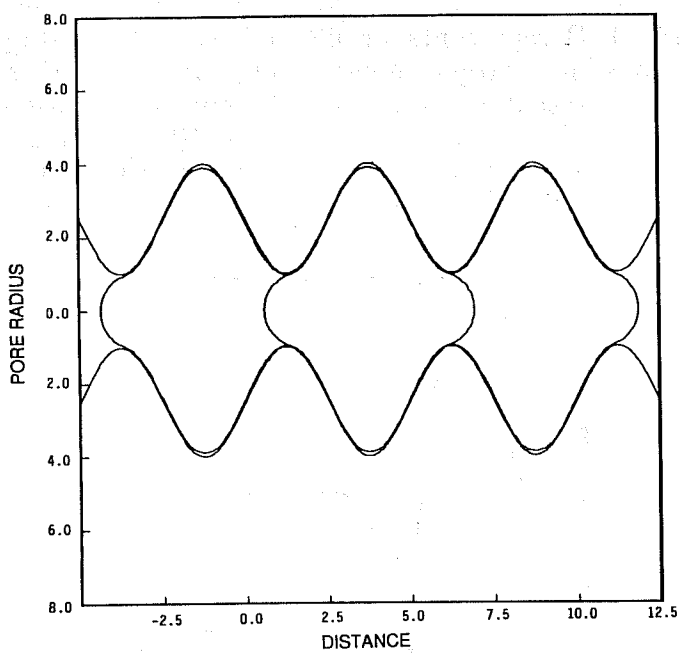

Figure 11. Discrete blob profiles from Figure 9 and Branch A.

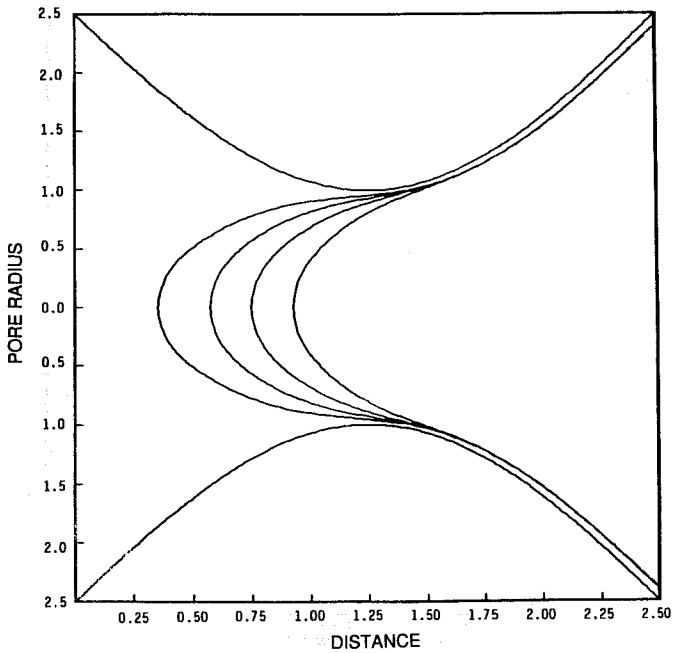

Figure 12. Onset of instability as meniscus advances beyond the pore throat.

Branches for the $\lambda = 20$ geometry are presented in Figure 10. Again, Branch A represents menisci profiles of blobs expanding symmetrically about a pore body, and Branch B represents profiles of blobs expanding about a pore throat. The solutions for larger non-wetting fluid volumes ($V_{nw} > 2.5$) corresponding to those presented for the $\lambda = 5$ geometry in Figure 9 also exist, but as isolated branches like Branch B in Figure 10. From a dumbell-shaped blob with $V_{nw} \sim 2$, both an increase and a decrease in the blob volume result in choke-off or fissioning of the blob at the pore throat (see Figure 14).

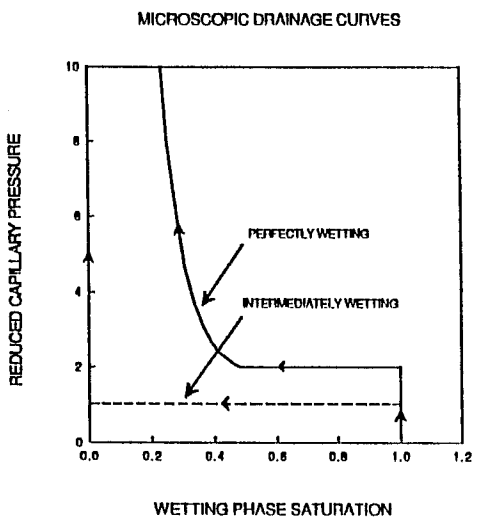

Figure 13. Microscopic drainage curves for perfectly wetting (solid) and intermediately wetting (dashed) fluids.

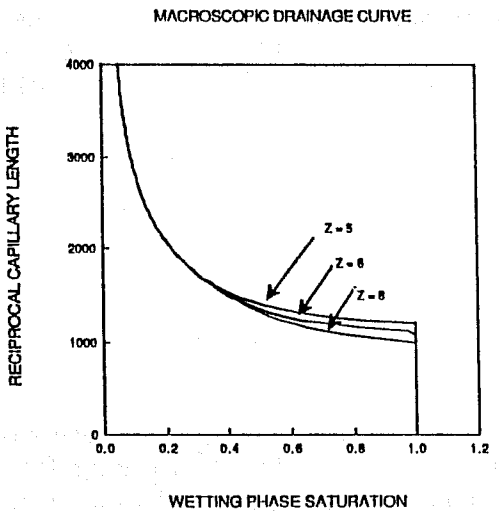

Figure 14. Drainage curves for $r_{max} = 10\mu$, coordination number z = 5, 6, 8.

These predictions indicate that for certain pore geometries (i.e. geometries in which $k > 1$) choke-off will occur behind an advancing front, leading to generation of a foam or emulsion , and behind a retreating front, acting to isolate clusters of non-wetting phase and preventing complete recovery of the retreating non-wetting phase.

Macroscopic Drainage Behavior

Having presented a detailed microscopic picture of the structure and stability of menisci in an idealized pore (or pores), we now use the statistical approach outlined in Section 2 to translate the microscopic menisci geometries into macroscopic properties of a porous medium. The microscopic (single pore) drainage curve for a perfectly wetting fluid ($\theta = 0^\circ$), corresponding to the solution branches presented in Figure 3, is represented in Figure 13 by the solid curve. Below $\Delta p^* = 2$, the entry level capillary pressure, the non-wetting phase is unable to invade the pore. Above that value, the non-wetting phase invades and leaves behind a stable wetting film (see solution branch 1 in Figure 3 and the mensci profiles in Figure 5). The analogous drainage curve for an intermediately wet fluid ($\theta = 45^\circ$) is represented by the dashed curve in Figure 13. For the intermediately wet case, a pore is either completely occupied by the wetting phase (below the invasion capillary pressure) or completely occupied by the non-wetting phase (above the invasion capillary pressure); no films or pendular structures exist in this case. Note also that in accordance with Equation (5), the invasion capillary pressure for the intermediately wet case is one-half that for the perfectly wet case.

These microscopic drainage curves for perfectly wetting fluids were calculated for values of the reduced Hamaker constant ranging from $A^* = 10^{-2}$ to $A^* = 10^{-10}$. For a solid-fluid system with known interfacial

tension and Hamaker constant and at a known applied capillary pressure, the pore throat radius uniquely determines the reduced values of the Hamaker constant and the capillary pressure and thus also uniquely determines the wetting saturation for an individual pore. Restating Equation (9) in terms of the dimensionless variables, we find

$$S_n = \frac{X^A(Q)\int_{r_*}^{\infty} p(r)s_n(\Delta p^*, A^*)v_p(r)dr}{Q\int_0^{\infty} p(r)v_p(r)dr} \qquad (17)$$

The microscopic saturation $s_n(\Delta p^*, A^*)_*$ is interpolated from microscopic capillary curves calculated for values for A^* ranging from $10^{-2}$to 10^{-10}. Using Equation (17), we can calculate the capillary drainage curve for a macroscopic medium with a known pore-size distribution (a Rayleigh distribution was used).

Four studies have been performed to determine the impact of pore-size distribution, aspect ratio, coordination number, and wettability on the predicted drainage behavior of the model. The results show that for all the cases studied with the sole exception of changes in wettability, variations in the input parameter produce no new qualitative features in the predicted drainage curves. In Figures 14-16, we summarize the quantitative comparisons for different coordination number, aspect ratio and pore-size distribution, respectively. Variations in coordination number affect the threshold capillary pressure. The higher the coordination number, the lower the percolation threshold and the lower the threshold capillary pressure required to create a percolating cluster of allowable pores (see Figure 14). We have also compared the predictions for cylindrical pores, aspect ratio equal to one, and pores with aspect ratio equal to four. As is shown in Figure 15, there are some small differences due to the shape of the pores. For the pore-size distribution, we used a Rayleigh distribution, $p(r) = 2\alpha r \exp\{-\alpha r^2\}$, where α is an adjustable parameter controlling the location of the peak of the pore-size distribution (r_{max}). In tighter media (smaller pore-sizes and larger α) the percolating cluster consists of smaller pores and thus the threshold capillary pressure must be higher (see Figure 16).

Comparisons between perfectly and intermediately wetting fluids (see Figure 17) show both qualitatively and quantitatively different drainage behavior, particularly at low wetting-phase saturations. There are two primary differences in the displacement curves: one at high wetting-phase saturations the other at low wetting-phase saturations. At high wetting-phase saturations, the threshold capillary pressure for the macroscopic displacement process is lower for the intermediately wet case, again as a consequence of Equation (7). A more profound difference exists at low wetting phase saturations. The difference in the predictions of the model at low wetting saturations reflects a difference in the dominant transport mechanisms near the wetting phase percolation threshold. For the intermediately wetting case, as the drainage process proceeds to low wetting- phase saturations, the non-wetting-phase displaces the wetting phase from increasingly smaller pores. Finally, when the wetting phase percolation

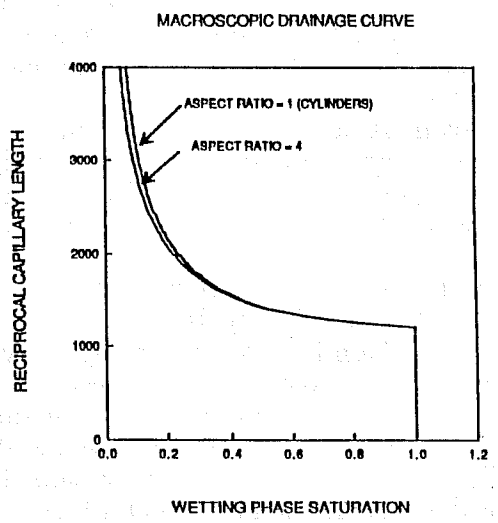

Figure 15. Drainage curves for pore aspect ratios of one and four

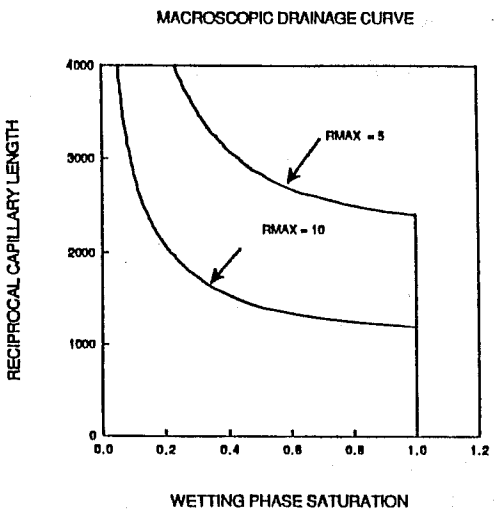

Figure 16. Drainage curves for z = 5 and $r_{max} = 10\mu m$ and $r_{max} = 5\mu m$.

threshold or irreducible wetting saturation is reached, the wetting phase exists only in isolated clusters and subsequent increases in capillary pressure produce no further reductions of the wetting phase saturation (the drainage curve becomes vertical). In contrast, for the perfectly wetting case, the wetting phase is completely connected throughout the porous medium. Clusters of occupied pores are never isolated; even at low saturations, clusters can drain through continuous film pathways along pore surfaces. Consequently, there is no irreducible wetting saturation for a perfectly wetting fluid. Such a fluid will continue to drain down to very low saturations at extremely high capillary pressures.

The crossover behavior in the drainage curves at the percolation threshold, seen in predictions of the statistical theory in Figure 17, have also been seen experimentally. Morrow[14] has found crossover of this type for displacement experiments in porous cores of sintered teflon. In these experiments the wetting fluids were either pentane, hexane, or heptane, and the intermediately wetting fluids were ethylene glycol and water. In the displacement tests, air was used as the non-wetting invading phase. An example of this behavior is shown in Figure 18. Our model predicts a much lower percolation threshold (crossover saturation) than was measured by Morrow. The discrepancy between the two is the result of the cubic dependence of the pore volume on the pore throat radius in the idealized pore geometry used here.

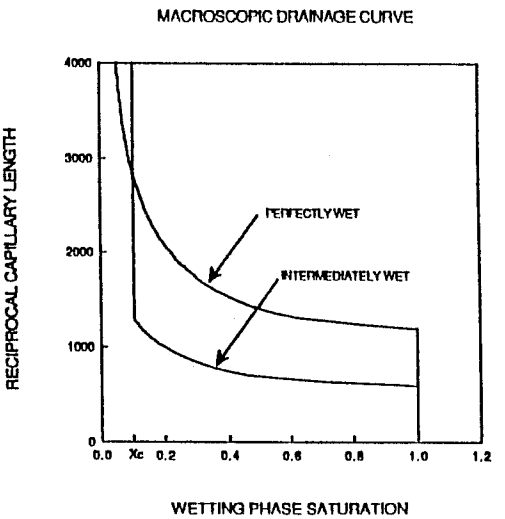

Figure 17. Macroscopic drainage curves for perfectly wetting (solid) and intermediately wetting (dashed) fluids; Xc is the percolation threshold.

Conclusions

In this paper, we have established two points: (i) the augmented Young-Laplace equation is a useful tool for studying equilibrium configurations of wetting menisci in idealized pore geometries and is also a probe of the stability of

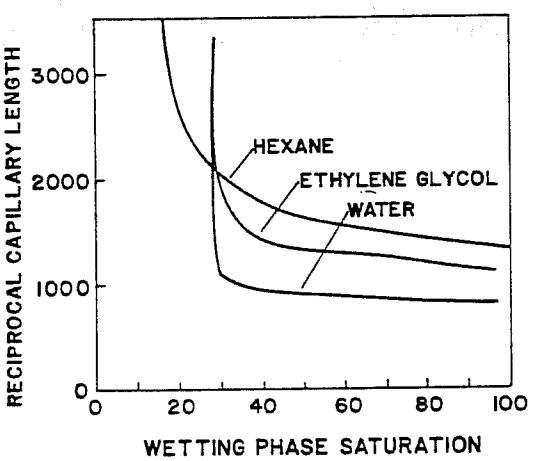

Figure 18. Drainage data for perfectly wetting and intermediately wetting fluids in sintered teflon cores, after Morrow[14] .

these menisci; and (ii) a statistical approach can be coupled to this or any other simple microscopic model to yield macroscopic predictions that qualitatively agree with experiment and which sheds light on the microscopic transport mechanisms responsible for the macroscopic experimental results. Displacement of an intermediately wet fluid is a percolative process that ends when the irreducible saturation (percolation threshold) is reached. In contrast, a perfectly wetting fluid drains through films and pendular structures along connected surface pathways beyond the percolation threshold. If these films become unstable as they thin, a surface percolative process will eventually limit the extent to which drainage can occur. Better agreement with theory can be achieved by a more judicious choice for the pore geometry.

References

1. Sweeney, J.B., Zasadzinski, J.A., Davis, H.T., and Scriven, L.E., to be submitted.
2. Deryaguin, B.V., Proc. 2nd Int. Congr. Surface Activity **2**, 609 (1957).
3. Deryaguin, B.V., Starov, V.M., and Churaev, N.V., Kolloinyi Zhurnal **38**, 875 (1976).
4. Philip, J.R., J. Chem. Phys. **66**, 5069 (1977).
5. Heiba, A.A., Davis, H.T., and Scriven, L.E., SPE 12172, presented at the 58th Annual Technical Conference, San Francisco,1983.
6. Everett, D.H. and Haynes, J.M., J. Coll. Interf. Sci. **38**, 125 (1972).
7. Fisher, M.E. and Essam, J.W., J. Math. Phys. **2**, 609 (1961).
8. Sweeney, J.B., Davis, H.T., and Scriven, L.E., to be submitted.
9. Huh, C., Ph.D. Thesis, University of Minnesota, unpublished (1969).
10. Brown, R.A. and Scriven, L.E., J. Coll. Interf. Sci. **78**, 528 (1980).

11. Marmur, A., J. Coll. Interf. Sci. **93**, 18 (1983).
12. Brown, R.A. and Scriven, L.E. Proc. R. Soc. Lond. A **371**, 331-357, 1980.
13. Benner, R.E., Ph.D. Thesis, University of Minnesota, unpublished (1983).
14. Morrow, N.R., J. Canad. Pet. Technol. **15**, 49 (1976).

5. THEORY AND COMPUTER SIMULATION OF STRUCTURE, TRANSPORT AND FLOW OF FLUID IN MICROPORES

Synopsis

An overview is given of recent progress made in our laboratory on this topic. The density profiles of fluid in micropores are found by solving numerically an approximate Yvon-Born-Green equation. A related local average density model (LADM) allows prediction of transport and flow in inhomogeneous fluids from density profiles. A rigorous extension of the Enskog theory of transport is also outlined. Simple results of this general approach for the tracer diffusion and Couette flow between planar micropore walls are presented. Equilibrium and flow (molecular dynamics) simulations are compared with the theoretical predictions. Simulated density profiles of the micropore fluid exhibit substantial fluid layering. The number and sharpness of fluid layers depend sensitively on the pore width. The solvation force and the pore average density and diffusivity are oscillating functions of the pore width. The theoretical predictions for these quantities agree qualitatively with the simulation results. The flow simulations indicate that the flow does not affect the fluid structure and diffusivity even at extremely high shear rates ($10^{10}s^{-1}$). The fluid structure induces large deviations of the shear stress and the effective viscosity from the bulk fluid values. The flow velocity profiles are correlated with the density profiles and differ from those of a bulk fluid. The LADM and extended Enskog theory predictions for the velocity profiles and the pore average diffusivity agree very well with each other and with the simulation results. The LADM predictions for the shear stress and the effective viscosity agrees fairly well with the simulation results.

Examples of fluids confined in pores and spaces of molecular or nanometer dimensions abound in technological and natural products and processes. These include wetting and lubrication, zeolite-supported catalysis, silica gel based chromatrographic separations, drying of paper products and clay dispersions, aggregation of colloids, permeation of Vicor and other sintered glasses, the formation of soap films, foams and emulsions, and water or oil rich zones in lytropic liquid crystals and vesicular bilayer structures. In such confinement the fluids can be strongly inhomogeneous and so the usual theories of fluid structure and dynamics may not be applicable. Owing to the molecular dimensions involved, experimental characterization of fluid in micropores is also difficult. Thus, computer simulation on model systems becomes an important tool to test ideas and supplement experiments on real systems in trying to understand the behavior of fluids confined on the nanometer scale.

In this paper, we report recent progress made in our laboratory in using molecular theory and computer simulation to understand the structure, flow and transport of fluids confined by planar solid walls separated by a few molecular diameters.

Molecular Theory of Structure and Transport

Equilibrium Theory of Fluid Structure

In all the theoretical work reported herein, we assume that the particles interact with pair additive forces whose pair potentials can be approximated by

$$u(s) = u_R(s) + u_A(s) , \tag{1}$$

where

$$\begin{aligned} u_R(x) &= \infty , \quad s < \sigma \\ &= 0 , \quad s > \sigma \end{aligned} \tag{2}$$

and $u_A(s)$ is the continuous, attractive part of the pair potential. The pore walls confining the fluid will be represented by the conservative potential $u^e(\mathbf{r})$. At equilibrium the density $n(\mathbf{r})$ of the fluid obeys the Yvon-Born-Green (YBG) equation

$$k_B T \nabla n + n \nabla u^e - n \int n(\mathbf{r}+\mathbf{s}) g(\mathbf{r}, \mathbf{r}+\mathbf{s}) \frac{\mathbf{s}}{s} u_A'(s) d^3 s$$

$$+ n k_B T \int n(\mathbf{r} + \sigma \mathbf{k}) g(\mathbf{r}, \mathbf{r} + \sigma \mathbf{k}) \sigma^2 \mathbf{k} d^2 k = 0 . \tag{3}$$

where $g(\mathbf{r},\mathbf{r}')$ is the pair correlation function, k_B is Boltzmann's constant and T is the absolute temperature. $\mathbf{k}$ is a unit vector lying along the line of centers of a pair of molecules in contact. d^2k denotes an element of solid angle associated with $\mathbf{k}$.

Equation 3 is exact for fluids obeying Equations. 1 and 2. However, in order to compute the density $n(\mathbf{r})$ from the YBG equation one must know the relationship between density distribution and the pair correlation function of inhomogeneous fluid. Such a relationship is not available in general. However, an approximation introduced by Fischer and Methfessel[1] has been shown to give fairly accurate predictions of the density profiles in liquid-vapor and liquid-solid interfaces. It has also been shown that their approximation gives the exact density distribution for one-dimensional hard rods in an external potential u^e. The main assumption of Fischer and Methfessel is that the pair correlation function can be approximated as

$$g(\mathbf{r},\mathbf{r}+\mathbf{s}) = g^o(s;\bar{n}(\mathbf{r} + \tfrac{1}{2}\mathbf{s})) , \tag{4}$$

where g^o is the correlation function of homogeneous fluid and $\bar{n}$ is a local average density defined by

$$\bar{n}(\mathbf{r}) = \frac{1}{(\pi\sigma^3/6)} \int_{R < \sigma/2} n(\mathbf{r} + \mathbf{R}) d^3R \ . \tag{5}$$

Equation 4 renders the YBG equation solvable. However, as did Fischer and Methfessel, we shall further simplify the theory by making the van der Waals' structureless fluid approximation ($g = 0$, $s < \sigma$, $g = 1$, $s > \sigma$) in the integral involving the long-ranged continuous force u_A'. The YBG equation thus becomes

$$\nabla[k_BT\ln n + u^e + \int n(\mathbf{r}+\mathbf{s})u_A(s)d^3s] + k_BT\int g^o(\sigma;\bar{n}(\mathbf{r}+\frac{\sigma}{2}\mathbf{k})\sigma^2\mathbf{k}d^2k = 0 \ . \tag{6}$$

To finally complete the model a formula for the contact value of the pair correlation function g^o must be given. We choose the Carnahan formula

$$g^o(\sigma;\bar{n}) = \frac{1 - \frac{\pi}{12}\sigma^3\bar{n}}{(1 - \frac{\pi}{6}\sigma^3\bar{n})^3} \ , \tag{7}$$

shown by Carnahan and Starling[2] to be accurate in hard sphere fluids.

In the calculations to be reported in what follows we shall consider planar systems, i.e., flat pore walls so that $u^e = u^e(x)$ and $n = n(x)$, where x is the distance from a pore wall. In this case Equation 6 can be integrated to give

$$\mu^* = l\ln n(x) + \frac{1}{k_BT}\int_{-\infty}^{+\infty} n(x')\bar{u}_A(x - x')dx'$$

$$+ 2\pi\sigma^2\int_0^x dx'\int_{-1}^{1} d\zeta\zeta n(x' + \sigma\zeta)g(\bar{n}(x' + \frac{1}{2}\sigma\zeta)) - \frac{u^e(x)}{k_BT} \tag{8}$$

where

$$\bar{n}(x) = (6/\sigma^3)\int_{-\sigma/2}^{+\sigma/2} (.25\sigma^2 - (x - x')^2)n(x')dx' \tag{9}$$

The parameter μ^* is the constant of integration. It plays the role of the chemical potential.

The external potential, $u^e(x)$, arises from the solid walls at $x = 0$ and $x = h$.

$$u^e(x) = \phi_w(x) + \phi_w(h - x) \tag{10}$$

where each wall exerts a 10-4-3 potential[3]:

$$\phi_w = \epsilon_w \left[\left(\frac{2}{5}\right)\left(\frac{\sigma_w}{x}\right)^{10} - \left(\frac{\sigma_w}{x}\right)^4 - \frac{\sqrt{2}\sigma_w^3}{3(x + \frac{0.61\sigma_w}{\sqrt{2}})^3} \right], \quad x > 0 \tag{11}$$

ϵ_w and σ_w are characteristic wall-fluid particle energy and separation distance parameters.

The fluid-fluid intermolecular potential,

$$\bar{u}_A(x) = \int_{-\infty}^{+\infty} \int u^A(s) dy dz \tag{12}$$

is taken to be

$$\begin{aligned} \bar{u}_A(x) &= -2\pi\epsilon\sigma^2, \quad |x| < \sigma \\ &= -\frac{2\pi\epsilon\sigma^6}{x^4}, \quad |x| > \sigma \end{aligned} \tag{13}$$

This corresponds to the attractive part of a "6 - ∞" Lennard-Jones potential; namely,

$$\begin{aligned} u^A(s) &= -4\epsilon\left(\frac{\sigma}{s}\right)^6, \quad s > \sigma \\ &= 0, \quad s < \sigma \end{aligned} \tag{14}$$

The normal pressure P_N in the fluid confined between the walls varies with wall separation and is not, in general, equal to the bulk pressure P_B of fluid at the same chemical potential. The difference $P_N - P_B$ is the solvation force per unit area,[4] f_s, and can be calculated from the equilibrium density profiles by

$$f_s = -\int_0^h n(x)\frac{d\phi_w(x)}{dx}dx + \int_0^\infty n(x)\frac{d\phi_w(x)}{dx}dx \tag{15}$$

The equilibrium density profiles are obtained by solving Equations 8 and 9 for a modified density $n^*(x)$, where

$$n^*(x) = n(x)e^{u^q(x)/kT}, \tag{16}$$

This modified density is a more slowly varying function of x than the density. The domain of interest, $0 < x < h$, is discretized uniformly and the trapezoidal rule is used to evaluate the integrals in Equations 8 and 9. This results

in a system of nonlinear, coupled, algebraic equations for the nodal values of n^* and $\bar{n}$. Newton's method is used to solve for n^* and $\bar{n}$ simultaneously. The domain is discretized finely enough so that the solution changes negligibly with further refinement. A mesh size of 0.05σ was adopted in our calculations.

Solutions were obtained initially for a wall separation $h = 40\sigma$, where at the midpoint the density is equal to the bulk fluid density, n_b. Then, solutions for decreasing pore width were found using the previous solution at larger h as a first guess for the next width. Pore width was gradually decreased to $h = 2.25\sigma$ using small enough steps to ensure that quadratic convergence was observed at each new pore width. Step sizes ranged from a few σ's to 0.05σ.

Local Average Density Model (LADM) of Transport

In the spirit of the Fischer-Methfessel local average density model, Equation 4, for the pair correlation function of inhomogeneous fluid, a local average density model (LADM) of transport coefficients has been proposed[5] whereby the local value of the transport coefficient, $\lambda(\mathbf{r})$, is approximated by

$$\lambda(\mathbf{r}) = \lambda^\circ(\bar{n}(\mathbf{r})). \tag{17}$$

$\lambda^\circ(\bar{n}(\mathbf{r}))$ is the transport coefficient of homogeneous fluid at the local average density $\bar{n}(\mathbf{r})$.

According to this model the diffusivity of a molecule at position x in the planar pore system of interest in this paper is $D^\circ(\bar{n}(x))$ and so the pore diffusivity is

$$D_{pore} = \int_0^h n(x)D^\circ(\bar{n}(x))dx \Big/ \int_0^h n(x)dx \quad , \tag{18}$$

since $D^\circ(\bar{n}(x))n(x)Adx/N$ is the probable diffusivity of a particle lying between x and $x + dx$ in the pore.

The stress tensor $\boldsymbol{\tau}$ according to LADM is

$$\tau(\mathbf{r}) = \frac{\eta^\circ(\bar{n}(\mathbf{r}))}{2}\left[\nabla\bar{\mathbf{v}} + \nabla\bar{\mathbf{v}}^T\right] + [\eta_b^\circ(\bar{n}(\mathbf{r})) - \frac{2}{3}\eta^\circ(\bar{n}(\mathbf{r}))]\nabla\cdot\bar{\mathbf{v}}\mathbf{I} \tag{19}$$

where $\bar{\mathbf{v}}$ is the mean flow velocity, $\nabla\bar{\mathbf{v}}^T$ is the transpose of $\nabla\bar{\mathbf{v}}$, $\eta^\circ(\bar{n})$ and $\eta_b^\circ(\bar{n})$ the shear and bulk viscosity coefficients of homogeneous fluid at density $\bar{n}$.

The attractive feature of LADM is that once the fluid structure is known (e.g., by solution of the YBG equations given in the previous section or by a computer simulation) then theoretical or empirical formulas for the transport coefficients of homogeneous fluids can be used to predict flow and transport in inhomogeneous fluid. For diffusion and Couette flow in planar pores LADM turns out to be a surprisingly good approximation, as will be shown later.

Enskog Theory of Transport

Enskog's theory of hard spheres, with introduction of a temperature dependent hard sphere diameter, gives surprisingly accurate estimates of the diffusivity and viscosity of real fluids[6]. This is because in simple fluids the short-ranged repulsive forces between molecules dominate in the collisional dissipation leading to transport phenomena. The long-ranged attractive interactions contribute importantly to the energy of the fluid, and thus to phase transitions and interfacial structure, but apparently are less effective in collisional dissipation. With this view of fluid behavior Enskog's theory of transport in bulk fluid has been generalized to strongly inhomogeneous fluids.

Consider a fluid of molecules interacting with pair additive, centrally symmetric forces in the presence of an external field and assume that the collisional contribution to the equation of motion for the singlet distribution function is given by Enskog's theory. In a multicomponent fluid, the distribution function $f_i(\mathbf{r},\mathbf{v}_i,t)$ of a particle of type i at position $\mathbf{r}$, with velocity $\mathbf{v}_i$ at time t obeys the equation of change[7]

$$\frac{\partial f_i}{\partial t} + \mathbf{v}_i \cdot \nabla f_i - \frac{1}{m_i} \nabla u_i^e \cdot \nabla_{\mathbf{v}_i} f_i$$

$$- \sum_j \frac{1}{m_i} \int \nabla u_{ij}^A(r-r') \cdot \nabla_{\mathbf{v}_i} f_i f_j g_i(r,r',t)\, d^3r' d^3v_j$$

$$= \sum_j \int_{\mathbf{v}_{ji}\cdot\mathbf{k} > 0} \left[g_{ij}(\mathbf{r},\mathbf{r}+\sigma_{ij}\mathbf{k}) f_i(\mathbf{r},\mathbf{v}^{i\prime},t) f_j(\mathbf{r}+\sigma_{ij}\mathbf{k},\mathbf{v}_j',t) \right.$$

$$\left. - g_{ij}(\mathbf{r},\mathbf{r}-\sigma_{ij}\mathbf{k}) f_i(\mathbf{r},\mathbf{v}_i,t) f_j(\mathbf{r}-\sigma_{ij}\mathbf{k},\mathbf{v}_j,t) \right] \sigma_{ij}^2 \mathbf{v}_{ji}\cdot\mathbf{k}\, d^2k d^3v_j \quad , \tag{20}$$

where ∇ and $\nabla_{\mathbf{v}_i}$ are gradient operators with respect to $\mathbf{r}$ and $\mathbf{v}_i$, m_i molecular mass, u_i^e the potential of the external force, u_{ij}^A the pair potential of attractive forces between particles of types i and j, g_{ij} the pair correlation function between i and j, $\sigma_{ij} \equiv (\sigma_{ii} + \sigma_{jj})/2$, σ_{ii} the hard sphere diameter of i, $\mathbf{k}$ a unit vector directed from the center of i to that of j, and $\mathbf{v}_i'$ the velocity of i after a hard-sphere collision with j. We recall that $\mathbf{v}_i' = \mathbf{v}_i - \mathbf{v}_{ij}\cdot\mathbf{kk}$, where $\mathbf{v}_{ij} \equiv \mathbf{v}_i - \mathbf{v}_j$[7]. The attractive interaction u_{ij}^A is assumed to be sufficiently slowly varying that it does not contribute to collisional dissipation.

The local density n_i of species i is related to the velocity distribution function by

$$n_i(\mathbf{r},t) = \int f_i(\mathbf{r},\mathbf{v}_i,t) d^3v_i \tag{21}$$

At equilibrium the distribution function is of the form

$$f_i = n_i(\mathbf{r})\phi_i(\mathbf{v}_i) \tag{22}$$

where ϕ_i is the Maxwell velocity distribution function,

$$\phi_i(\mathbf{v}_i) = \left(\frac{m_i}{2\pi k_B T}\right)^{3/2} \exp(-\, m_i v_i^2/2k_B T). \tag{23}$$

With this distribution function, velocity factors out of Equation 20 yielding the exact YBG equation, Equation 3, for equilibrium fluids whose interaction potential is given by Equation 1.

The Chapman-Enskog method has been used to solve for steady state tracer diffusion[8]. According to the method the singlet distribution function for the diffusing species 1, present in a trace amount ($n_1 \ll n_i$, $i \neq 1$) in an otherwise equilibrium fluid, is approximated by

$$f_1 = n_i(\mathbf{r})\phi_1(\mathbf{v}_1)\,[\,1 + \mathbf{a}_1(\mathbf{r})\cdot\mathbf{v}_1\,] \tag{24}$$

and $\mathbf{a}_1(\mathbf{r})$ is obtained from the Enskog equation. The result for the linearized diffusion flux $\mathbf{J}_1$ of species 1:

$$\mathbf{J}_1 = \int f_1 \mathbf{v}_1 d^3v_1 = -\, n_1^\circ k_B T \zeta_1^{-1} \cdot \nabla ln(n_1/n_1^\circ) \tag{25}$$

where ζ_1 is the friction tensor,

$$\zeta_1(\mathbf{r}) = \sum_{j\neq 1} \frac{m_1}{\pi}\left(\frac{2\pi k_B T}{m_{1j}}\right)^{1/2} \int g_{1j}(\mathbf{r},\mathbf{r}+\sigma_{1j}\mathbf{k}) n_j^\circ(\mathbf{r}+\sigma_{1j}\mathbf{k})\sigma_{1j}^2 \mathbf{k}\mathbf{k} d^2k\,, \tag{26}$$

$m_{1j} \equiv m_1 m_j/(m_1+m_j)$, $g_{1j}(\mathbf{r},\mathbf{r}+\sigma_{1j}\mathbf{k})$ the equilibrium pair correlation function, $n_1^\circ(\mathbf{r})$ the equilibrium density distribution of species 1, and $n_1(\mathbf{r})$ the diffusive density distribution.

As expected from continuum theory, the friction and diffusion coefficients are replaced in inhomogeneous fluid by tensors whose symmetry reflects that of the inhomogeneous media.

For the special case of self-diffusion (tracer molecules dynamically identical to solvent molecules) in the y-direction in a planar pore, it follows from Equation 25 that the pore average flux obeys[9]

$$J_{pore} = \frac{1}{h}\int_o^h J_{1y} dx = -\, D_{pore}\frac{dn_{pore}}{dx} \tag{27}$$

where $n_{pore} = h^{-1}\int_o^h n_1 dx$ and

$$D_{pore} = \int_0^h D_T(x) n^\circ(x) dx \Big/ \int_0^h n^\circ(x) dx \quad . \tag{28}$$

$D_T(x)$, the local diffusivity parallel to the pore walls, is given by

$$D_T(x) = \frac{(k_B T/\pi m)^{1/2}}{4\sigma^2 \int_{-1}^{1} g^\circ(\sigma, \bar{n}^\circ(x + \frac{\sigma}{2}\xi)) n^\circ(x + \sigma\xi)(1 - \xi^2) d\xi} \quad , \tag{29}$$

a result enabling one to calculate the pore diffusivity from the equilibrium density distribution function.

Equation 28 is similar to the LADM formula for pore diffusivity, except that in LADM $D_T(x)$ is replaced by

$$D^\circ(\bar{n}(x)) = \frac{(k_B T/\pi m)^{1/2}}{(8\sigma^2/3) g^\circ(\sigma, \bar{n}(x)) \bar{n}(x)} \tag{30}$$

The Chapman-Enskog theory of flow in a one-component fluid yields the following approximation to the momentum balance equation[10].

$$n\partial_t \bar{\mathbf{v}} + n\bar{\mathbf{v}} \cdot \nabla \bar{\mathbf{v}} + \frac{n}{m} \nabla u^e - \nabla \cdot \mathbf{P} = - \mathbf{M}_1 : \nabla \bar{\mathbf{v}} + \mathbf{M}_2 : \nabla \nabla \bar{\mathbf{v}} \quad , \tag{31}$$

where $\mathbf{P}$ is the local pressure tensor and $\mathbf{M}_1$ and $\mathbf{M}_2$ are third and fourth rank tensors accounting for viscous dissipation. In isotropic fluid $\mathbf{P} = P\mathbf{I}$, $\mathbf{I}$ the unit tensor, $\mathbf{M}_1 = 0$ and $\mathbf{M}_2$ is a fourth rank isotropic tensor. The symmetries of $\mathbf{P}$, $\mathbf{M}_1$ and $\mathbf{M}_2$ depend on the symmetry of the inhomogeneous fluid. The general Chapman-Enskog formulas for $\mathbf{M}_1$and $\mathbf{M}_2$ are very complicated and will not be recorded here. However, if the deviation of the velocity distribution function from its local Maxwellian form ($\phi = (m/2\pi k_B T)^{3/2} \exp[- m(\mathbf{v} - \bar{\mathbf{v}}(r))^2/k_B T]$) is neglected, the following relatively simple formulas are obtained[10]

$$\mathbf{M}_1(\mathbf{r}) = \left(\frac{m k_B T}{\pi}\right)^{1/2} \sigma^3 n(\mathbf{r}) \int n(\mathbf{r} + \sigma\mathbf{k}) g(\mathbf{r}, \mathbf{r} + \sigma\mathbf{k}) \mathbf{kkk} d^2k \tag{32}$$

$$\mathbf{M}_2 = \left(\frac{m k_B T}{\pi}\right)^{1/2} \sigma^4 n(\mathbf{r}) \int n(\mathbf{r} + \sigma\mathbf{k}) g(\mathbf{r}, \mathbf{r} + \sigma\mathbf{k}) \mathbf{kkkk} d^2k \quad . \tag{33}$$

These formulas become increasingly better approximations as the density increases[11].

For the steady, planar Couette flow to be examined in a later section, the momentum balance equation yields

$$n\frac{du^e}{dx} + \frac{dP_N}{dx} = 0 \tag{34}$$

and

$$0 = M_1(x)\frac{\partial \bar{v}_y}{\partial x} + M_2(x)\frac{\partial^2 \bar{v}_y}{\partial x^2} \quad , \tag{35}$$

where

$$M_1(x) = 2(\pi m k_B T)^{1/2}\sigma^3 n(x)\int_{-1}^{1} n(x + \sigma\xi)g(\sigma;x,x + \sigma\xi)(1 - \xi^2)\xi d\xi \tag{36}$$

$$M_2(x) = (\pi m k_B T)^{1/2}\sigma^4 n(x)\int_{-1}^{1} n(x + \sigma\xi)g(\sigma;x,x + \sigma\xi)(1 - \xi^2)\xi^2 d\xi \tag{37}$$

It can be shown that Equation 34 is the YBG equation determining the density distribution n(x) of the fluid. With the Fischer-Methfessel closure, the density distribution is all that is needed to calculate the coefficients $M_1(x)$ and $M_2(x)$. Integrating Equation 35, we find

$$\bar{v}_y(x) = \bar{v}_y(o) + [\bar{v}_y(h) - \bar{v}_y(o)]\frac{\int_o^x dx'' Q(x'')}{\int_o^h dx'' Q(x'')} \tag{38}$$

where

$$Q(x'') = \exp\left[-\int_o^{x''} dx' M_1(x')/M_2(x')\right] . \tag{39}$$

LADM also leads to Equation 35, but with $M_1 = d\eta^\circ(\bar{n}(x))/dx$ and $M_2 = \eta^\circ(\bar{n}(x))$, which yields

$$\bar{v}_y(x) = \bar{v}_y(o) + [\bar{v}(h) - \bar{v}_y(o)]\frac{\int_o^x dx''[\eta^\circ(\bar{n}(x''))]^{-1}}{\int_o^h dx''[\eta^\circ(\bar{n}(x''))]^{-1}} \quad . \tag{40}$$

The theories of structure and transport outlined above will be compared with molecular dynamics in what follows.

Molecular Dynamics

Equilibrium Simulation

The equilibrium simulations described here were carried out by Magda *et al.*[12]. The pore walls modelled are two flat, semi-infinite solids separated by a distance h in the x-direction. The wall-fluid potential is the 10-4 or 10-4-3 potential, i.e.,

$$\phi_w(x) = \epsilon_w \left\{ 0.4(\sigma_w/x)^{10} - (\sigma_w/x)^4 + \frac{\sqrt{2}\delta}{3(x/\sigma_w + 0.61/\sqrt{2})^3} \right\} , \qquad (41)$$

where $\delta = 1$ in some simulations and $\delta = 0$ in others. The particle-particle potential energy is chosen to be the truncated 6-12 Lennard-Jones potential

$$\begin{aligned} u(r) &= \phi_{LJ}(r) - \phi_{LJ}(r_e) , \quad && r < r_e \\ &= 0 , && r > r_e \end{aligned} \qquad (42)$$

where

$$\phi_{LJ}(r) = 4\epsilon \left[\left(\frac{\sigma}{r} \right)^{12} - \left(\frac{\sigma}{r} \right)^{6} \right] \qquad (43)$$

ϵ and σ are energy and particle size parameters and r_e is the truncation distance (typically taken to be 2.5 to 3.5σ in computer simulations).

The temperature, pore width and average pore densities were the same as those used by Snook and van Megen in their Monte Carlo simulations, which were performed for a constant chemical potential[13]. Periodic boundary conditions were used in the y and z directions. The periodic length was chosen to be twice r_e. Newton's equations of motion were solved using the predictor-corrector method developed by Beeman[14]. The local fluid density was computed form

$$n(x) = \frac{1}{A} \frac{dN}{dx}(0 \rightarrow x) , \qquad (44)$$

where A is the area of a pore wall and $N(0 \rightarrow x)$ is the long time average of the number of molecules found between 0 and x. The normal pressure exerted by the fluid on the pore wall was computed from

$$P_N = \frac{1}{2A} < - \sum_{i=1}^{N} \frac{du^e(x_i)}{dx} >$$

$$= -\frac{1}{2}\int_0^h n(x)\frac{du^e(x)}{dx}dx \quad , \tag{45}$$

or the Irving-Kirkwood pressure tensor mentioned below[15]. <---> denotes an ensemble average or a long-time average (used in molecular dynamics).

The self-diffusion coefficient parallel to the pore walls was computed form the mean square particle displacement,

$$D_{pore} = \lim_{t\to\infty}\frac{1}{N}\sum_{i=1}^{N}\frac{1}{4t} < [y_i(t) - y_i(0)]^2 + [z_i(t) - z_i(0)]^2> \quad , \tag{46}$$

and the Green-Kubo formula

$$D_{pore} = \frac{1}{2}\int_0^\infty [\psi_y(t) + \psi_z(t)]dt \quad , \tag{47}$$

where the velocity autocorrelation function $\psi_\nu(t)$ is defined by

$$\psi_\nu(t) \equiv \frac{1}{N}\sum_{i=1}^{N}<v_{i\nu}(t)v_{i\nu}(0)> \ , \ \nu = x, y, \text{ or } z. \tag{48}$$

Couette Flow Simulation

MD typically simulate systems at thermodynamic equilibrium. For the simulation of systems undergoing flow various methods of nonequilibrium MD have been developed[16,17]. In all of these methods the viscosity is calculated directly from the constitutive equation.

The nonequilibrium MD method we employed[5] is the reservoir method[16] which simulates plane Couette flow. The effective viscosity is calculated from the constitutive relation

$$\tau_{xy} = \eta_{eff}\dot{\gamma}_{imp} \tag{49}$$

where τ_{xy} is the xy component of the stress tensor, η_{eff} an effective coefficient of shear viscosity, $\dot{\gamma}_{imp}$ is the imposed shear rate.

In this method the liquid of interest is sheared between two semi-infinite reservoirs. The reservoirs contain particles identical with the ones in the main liquid slab and at the same density. The reservoir particles and the particles of the main liquid slab interact by exerting forces on each other but they do not mix because they are separated by impenetrable hard walls extending on the yz plane. Therefore, the reservoirs are fluid-like and confine the main liquid slab in the x direction. Despite appearances, the main liquid slab behaves like a bulk fluid because the reservoirs induce no significant structure in the confined liquid. Furthermore, the hard impenetrable reservoir walls are not to be

confused with the flat 10-4 LJ pore walls mentioned in the previous subsection.

The flow is induced in the following way: External forces are applied on the particles of each reservoir in order to keep the average y velocities of the reservoir constant. The imposed motion of the reservoir shears the liquid slab. The work supplied in order to keep the reservoirs moving eventually is dissipated and heats up the liquid. In order to remove this extra heat from the system the velocities of the reservoir molecules are scaled at each time step so as to keep the average reservoir temperatures constant. The imposed shear rate is obviously

$$\dot{\gamma}_{\text{imp}} = (\bar{v}_{y,u} - \bar{v}_{y,l})/s \tag{50}$$

where, $\bar{v}_{y,u}$ is the average velocity of the upper reservoir particles, $\bar{v}_{y,l}$ the average velocity of the lower reservoir particles, and s the width of the main liquid slab.

Depending on the density in the vicinity of the reservoir walls some slip might be observed. Therefore, the actual shear rate that the liquid slab experiences might be lower than the imposed one. This actual shear rate $\dot{\gamma}$ is determined empirically from the simulation by calculating the average velocity of the liquid slab particles which are located next to the reservoir walls. The actual shear rate $\dot{\gamma}$ rather than the imposed shear rate $\dot{\gamma}_{\text{imp}}$ is to be used in Equation 49 for the calculation of the effective viscosity η_{eff}.

The structure is induced by a pore wall potential, which has the form of the potential used in the equilibrium simulations (Equation 41.) with $\delta = 0$, $\epsilon_w = 4\epsilon$ and $\sigma_w = \sigma$, (ϵ, σ are the parameters of the truncated 12-6 LJ potential of the pair interactions of particles in the main liquid slab and the reservoirs.)

The arrangement described above allows one to turn off the flow and/or the wall potential at will and, therefore, to simulate bulk fluid and fluid confined between planar micropore walls both at equilibrium and under flow.

We simulated two systems: (1) bulk fluid (no wall potential) at equilibrium and undergoing Couette flow, and (2) fluid confined between planar micropore walls at equilibrium and undergoing Couette flow.

The location of the pore walls does not coincide with the location of the reservoir walls that confine the particles of the main liquid slab. This was done in order to minimize the slip at the reservoir walls as explained in detail in Referrence 5.

In the flow simulations we address the following issues:

- the effect of density structure on the flow properties, such as the flow velocity profile, the shear stress and the viscosity, by comparing the bulk and the structured systems under flow.

- the effect of flow on the density structure and the diffusivity by comparing the density profiles and the diffusivities of both systems at equilibrium and under flow. Furthermore, we compare the two

diffusivities on the plane parallel to the reservoir walls, i.e., the diffusivity in the direction of flow and the one normal to the flow, for both systems undergoing flow.

- the effect of structure on the diffusivity by comparing the diffusivities of the structured and the bulk system at equilibrium.

The density profile for the micropore fluid was determined as in the equilibrium simulations. In a similar way the flow velocity profile for both systems was determined by dividing the liquid slab into ten slices and calculating the average velocity of the particles in each slice. The velocity profile for the bulk system must be linear as macroscopic fluid mechanics predict.

The diffusivities parallel to the pore walls at equilibrium were determined from the mean square particle displacements and the Green-Kubo formula as described in the previous subsection. The Green-Kubo Formula cannot be applied, at least in principle, for the calculation of the diffusivity under flow. The diffusivity can be still calculated from the mean square particle displacements provided that the part of the displacement that is due to the macroscopic flow is excluded. The presence of flow in the y direction destroys the symmetry on the yz plane. Hence the diffusivities in the y direction (parallel to the flow) and the z direction (normal to the flow) can in principle be different. In order to calculate the diffusivities that is due to the flow must of course be excluded. Therefore,

$$D_{y,pore} = \lim_{t \to \infty} \frac{1}{N} \sum_{i=1}^{N} \frac{1}{2t} < [y_i(t) - \bar{v}t - y_i(0)]^2 > \qquad (51)$$

where $\bar{v}$ is the flow velocity at the location of particle i and

$$D_{z,pore} = \lim_{t \to \infty} \frac{1}{N} \sum_{i=1}^{N} \frac{1}{2t} < [z_i(t) - z_i(0)]^2 > \qquad (52)$$

since there is no flow in the z direction.

The shear stress is uniform throughout the main liquid slab for Couette flow[5]. Therefore, two independent methods for the calculation of the shear stress are available; it can be calculated either from the y component of the force exerted by the particles of the liquid slab upon each reservoir or from the volume average of the shear stress developed inside the liquid slab from the Irving-Kirkwood formula[15]. For reasons explained in Reference 5 the simpler version of this formula can be used in both our systems although this version does not apply in general to structured systems. The Irving-Kirkwood expression for the xy component of the stress tensor used in our simulation is

$$\bar{\tau}_{xy} V_{pore} = < \sum_{i=1}^{N_l} m v_{x,i} (v_{y,i} - \bar{v}_y(y_i)) + \frac{1}{2} \sum_{j,k=1}^{N} (x_j - x_k) F_{kj}^{(y)} + \sum_{j=1k=1}^{N_r} \sum^{N_l} (x_k - x_{GDS}) F_{kj}^{(y)} > \quad (53)$$

where $\bar{\tau}_{xy}$ is the average shear stress over the main liquid slab
V_{pore} is the volume of the main liquid slab.
N_l is the number of particles in the main liquid slab
N_r is the number of particles in both reservoirs.
$v_{x,i}, v_{y,i}$ are the x and y components of the velocity of particle i
$\bar{v}_y(y_i)$ is the y component of the flow velocity at the current position of particle i
x_i, y_i are the x and y coordinates of particle i
x_{GDS} is the location of the Gibbs dividing surface between the main liquid slab and the reservoirs.

Discussion of Results

Equilibrium Systems

Magda *et al.* have carried out an equilibrium molecular dynamics simulation on a 6-12 Lennard-Jones fluid in a slit pore described by Equation 41 with $\delta = 1$ with fluid particle interactions given by Equation 42. They used the Monte Carlo results of Snook and van Megan to set the mean pore density so that the chemical potential was the same in all the simulations. The parameters and conditions set in work were $\epsilon_w = 2\pi\epsilon$, $\sigma_w = \sigma$, $r_e = 3.5\sigma$, $kT/\epsilon = 1.2$, and $n_b\sigma^3 = 0.5925$. ϵ and σ are the Lennard-Jones parameters of the fluid and n_b is the density of a bulk phase in equilibrium with the pore fluid.

To compare molecular theoretical and molecular dynamics results, we have chosen the same wall-particle potential but have used the 6 - ∞ fluid particle potential, Equation 14, instead of the truncated 6-12 LJ potential. This is done because the molecular theory is developed in terms of attractive particles with hard sphere cores. The parameter μ^* in Equation 8 is chosen so that the density of the bulk fluid in equilibrium with the pore fluid is the same , $n_b\sigma^3 = 0.5925$, as that in the MD simulations.

Figure 1 typifies the agreement found between the fluid density profiles predicted by Equation 8 and that obtained in the MD simulations. For this example the porewidth equals 4σ. The fluid density distribution has three large peaks (the maximum bulk density possible for a Carnahan-Starling fluid is $n_b\sigma^3 = 6/\pi 1.9$) indicating a strong layering effect of the pore walls on the confined fluid.

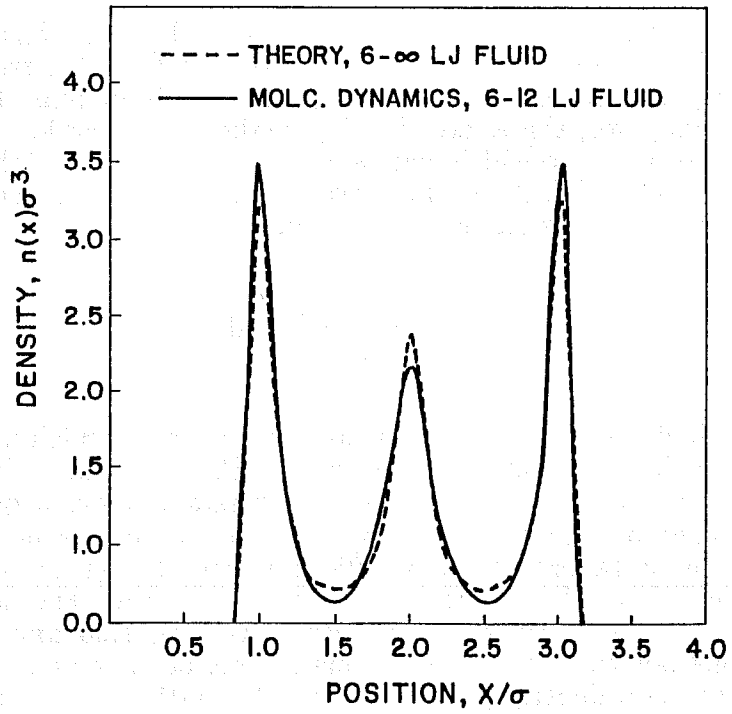

Figure 1. Fluid density versus distance from pore wall.

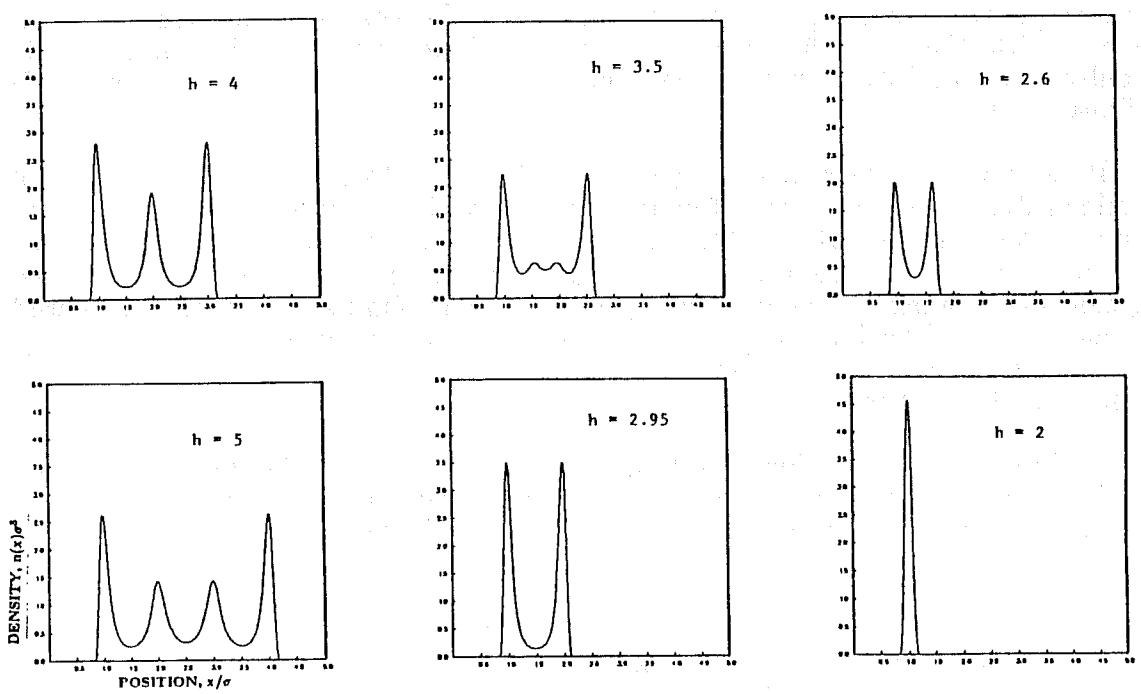

Figure 2. Density profiles illustrating effect of pore width on layering structure. Theory with 6-∞ LJ fluid.

The number and sharpness of fluid layers depend sensitively on the porewidth as is illustrated by the theoretical results (which agree qualitatively with simulations) plotted in Figure 2. As porewidth is increased from say $h = \sigma$, there appear one, two, three, etc. density peaks. A transition from N to N + 1 peaks occurs as the porewidth varies from a value at which N layers are favored to a value at which N + 1 are favored. A quantity which measures this tendency is the so-called restricted pore average density.

$$n_{ave} = \frac{1}{h - 2\Delta} \int_0^h n(x)dx \,, \tag{54}$$

where Δ is the thickness of the region near the pore wall which is empty of particles (Δ 0.8σ for the wall potential used here). Predicted and simulated values of n_{ave} are plotted in Figure 3. n_{ave} has local maxima where a given number N of layers is favored and local minima where this number is not favored. For example, one layer is favored at $h = 1.95\sigma$ and two layers are favored at $h = 2.95\sigma$, as witnessed by local maxima in n_{ave}, whereas the local minimum between 1.95 and 2.95σ indicates a defective layering 1.95 and 2.95σ state in which neither one nor two layers are optimal. This behavior can be seen in Figure 2 in which the two density peaks decrease dramatically as the pore width is decreased from $h = 2.95\sigma$ to 2.60σ.

In the simulations the maxima and minima of n_{ave} are shifted to slightly smaller porewidths compared to predictions of the theory. This trend is consistent with the fact that the 6-12 Lennard-Jones potential is not infinitely repulsive at an interparticle separation of σ, whereas the 6-∞ potential is infinitely repulsive at σ.

It is now well established experimentally that the solvation force, f_s, of confined fluid is an oscillating function of pore wall separation. In Figure 4 we compare the theoretical and MD results for f_s as a function of h. Given that pressure predictions are very demanding of a molecular theory, the observed agreement between our simple theory and the MD simulations must be viewed as quite good. The local maxima and minima in f_s coincide with those in n_{ave} and therefore also reflect porewidths favorable and unfavorable to an integral number of fluid layers.

Similarly, the pore diffusivity D_{pore} (Figure 5) has local maxima and minima resulting from the layering structure of the confined fluid. As one might expect the local maxima and minima in D_{pore} coincide with the minima and maxima in n_{ave}.

In Figure 5, the MD results are compared with predictions of the Vanderlick-Davis extension of Enskog's theory and with LADM predictions using for D° the Enskog formula, Equation 30, and the theoretical density profile. The extended Enskog theory and LADM agree quite well with one another and are in qualitative agreement with the MD results. The maxima and minima of the MD results are shifted to smaller porewidths because of the softer core of the 6-12 LJ potential as compared to the 6-∞ potential. For the

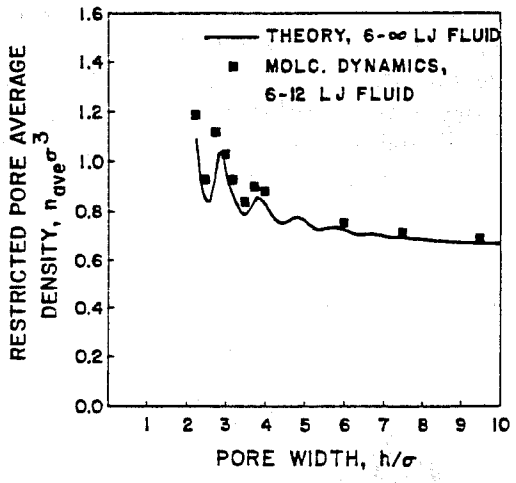

Figure 3. Restricted pore average density versus pore width. MD from Ref. 12.

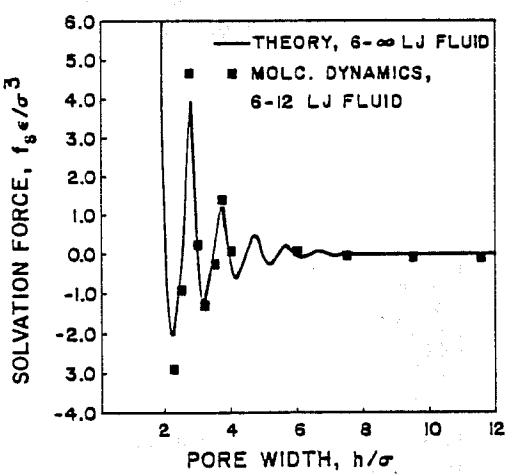

Figure 4. Solvation force versus pore width. MD from Ref. 12.

same reason, the bulk diffusivities of the theories are lower than that of the simulation. If, as is done in applying the Enskog theory of bulk phase transport coefficients to real fluids, we choose for the 6-∞ model an effective diameter σ_{eff} the agreement between theory and simulation can be improved. For example, with $\sigma_{eff} = 0.972\sigma$ Enskog's diffusivity of bulk fluid agrees with the simulation and improved agreement pore diffusivities result (Figure 6).

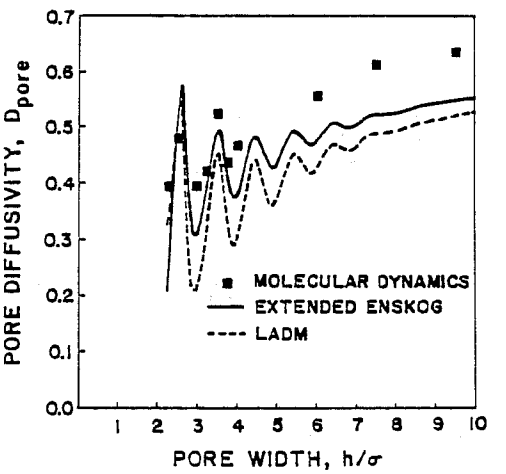

Figure 5. Pore diffusivity versus pore width. MD from Ref. 12. Theory is for 6-∞ LJ fluid. Units of diffusivity are $(3\sigma/8)(k_BT/\pi m)^{1/2}$.

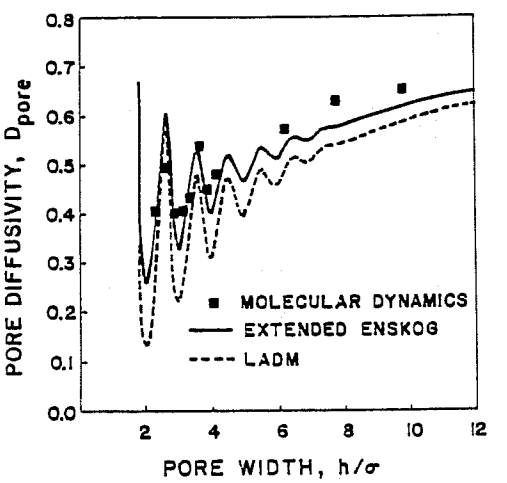

Figure 6. Pore diffusivity versus pore width. MD from Ref. 12. Theory is for 6-∞ LJ fluid with an effective hard sphere diameter $\sigma_{eff} = 0.972$.. Units of diffusivity are $(3\sigma/8)(k_BT/\pi m)^{1/2}$.

Beyond a porewidth of about 12σ, the theory and the MD results agree that the fluid profile is fully developed at each pore wall and further wall separation simply recruits more almost bulk fluid the middle region of pore with very little change in the density profile of the four or five layers near the pore wall.

Flow systems

In this subsection we present the results of our Couette flow simulations. Most of these results were first presented in Reference 5.

i) *Density profiles*: The density profiles for the bulk fluid and the micropore fluid are shown in Figures 7 and 8. We first note that the density profile for the bulk fluid is uniform throughout the pore except from a very narrow region next to the reservoir walls. But even there, the density gradients are entirely insignificant compared to the extremely strong density gradients of the micropore fluid caused by the pore wall potential. Therefore, we conclude that the presence of the reservoirs does not induce any significant structure in the fluid.

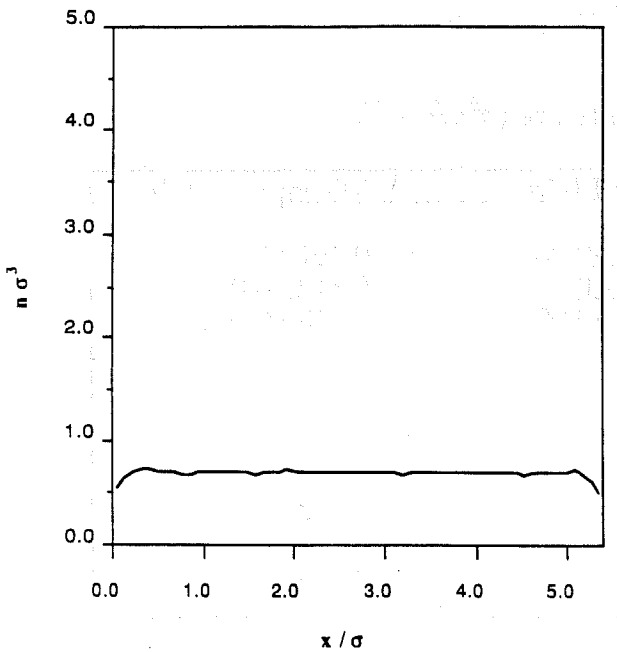

Fig. 7: Density profile of the bulk system.

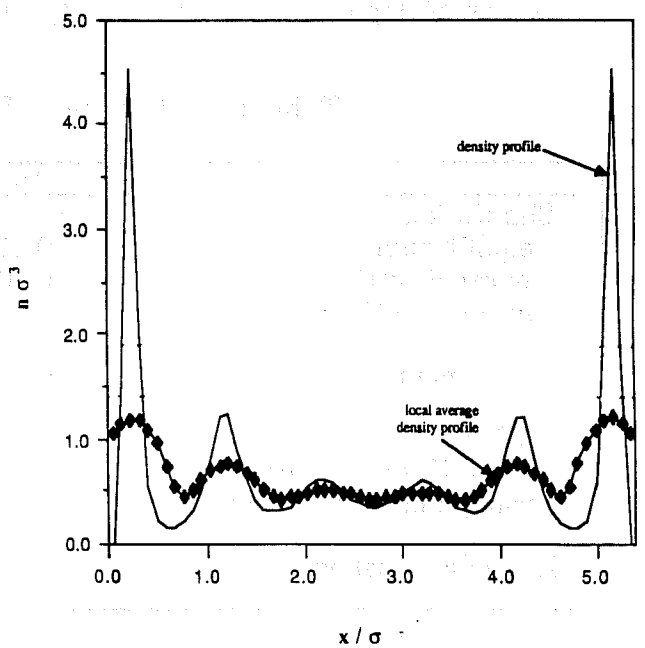

Fig.8: Density and local average density profiles of the micropore fluid

The density profile for the micropore fluid is highly structured, showing substantial fluid layering. The local average density profile (see Section 1) of this system is also shown in Figure 8. A very important feature of the local average density that results from the smoothing procedure involved in its calculation is that it varies slowly and remains bound to physically possible homogeneous fluid densities. This is essential if one is to employ some theory for the viscosity of homogeneous fluids to predict local viscosities and flow velocity profiles as explained in Section 1. From Figure 8 we see that the local average density of the micropore fluid is everywhere lower than the hard-sphere closest packing density ($\sqrt{2}/\sigma^3$) and the maximum density for the solution of the Percus-Yevick equation ($6/\pi\sigma^3$).

Although only one density profile is shown in each of the Figures 7 and 8 the density profiles of the two systems both at equilibrium and in the presence of flow that have been determined. *A conclusion of great importance that is suggested by the Couette flow simulations is that the density profiles of the two systems in the presence of flow coincide with the equilibrium density profiles, even at the extremely high shear rates employed in our simulation.* A detailed statistical analysis that justifies this point was presented in Reference 5.

ii)*Diffusivities.* Our results for the diffusivities of both systems are summarized in Table I. The pore average transverse diffusivity for the bulk fluid at equilibrium agrees very well with experimental and simulation values for the diffusivity of Argon at the same density and temperature[18,12,5].

Table I. Diffusivities. Units are $(\sigma^2\epsilon/m)^{1/2}$.

	Bulk Fluid	Micropore Fluid
Simulation		
equilibrium	0.109±0.002	0.107±0.002
parallel to the flow	0.109±0.003	0.114±0.004
normal to the flow	0.109±0.002	0.113±0.003
Experiment	0.111	
LADM		
using Enskog theory		0.107
using empirical formula		0.112
Extended Enskog		0.108

As explained in Section 1 three diffusivities were calculated for each system. These were the equilibrium transverse diffusivity and the two nonequilibrium (flow) diffusivities parallel and normal to the direction of flow. As we can see from Table I, they all agree with each other within the limits of statistical uncertainty. *We conclude, therefore, that the flow has no effect on the diffusivity even at such high shear rates as the ones employed in our simulation.* At even higher shear rates a significant dependence of the diffusivity on the shear rate has been reported[19] but one should consider that our shear rate is already orders of magnitude higher than the ones encountered in realistic flow situations.

As shown in Table I the LADM predictions agree very well with the simulation results. The first of these values employed the Enskog hard-sphere theory for homogeneous fluids for the prediction of the local diffusivities. The second value employed an empirical formula that fits MD results for the diffusivity of liquid Argon[5,18]. As we can see much of the disagreement is due to the inaccuracy of the Enskog theory and not to the LADM. The third value is the prediction of the generalization of the Enskog theory for tracer diffusion in strongly inhomogeneous fluids[8,9]. This value also agrees very well with the simulation result.

A final point has to do with the relative insensitivity of the pore averaged diffusivity on the density structure. Both the LADM and the generalized tracer diffusion theory provide a rational explanation for this fact. The reasons for the insensitivity may be identified in the double (triple for the tracer diffusion theory) smoothing induced by the volume averaging and by the very nature of the molecular interactions in liquids which makes some type of averaging over the densities in the neighborhood of a certain point necessary.

iii) *Velocity profiles.* The velocity profiles for the bulk fluid and the micropore fluid are shown in Figures 9 and 10. The profile for the bulk system is linear in agreement with the macroscopic prediction of fluid mechanics. This fact shows that the flow properties of our first system are identical with the ones of a bulk fluid, despite the presence of the reservoirs.

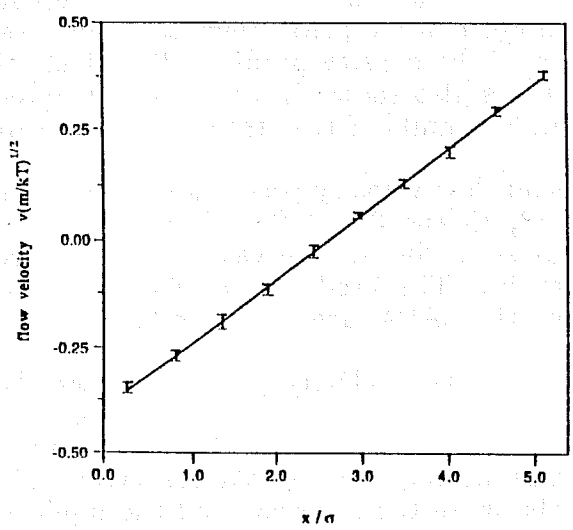

Figure 9. Velocity for the bulk system.

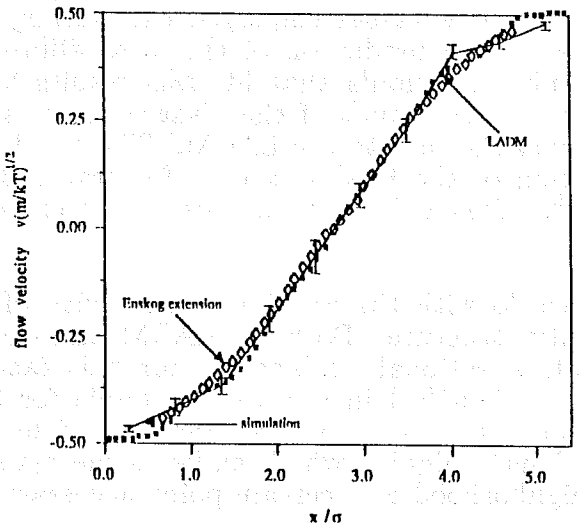

Figure 10. Theoretical and simulation velocity profiles for the micropore fluid.

The velocity profile for the micropore fluid exhibits large deviations form linearity. An extremely important point which motivated the development of the LADM is the *clear correlation between the velocity and the density profiles of the micropore fluid.* One can easily distinguish two regions of low slope (shear rate) next to the reservoir walls and a center region of high slope. These clearly correspond to the two large density peaks next to each reservoir wall and the low density center region of the density profile. The theoretical velocity profile predicted from the LADM is also shown in Figure 4. It agrees with the simulation profile almost within the limits of the statistical uncertainty.

In Figure 10, we present flow velocity predictions of the high density approximation, Equations 32 - 33, 38 and 39, of Davis' extension of Enskog's theory to flow in strongly inhomogeneous fluids. The velocity profile predicted in this way is also plotted in Figure 10. The predicted profile, the simulated profile, and the profile predicted from the LADM are quite similar.

Finally the knowledge of the velocity profiles allows the determination of the actual shear rate exerted upon the liquid slab. For the bulk system some slip is observed at the reservoir walls. No slip is observed for the micropore fluid as a result of the high density close to the reservoir walls, which facilitates the momentum transfer between the reservoir and the liquid slab particles.

iv) *Shear stress and viscosity.* As explained in Section 1 three independent estimates of the shear stress can be made for this particular type of flow. For both systems they all agree within the limits of statistical uncertainty as shown in Table II. The shear stress in the micropore fluid is significantly lower than the bulk fluid, which shows that *strong density inhomogeneities can induce large changes of the shear stress.*

Table II. Shear stress and viscosity

Bulk fluid in planar Couette flow			
	Shear Stress	Shear Rate	Viscosity
Simulation			
force on upper reservoir	0.182		
force on lower reservoir	0.180		
Irving-Kirkwood formula	0.181		
average	*0.181±0.004*	*0.149±0.005*	*1.21±0.04*
Experiment			1.23
Enskog			1.14

Micropore fluid in planar Couette flow			
	Shear Stress	Shear Rate	Viscosity
Simulation			
force on upper reservoir	0.119		
force on lower reservoir	0.122		
Irving-Kirkwood formula	0.122		
average	*0.121±0.003*	*0.186*	*0.65±0.02*
LADM			
using Enskog theory			0.77
using empirical fit			0.70
Units	ϵ/σ^3	$(\epsilon/m\sigma^2)^{1/2}$	$(m\epsilon)^{1/2}\sigma^2$

For the bulk system the constitutive equation

$$\eta = \tau_{xy}/\dot{\gamma} \tag{55}$$

is rigorously valid. The simulation result for the viscosity of the bulk system agrees with the experimental argon viscosity within the limits of the statistical uncertainty.

If one insists on Equation 55 for the micropore fluid an effective viscosity (which is an experimental observable) must be used instead, i.e.,

$$\eta_{eff} = \tau_{xy}/\dot{\gamma} \tag{56}$$

The simulation value for the effective viscosity is almost half the viscosity of the bulk fluid. According to the LADM the effective viscosity for plane Couette

flow can be identified as

$$\eta_{\text{eff}}^{-1} = s^{-1} \int_{o}^{s} [\eta^{\circ}(\bar{n}(x)]^{-1} dx \qquad (57)$$

where s is the distance between the reservoir walls, $\bar{n}(x)$ the local average density at x (defined by Equation 9), and $\eta^{\circ}(\bar{n}(x))$ is the local viscosity at x, i.e., the homogeneous fluid viscosity at density $\bar{n}(x)$

Two predictions of the LADM for the effective viscosity are shown in Table II. The first was made by using the Enskog hard-sphere theory for the calculation of the local viscosities. It agrees qualitatively with the simulation result in that it predicts a large decrease of the effective viscosity as a result of the density structure. For the second prediction the local viscosities were calculated from an empirical formula[23] that fits experimental value of the argon shear viscosity over a wide range of densities and temperatures[20,21]. The agreement with the simulation result is much better, which suggests that much of the discrepancy is a result of the poor Enskog predictions at high densities and not a deficiency of the LADM.

A final comment has to do with the concept of effective viscosity in strongly inhomogeneous fluids. For these systems the definition of the effective viscosity depends on the type flow, hence different effective viscosities will be measured for different flow situations in the same system with the same density profile. Therefore, the effective viscosity is a concept of limited value and measurements of this quantity do not provide much information about the effects of density structure on the flow behavior.

References

1. Fischer, J.; Methfessel, *Phys. Rev A* 1980 **22**, 2836.
2. Carnahan, N. F. ; Starling, K. E. *J. Chem. Phys.* 1969 **51**, 635.
3. Steele, W. A., *The Interaction of Gases with Solid Surfaces* Pergamon, New York, 1974; Chap. 2.
4. Horn, R. G. ; Israelachvili, J. N. *J. Chem. Phys.* 1981 **75**, 1400
5. Bitsanis, I.; Tirrell, M. V.; Davis, H. T. *J. Chem. Phys.* (accepted).
6. Dymond, J. H.; Woolf, *J. Chem. Soc. Faraday Trans.* 1982 **1**, 991.
7. Chapman, S.; Cowling, T. G. *The Mathematical Theory of Non-Uniform Gases and Liquids*, Cambridge University Press, New York, 1954.
8. Davis, H. T., *J. Chem. Phys.* (accepted).
9. Vanderlick, T. K.; Davis, H. T. *J. Chem. Phys.* (accepted).
10. Davis, H. T., *Chem. Eng. Comm.* (accepted).
11. Luks, K.D.; Miller, M.; Davis, H. T. *AIChE J.* 1966 **12**, 1079.
12. Magda, J. J.; Tirrell, M. V.; Davis, H. T. *J. Chem. Phys.* 1985 **83**, 1888.
13. Snook, I. K.; van Megen, W. *J. Chem. Phys.* 1980 **72**, 2907.
14. Beeman, D. *J. Comput. Phys.* 1976 **20**, 130.
15. Irving, J. H.; Kirkwood, J. G. *J. Chem. Phys.* 1950 **18**, 817.
16. Ashurst, W. T.; Hoover, W. G. *Phys. Rev. A* 1975 **11**, 658.
17. Heyes, D. M.; Montrose, C. J.; Litovitz, T. A. *J. Chem. Soc. Faraday Trans. 2* 1983 **79**, 611.
18. Levesque, D.; Verlet, L. *Phys. Rev. A* 1970 **6**, 2514.

19. Heyes, D. M. *J. Chem. Soc. Faraday Trans. 2 fR 1985* **82**, 1365.
20. Haynes, W. M. *Physica* 1973 **67**, 440.
21. Michels, A.; Sengers, J. V.; van der Klundert, L. J. M., *Physica* 1963 **29**, 149.

6. SIMULATION OF ONE-DIMENSIONAL, TWO-PHASE, DARCY FLOW

Synopsis

In developing a two-dimensional, and subsequently a three-dimensional, two-phase flow simulator, it is logical to tackle the simpler one-dimensional case first. Using this relatively simple system as a foundation has several advantages. From the standpoint of computer programming, developing first a simpler algorithm and then building upon it is much easier than attempting a large problem at once and then having to spend weeks to exterminate the bugs. More importantly, analytical solutions of special cases of the one-dimensional case are more likely to be available than of any two-dimensional case. The best way of assessing a numerical routine's performance is to compare its results to the analytical solution, if one is available. Fortunately, in 1982 Fokas and Yortsos[1] published a closed-form solution of a realistic one-dimensional, two-phase flow problem. The one-dimensional flow simulator developed here is tested by solving their problem for nine cases displaying a range of saturation front behavior.

This chapter presents the details of the numerical algorithm, the two-phase flow model and solution of Fokas and Yortsos, comparisons of simulated and analytical results, and CRAY-2 considerations, such as timing, vectorization, and multitasking of code.

Physical Model

The physical situation is one of immiscible, two-phase, one-dimensional, incompressible flow through a homogeneous, isotropic porous medium. The medium (e.g. rock) is initially saturated with oil, apart from the so-called irreducible saturation of water (a misnomer, actually). At time $t = 0^+$ water is injected at constant flow rate into the sample through one face, displacing the oil until the irreducible oil saturation is attained.

The relevant property of the porous medium is its absolute permeability, k, a measure of how easily a fluid can be forced through the medium by a mechanical potential gradient. For single-phase flow, k is the proportionality constant in Darcy's Law, the generally-accepted foundation for describing "slow" flow in porous media:

$$\mathbf{v} = -\frac{k}{\mu} \nabla P \tag{1}$$

$\mathbf{v}$ is the vector velocity of the fluid phase, μ is its viscosity, and ∇P is the imposed mechanical potential gradient, which may include pressure, gravitational, or centrifugal contributions, among others.

Darcy's Law is extended to multiphase flow by introducing the concept of relative permeability, a measure of how one phase's presence affects the flow rate of another phase. The presence of another fluid generally decreases a fluid's flow rate under a given mechanical potential gradient. The two phase relative permeability of an incompressible phase A is defined as the ratio of its volumetric flow rates at a given ∇P 1) with phase B present in significant amounts to 2) B at its irreducible saturation. This quantity is most strongly a function of saturation and saturation history, although other parameters such

as viscosity ratio may have small effects.[2,3] Darcy's Law for multiphase flow is

$$\mathbf{v}_i = -\frac{k\,k_{ri}}{\mu_i}\,\nabla P \tag{2}$$

where subscript i denotes phase i, and k_{ri} is its relative permeability. Figure 1 summarizes the physical situation as well as the relevant properties of the medium and the fluid phases.

Mathematical Formulation

The final parabolic partial differential equation which describes the evolution of the oil saturation profile is derived from the equations of continuity and Darcy's Law for each of the two phases, in conjunction with the physical assumptions stated above. The equations of continuity for each phase are

$$\phi\,\frac{\partial S_w}{\partial \tau} + \frac{\partial q_w}{\partial \xi} = 0 \tag{3}$$

$$\phi\,\frac{\partial S_o}{\partial \tau} + \frac{\partial q_o}{\partial \xi} = 0 \tag{4}$$

ϕ is the porosity (void fraction) of the medium, S_i is the saturation of phase i, and q_i is the volumetric flow rate of phase i per unit cross sectional area perpendicular to the flow direction. ξ and τ are dimensional position and time coordinates, respectively. The one-dimensional form of Darcy's Law for each phase, with the imposed pressure drop as the sole contribution to the mechanical potential gradient, is

$$q_w = -\frac{k\,k_{rw}}{\mu_w}\,\frac{\partial P_w}{\partial \xi} \tag{5}$$

$$q_o = -\frac{k\,k_{ro}}{\mu_o}\,\frac{\partial P_o}{\partial \xi} \tag{6}$$

Completing the system are these boundary conditions. Before water injection, the oil is at its maximum saturation throughout. Also, in this semi-infinite medium, the oil concentration sufficiently far from the injection face remains at this maximum value for all time. Finally, water is injected at constant flow rate q into one face of the medium. These three conditions are, respectively,

$$S_o(\xi,0) = 1 - S_{wr} \tag{7}$$

$$S_o(\infty,\tau) = 1 - S_{wr} \tag{8}$$

$$q_w(0,\tau) = q \tag{9}$$

The best starting point for combining Equations (3) through (6) is a statement of the incompressibilities of the water and oil phases:

$$q = q_o + q_w \tag{10}$$

Equation (6) is inserted for q_o, and the definition of capillary pressure

$$P_c \equiv P_o - P_w \tag{11}$$

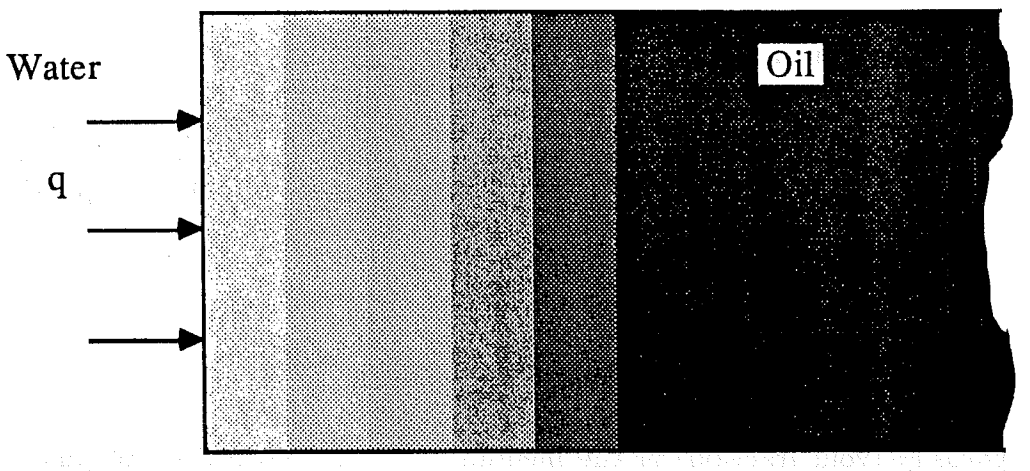

Relevant Properties

Porous Medium :	Absolute Permeability	k
Fluid Phases :	Relative Permeabilities	k_{rw} k_{ro}
	Viscosities	μ_w μ_o

Figure 1. Diagram of the physical setup. Water is injected at a constant flow rate q, displacing the oil, originally at its maximum saturation.

is inserted for P_o. The spatial derivative of P_w is eliminated by Equation (5). Finally, this equation is solved for q_w and inserted into Equation (3). Dimensionless variables are defined as

$$x \equiv \frac{\xi}{L} \tag{12}$$

$$t \equiv \frac{\tau q}{L \phi} \tag{13}$$

where L is a characteristic length of the system, resulting in the following nonlinear, parabolic partial differential equation:

$$\frac{\partial S}{\partial t} = h(S) \frac{\partial S}{\partial x} + \frac{\partial}{\partial x} \left[g(S) \frac{\partial S}{\partial x} \right] \tag{14}$$

S denotes the oil saturation, and

$$h(S) \equiv \frac{\partial}{\partial S} \left[\frac{\lambda_w}{\lambda_o + \lambda_w} \right] \tag{15}$$

$$g(S) \equiv \frac{k\, k_{ro}}{L\, q\, \mu_o} \frac{\lambda_w}{\lambda_o + \lambda_w} \frac{\partial P_c}{\partial S} \tag{16}$$

where λ_i is the mobility of phase i,

$$\lambda_i \equiv \frac{k_{ri}}{\mu_i} \tag{17}$$

g(S) and h(S) are functions of oil saturation through the relative permeabilities.

Boundary conditions (7) and (8) translate directly to the derived system; condition (9), however, requires special treatment. Integration of Equation (3) and insertion of the dimensionless variables yields

$$\int_{\infty}^{x} \frac{\partial S}{\partial t} dx' = \frac{q_w}{q} \tag{18}$$

Replacing the time derivative by Equation (14), integrating, and applying the result to the face at x=0 (where $q=q_w$) provide the third boundary condition:

$$\frac{\partial S}{\partial x}(0,t) = \frac{1}{g(S|_{x=0})} \left[1 - \int_{1-S_{wr}}^{S|_{x=0}} h(S')\, dS' \right] \tag{19}$$

In general, Equation (14) does not possess a known closed-form solution. Therefore, a numerical scheme is required to obtain the evolution of the oil saturation profile.

Galerkin Finite Element Formulation

The Galerkin finite element method is a special case in the broad class of methods of weighted residuals. An approximate solution to a partial or ordinary differential equation

$$L[u] = f(\mathbf{x}) \qquad \text{on } \Omega \tag{20}$$

is expressed as a linear combination of linearly-independent basis functions ϕ_j:

$$\hat{u} = \sum_{j=1}^{N} u_j \phi_j \tag{21}$$

$\hat{u}$ is required to be a solution to Equation (20) by forcing the inner products of the residual $L[\hat{u}]$-f with each member of a set of weighting functions $\{w_i\}$ to be zero:

$$\int_{\Omega} (L[\hat{u}] - f) w_i \, d\Omega = 0 \tag{22}$$

Hence the name methods of weighted residuals. If the weighting functions are chosen as the basis functions of $\hat{u}$, Galerkin's Method results.

$$\int_{\Omega} (L[\hat{u}] - f) \phi_i \, d\Omega = 0 \qquad i=1,2,...N \tag{23}$$

Finally, if the spatial domain Ω is divided into discrete subdomains and convenient "nearly orthogonal" finite element basis functions are used, this becomes the *Galerkin Finite Element Method,* commonly referred to as *finite elements.* A partial differential equation is thus reduced to a finite set of N equations in the coefficients u_i.

In this work, piecewise linear (also known as "hat") basis functions are used. Each function ϕ_i is nonzero only on the elements immediately to the left and right of its peak. Figure 2 gives the traditional element and node numbering as well as a segment of the linear basis function set for a general one-dimensional mesh. With the maximum value of each basis function equal to unity, the linear combination coefficients u_i are the values of the approximate solution $\hat{u}$ at the nodes (element boundaries).

Application of the Galerkin finite element method to the partial differential equation (14) involves two complications. First, this is a transient problem. Instead of obtaining N (generally nonlinear) algebraic equations immediately, a set of N nonlinear first order differential equations in the u_i results:

$$\mathbf{A}\dot{\mathbf{u}} = \mathbf{F}(\mathbf{u}) \tag{24}$$

Integration of these equations is possible through either simpler methods (e.g. Euler, Crank-Nicholson) or software packages, which generally employ more sophisticated techniques. To obtain the results presented here, implicit Euler and Crank-Nicholson time stepping are used; further details appear later. The second complication is the nonlinear character of the PDE — the presence of the nonlinear functions g(S) and h(S). The usual derivation of the residual equation set yields terms such as

$$\int_{\Omega} \frac{d\phi_i}{dx} \frac{d}{dx}\left[p(S)\right] dx \qquad \text{or} \qquad \int_{\Omega} \frac{d\phi_i}{dx} \frac{d}{dx}\left[p\left(\sum_{j=1}^{N} u_j \phi_j\right)\right] dx$$

where p(S) is a nonlinear function of S. Applying the Swartz-Wendroff approximation

$$p\left(\sum_{j=1}^{N} u_j \phi_j\right) \approx \sum_{j=1}^{N} p(u_j)\phi_j \tag{25}$$

linearizes the equations in ϕ_j so the above term becomes

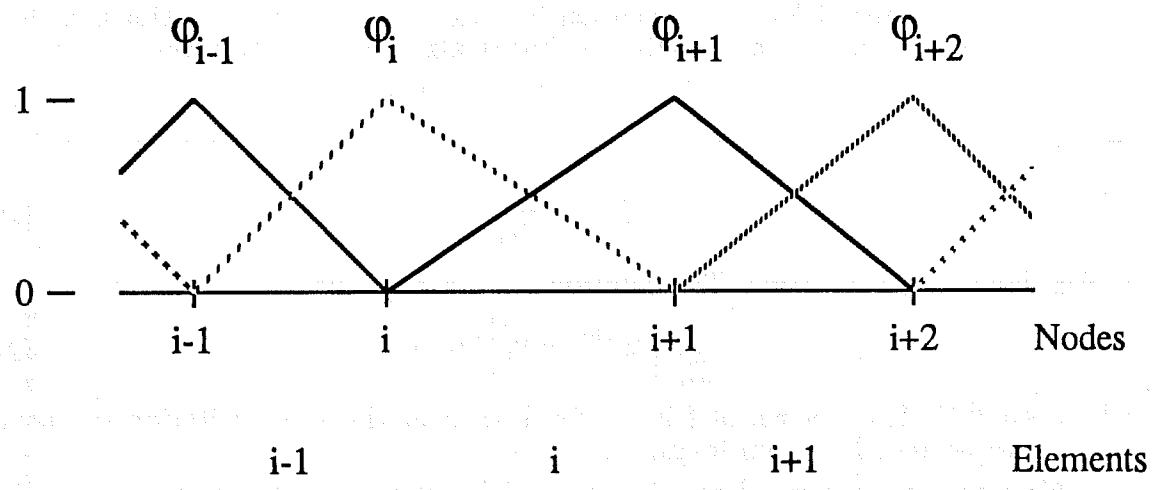

Figure 2. Segment of the finite element mesh, with piecewise linear, "nearly orthogonal" basis functions.

$$\sum_{j=1}^{N} p(u_j) \int_{\Omega} \frac{d\phi_i}{dx} \frac{d\phi_j}{dx} dx$$

The Swartz-Wendroff approximation is known to have a global error proportional to $(\Delta x)^4$, better than the Galerkin method itself with linear basis functions, in cases of "non-extreme" curvature on any given element.[3] Therefore, concentrating elements in regions of high curvature (adapting the mesh), aids this approximation.

Application of the Swartz-Wendroff approximation and a time integration scheme transforms the residual equations into a set of nonlinear algebraic equations

$$\mathbf{f}(\mathbf{u}) = \mathbf{0} \tag{26}$$

The solution vector is found by Newton iteration with no modifications, such as relaxation or late Jacobian updating. A linear algebraic equation set results:

$$\mathbf{J}(\mathbf{u}^k)[\mathbf{u}^{k+1} - \mathbf{u}^k] = -\mathbf{f}(\mathbf{u}^k) \tag{27}$$

where

$$J_{ij} = \frac{\partial f_i}{\partial u_j} \tag{28}$$

and k denotes the iteration. The solution is accepted when

$$\sum_{i=1}^{N} \left| u_i^{k+1} - u_i^k \right| < \epsilon \tag{29}$$

where $\epsilon = 10^{-9}$. The 1-norm of $\mathbf{f}$ is required to meet the same criterion to ensure that a proper root has been found.

Newton's method requires a "reasonable" initial guess for convergence. The initial guess used in this algorithm is derived from the most recent solution available, whether it is from the previous time step or from the previous mesh on the current time step. If the nodes' positions have changed, the Newton iteration guess is linearly interpolated in x from the previous solution and its mesh. If quadratic basis functions are used, quadratic interpolation would be appropriate.

Solution Algorithm of the Transient Discretized System

The flow diagram of the general algorithm used appears in Figure 3. Details of the specific tasks appear in subsequent sections. Adaptation of the spatial mesh is performed so that elements are concentrated in regions which would otherwise have higher local error. For linear basis functions, these regions are those of high solution curvature. (For quadratic basis functions, the third derivative of the solution is of interest, and so on.) In general, a solution is found on a given mesh, the estimated error of this solution on each element is computed, and the nodes are repositioned to equidistribute the total error across each new element. This process is termed continuation-adaptive; it is repeated until the average absolute motion of each node from one mesh to the next is below a specified tolerance. When this tolerance is satisfied, the solution for the current time level is accepted. This entire strategy is very similar to that used by Benner[4] and Heiba.[5]

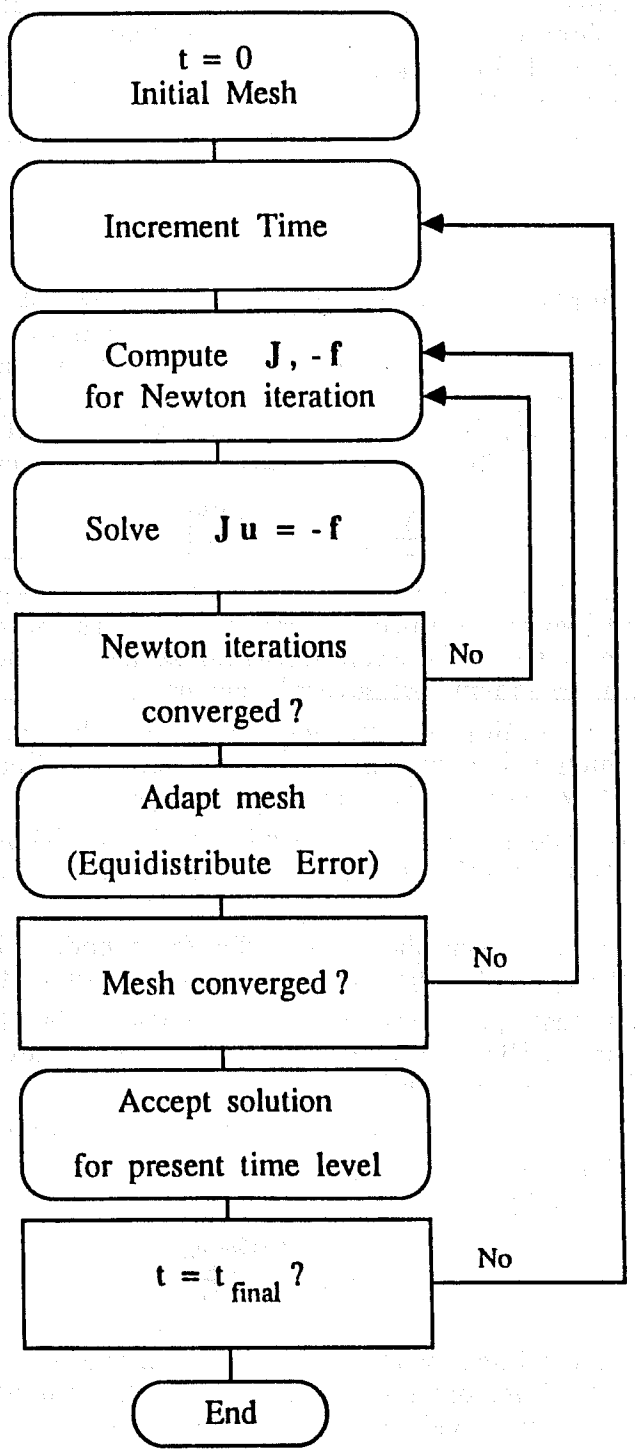

Figure 3. Flow diagram of the simulator's algorithm, showing the continuation-adaptive nature of the mesh refinement.

Figure 3 suggests that most of the computational burden involves solving the Newton iterations on each mesh for the values of u_i, for solving **Ax=b** is typically expensive and this task is performed most often. The other tasks, such as mesh adaptation and the computation of the Jacobian **J** and the right-hand side **-f**, are less time consuming. Details of the computational work for each task are presented later.

Mesh Adaptation

The mesh adaptation scheme equidistributes the total estimated error of the solution on the "old" mesh by repositioning the nodes so the total error is divided evenly among the elements, resulting in the "new" mesh. This new mesh is used to solve the problem again. Such a scheme, termed continuation-adaptive or explicit-adaptive, has been used previously at Minnesota.[5–7] This process is repeated until the mesh converges in the sense that

$$\frac{1}{N}\sum_{i=1}^{N}\left|x_i^{old}-x_i^{new}\right| < \epsilon$$

where N is the number of nodes and ϵ is 5×10^{-3}, for example. An alternative algorithm, termed Newton-adaptive, computes both the solution values and the nodal positions in a single Newton iteration series. Benner[5] recommends the continuation-adaptive scheme for several reasons.

(1) The continuation-adaptive method preserves the Jacobian's tridiagonal structure (which exists by virtue of the piecewise linear basis functions), whereas the Newton-adaptive method does not.

(2) A good initial guess for the convergent nodal positions is not required in the continuation-adaptive scheme, since they are not determined by Newton iteration.

(3) The Newton-adaptive method can suffer from nodal bifurcations, i.e. non-uniqueness of the mesh which satisfies the error equidistribution criterion.

(4) For Benner's test problems, the continuation-adaptive scheme requires significantly less CPU time to achieve a given error level, since fewer equations are solved per Newton iteration.

Accordingly, the continuation-adaptive scheme is used exclusively here.

Since the basis functions are piecewise linear, the error is estimated from the curvature on element i:

$$E_i \approx (\Delta x_i)\int_{x_i}^{x_{i+1}}\left|\frac{d^2u}{dx^2}\right| dx \qquad (30)$$

Because the solution is linear within each element, the only contributions to the integral are from the element's endpoints. Basically, Equation (30) reduces to the average of the absolute values of the change in slope between element i and the neighboring elements i-1 and i+1. For boundary elements 1 and N-1, the absolute slope change with the single neighboring element is used for E_1 and E_{N-1}.

Once the E_i have been computed, the equidistributed error on the new mesh is

$$e_o = \frac{1}{N-1} \sum_{i=1}^{N-1} E_i \tag{31}$$

Figure 4 shows the graphical representation of the adaptive process, including the interpolation resulting in the new nodal positions. Note that the nodes remain ordered; i.e. they do not jump over each other.

If the error is distributed in such a way that nodes jump relatively far from the old to the new mesh, convergence on two fronts is hindered. First, the node positions may experience overshoot and oscillate, converging only slowly. Second, large node jumps hinder the convergence of the succeeding Newton iterations, for the initial guess vector is linearly interpolated from the solution on the old mesh. If the mesh adapts too quickly, the solution on the new mesh may be outside the Newton radius of convergence. To address these problems, roots of the estimated errors E_i are summed, as opposed to the E_i themselves.

$$e_o = \frac{1}{N-1} \sum_{i=1}^{N-1} E_i^{1/r} \tag{32}$$

Thus, node motion is damped, and mesh convergence is smooth. After experimentation, r=4 was found to be successful in the cases run here. A smaller value (e.g. $r<2$) may underdamp the mesh, while larger values (e.g. $r>6$) may overdamp it, wasting computer time since more mesh iterations are required to achieve the tolerance ϵ.

Spatial Domain Truncation

Since the physical model involves a semi-infinite medium, and finite elements use a finite domain, the related questions of where to truncate the semi-infinite domain (at x=L) and how to treat the $S(\infty,t)$ boundary condition must be addressed.

The simplest treatment is to use the boundary condition

$$\frac{\partial S}{\partial x}(L,t) = 0$$

(equivalently, $S(L,t)=1-S_{wr}$), where L is large enough such that when L is increased, the solution profiles remain unchanged. This is fine for steep saturation fronts, but for fronts greatly dispersed by capillary forces, L would need to be ridiculously large. Furthermore, a new, less empirical treatment is available which provides a basis for setting L on mathematical grounds.

An asymptotic analysis of the PDE can be used both to estimate the proper domain boundary L and to provide a Robin boundary condition there. Figure 5 is a graphical representation of the ideas that follow. Far from the developing front, where $S=1-S_{wr}\equiv S_\infty$, the coefficient functions h(S) and g(S) are approximately constant, producing the asymptotic form of Equation (14):

$$\frac{\partial S}{\partial t} = h(S_\infty)\frac{\partial S}{\partial x} + g(S_\infty)\frac{\partial^2 S}{\partial x^2} \tag{33}$$

The first order spatial derivative is eliminated using the transformation

$$\xi = x + h(S_\infty)t \tag{34}$$

to yield an equation in the transformed variable $S(\xi,t)$

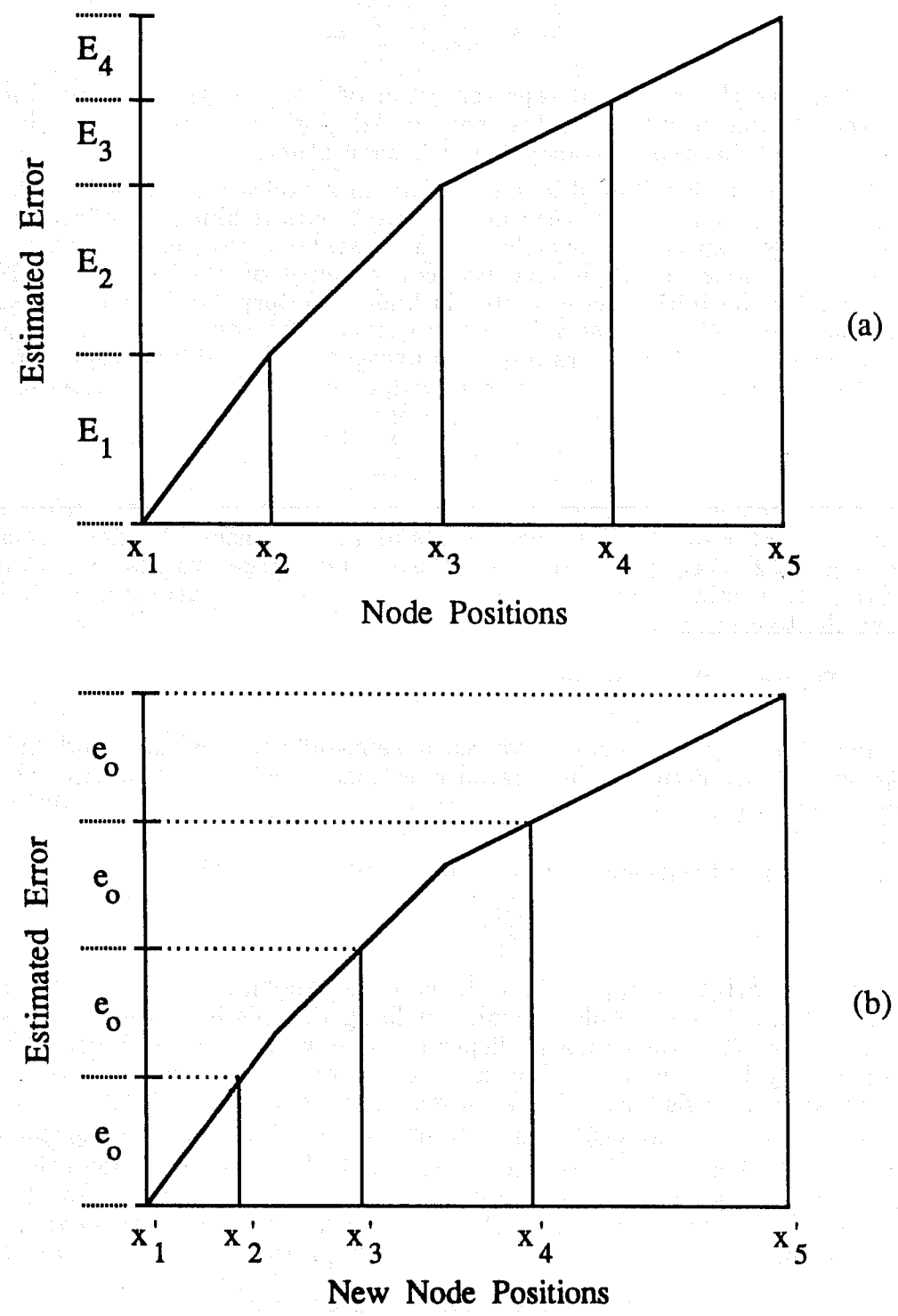

Figure 4. After the solution on the mesh in (a) is found, the estimated error on each element is summed and equidistributed to produce the new mesh in (b).

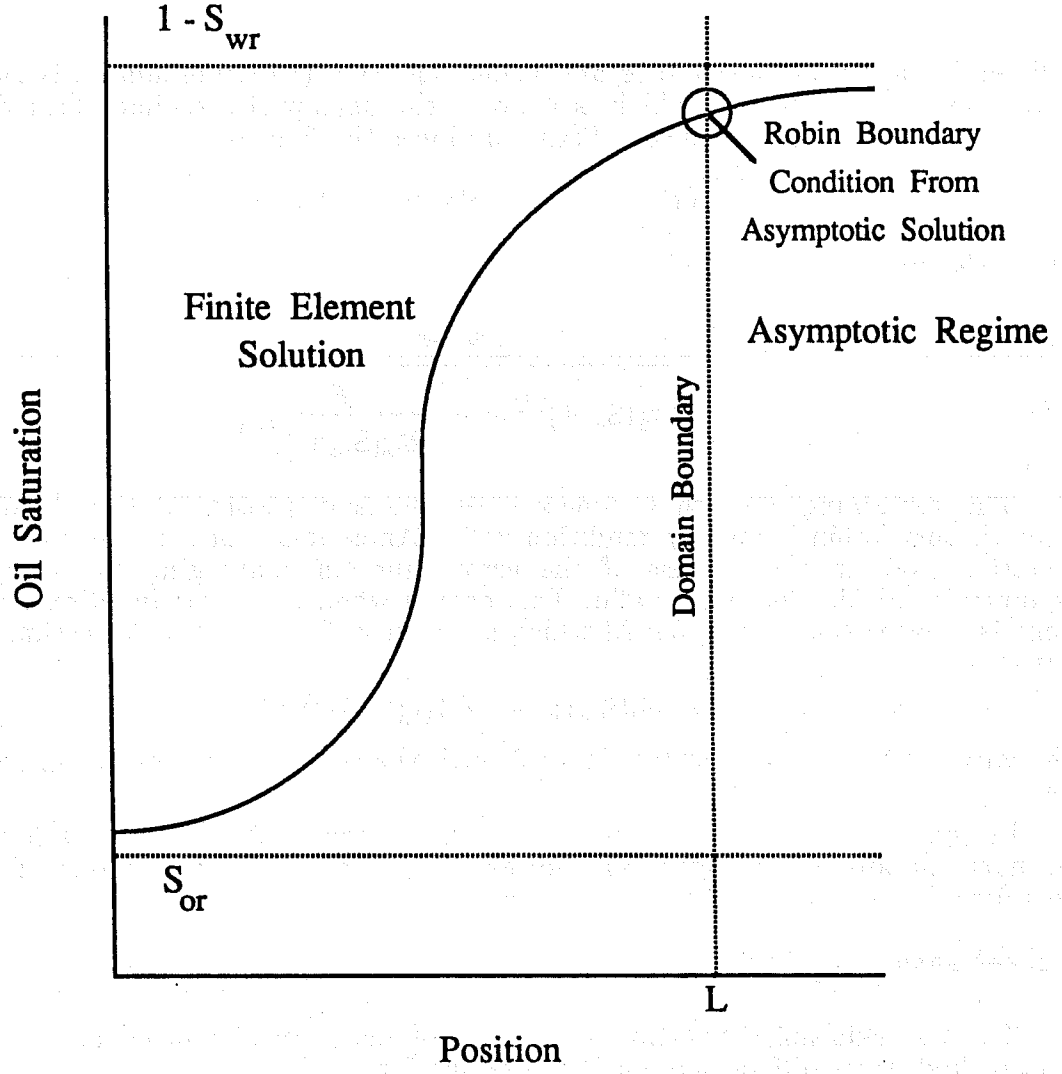

Figure 5. Truncation of the semi-infinite domain at L, using the asymptotic solution to obtain a Robin boundary condition for the finite element problem.

$$\frac{\partial S}{\partial t} = g(S_\infty)\frac{\partial^2 S}{\partial \xi^2} \tag{35}$$

Applying the boundary condition $S(\infty,t)=S_\infty$ to the general solution of this equation yields

$$S(\xi,t) = (S_\infty - B)\,\mathrm{erf}\left[\frac{\xi}{2(g(S_\infty)t)^{1/2}}\right] + B \tag{36}$$

Differentiating with respect to ξ and using Equation (36) to eliminate B gives a Robin boundary condition which is valid in the asymptotic regime. Transforming $S(\xi,t)$ to the original function $S(x,t)$ produces the final result:

$$\frac{\partial S}{\partial x}(x \geq L,t) = \omega[S(x \geq L,t) - S_\infty] \tag{37}$$

where the coefficient ω is

$$\omega = -\frac{e^{\frac{-\xi^2}{4g(S_\infty)t}}}{(\pi g(S_\infty)t)^{1/2}\,\mathrm{erfc}\left[\frac{\xi}{2(g(S_\infty)t)^{1/2}}\right]} \tag{38}$$

The remaining concern is where does the asymptotic solution hold, i.e. where is this Robin boundary condition valid? An estimate of L is obtained from Equation (36). In the process of the error function converging to unity, the asymptotic solution becomes valid. This occurs when the error function's argument is greater than a number M which is about 3, for example. An estimate of L is then

$$L = -h(S_\infty)t + 2M(g(S_\infty)t)^{1/2} \tag{39}$$

The value of M is increased from 2 or 3 until the solution profiles are unchanging.

In general, the value of L monotonically increases from one time level to the next. Details of the algorithm, however, require that a fixed value of L be used for all time levels — the value at $t=t_{max}$.

Discretization of Time

The Galerkin finite element formulation of this transient problem results in a set of first order differential equations of the form

$$\mathbf{A}\dot{\mathbf{u}} = \mathbf{F}(\mathbf{u}) \tag{40}$$

where **A** has tridiagonal structure. Implicit Euler and Crank-Nicholson (also known as modified Euler) time integration schemes were applied to the set of residual equations. These standard methods are preferred over software packages for two reasons. First, no "black box" exists which could cause problems without adequate warning. Second, evaluation of the various time integration methods, one goal of this work, is more straightforward. Software routines will be substituted in the future to conserve computational effort by, for example, using adaptively sized time steps.

Implicit schemes are preferred, since these employ information from all mesh points at the current time level, whereas explicit schemes use information

from the previous time step only.[8] Especially for hyperbolic problems (such as this one in the zero-capillary pressure limit), which are characterized by waves travelling in the spatial domain, explicit schemes often require prohibitively small time steps to ensure reliable solution or even stability. If a component wave travels farther than the mesh spacing in one time step, unphysical results ensue; the Courant number is based on this principle. The tradeoff, as expected, is computational effort. These implicit schemes require solution of a system of coupled algebraic equations, whereas explicit schemes allow simple updates at each mesh point.

The implicit Euler approach replaces the time derivative by a difference quotient and evaluates the right-hand side F at the new time level (hence "implicit"):

$$\mathbf{A}\,(\mathbf{u}^{t+1} - \mathbf{u}^{t}) = \mathbf{F}(\mathbf{u}^{t+1})\,\Delta t + O(\Delta t) \tag{41}$$

An advantage of this method is that the Jacobian in each Newton iteration is tridiagonal: $\mathbf{J}\Delta\mathbf{u}=-\mathbf{f}$ is solved for $\Delta\mathbf{u}$ by a simple recursive algorithm derived using LU-decomposition. Unfortunately, the implicit Euler scheme has $O(\Delta t)$ error, requiring smaller time steps to obtain the same accuracy as an $O(\Delta t)^2$ method, such as Crank-Nicholson.

Crank-Nicholson time stepping has been recommended in the literature for such problems as these[9] and is the method used currently in the one-dimensional, two-phase flow simulator. Its formula is obtained by subtracting the Taylor series for $\mathbf{u}$ in t at two adjacent time levels

$$\mathbf{u}^{t+1} = \mathbf{u}^{t} + (\Delta t)\dot{\mathbf{u}}^{t} + \frac{1}{2}(\Delta t)^2\ddot{\mathbf{u}}^{t} + \cdots \tag{42}$$

$$\mathbf{u}^{t} = \mathbf{u}^{t+1} - (\Delta t)\dot{\mathbf{u}}^{t+1} + \frac{1}{2}(\Delta t)^2\ddot{\mathbf{u}}^{t+1} - \cdots \tag{43}$$

and applying Equation (40):

$$\mathbf{u}^{t+1} = \mathbf{u}^{t} + \frac{1}{2}(\Delta t)\,\mathbf{A}^{-1}[\mathbf{F}(\mathbf{u}^{t+1}) + \mathbf{F}(\mathbf{u}^{t})] + O(\Delta t)^2 \tag{44}$$

Unlike the implicit Euler method, however, the tridiagonal structure of the Jacobian is not preserved, and a *full* system $\mathbf{J}\Delta\mathbf{u}=-\mathbf{f}$ is solved at each Newton iteration. While this adds to the computational burden, the increased accuracy of the solution after many time steps justifies the extra effort.

A more advanced, predictor-corrector time integration scheme found favor at Minnesota in the research of Benner[5] and Heiba,[6] who use an algorithm based on the work of Gresho, Lee, and Sani.[10] Predicted saturation profiles at the new time level are obtained by approximating the time derivative in Equation (40) by either a first-order-accurate explicit Euler time step, in which case the corrector is implicit Euler, or by a second-order-accurate Adams-Bashforth predictor, in which case the corrector is the trapezoid rule. Furthermore, Benner and Heiba incorporate adaptively sized time steps based on estimates of the time truncation error computed from the saturation profile.[10] Four implicit Euler steps are used initially to provide necessary smoothing before the higher-order trapezoidal rule integration commences.[5] A high priority is to replace the current implicit Euler and Crank-Nicholson schemes with this more advanced method.

How to evaluate the integrals present in the term $\mathbf{F}(\mathbf{u}^t)$ is a subtle concern which results from mesh adaptation: the nodes at time level t+1 are not in the

same positions as those in the convergent mesh of time level t. A simple approach is to interpolate linearly the values from the "old" mesh to the "new," but Heiba[6] correctly asserts that this violates a mass balance. Heiba evaluates integrals involving saturations from the previous time step exactly by using Gauss quadrature and demonstrates this method's superiority over Benner's. The error in mass associated with Benner's strategy decreases as the number of elements increases, for the nodes are more concentrated and linear interpolation more accurately represents the true values. Since 50 elements are used here, the simple strategy of Benner produces no ill effects. As the solutions do not change with increasing the number of elements beyond 50, any mass balance error is of negligible magnitude.

Up to this point, solving efficiently the full set of equations is not a major concern — the IMSL routine LEQT2F (IMSL User's Manual), which employs Gaussian elimination with partial pivoting to obtain a "high accuracy" solution, is used. The routine accepts the digits of accuracy desired of the solution and performs iterative improvement, if necessary, to meet this criterion. Five-digit accuracy is demanded of all solutions; examining their sensitivity to the number of digits demanded confirms this. Since the one-dimensional simulator is now performing well, emphasis soon shifts to minimizing computer time, beginning with solving the matrix equation more efficiently.

System with a Closed-Form Solution

The algorithm used applies to a wide range of physical situations, especially those of different relative permeability and fractional flow relations. Results presented here, however, use one model for which the partial differential equation

$$\frac{\partial S}{\partial t} = h(S)\frac{\partial S}{\partial x} + \frac{\partial}{\partial x}\left[g(S)\frac{\partial S}{\partial x}\right] \tag{45}$$

with the boundary conditions

$$S_o(x,0) = 1 - S_{wr} \tag{46}$$

$$S_o(\infty,t) = 1 - S_{wr} \tag{47}$$

$$\frac{\partial S}{\partial x}(0,t) = \frac{1}{g(S|_{x=0})}\left[1 - \int_{1-S_{wr}}^{S|_{x=0}} h(S')\,dS'\right] \tag{48}$$

has a closed-form solution.

In the particular case where the coefficient functions take the form

$$g(S) = (\beta S + \gamma)^{-2} \tag{49}$$

$$h(S) = \alpha(\beta S + \gamma)^{-2} \tag{50}$$

Equation (45) and the associated boundary conditions are mapped into the heat equation by an integral transformation of x, thus admitting a closed-form solution.[1] Because of its complexity, the solution is not reproduced here (see Appendix A). *At each point* (x_o,t_o) where the solution is desired, a single nonlinear algebraic equation is solved (e.g. by Newton iteration) for an auxiliary variable; this value is then used to compute $S(x_o,t_o)$.

The fact that an analytical solution exists could be a moot point if the corresponding physical situation is unrealistic. Fortunately, this is not the case. In terms of the model parameters γ and β, the viscosity ratio M of the fluids is

$$M \equiv \frac{\mu_w}{\mu_o} = \frac{1 - S_{wr} + \frac{\gamma}{\beta}}{S_{or} + \frac{\gamma}{\beta}} \tag{51}$$

Furthermore, the parameter β^2 expresses the ratio of the magnitudes of viscous forces to capillary forces:

$$Ca \equiv \beta^2 = \frac{qL\mu_o}{k\left(\frac{dP_c}{dS}\right)} \tag{52}$$

Although this is not the strict definition of the capillary number, Ca is used to convey the same qualitative meaning. Specifying the above forms of g(S) and h(S) also sets the functional form of the capillary pressure gradient and the ratio of the relative permeabilities. The dimensionless capillary pressure gradient is

$$\left(\frac{dP_c}{dS}\right)^* = \frac{1}{k_{ro}\left(S + \frac{\gamma}{\beta}\right)^2}\left[1 + M\frac{S - S_{or}}{1 - S - S_{wr}}\right] \tag{53}$$

and the ratio of the relative permeabilities is

$$\frac{k_{ro}}{k_{rw}} = \frac{S - S_{or}}{1 - S - S_{wr}} \tag{54}$$

Figures 6 and 7, respectively, depict capillary pressure gradient curves for typical parameter values and the allowable range of relative permeability curves. Their limiting behaviors are correct for typical water-oil-reservoir systems, and the intermediate shapes display the generally observed monotonicity.[1] One aspect which is lacking, however, is associated with the fractional flow curves. While most fractional flow curves have an inflection point, which is a crucial feature for the Buckley-Leverett (zero-capillary pressure) solution, the fractional flow curves of this model cannot. Figure 8 shows typical fractional flow curves. These do display the proper monotonicity.

Even with a minor shortcoming, Yortsos and Fokas' model is physically meaningful and is a great aid in evaluating the performance of the one-dimensional, two-phase flow simulator. This specific model is employed in the remainder of this chapter.

Discussion of Cases Solved

Physical Basis of Macroscopic Dispersion

The evolving oil saturation fronts display a range of behavior from highly dispersed to not dispersed (resembling plug flow), depending on the physics of the particular situation.

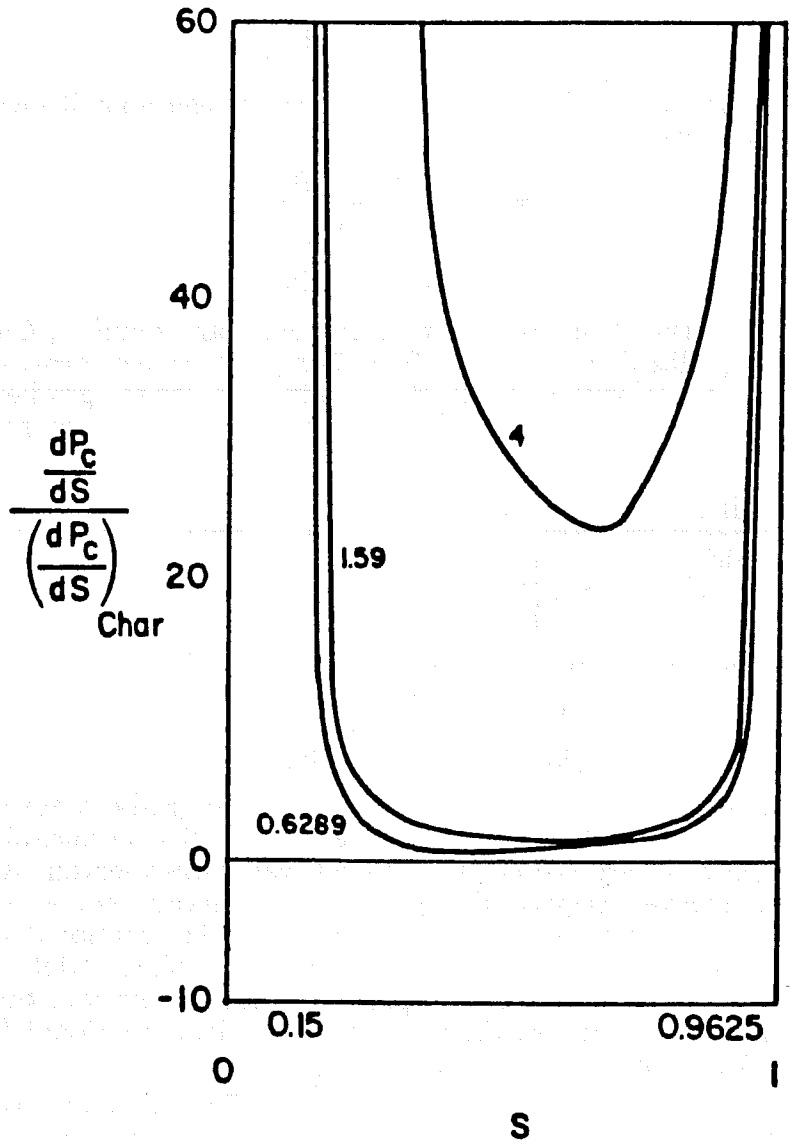

Figure 6. Dimensionless capillary pressure gradient curves for three viscosity ratios.[11]

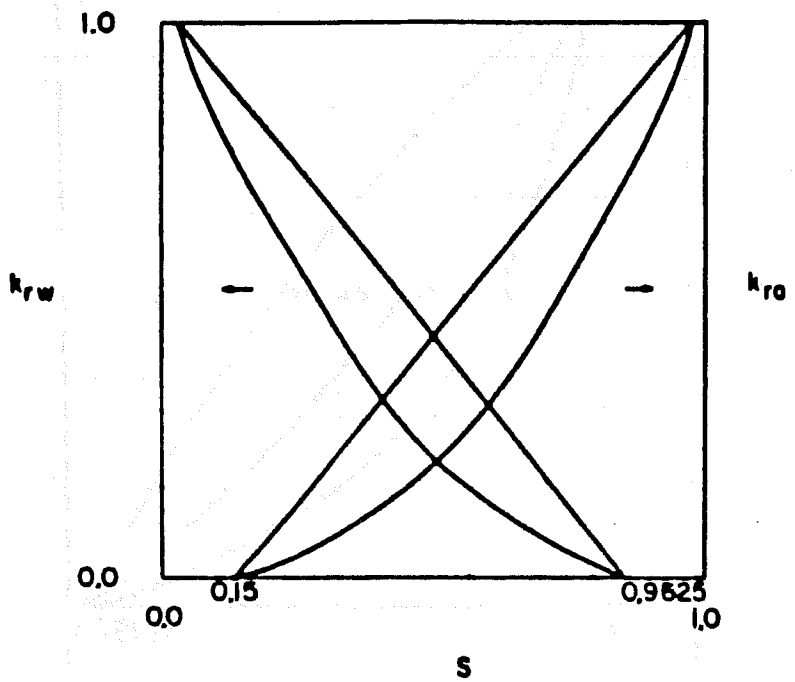

Figure 7. Allowable relative permeabilities resulting from specifying the functional form of their ratio (Equation 54). The straight-line relative permeability of one phase produces the curved line for the other phase.[11]

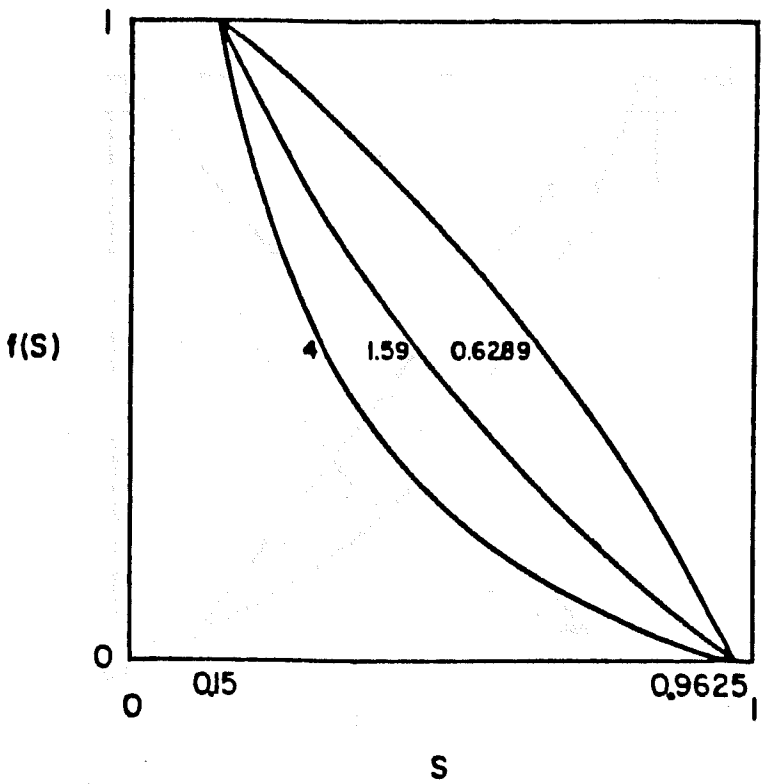

Figure 8. Fractional flow curves (for water) at three viscosity ratios. Note the lack of inflection points, which are observed generally for porous media.[11]

Capillary pressure, here defined as the excess of pressure in the oil phase over that in the water phase, acts through its spatial gradient, ∇P_c. A large capillary pressure gradient at a given saturation implies that one phase is under a greater driving force (i.e. mechanical potential gradient) than its rival. Thus, that phase always moves with a greater velocity, if the effects of relative permeability and viscosity are neglected. This is the essence of macroscopic capillary dispersion. For the water/oil displacement process here, significant capillary forces imply a greater mechanical potential gradient in the water phase, driving it at a greater velocity than the oil. The saturation front is therefore dispersed. In the limit of zero capillary pressure gradient, the driving forces in each phase are nearly equal, resulting in plug flow: a sharp front. From a mathematical point of view, when capillarity is negligible, the second-order derivative in the associated PDE is insignificant; the equation becomes first-order and hyperbolic, a classification whose solutions can have shocks, i.e. discontinuities.

The second factor which determines the front's shape arises from the viscosity difference between the fluids and acts through the fractional flow relation. Temporarily ignoring the second-order term in the partial differential equation (yielding the Buckley-Leverett problem) leads to an expression for the velocity of each saturation on the front:

$$v(S) = -h(S) = -\frac{\partial f}{\partial S}(S) \tag{55}$$

f(S) is the fractional flow of water as a function of oil saturation. In reality, however, not all velocities are allowed. For example, if the lower saturations on a shock front are moving at a higher velocity, a saturation function with triple valued regions arises. This dilemma was unravelled in the 1950s by applying the concept of shock formation and the method of characteristics.[12–14] Essentially, the physical basis of the Buckley-Leverett equation breaks down for fronts with discontinuities, before triple-valued solutions can appear. Analysis using the method of characteristics shows that a shock front which has a tendency to become triple-valued retains its discontinuity and moves with a velocity equal to the slope of the secant on the fractional flow curve which connects the shock's bounding saturations. Fronts with shocks cannot occur in porous media, for they imply a discontinuity in the saturation profile, a finite change of saturation over zero distance. The steepest front practical is one which changes saturation abruptly over a length scale of a few grains.

The velocity of each saturation value as a function of viscosity ratio is shown in Figure 9. For viscosity ratios of unity and greater, the Buckley-Leverett solution is a discontinuous front; otherwise, the profile would contain triple-values. For viscosity ratios less than unity, however, higher saturation values move faster (legally), effectively broadening the front. Saturation profiles for systems of viscosity ratios less than unity then, are dispersed both by capillary forces and by this fractional flow phenomenon.

Predicting Dispersion in the Simulated Cases

The one-dimensional, two-phase flow simulator must treat successfully a variety of cases — including steep and diffuse fronts. As a test, an array of nine cases was run: the possible combinations of three viscosity ratios and three capillary numbers (as defined in Equation 52). These are given in Table 1 with the case numbers. Viscous forces are greater in the first and third rows than in

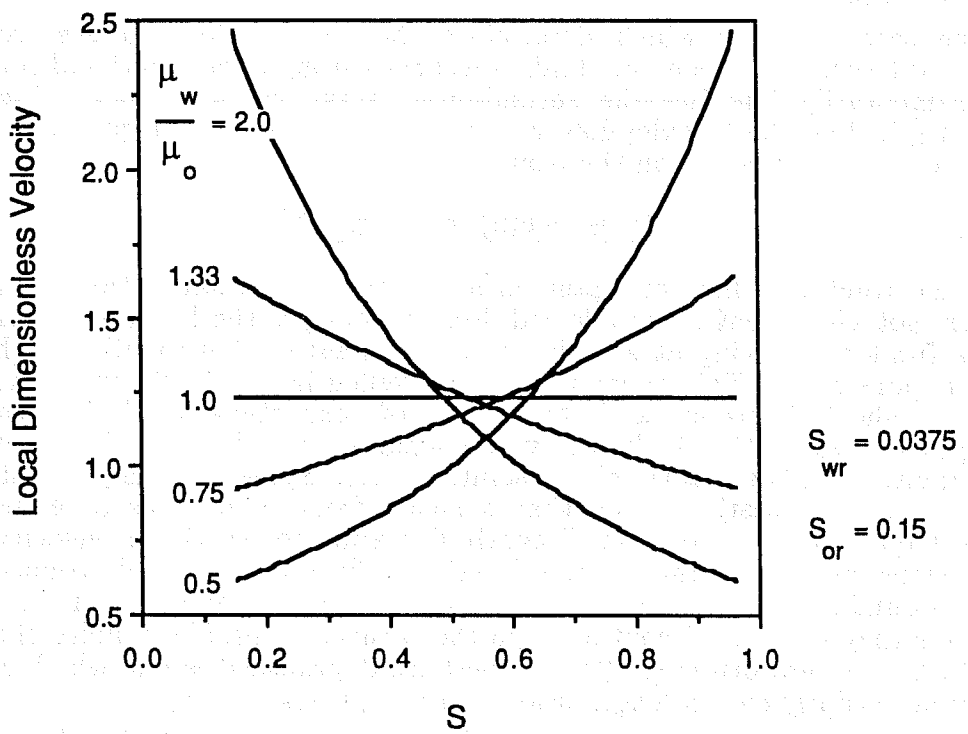

Figure 9. Velocities of different saturations (in the Buckley-Leverett problem) for various viscosity ratios. The velocities for M>1 are not allowed, as triple-valued solutions would arise.

Table 1. Array of Nine Test Cases

μ_w/μ_o	Ca † 25.0	1.0	0.04
2.0	#1	#2	#3
1.1	#4	#5	#6
0.5	#7	#8	#9

† Ratio of viscous forces to capillary forces

the second row, where the fluids' viscosities are nearly equal. Since the first and third viscosity ratios are both a factor of two from unity, their magnitudes of viscous forces are comparable. A convenient scheme for comparing the viscous forces among the nine cases appears in Figure 10. Analyzing the trends in capillary forces is not as straightforward, however, since the *ratio* of viscous to capillary forces is varied, not the capillary forces directly. The capillary number is constant down each column, ensuring that capillary forces decrease and then increase as do the viscous forces. Furthermore, one expects the fronts to be more broad from left to right across a given row as capillary forces increase while viscous forces are held constant. This reasoning produces Figure 11, the gray-scale diagram for comparing the magnitudes of capillary forces among the cases.

Predicting the shapes of the saturation fronts requires combining the effects of the viscous and capillary forces. A key fact is that only viscosity ratios less than unity (cases 7-9) exert a dispersive influence on the front, for only then (with negligible capillary forces) do the higher oil saturations travel faster than the lower ones (see Figure 9). The Buckley-Leverett (zero-capillary pressure) solutions of cases 1-6 are thus identical. The viscous forces in cases 7-9 alone need consideration in arriving at the total dispersion picture. This serves to increase the dispersion in cases 7-9 over that in cases 1-3, respectively; Figure 12 presents the final expected front dispersion levels for all nine cases. Case 4 is predicted to have the sharpest displacement front, whereas case 9 should have the most dispersed front.

Simulation Results

The saturation fronts for these nine cases *do* have the predicted dispersion characteristics. Figures 13 through 21 present the adaptive Galerkin finite element solution (only odd-numbered nodes are shown), the analytical solution of Yortsos and Fokas, and the Buckley-Leverett solution at three time levels for

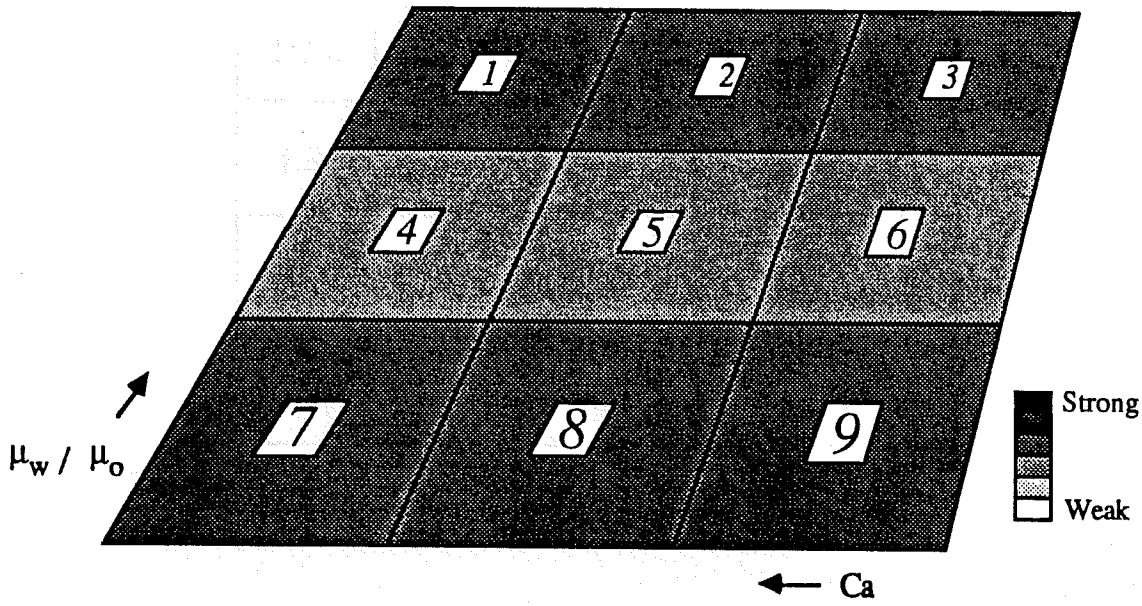

Figure 10. Relative strengths of *viscous forces* across the array of cases.

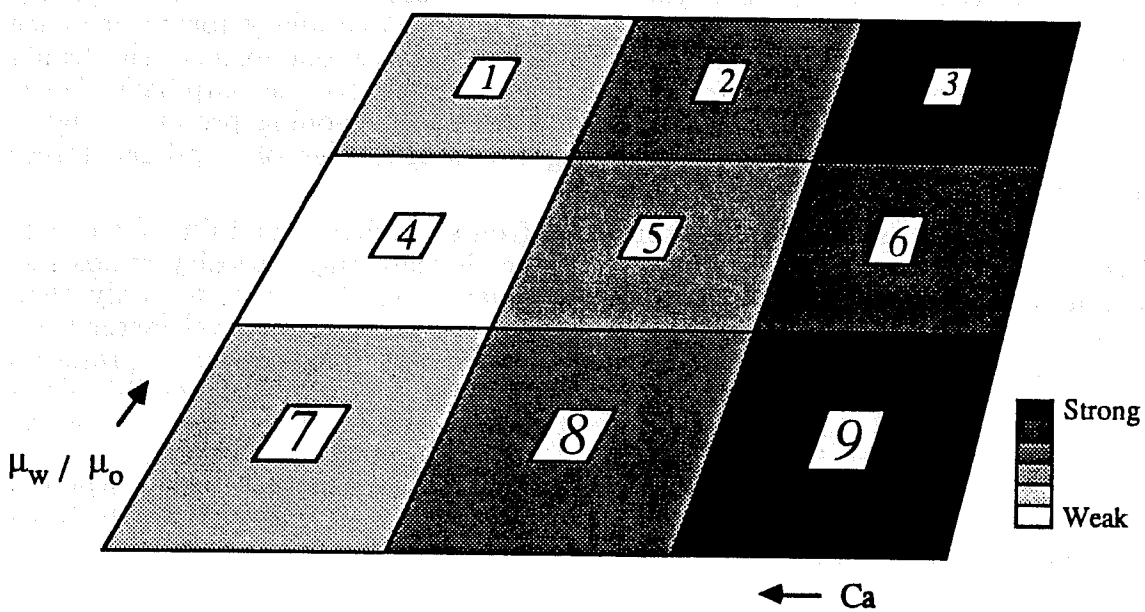

Figure 11. Relative strengths of *capillary forces* across the array of cases.

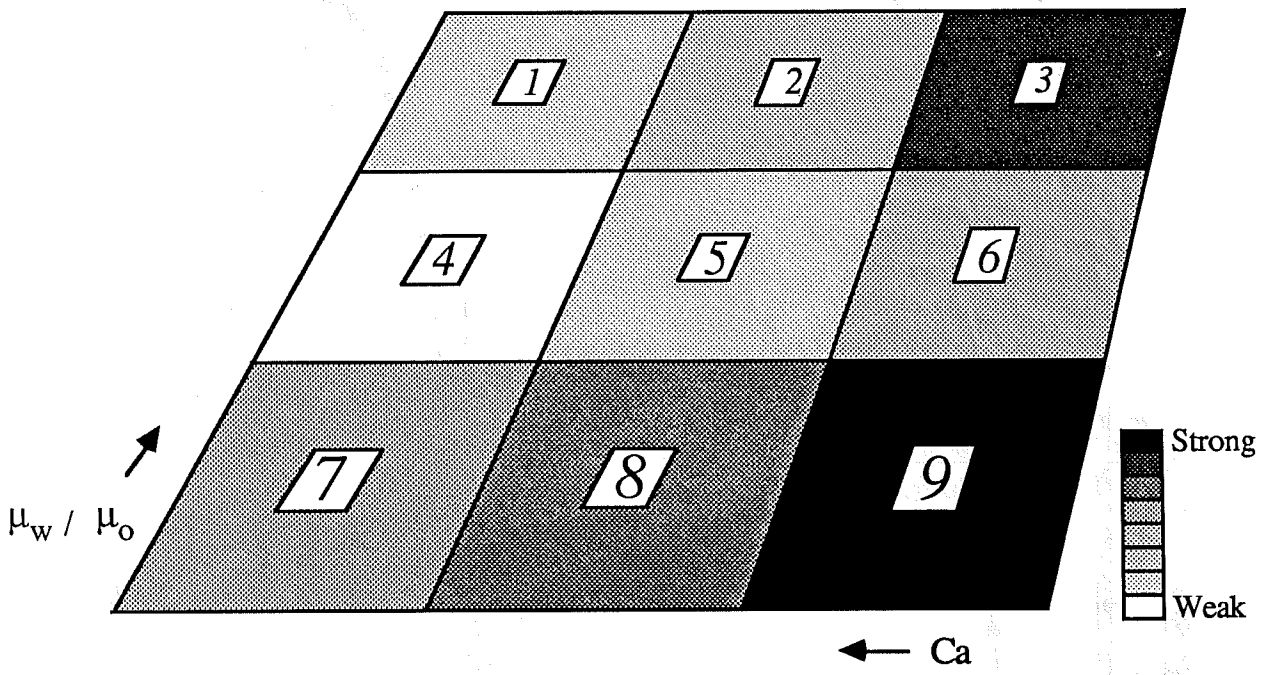

Figure 12. Relative strengths of *dispersion* across the array of cases.

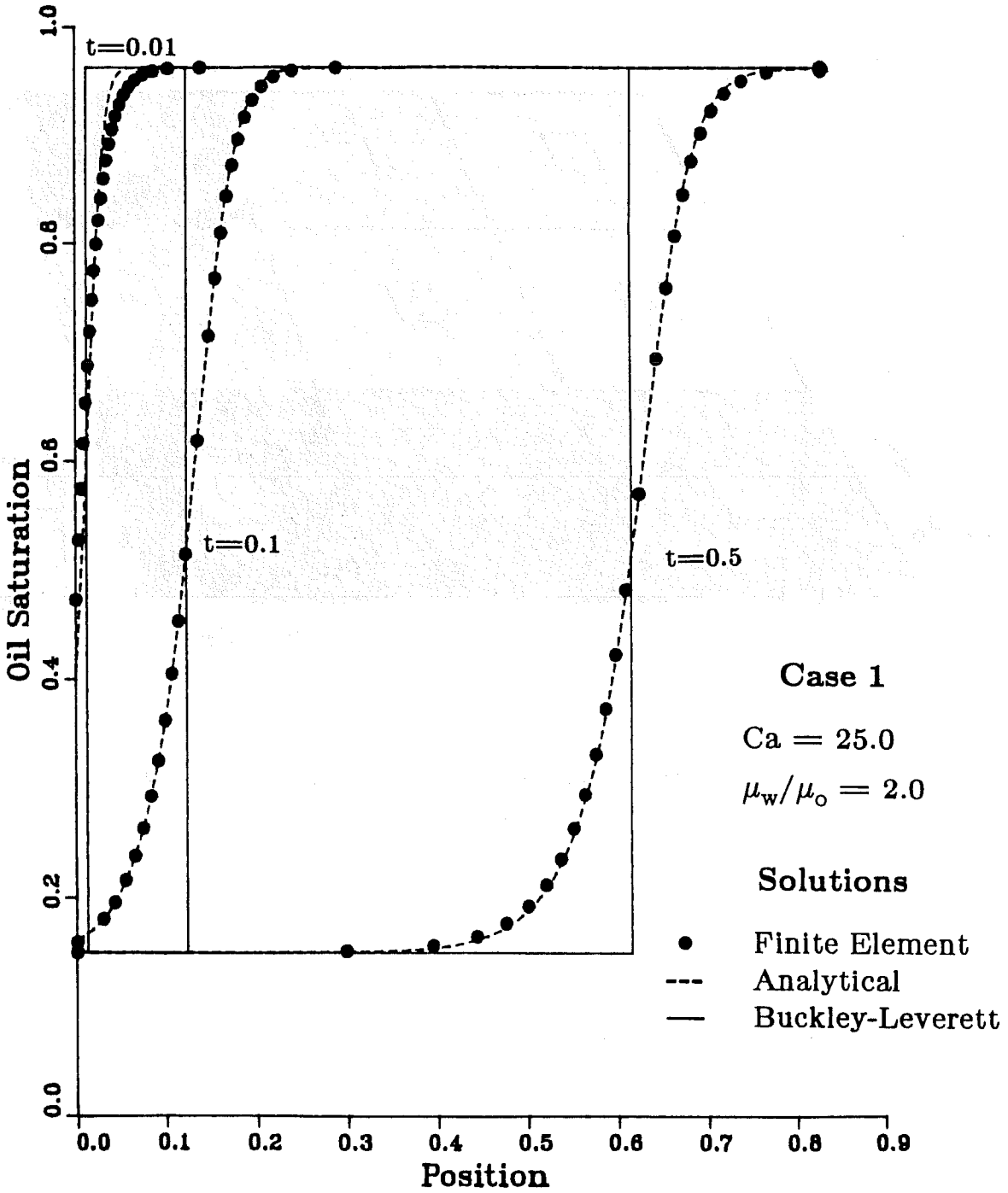

Figure 13. Case 1 solutions at three time levels.

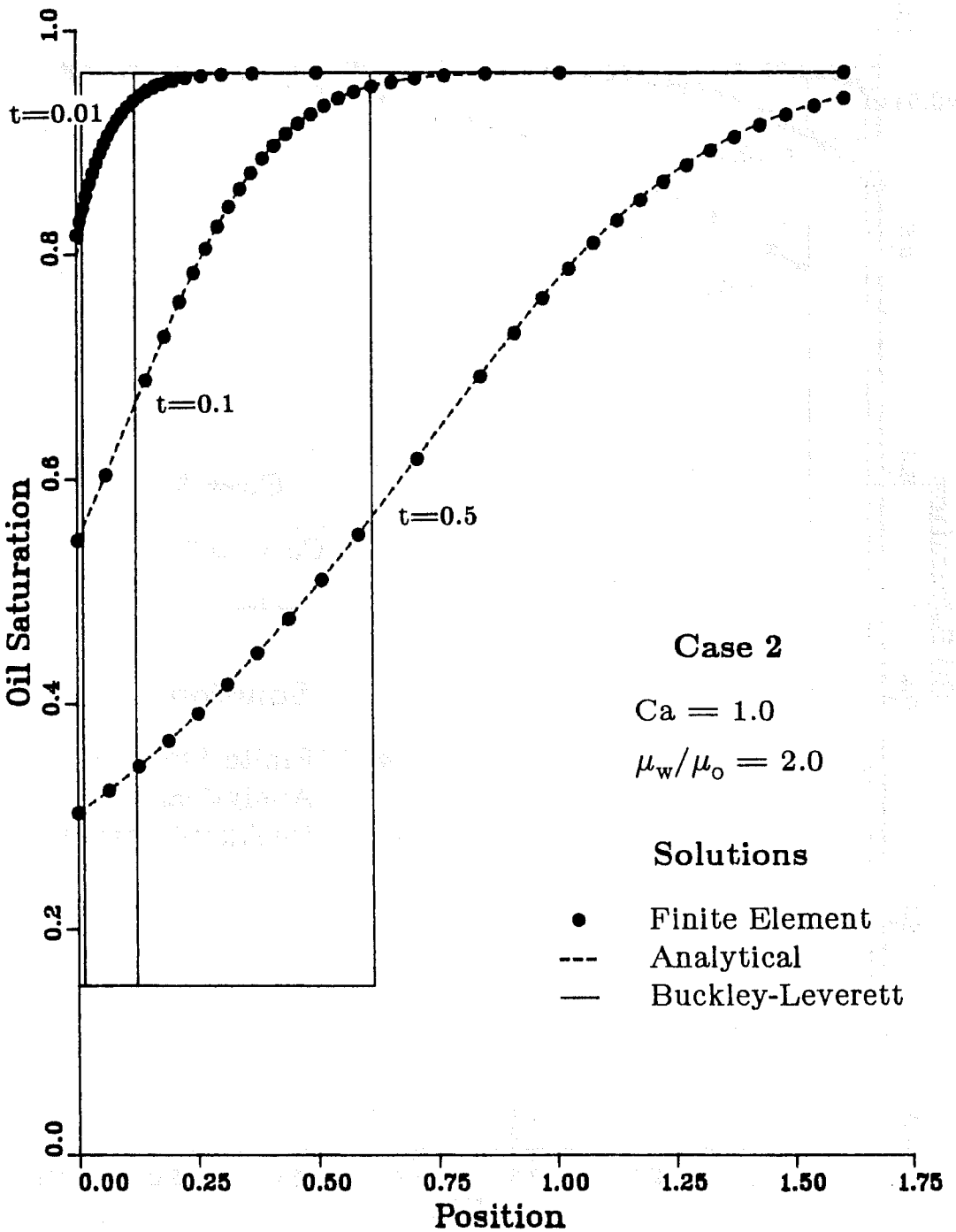

Figure 14. Case 2 solutions at three time levels.

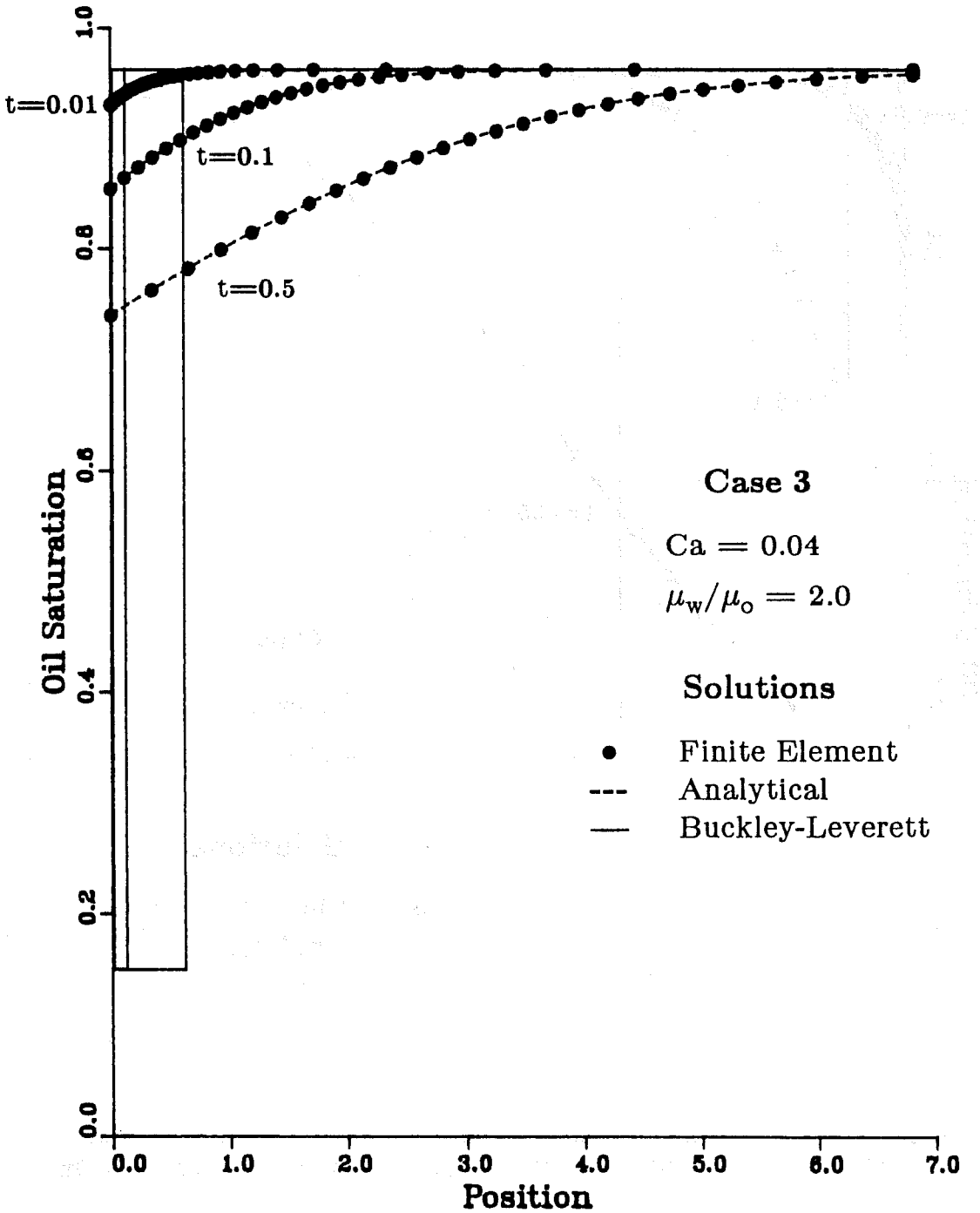

Figure 15. Case 3 solutions at three time levels.

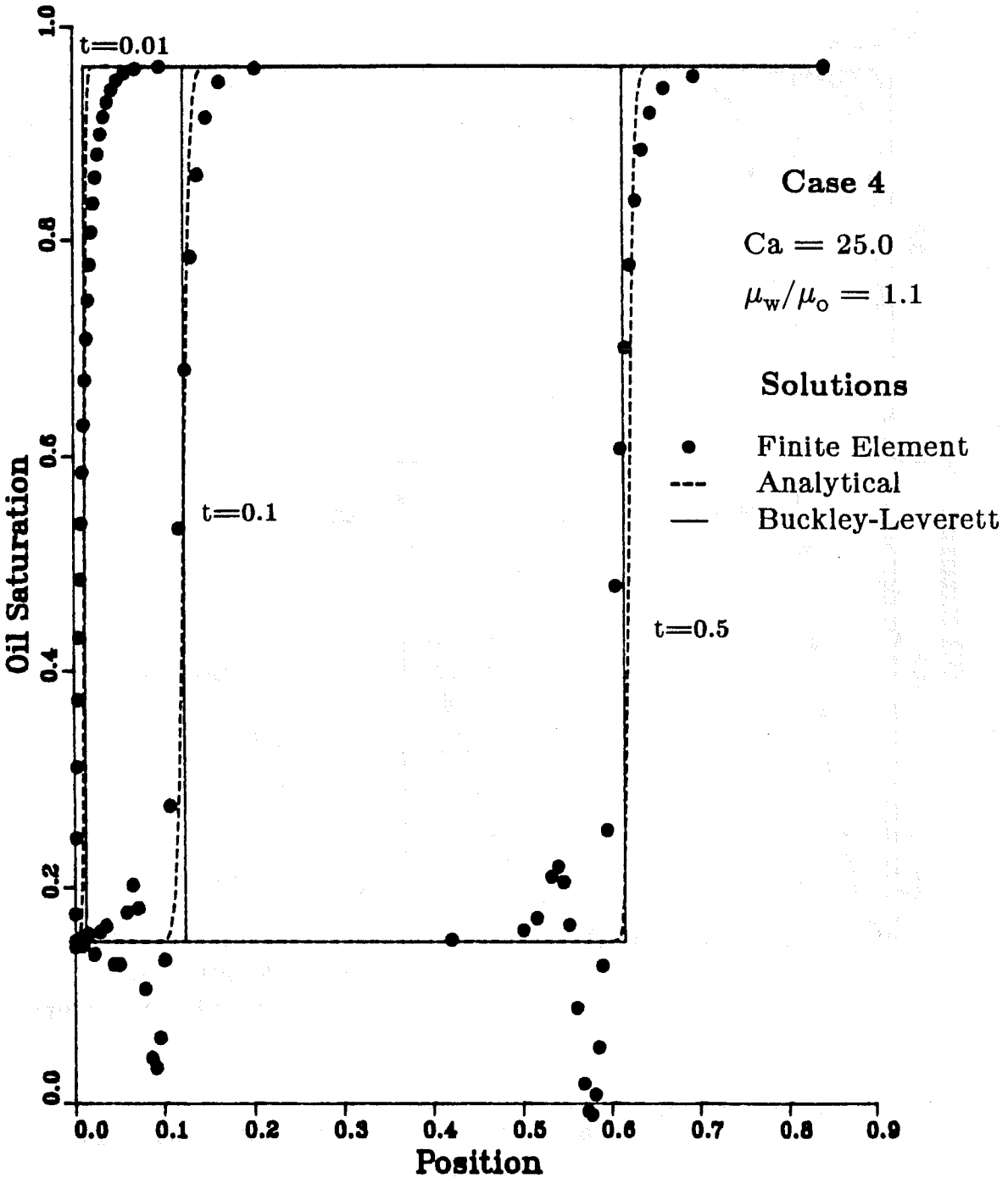

Figure 16. Case 4 solutions at three time levels.

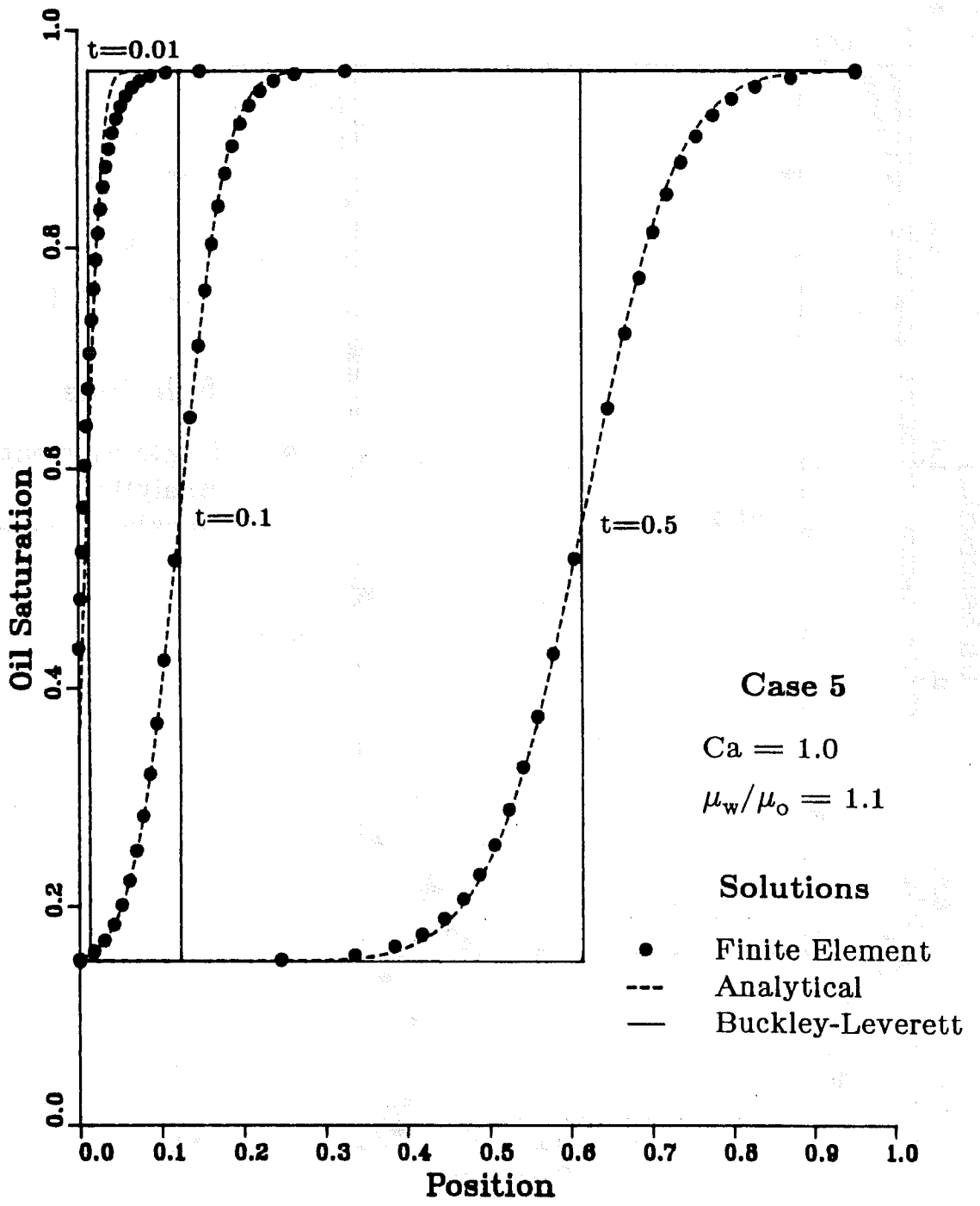

Figure 17. Case 5 solutions at three time levels.

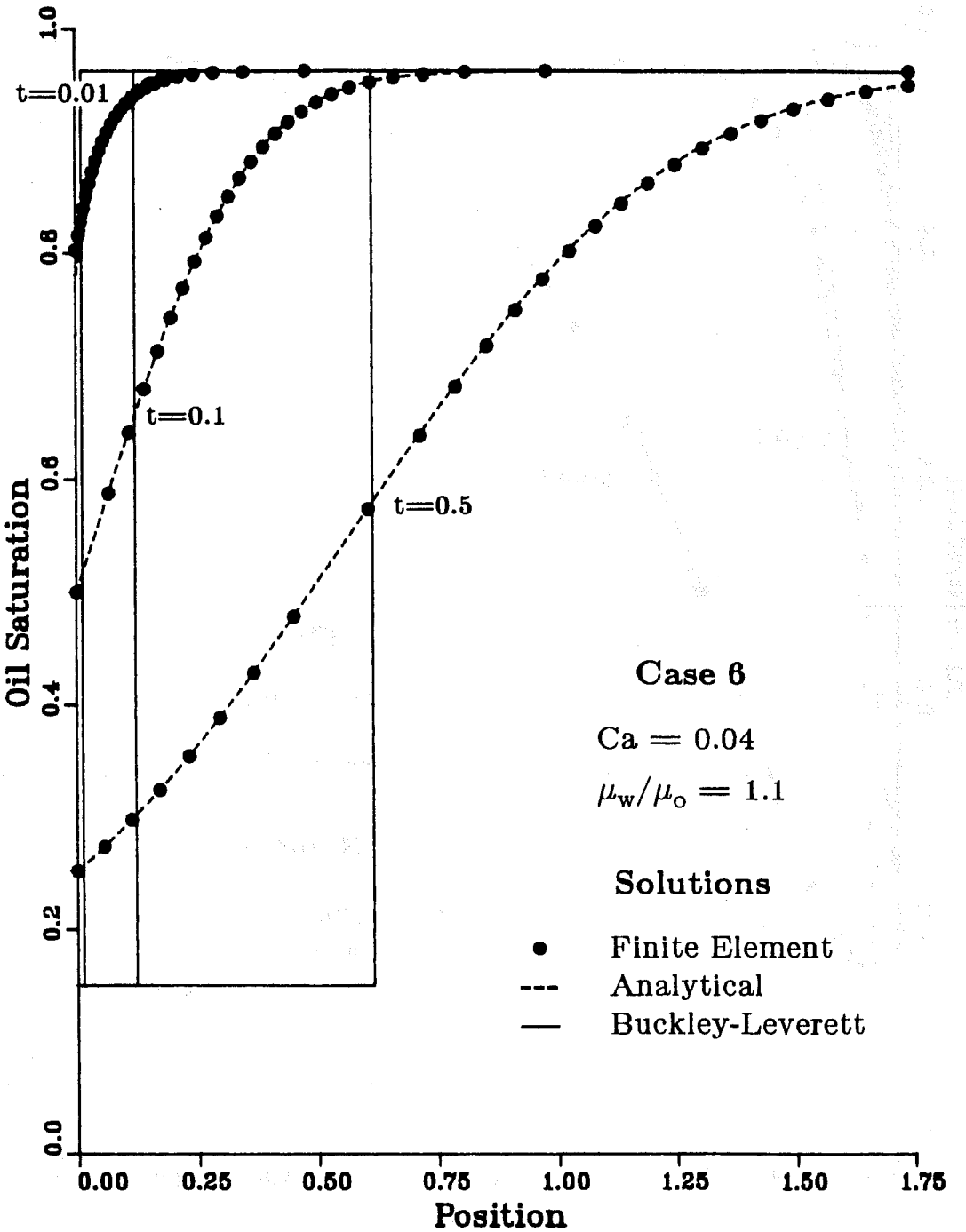

Figure 18. Case 6 solutions at three time levels.

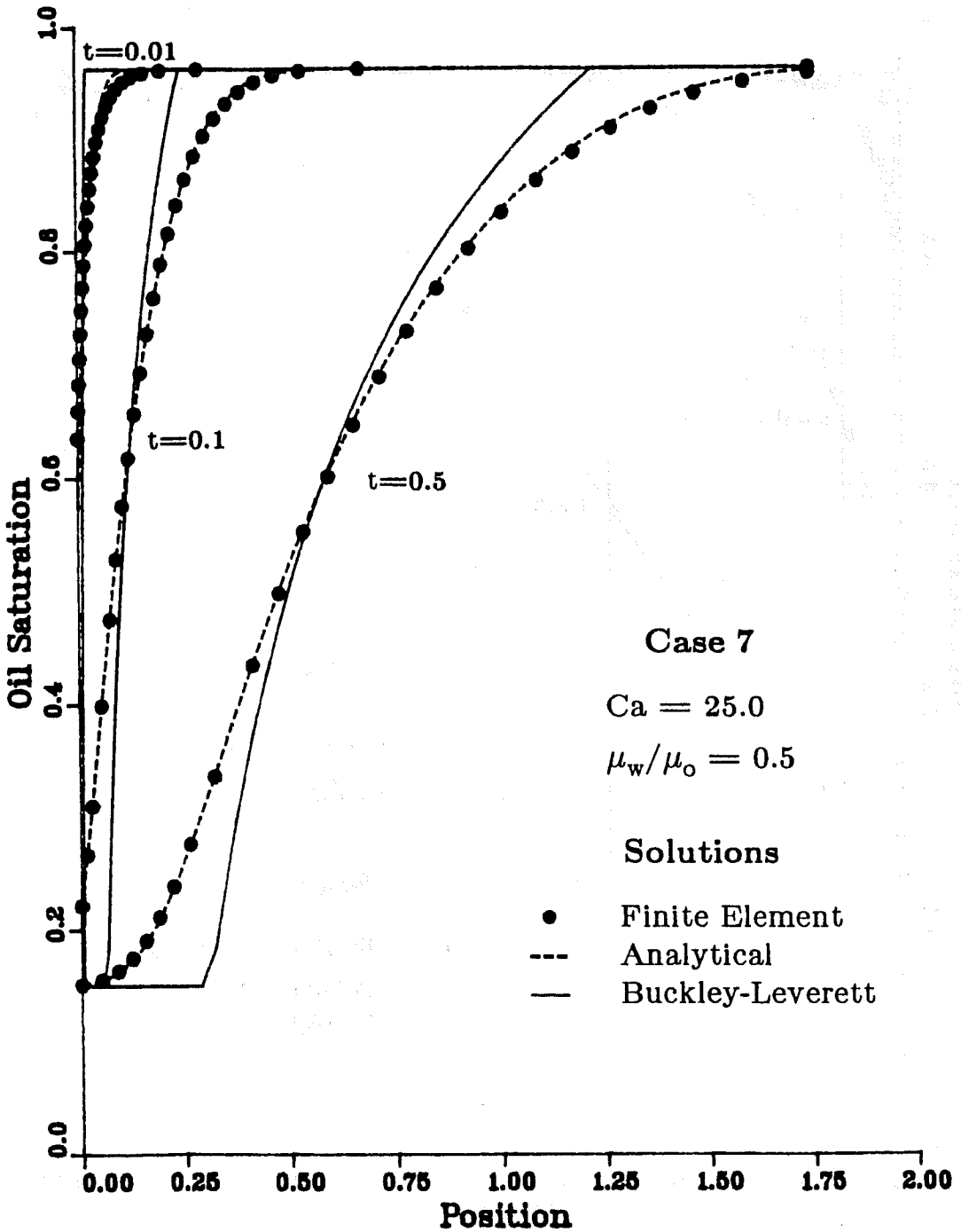

Figure 19. Case 7 solutions at three time levels.

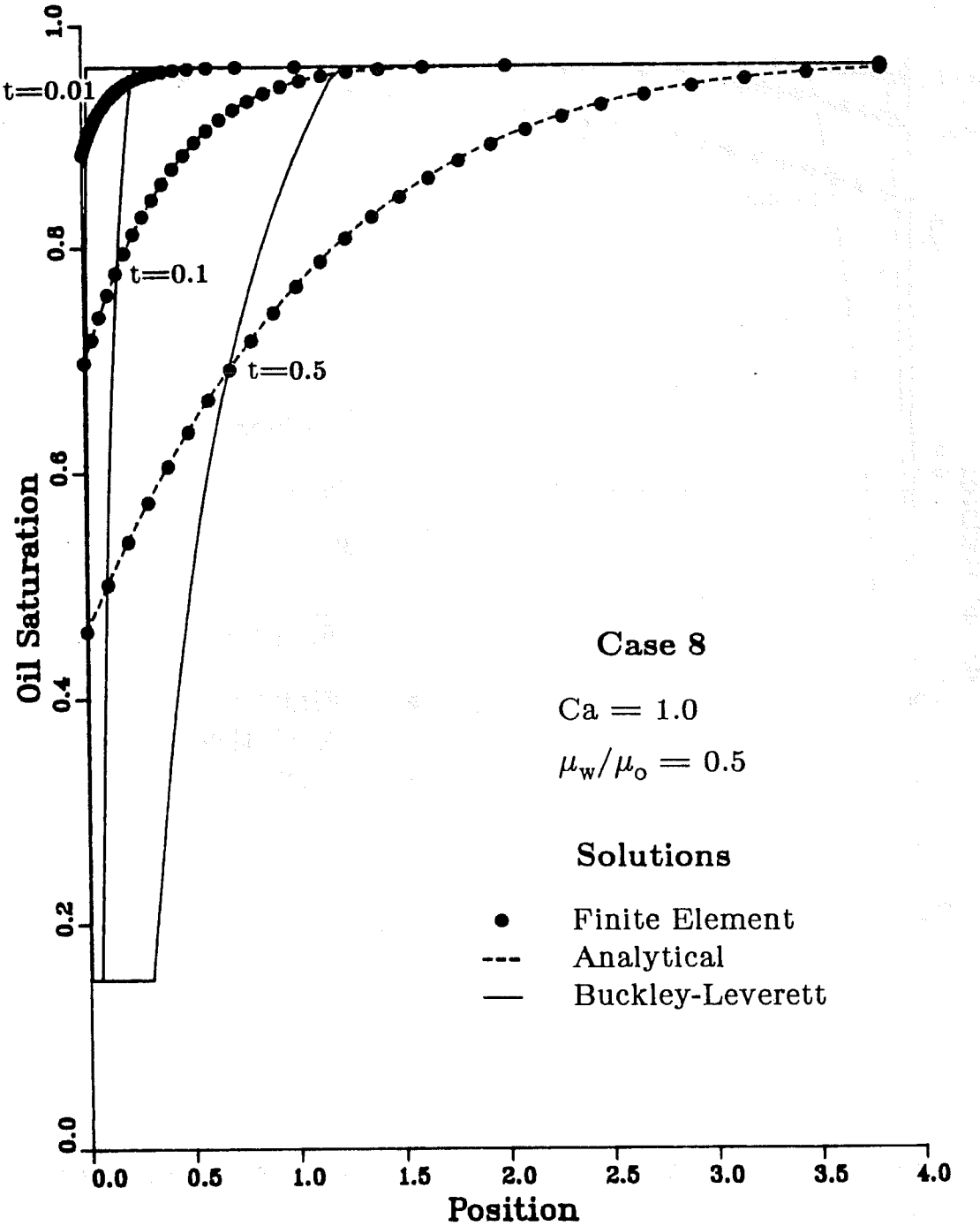

Figure 20. Case 8 solutions at three time levels.

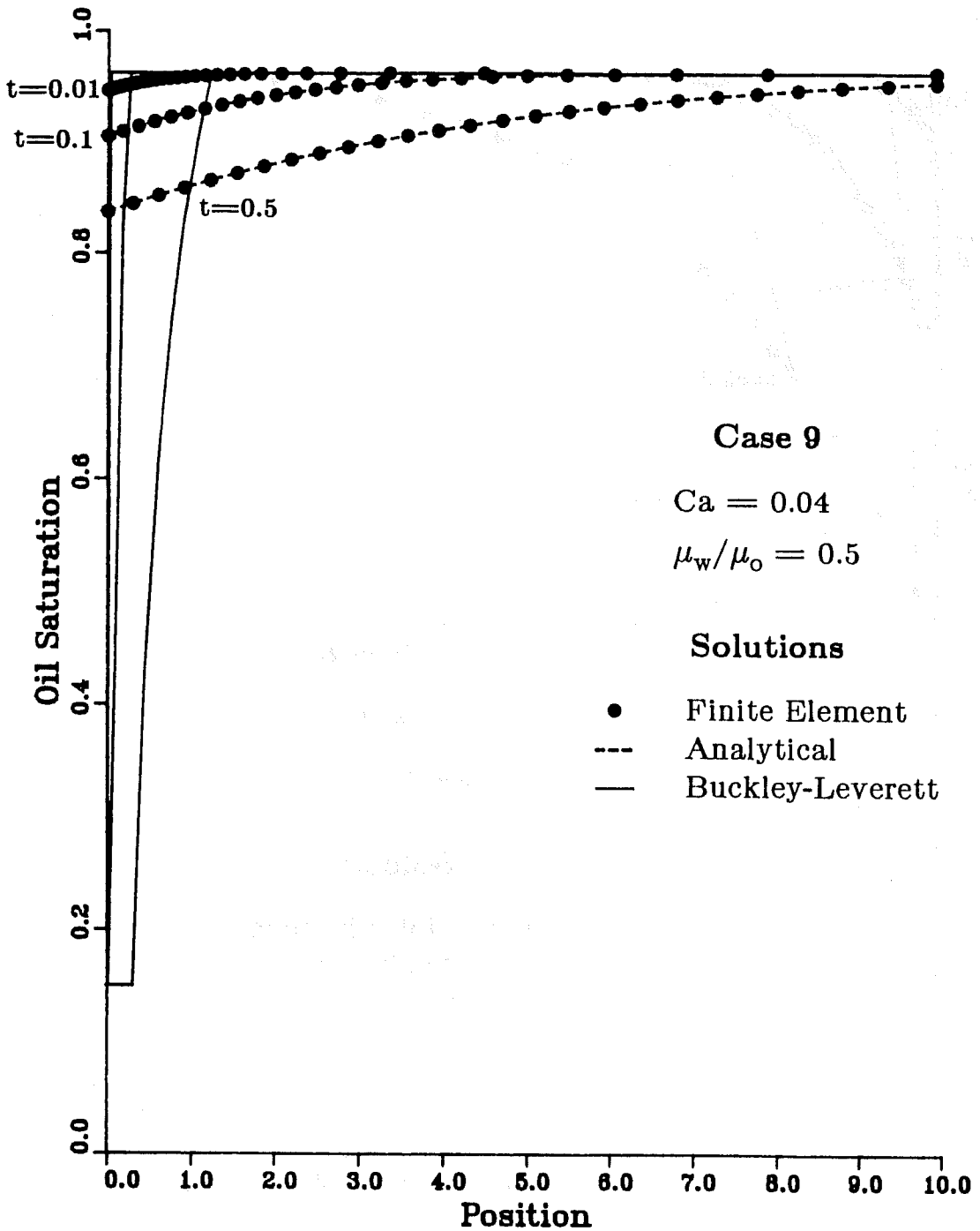

Figure 21. Case 9 solutions at three time levels.

each of the nine cases in numerical order. Plotting the Buckley-Leverett solution emphasizes the degree of capillary (physical) dispersion, whereas the amount of numerical (unphysical) dispersion is evaluated by comparing the analytical solution to the Galerkin finite element results. The parameter values given in Table 2 are used for all nine cases. Clearly, the Galerkin finite element technique performs well in all cases, with the exception of case 4.

Case 4 merits discussion and serves to introduce a detail which concerns the time stepping. It is no coincidence that the steepest front suffers from numerical stability problems. The physical situation at time $t=0^+$ is responsible for this instability as follows. At the initial condition, $S=1-S_{wr}$ throughout the medium. After a finite time step, however, an abrupt change in saturation has occurred near the injection face, especially if the displacement front is sharp. Since Crank-Nicholson time stepping employs the saturation values from the previous time level (both to evaluate $\mathbf{F}(\mathbf{u}^t)$ and to update $\mathbf{u}^t$ itself), this severe change sets off an instability which ripples through succeeding time levels. In case 4, the initial instability is above the critical amplitude — it does not decay with time.

In fact, *all nine cases are run with one initial implicit Euler time step,* unless otherwise noted. Since Euler time stepping uses the previous time level's front only as a datum (to which $\mathbf{F}(\mathbf{u}^{t+1})$ is added to obtain $\mathbf{u}^{t+1}$), it is less susceptible to such instabilities. The tradeoff is numerical dispersion: there is a clear difference between the analytical and Galerkin finite element solutions in the cases of sharp fronts at time t=0.01, after the Euler time step.

Another possible fix to this stability problem is to begin with a saturation front at time t=0 which will evolve smoothly, without severe changes. In fact such a situation is more realistic: discontinuous fronts are simply unphysical — even the basis of the working equations becomes invalid, as noted earlier. Unfortunately, altering the initial conditions in any way strictly abandons the analytical solution.

This instability deserves further analysis, perhaps quantitative. While the above qualitative discussion serves the current purpose, a rigorous treatment is more powerful and may be of use in similar problems. Furthermore, when the

Table 2. Parameter Values for All Nine Cases

Number of Elements	50
Time Step	0.010
Critical Average Node Movement, ϵ	0.0005
Root of Estimated Error Summed, r	4
Irreducible Water Saturation, S_{wr}	0.0375
Irreducible Oil Saturation, S_{or}	0.15

two-dimensional simulation work begins, the difference between numerical instability and physical instability (viz., that which produces viscous fingers) must be clear.

Mesh Evolution Results

The final topic of discussion in this section is the evolution of the finite element meshes in the nine cases. Given the error equidistribution scheme used (see above section), the nodes should be concentrated in regions of high solution curvature, since piecewise linear basis functions are used.

At one extreme, a sharp S-shaped front must have nodes clustered at the two curves in the "S" with the linear portions remaining sparsely populated. Ideally, this node density profile persists as the front advances through the medium, i.e. the dense regions move with the front. As proof of the algorithm's success, Figure 22 presents the evolution of the mesh for case 1, which has a sharp front (see Figure 13). Each row of dots shows the positions of the nodes on the convergent mesh at that time level. The two dense branches which evolve mark the regions of greatest solution curvature, which are successfully tracked by the algorithm. An interesting feature is the narrow sparse region between the densest areas — this marks the short, linear, central portion of the front. Also, there is a temporal oscillation in the position of the interior nodes nearest the injection face; at these early time levels, the front is yet developing. This minor instability is caused by the rapidly-changing curvature in that region; again, the effects of the abrupt saturation change at the injection face are felt. Fortunately, the oscillations are damped quickly, and all nodes assume a smooth velocity.

At the other extreme, a highly dispersed front, the mesh is expected to become uniform with no regions of high density. In fact, that is what occurs for case 9, which experiences the most dispersion (see Figure 21). The corresponding mesh evolution profile appears in Figure 23, which has initially a high-density region as the front enters the medium and later a uniform density when the front is fully developed. There is no hint of the node oscillation mentioned above, for the saturation at the face changes relatively slowly.

These evolution profiles suggest an improvement to the mesh adaptation algorithm. Currently, the initial mesh for a new time level is the convergent mesh from the previous time level. The continuation-adaptive scheme is then applied. A method of reducing the number of mesh iterations required is to predict the initial mesh at a new time level by extrapolating from the positions of the convergent nodes at the previous two or three time levels. The steady node motion displayed in Figures 22 and 23 suggests that this is feasible, although there is a point of caution. Small oscillations in nodes' positions upset this scheme, as nodes must not cross over each other (they should remain ordered). These concerns can likely be allayed through minor "bookkeeping" work, which would not consume the gains made in execution time by not solving $\mathbf{J\Delta u=-f}$ as often. Evaluating this idea is a high priority, as a possibly analogous method in two dimensions would be a significant time saver.

Effects of Varying the Numerical Solution's Parameters

Brief discussions of the impact of changing six key parameters follow. The six include number of elements, mesh convergence criterion, root of estimated

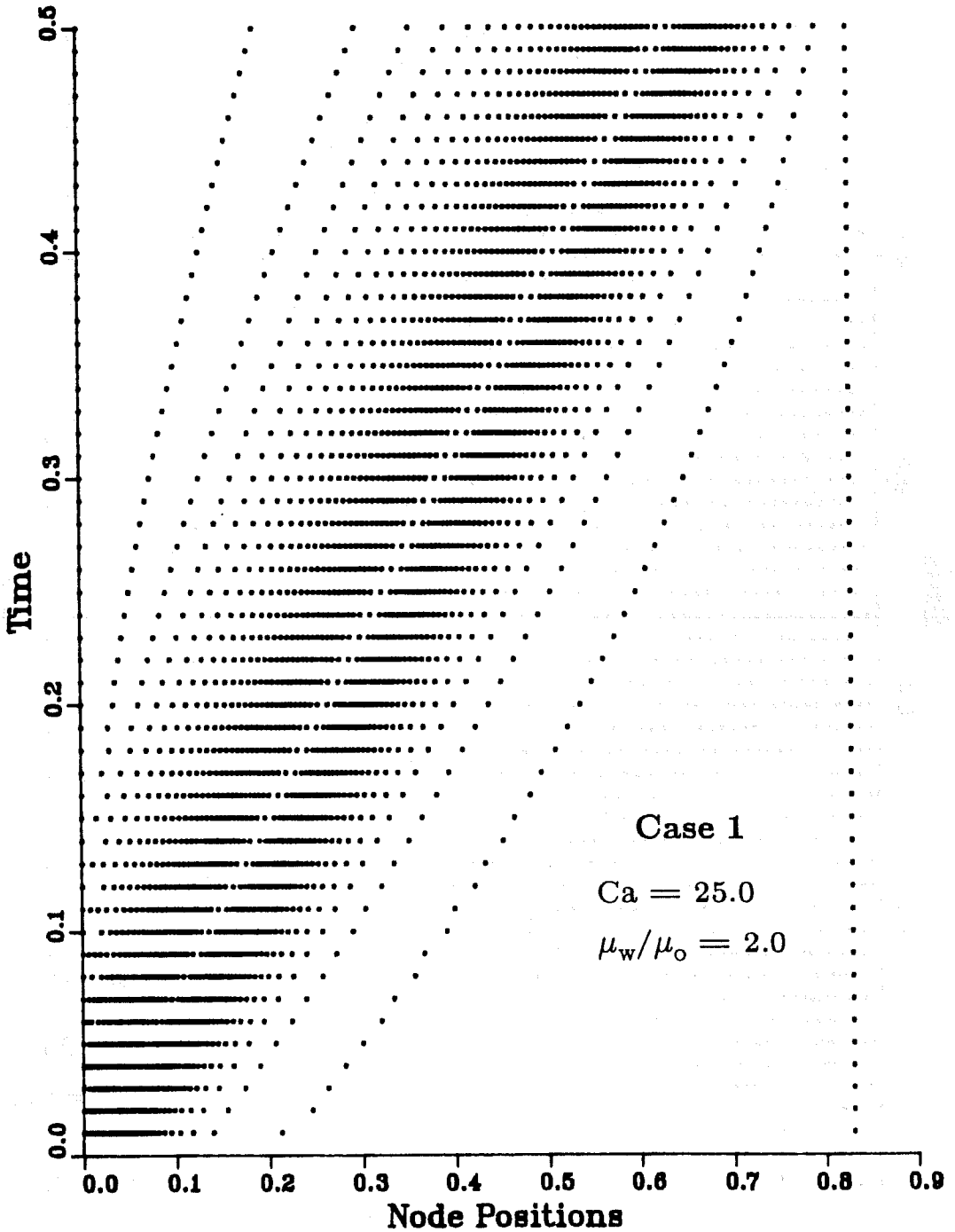

Figure 22. Evolution of the finite element mesh for case 1, which has a sharp, S-shaped front.

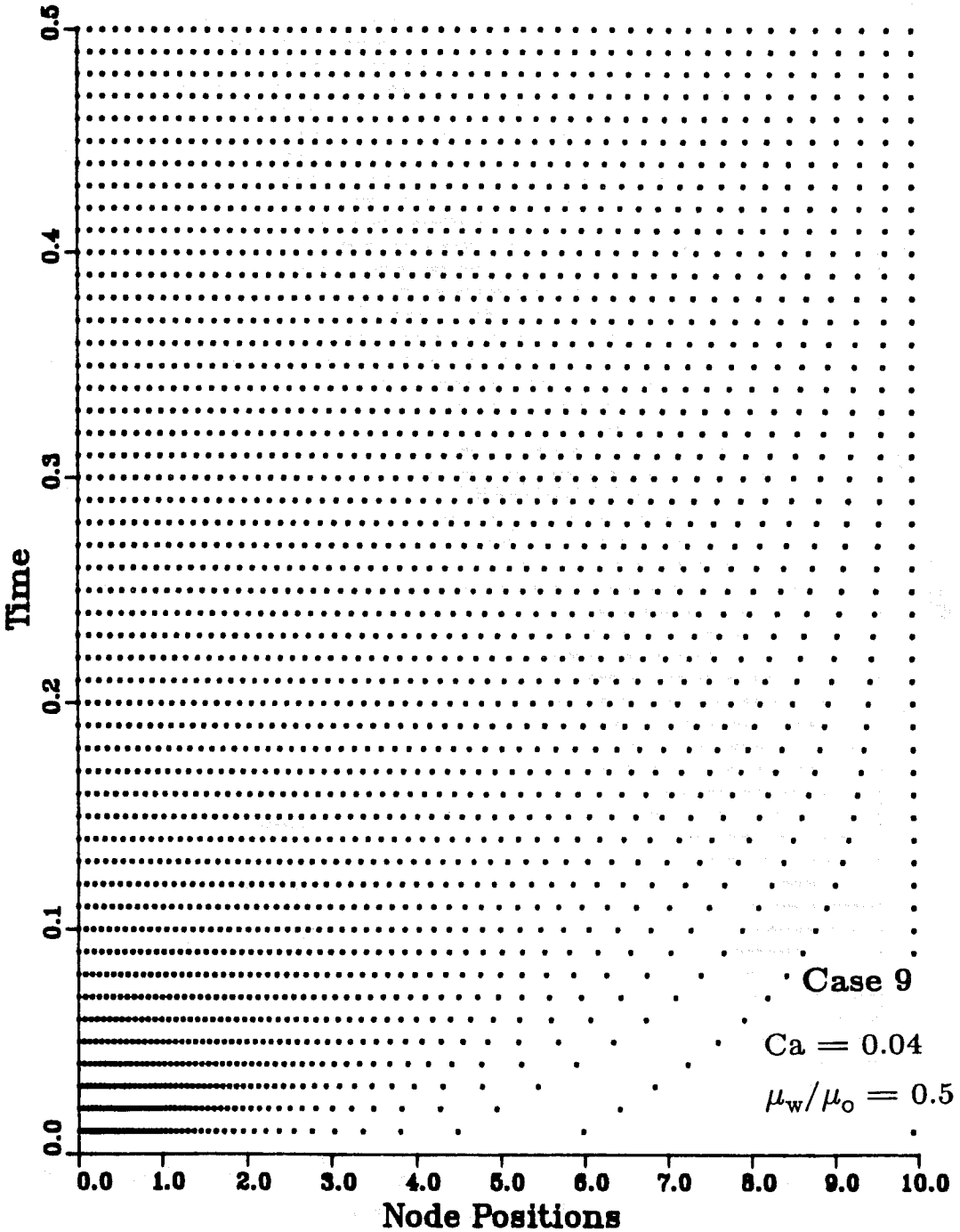

Figure 23. Evolution of the finite element mesh for case 9, which has a highly-dispersed front.

error summed, time step, number of initial Euler time steps, and finally, the domain truncation point. Such a task could easily constitute an entire chapter, but the goal is to provide succinct, qualitative discussions with some quantitative information.

Number of Elements, N-1

The effect of changing the number of elements in the mesh is perhaps the simplest to explain, at least qualitatively. Too few elements distributed across the domain become too sparse when a front possesses any regions of curvature, to which the nodes migrate. Since piecewise linear basis functions are used, poor approximations of the solution result as curvature cannot be well represented in all areas. After many time steps, error accumulates and the solution becomes unacceptable. On the other hand, using too many elements unnecessarily consumes computer time. Using more elements entails more work for all the separate tasks, especially mesh adaptation and solving $\mathbf{J\Delta u=-f}$, the rank of which equals the number of nodes, N.

As is very common in computational work (among other endeavors), a balance must be reached between the faster-but-poorer solution on a sparse mesh and the slower-but-better solution on a dense mesh. Finally arriving at the proper number of elements is done by trial and error, with some intuition initially. A variety of cases is solved with increasing numbers of elements until the solutions no longer change with N. This is a basic numerical principle: *the solution should be invariant to the parameters of the computational scheme.* In the nine cases presented here, fifty elements met this criterion. Fortunately, computational times remained reasonable: all cases required less than one minute of CPU time on the CRAY-2.

Mesh Convergence Criterion, ϵ

A similar balance must be found for the mesh convergence criterion, the tolerable average absolute node motion from one mesh to the next at a given time level. Setting ϵ too large (e.g. ϵ=0.05) ceases mesh adaptation prematurely; nodes fail to migrate to regions of high curvature and, therefore, do not track the front well. A qualitative picture of an actual case appears in Figure 24. Choosing ϵ too small causes problems as well. Even worse than needlessly adapting the mesh (beyond the point of solution invariance with respect to ϵ) is the possibility that the mesh may not even converge with an over-strict tolerance, for example, $\epsilon=10^{-6}$. At this fine level, oscillations in the solutions produced by the continuation-adaptive scheme prevent convergence.

The value of ϵ used was determined by decreasing ϵ until the solution of representative cases became invariant to further change. The value used for all nine cases is $\epsilon=5\times10^{-4}$, above the value at which mesh convergence becomes stubborn and below values which influence the solution when changed.

Root of Element Error, r

As explained above, node motion is damped to aid the convergence of the mesh itself and of the Newton iterations on the next mesh. A *root* of each element's error, rather than the error itself, is summed to compute the equidistributed error value (Equation 32). This effectively damps the motion of the

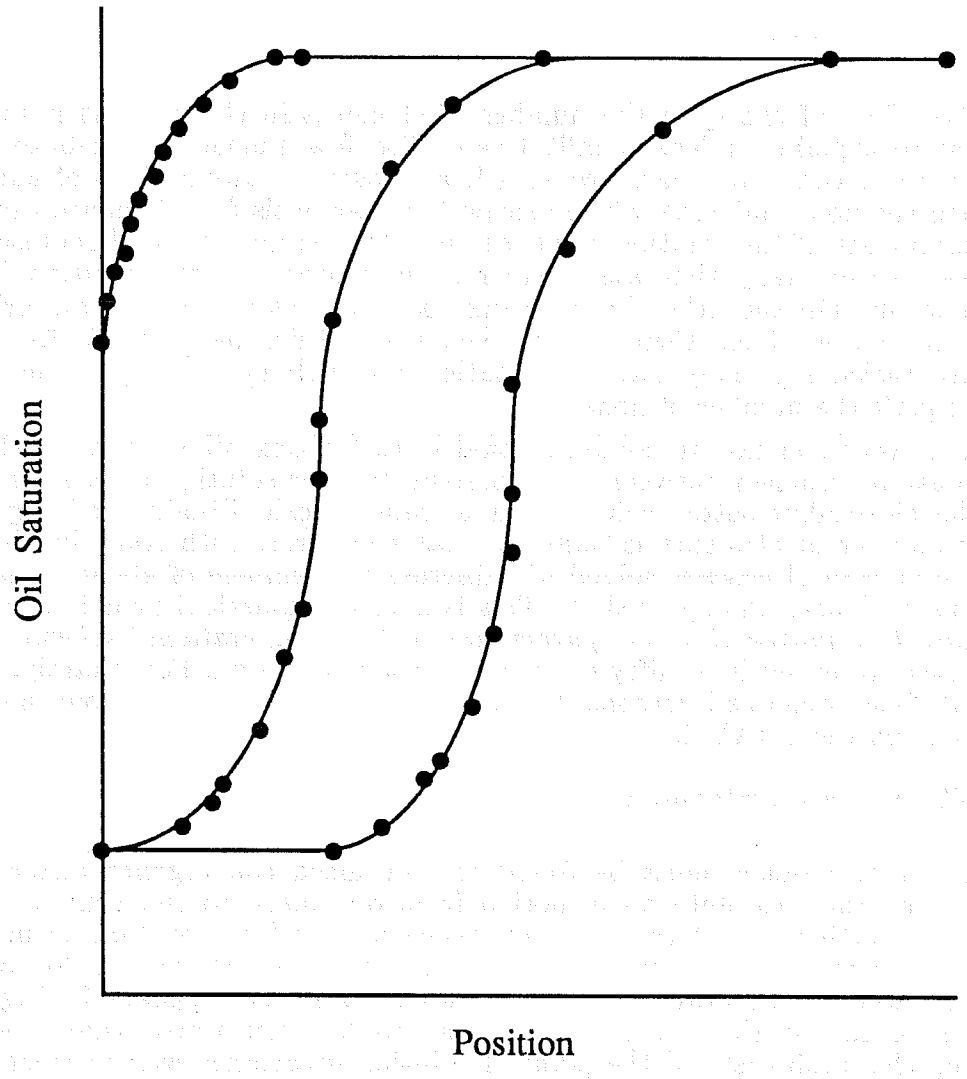

Figure 24. Qualitative diagram showing rarefaction of the mesh in the upper region of curvature, caused by a large value of ϵ. Based on an actual simulation.

nodes. If r is too small, either the convergence of the mesh itself or of the Newton iterations fails and the algorithm breaks down. If r is too large, the mesh is overdamped, and many mesh adaptations are necessary for convergence, wasting computational effort.

The proper value of r is obtained as those of N and ϵ. The root is set large enough for the algorithm to succeed and then increased until the solutions are invariant. Quantitative details for a typical case appear in Figure 25, which clearly shows the types of behavior. The critical value of r is evidently dependent on ϵ: a smaller value of ϵ necessitates a larger value of r. Finally, if a mesh is evolving slowly, ϵ must be sufficiently small so that the adaptation is not stopped prematurely. The parameters ϵ and r must be considered in combination.

Time Step, Δt

Choosing the proper time step is a concern common to every discretized transient system. In general, very small time steps produce the most accurate solutions for a cost, while large steps risk increased time discretization error and numerical instability. A proper time step is found using the solution invariance principle applied to the above parameters; t=0.01 is the value used here throughout with success. More work is required in this area to draw quantitative conclusions; if possible, a theoretical analysis could be attempted.

Number of Initial Euler Time Steps

As discussed in above, one initial implicit Euler time step is used before the Crank-Nicholson steps in all cases. Its purpose is to insulate the developing front from the unphysical shock associated with the entrance of a steep front into the medium. A single Euler step is sufficient for all nine cases except case 4, which has the steepest front. In this case, instability persists in the Crank-Nicholson steps, even after five or ten initial implicit Euler steps, suggesting that the cause may be the change in time stepping methods, not the steepness of the front only. As shown earlier, since the Euler time stepping error is $O(\Delta t)$, its use should be minified to avoid unnecessary numerical dispersion.

Domain Truncation Point, L

The boundary of the finite element solution domain must be in the region where the asymptotic solution of the controlling partial differential equation is valid. The details, including a general starting guess for L and the Robin boundary condition obtained from the asymptotic analysis, are discussed above. Basically, L is increased until the solution is invariant. Minor caution must be taken in not making L too large, for then the mesh could become too sparse.

CRAY-2 Considerations

All results presented were obtained on the CRAY-2/1 supercomputer, a machine at the forefront of computing technology. The two special features of the CRAY-2 are vectorization and multitasking of code, which, respectively, enable speedup as measured in CPU time (and, therefore, real time) and in real time only. This section provides general definitions of these two features, their

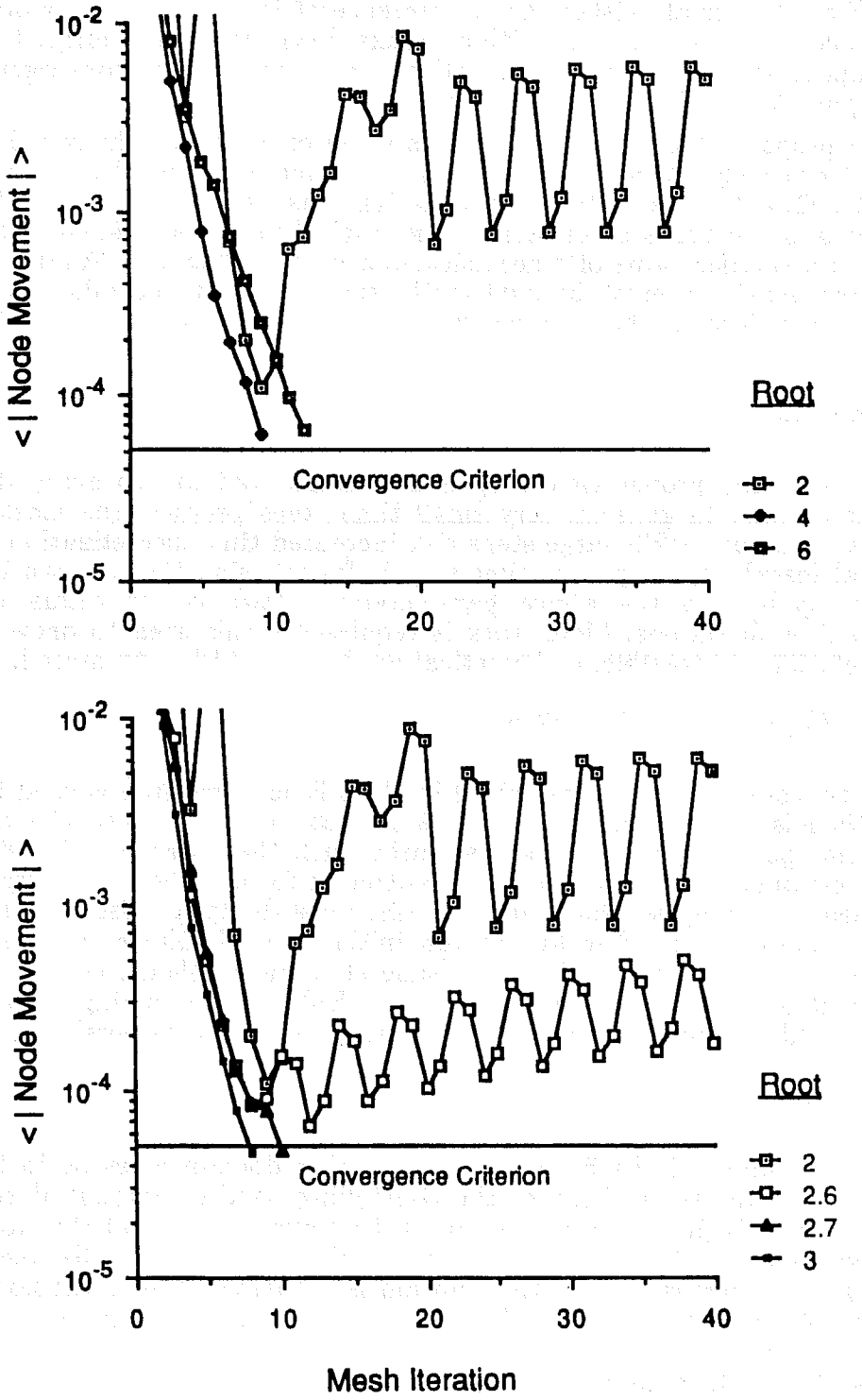

Figure 25. Mesh convergence progress for various r-values at a given time level. Case: Ca=25.0, μ_w/μ_o=1.6. Plot (b) refines the critical value of r for the given tolerance ϵ=5X10^{-5}.

relevance to the finite element algorithm, and specific execution times of the major tasks in the algorithm.

Vectorization

In general, vectorization is the performance of floating point operations (+ - * /) on an entire string of scalar values (i.e. a vector) at once, versus on each scalar value separately. For example, consider the following loop.

```
DO I = 1, N
  A(I) = A(I) + K * B(I)
CONTINUE
```

A scalar processor sequentially references *each* value of the vector B, multiplying it by K and adding it to the appropriate value in vector A. On the other hand, a vector processor references *all* values of B at once, multiplying them all by K and adding them to the vector A. This simultaneous execution of the floating point operations can easily reduce execution time by an order of magnitude, depending on the vectors' length. In reality, the CRAY-2 processors operate on 64-word sections of the vectors; if a vector is larger than this, it is divided into segments of that length.

Unfortunately, not all loops are vectorizable. First, only innermost DO loops can be vectorized. Second, even some of these have characteristics which prevent vectorization. A simple example is the following loop, which, if vectorized, would destroy the values of A which are intended to be assigned to C:

```
DO I = 1, N
  A(I) = B(I)
  C(I) = A(I+1)
CONTINUE
```

Also, loops which contain recurrences such as

```
DO I = 1, N
  A(I) = B(I) - C * A(I-1)
CONTINUE
```

must be scalar processed. In general, by examining a loop with the process of vectorization in mind, one can tell if a loop will vectorize or not.

At compilation, a source code can be requested which provides specific vectorization data, listing the vectorization status of each inner loop. This identifies where potential modifications could be of great help in speeding execution.

Multitasking

Multitasking (also known as parallel processing) is the simultaneous execution of two or more sections of code (i.e. tasks) by separate processors. This

feature can reduce the wall-clock time of execution only, not the CPU time, since a given code requires a fixed amount of computational work regardless of the number of processors employed. In fact, multitasking *increases* total CPU time, owing to the overhead associated with coordinating the processors.

Unfortunately, parallel processing does not enjoy the relatively easy implementation of vectorization. There are several drawbacks.

(1) Parallel processing is inherently more complex than vectorization, since segments of code which can be run independently must be identified. Many algorithms do not make this convenient or even possible.

(2) There are lines in any code at which all processors must have completed their respective tasks before execution can continue. If the simultaneously-executing tasks require different amounts of computational effort, processors which finish first must wait idle, decreasing efficiency.

(3) Amdahl's Law, which specifies the real-time speedup associated with multitasking (the decrease in wall-clock time relative to single-processor execution), places a strict theoretical limit on the possible real-time decrease. For example, on the four-processor CRAY-2, the *best possible* speedup for a code which has 75% of its execution time parallel processed is only 2.28 (CRAY-2 Multitasking Programmer's Manual). Amdahl's Law assumes no multitasking overhead or delays, which are present in any parallel-processed code.

(4) Of great importance is attempting parallel processing in the current timeshared environment. As a requirement for the course CSci5399, a multitasked conjugate gradient code (for solving Ax=b with symmetric, positive definite A) was composed and executed on the CRAY-2/4. At a rare time when only five or ten users were logged in, a 10% speedup was observed. This is modest, but a speedup was possible nonetheless. Most often, the number of users demanding memory and CPU time encumbers severely the performance of multitasked code, resulting in a great *slowdown* versus a *speedup*. Typically, with over 35 users logged in, the multitasked code runs six or seven times slower than the single-processor code.

This experience and the other limitations listed above discourage multitasking of the finite element code used in this work. At any rate, multitasking always consumes more CPU time (investigators' resources) than single-processor code, and a real time speedup is not significant for a code which takes one minute to execute.

Timing of Major Tasks in the Algorithm

The CRAY-2 provides routines for measuring CPU time spent in the various tasks of an algorithm. This enables identification of key tasks which should be modified, if possible, to improve the code's overall efficiency. Timing results for the nine cases are similar; thus, Table 3 presents CPU time data for case 1 only. (Figure 3 presents the algorithm.)

A surprise is the amount of time required to compute the analytical solution at the 51 nodes for a given time step. Yortsos and Fokas' solution and algorithm for finding $S(x_o,t_o)$ requires one root-finding task at each value of x_o and t_o. While the time per call is high, this solution is required only at the time steps plotted for comparison to the finite element results. An algorithm

Table 3. CPU Time Spent in the Major Tasks, Case 1

Task	Total (s)	Total (%)	Times Executed	Time/Execution(ms)
All executable statments	59.93			
Inverting **A** (tridiagonal)	1.33	2.22	251	5.30
Evaluating **J**,-**f**	0.52	0.87	805	0.65
Solving **J**Δ**u**=−**f** (IMSL)	55.67	92.89	805	69.2
Adapting mesh	0.51	0.85	251	2.0
Computing analytical soln.	1.37	2.28	3	457.
Remainder	0.53	0.89		

suggested by H. T. Davis[15] eliminates the root finding and should greatly reduce the execution time for this task.

As expected, most computational effort is required to perform the Newton iterations. This task has the second-highest time per execution and is the task performed the most. A 51×51 system of linear algebraic equations is solved each Newton iteration; these iterations are performed on each mesh on each time step. Thus reducing this task's execution time can be attacked from two fronts:

(1) Reduce the time per call by using a faster **Ax=b** solver, or perhaps re-express the formulas so that a full **Ax=b** system does not result, i.e. try to preserve the tridiagonal matrix structure associated with piecewise linear basis functions. Late Jacobian updating would also reduce the time per **Ax=b** solution since **J** needs to be inverted only once per Jacobian update. Thus, several Newton iterations at constant **J** are less expensive than iterations in which **J** is updated for each. If late updating results in more iterations, however, the decrease in execution time is reduced.

(2) Reduce the number of Newton iterations directly or the number of mesh adaptations (more likely, perhaps by using the nodal position extrapolation scheme proposed above. The Newton iterations will then need to be performed fewer times. Also, this end can be achieved by using larger time steps — an advantage of using an efficient time integration software package.

Conclusions

The adaptive Galerkin finite element algorithm based on Benner's work successfully simulates one-dimensional, two-phase flow in porous media in eight of the nine cases studied. Comparing the finite element results to the analytical solution of Yortsos and Fokas provides strong evidence to support this claim. The lone failure is for a nearly discontinuous front, which imparts instabilities.

Possible fixes include using a sharp front as the initial condition, versus a medium saturated with oil which is immediately penetrated by a sharp front.

For this work, vectorization is the greatest advantage of the CRAY-2, not multitasking. The gains from vectorization are independent of the number of users working on the CRAY-2, whereas experience with a project in CSci5399 indicates that multitasking produces a slowdown (versus a speedup) in a timeshared environment, even for a code which is highly multitasked. The simulator's execution time is between 50 and 60 seconds for all nine cases, not an excessive amount. Improvement in overall efficiency is best addressed by modifying the solution of $\mathbf{J\Delta u=-f}$ for each Newton iteration or by reducing the number of iterations per time step. Decreasing the number of steps required to reach the final time level would help as well; using adaptively-sized time steps is suggested.

A goal in simulating one-dimensional displacement before tackling the two-dimensional, or three-dimensional, problem is to obtain insight from the simpler case. This experience leads to these suggestions for future work:

- The continuation-adaptive strategy performs well, and Benner finds it more efficient than the implicit-adaptive strategy, in which the nodes' positions and the saturation values are computed simultaneously.

- Implicit Euler and Crank-Nicholson time integration routines are effective initial tools; however, once these are applied successfully, a more efficient software package or the scheme used by Benner and Heiba based on that of Gresho *et al.* is preferred. Performance of these routines can be evaluated by comparison with the simpler Euler or Crank-Nicholson results.

- Damping the movement of nodes from one mesh iteration to the next prevents mesh and Newton iteration convergence problems, although higher-order roots (4, not 2) are required here.

- Mesh adaptation in two or three dimensions is inherently more complex than in one dimension. Digestion of the relevant literature is mandatory, as is taking advantage of experience at Minnesota (Christodoulou, Pranckh). Simpler schemes should be tried initially, building a foundation for research into more complex methods.

- The asymptotic analysis used to determine a proper domain boundary and a Robin boundary condition there is a new means of addressing the domain truncation issue. A two-dimensional analogy should be derived.

- Computer programs must be composed which take full advantage of the CRAY-2's vectorization capabilities. On the other hand, the prospect of multitasking future codes is bleak because real time speedup is not crucial and not even possible in the current timeshared environment. Fortunately, the CRAY-2 has convenient timing devices for pinpointing the most inefficient portions of a code.

References

1. Fokas, A. S., and Yortsos, Y. C., SIAM J. Appl. Math. **42**, 318 (1982).

2. Yuster, S. T., Proc. 3rd World Petrol. Congr. **2**, 436 (1951).
3. Lefebvre du Prey, E. J., Soc. Pet. Eng. J. (February 1973), 39.
4. Davis, H. T., Advanced Mathematics for Chemical Engineers Course Notes, ChEn 8202, University of Minnesota, Minneapolis, 1986.
5. Benner, R. E., Jr., *Equilibria, Stability, and Bifurcations in the Physics of Fluid Interfaces*, Ph.D. Thesis, University of Minnesota, Minneapolis, 1983.
6. Heiba, A., *Porous Media: Fluid Distributions and Transport with Applications to Petroleum Recovery*, Ph.D. Thesis, University of Minnesota, Minneapolis, 1985.
7. Jerauld, G. R., H. T. Davis, and Scriven, L. E., SPE 13164, presented at the 59th Annual Technical Conference and Exhibition, Houston, September 16-19, 1984.
8. Press, W. H., Flannery, B. P., Teukolsky, S. A., and Vetterling, W. T., *Numerical Recipes*, Cambridge University Press, New York, 1986.
9. Burden, R. L., Faires, J. D., and Reynolds, A. C., *Numerical Analysis*, 2nd ed., PWS Publishers, Boston, 1981.
10. Gresho, P. M., Lee, R. L., and Sani, R. C., in *Recent Advances in Numerical Methods in Fluids, Vol. 1*, ed. by C. Taylor and K. Morgan, Pineridge Press, Swansea, U.K., 1979.
11. Yortsos, Y. C., and Fokas, A. S., Soc. Pet. Eng. J. (February 1983), 115.
12. Welge, H. J., Trans. AIME **195**, 91 (1952).
13. Cardwell, W. T., Jr., Trans. AIME **216**, 271 (1959).
14. Sheldon, J. W., and Cardwell, W. T., Jr., Trans. AIME **216**, 290 (1959).
15. Davis, H. T., Personal Communication, 1987.

ABSTRACTS OF PUBLICATIONS

Studies in the Microstructure of Microemulsions, Ph.D. Thesis, University of Minnesota, June 1986. By D. M. Anderson.

A microemulsion is a thermodynamically stable liquid phase in which oil and water are cosolubilized with a surfactant. Microemulsions show great promise in enhanced oil recovery processes, and in polymerization reactions. Recent experimental evidence indicates that some microemulsions are bicontinuous, i.e., both water continuous and oil continuous. The geometric requirements governing the surfactant-rich interfacial film that divides oleic from aqueous microdomains are elucidated in this thesis, and incorporated into new microstructural models that are then applied to scattering experiments. Particular attention is paid to the relation between microemulsions, and cubic phase and hexagonal phase liquid crystals.

While there are eighteen triply periodic minimal surfaces that reportedly are free of self intersections, to date there has been no example of a triply periodic surface of constant, *nonzero* mean curvature that is embedded in $\mathbf{R}^3$. In this thesis five families of such surfaces are computed and displayed with computer graphics. Three of the families evolve continuously from close-packed sphere configurations, through bicontinuous structures, to sphere packs with mean curvature of the opposite sign as the original sphere pack. These families demonstrate that the transition from oil-in-water dispersions to water-in-oil dispersions can proceed through bicontinuous structures without an abrupt inversion, even under the constraint of a constant-mean-curvature surfactant film.

A penetrable cylinders structure is proposed as a model of microemulsion microstructure, and small-angle X-ray scattering (SAXS) data on microemulsions made from three pure components are shown to be consistent with the model but not with previously proposed models. The penetrable cylinders structure is naturally related to hexagonal phase structure which consists of ordered arrays of cylinders, and, it is shown, to one of the families of periodic models presented. In the pure-component system, and in another system with a commercial surfactant, SAXS and conoscopy data indicate a close relationship between the microemulsions and liquid crystals studied. The structures of bicontinuous microemulsions, hexagonal phase, and bicontinuous cubic phase liquid crystals are all shown to fall under a single framework.

Bicontinuous Microemulsions and the Mean Curvature of the Oil-Water Interface, J. Phys. Chem. (to be submitted). By D. M. Anderson, H. T. Davis, D. F. Evans, and L. E. Scriven.

Recent experimental evidence indicates that some microemulsions are bicontinuous, i.e., both water continuous and oil continuous. Geometric requirements governing the surfactant-rich interfacial film that separates the water and oil labyrinths have not been carefully addressed. We elucidate these requirements and show how they are exhibited in proposed

microstructural models. Particular attention is paid to the relation between microstructural models for microemulsions and for cubic phase and hexagonal phase liquid crystals, and it is shown that the area-averaged mean curvature of the interface provides a structural characterization. We introduce a model bicontinuous structure constructed from randomly placed fully penetrable cylinders; the structure is thus related to that of hexagonal phase liquid crystals. The results of scattering calculations for penetrable cylinders are applied to small-angle X-ray scattering (SAXS) data from microemulsions containing the surfactant didodecyldimethyl ammonium bromide, water, and decane at 23 °C. As water content is increased at equal weight fractions surfactant and decane, the estimated penetrable cylinder diameter increases as does the average area per surfactant head group, indicating head group hydration and lower curvature toward water. At the same ratio of surfactant to decane and 56.3 wt.% water, SAXS indicates a hexagonal phase. In the system Petronate TRS 10-80/ t-amyl alcohol / dodecane / NaCl brine, SAXS and conoscopy are used to examine a birefringent phase that is in equilibrium with a microemulsion over some composition ranges. A hexagonal phase structure is proposed for the birefringent phase, which has been previously shown to share shear-thinning behavior with microemulsions in the same salinity scan.

Periodic Surfaces of Prescribed Mean Curvature, Phil. Mag. (to be submitted). D. M. Anderson, H. T. Davis, J. C. C. Nitsche, and L. E. Scriven.

While there are eighteen triply periodic minimal surfaces that reportedly are free of self intersections, to date there is no known example of a triply periodic surface of constant, *nonzero* mean curvature that is embedded in $\mathbf{R}^3$. We compute and display five families of such surfaces, where every surface in a given family has the same space group, the same Euler characteristic per lattice-fundamental region, and the same dual pair of triply periodic graphs that define the connectivity of the two labyrinthine subvolumes created by the infinitely connected surface. Each family is comprosed of two branches, corresponding to the two possible signs of the mean curvature, and a minimal surface. The branches have been tracked in mean curvature, and the surface areas and volume fractions recorded, with the relation $dA = 2H\, dV$ carefully checked to hold. The three families that contain the minimal surfaces P and Δ of Schwarz and the I. WP minimal surface of Schoen terminate at configurations that are close-packed spheres. However, one branch of the family that includes the F-RD minimal surface of Schoen, and both branches of the family that includes the Neovius surface C(P), contain self-intersecting solutions and terminate at self-intersecting spheres. On approach to the sphere limit, whether self intersecting or close packed, the gradual disappearance of small is in close analogy with the rotationally symmetric unduloids of Delauney. We give what we suspect are analytical values for the areas of the I-WP and F-RD minimal surfaces, and a possible limit on the magnitude of the mean curvature in such families is proposed and discussed. We also report that the I-WP and F-RD minimal surfaces each divide $\mathbf{R}^3$ into two subspaces of *unequal* volume fractions.

The numerical method is based on a new approach to the formulation of the Galerkin, or weak form of the problem of prescribed — not necessarily constant — mean curvature. The Surface Divergence Theorem is applied directly to a vector-valued function that is the product of a scalar weighting function and a vector field chosen to enforce the boundary conditions. This formulation applied in the context of the finite element method provides a robust algorithm for the computation of a surface with: 1) mean curvature a prescribed function of position, and 2) contact angle against an arbitrary bounding body a prescribed function of position or of arc length. A parametrization scheme for triply periodic surfaces is described that calls only for knowledge of the two 'skeletal' graphs; this is demonstrated by the computation of the triply periodic minimal surface S'-S" hypothesized by Schoen, who described only the skeletal graphs associated with the surface. The parametrisation allows for easy calculation of the scattering function for various density profiles based on the solutions, as well as of areas and volume fractions. For the three minimal surfaces — P, D, and C(P) — whose areas and volume fractions are known analytically, the numerical results are in agreement with these values. Furthermore, we review the history of such surfaces, and clear up some inconsistencies in the literature over the D minimal surface.

A Controlled Environment System for Vitrification of Liquid TEM Samples, Proceedings of the 44th Annual EMSA Meeting, New Mexico, Aug. 11-16, 1986. By J. R. Bellare.

Vitrification of aqueous samples has become an important technique for visualization of colloidal dispersions and aggregates by electron microscopy as it prevents phase separation and rearrangement. Thin films of aqueous samples, made by blotting a drop placed on a grid, can be vitrified with ultrafast cooling ($>$ 100,000 K/s) by rapid plunging into melting ethane. However, thinning the sample in uncontrolled laboratory environment causes evaporation, leading to ionic strength and pH changes which can drastically alter the microstructure, especially if the system is near a phase boundary. Such artifacts are prevented by the controlled environment system described here. A poly(methyl methacrylate) chamber encloses a vertical shaft that carries a tweezer holding a grid. Two rubber-septa covered ports in the chamber permit introduction of a drop of sample on the grid, and filter media to blot the drop. Wicked reservoirs in the chamber are filled with volatile components of the sample to prevent specimen evaporation during thinning. A shutter mounted in the chamber base is synchronized with a trigger mechanism that drops the specimen carrying shaft through the shutter opening into a cup of liquid ethane, thus vitrifying the specimen. The system was tested with a 2.0% solution of octyldodecyldimethyl ammonium bromide (which is near a phase boundary); no artifacts were seen when the sample was prepared with our system, while artifacts were present when samples were made without evaporation control. This success permits electron microscopy of systems like liquid crystals and micelles which have several concentration phase-boundaries.

An Improved Controlled-Environment Vitrification System (CEVS) For Cryofixation of Hydrated TEM Samples, Proceedings

of ICEM XIth International Congress on Electron Microscopy, Kyoto, Japan, Aug. 31-Sept. 7, 1986. By J. R. Bellare, H. T. Davis, L. E. Scriven, and Y. Talmon.

Vitrified specimens for TEM prepared in uncontrolled laboratory atmosphere are subject to evaporation, which concentrates solutions and suspensions, and to temperature changes. Moreover, it is difficult to examine microstructure of systems when conditions of interest are at temperatures other than ambient, e.g. liquid crystals and biological systems at in vivo temperature. We report here a temperature and saturation controlled environment vitrification system (CEVS) for vitrified-hydrated sample preparation. The system consists of a vertical shaft with a TEM grid mounted on tweezers, surrounded by a polycarbonate environmental chamber which has reservoirs with wicks to saturate the air, a capacitance sensor to measure humidity, a halogen-quartz heater, and a fan providing forced convection. Thermistors mounted near the grid are used to measure and control the temperature from ambient to 363K, stable to better than 0.1K. Split rubber septa permit introduction of a specimen drop, and filter paper to thin the drop. An opening on the bottom face of the chamber is closed with a camera lens shutter, synchronized to the shaft, so that the shutter opens as the specimen is dropped into melting ethane. Thus the chamber is kept gas-tight and insulated until the specimen is plunged, maintaining environmental control and preventing specimen pre-cooling. A 0.5% sonicated aqueous dispersion of dioctadecyldimethylammonium bromide, which has a phase transition at about 303K, was used to test the system. At 293K the system shows large surfactant sheets and smaller lens-shaped structures which are absent in samples prepared at 323K. The success of CEVS in preserving conditions very similar to the native state opens new avenues in biological and colloidal research.

Microstructural Studies of Surfactant Aqueous Dispersions by a Vitrification Technique, Proceedings of ICEM XIth International Congress on Electron Microscopy, Kyoto, Japan, Aug. 31-Sept. 7, 1986. By J. R. Bellare, H. T. Davis, L. E. Scriven and Y. Talmon.

When dispersed in water, surfactants form a variety of aggregates whose structure depends on the surfactant, its concentration, temperature and the presence of hydrocarbons, alcohols or other surfactants. These aggregates, e.g., micelles, vesicles, liposomes and microemulsions govern the behavior, properties, and applications of many systems encountered in biology, medicine, chemistry and engineering. Only transmission electron microscopy can provide direct high resolution images that may determine unequivocally the microstructure of these systems. We report results of our work on the liquid crystalline aqueous dispersion of sodium 4-(1'-heptylnonyl)benzene sulfonate (SHBS), and the micellar aqueous dispersion of cetyltrimethylammonium-3,5 dichlorobenzoate (CTA-3,5 DCB). The Controlled Environment Vitrification System (CEVS) was used to prepare thin film specimens on holey carbon film-covered grids. Micrographs of 1% aqueous SHBS dispersions water show a variety of structures that had not been seen or postulated before in surfactant dispersions, especially tubules made of surfactant bilayers, and vesicles and tubules encapsulated in bigger unilamellar liposomes. These tubules did not disappear even when

the liquid specimens were allowed to relax in the water vapor-saturated atmosphere of the specimen preparation chamber for 30 minutes prior to freezing. Micrographs of a 0.1% solution of CTA-3,5 DCB in water show a network of very long cylindrical micelles about 4 nm in diameter. This structure explains the viscoelastic properties (high viscosity at low shear rates, shear thinning) of this dilute solution. This is the first time that such cylindrical micelles have been directly visualized in their native, thermally fixed state. When this solution is cooled from 293K to 278K it becomes turbid. Vitrified specimens of this cooled solution show the formation of vesicles. These results, in addition to providing new data on the microstructure of aqueous surfactant dispersions, demonstrate the potential of the technique in colloid science research.

An Adaptive Finite Element Method for Steady and Transient Problems, SIAM (accepted). By R. E. Benner, Jr., H. T. Davis, and L. E. Scriven.

Distributing integral error uniformly over variable subdomains, or finite elements, is an attractive criterion by which to subdivide a domain for the Galerkin/finite element method when localized steep gradients and high curvatures are to be resolved. Examples are fluid interfaces, shock fronts and other internal layers, as well as fluid mechanical and other boundary layers, e.g. thin-film states at solid walls. The uniform distribution criterion is developed here into an adaptive technique for one-dimensional problems. Nodal positions can be updated simultaneously with nodal values during Newton iteration, but it is usually better to adopt nearly optimal nodal positions during Newton iteration upon nodal values. Three illustrative problems are solved: steady convection with diffusion; gradient theory of fluid wetting on a solid surface; and Buckley-Leverett theory of two-phase Darcy flow in porous media. The new adaptive technique resists entanglement of the nodes of the nodal mesh without requiring the special restrictions upon which the earlier moving finite element method relies.

Spin-Echo Pulsed-Gradient NMR Studies of Self-Diffusion in Hydrocarbon-Brine-Alcohol Solutions, J. Colloid and Interface Sci. (submitted). By J. F. Bodet, H. T. Davis, L. E. Scriven and W. G. Miller.

Pulsed-field gradient NMR was used to examine translational self diffusion of the components of solutions of monoethylene glycol n-butyl ether, brine (NaCl 0.2M), and decane and diethylene glycol n-hexyl ether, brine (NaCl 0.2M), and dodecane. Recent studies of those mixtures reveal association behavior and the presence of fluid microstructures similar to those in micellar solutions and microemulsions. However, our results distinguish these mixtures from microemulsion. The components of the mixtures studied here diffuse molecularly, indicating a very short life time or small population of any microstructures present. Viscosities are reported for all of the mixtures.

Molecular Theory of the Ionic Double-Layer at a Charged Wall, J. Chem. Phys. 86, 2309 (1987). By E. J. Boyle, L. E. Scriven, and H. T.

Davis.

The generalized van der Waals theory for ion density distribution is used with Poisson's equation to solve the electrical double-layer problem for 1:1, 2:1, and 2:2 restricted primitive model electrolytes in contact with a diffusively charged, hard, planar surface. Electrical potential and ion density profiles are compared to Monte Carlo results and are shown to be more accurate at lower electrolyte concentration and surface charge density than at higher. In addition, values for the diffuse layer potential drop are shown to be less exact than those predicted by the hypernetted chain equation, modified Gouy-Chapman theory and modified Poisson-Boltzmann equation, but could be brought closer to Monte Carlo results by an appropriate choice of excluded volume parameter. Surface tension, ion adsorption and differential capacitance are also reported.

Completeness Theorem for a Product of Self-Adjoint Matrices Chem. Eng. Commun. 41, 267 (1986). By H. Ted Davis

It is proven that the matrices AB and BA formed from the product a positive definite self-adjoint matrix A and a self-adjoint matrix B has real eigenvalues and a complete set of eigenvectors. If B is positive (negative) semidefinite the eigenvalues are greater (less) than or equal to zero. These properties have been useful in the analysis of multicomponent diffusion and distillation processes.

On the Yvon-Born-Green Approach to the Density Distribution of Inhomogeneous Fluid, J. Chem. Phys., 85, 6806 (1986). By H. T. Davis.

In applying for Yvon-Born-Green (YBG) approach to the theory of inhomogeneous fluids, Fischer has introduced the assumption that the pair correlation function of hard spheres in contact can be approximated by the pair correlation function of homogeneous fluid at a locally averaged density $\bar{n}$. The purpose of this noise is to demonstrate that Fischer's approximation leads to the exact equation for the density distribution $n(x_1)$ of one-dimensional hard-rods in an external field. This result furnishes support for the accuracy of Fischer's approximation and perhaps helps explain the success Fischer and coworkers have had on applying the YBG equation to adsorption in porous media.

Some Recent Advances in Colloid and Interface Science: The Dynamics of Wetting and Fluids Confined between Solid Surfaces," Revista Mexicana de Fisics (Suplemento) 32 No. S1, S49-S99 (1986). By H. Ted Davis

These lecture notes consist of two independent parts: i) Fluids Confined Between Solid Surfaces and ii) The Dynamics of Wetting. In part i) we examine molecular dynamical simulations of the structure, pressure, tension and diffusivity of a simple fluid confined between flat, structureless solid walls. We show that the generalized van der Waals theory of

Nordholm and coworkers accounts for the fluid structure and explains the observed surface forces. The diffusivity results have implications for the apparent viscosity of the fluid layers confined between smooth walls. In section ii) we present some recent developements of the theory of spreading flows and its use in explaining the behavior of water droplets placed on glass slides. The drops and thin films are considered thick enough to justify description of the transport across a solvent substrate as convective flow.

Porous Media: Fluid Distributions and Transport with Applications to Petroleum Recovery, Ph.D. Thesis, University of Minnesota, Dec. 1985.
By A. A. Heiba.

Accurately modeling recovery processes mathematically and simulating their performance numerically requires (1) a consistent theory of capillary pressures, relative permeabilities, and dispersivities that characterize the flow and distribution of fluid phases, and (2) a flexible discretization of the governing equations that resolves the moving steep fronts that often develop. Recent advances in both are combined and applied to two-phase and three-phase displacements as in cores and reservoir streamtubes. Cases exemplifying one-dimensional displacement in various water drives and gas drives are examined. Such simulations can be used to design and interpret laboratory measurement of flow properties and test of process performance.

Mechanism Based Simulation of Oil Recovery Processes, SPE Reprint No. 15593, 61st Annual Technical Conference and Exhibition, New Orleans, LA, Oct. 5-8, 1986. By A. A. Heiba, H. T. Davis, and L. E. Scriven.

Accurately modeling recovery processes mathematically and simulating their performance numerically requires (1) a consistent theory of capillary pressures, relative permeabilities, and dispersivities that characterize the flow and distribution of fluid phases, and (2) a flexible discretization of the governing equations that resolves the moving steep fronts that often develop. Recent advances in both are combined and applied to two-phase and three-phase displacements as in cores and reservoir streamtubes. Cases exemplifying one-dimensional displacement in various water drives and gas drives are examined. Such simulations can be used to design and interpret laboratory measurement of flow properties and tests of process performance.

Stability and Sensitivity of Correlation Functions in a Single-Component Fluid, in *Supercomputer Applications*, R. W. Numrich ed., p. 117 (1985). By J. Kerins, L. E. Scriven, and H. T. Davis.

By computing the pair correlation function g(r;n,T) and the direct correlation function c(r;n,T) at a multitude of (n,T) points, we have mapped out the three solution spaces associated with the hypernetted-

chain, Percus-Yevick and Born-Green-Yvon-Kirkwood approximations for a single-component Lennard-Jones fluid. For each of the HNC, PY and BGYK approximations, we find a locus of turning-point singularities in the (n,T) plane. On each locus there is a critical temperature which we identify as the liquid-vapor critical temperature of the LJ fluid. To further characterize these solution spaces, we have investigated the parametric sensitivity of g(r) to c(r′). These calculations fully utilized supercomputer resources of large central memory and of vectorization for matrix construction and for full-matrix Gauss elimination.

Correlation Functions in Subcritical Fluid, Adv. Chem. Phys. 65, 215 (1986). By J. Kerins, L. E. Scriven, and H. T. Davis.

The pair correlation function g(r) and the direct correlation function c(r) of a homogeneous, Lennard-Jones fluid at density n and temperature T are calculated by solving the Ornstein-Zernike equation under the Percus-Yevick, hypernetted-chain and Kirkwood superposition closure approximations. Although some solutions are reported for supercritical temperatures, our main results concern the nature and structure of the solution space for g(r;n,T) and c(r;n,T) as the density parameter n changes at a subcritical temperature T. For all three closure approximations there is a characteristic or critical temperature T_c such that for $T < T_c$ turning points in the density are found in the solution space. Since a finite-element, Newton-Raphson method is used for the numerical solution of the correlation-function equations, we can easily track the solution, and its parametric sensitivity, around such turning points. These density turning points imply singularities in the thermodynamic bulk modulus B(n,T) as a function of n; in some cases these singularities occur outside the spinodal curve, i.e. where $B(n,T) > 0$. We conclude that turning-point singularities are likely to be generic features in the correlation-function solution space at subcritical temperatures, and propose that such singularities are the signature of an underlying clustering of particles. Finally we discuss the implications of our results for theories of inhomogeneous fluid in which uniform reference states are assumed, even if the uniform state at density n and temperature T would be thermodynamically unstable.

Microstructure in n-Alkane-Water-Electrolyte Mixtures with Small Ethoxylated Alcohol Amphiphiles, J. Colloid and Interface Science, (accepted). By P. K. Kilpatrick, H. T. Davis, L. E. Scriven, and W. G. Miller.

The ability of an amphiphilic molecule to form topologically-ordered, surfactant-like aggregates is probed by studying the ethoxylated alcohols ethylene glycol monobutyl ether (C_4E_1) and diethylene glycol monohexyl ether (C_6E_2). Density, refractive index, and nmr measurements indicated C_4E_1-water-(NaCl salt) solutions are ideal dilute solutions with no solute association up to a C_4E_1 mole fraction of about 0.018 (ca. 11 wt. %). Above this concentration, the amphiphile forms aggregates which appear to be at least weakly cooperative. At high C_4E_1 concentrations, ^{23}Na nmr and quasi-elastic light scattering (QLS) measurements indicated the

existence of small brine-rich domains (< 10 angstroms) which, though probably of short life, can interact and exchange with the amphiphile. Addition of n-decane to C_4E_1-water-salt and of n-dodecane to C_6E_2-water-salt mixtures leads to strong solution non-idealities evidenced by both brine-rich and oil-rich critical points. The spectroscopic and QLS data obtained from amphiphile-oil-brine mixtures at low brine content (1-13 wt. % brine) indicated larger brine-rich domain sizes (25-40 angstroms) than in the oil-free mixtures. The ^{23}Na nmr data in the oil-containing mixtures were very sensitive to nearness to the binodal separating one- and two-phase samples, which indicates that the domain size was largest when there was just enough amphiphile present to completely solubilize oil and brine. ^{13}C nmr measurements suggested that both amphiphiles were oriented in the oil-containing mixtures with ethylene oxide groups toward water and tail groups toward oil. From the magnitude of the chemical shifts observed, C_6E_2 appeared to be more oriented than C_4E_1. Hence, even with these simplest ethoxylated alcohols, there are indications of surfactant-like aggregation, i.e. topological ordering, between oil and brine domains.

Molecular Dynamics of Narrow, Liquid-Filled Pores, J. Chem. Phys. 83, 1888 (1985). By J. J. Magda, M. V. Tirrell, and H. T. Davis.

Molecular dynamics studies are reported for a 6-12 Lennard-Jones liquid in pore channels ranging from about 2-12 molecules wide. The pore walls are modeled as flat surfaces interacting with the fluid molecules via a continuous potential varying only with perpendicular distance from the wall. Liquid density profiles, solvation forces, interfacial tensions, and self-diffusion coefficients along the pore axis were computed. The density profiles indicate multilayer adsorption in the pore, whereas the locally defined diffusion coefficients do not vary significantly across the pore. The pore-averaged diffusivity as well as the solvation force oscillate with varying pore width at constant chemical potential. For pore widths greater than ten molecular diameters, the average diffusion coefficient is almost equal to its bulk value, and the solvation force equals the bulk pressure. In the smaller pores the mean square displacement normal to the pore walls never achieves linearity in time, and thus does not reach a diffusive limit. Thermodynamic equations relating the solvation force to the interfacial tension are derived, and the appropriate mechanical expressions for these quantities are identified. Simulation results are shown to be consistent with these thermodynamic equations. The simulations presented here will be useful in the development of the theory of fluid structure and transport in the tight pores occurring in such materials as vicor glass, clay dispersions, and biological pores and membranes.

On the Meaning and Structure of Amphiphilic Phases: Inferences From Video Enhanced Microscopy and Cryo-Transmission Electron Microscopy, J. Phys. Chem. (submitted). By D. D. Miller, J. R. Bellare, D. F. Evans, Y. Talmon, and B. W. Ninham.

This paper attempts to come to grips with a major issue confronting association colloid science which has for too long been buried. It does so by

illustrating some surprising features of aggregates of simple amphiphiles as revealed by two powerful complementary tools, video- enhanced microscopy (VEM) and cryo-transmission electron microscopy (cryo-TEM), both of which allow direct visualization. The nature of these aggregates challenge existing theories, and show up limitations of some other non-invasive, though indirect, techniques. The problem of the meaning of amphiphilic phases and their microstructure is discussed, and the necessity for a different descriptive language emphasized.

Interfacial Tensions and Phase Behavior of Alcohol-Hydrocarbon-Water-Sodium Chloride Systems, J. Phys. Chem. 91, 1137 (1986). By J. E. Puig, D. L. Hemker, A .Gupta, H. T. Davis, and L. E. Scriven.

The phase behavior and interfacial tensions of mixtures of alcohol, alkane, water, and sodium chloride that split into two or three liquid phases at 25 °C are reported as a function of type of alcohol and alkane, and sodium chloride concentration. The patterns of phase and tension behavior are similar to those observed with surfactant-based microemulsion systems but in a higher-tension regime. The qualitative patterns of phase and tension behavior in the alcohol systems appear to be characteristic of all amphiphile-oil-brine systems, although the magnitudes of the interfacial tensions of microemulsion against oil-rich or water-rich phases can be some hundred fold smaller than the corresponding tensions of the alcohol-rich phase against oil-rich or water-rich phases. This difference appears to be a distinguishing feature of microemulsions and presumably arises from the relatively large scale of microemulsion microstructure. Microemulsions in multiphase equilibria incorporate tenfold or more water or oil than do corresponding alcohol solutions, and this argues for the topology and persistence of that microstructure.

Optical Analysis of the Spinning Drop, J. Colloid and Interface Science (accepted). By J. E. Puig, Y. Seeto, C. V. Pesheck, and L. E. Scriven.

The accuracy with which the interfacial tension between two immiscible fluid phases can be determined by the spinning drop method is limited by the accuracy with which the spinning drop diameter can be found. Thus it is important to know the factor by which the cylindrical sample tube and its content magnify the on-axis drop or bubble. By the rigorous ray tracing method of geometric optics, we have analyzed the image formation and magnification factor of the spinning drop. Our analysis shows that when drop, outer wall and inner wall of the tube are concentric, the ratio of the diameter of the image, as measured by a traveling microscope, to the diameter of the drop is exactly the refractive index of the denser fluid surrounding the drop. Our analysis also reveals that the image, a virtual one, is formed concentric with the drop. We have also analyzed the effect of eccentricity of the walls of the sample tube on the magnification factor.

Sedimentation of Molecular Solutions in the Ultracentrifuge: I.

Equilibrium Phase Behavior, J. Colloid and Interface Science 113, 248 (1986). By W. R. Rossen, H. T. Davis, and L. E. Scriven.

A theory is presented for multicomponent, multiphase chemical equilibrium in a gravitational or centrifugal field. Bulk fluid in the field is stratified; the degree of stratification depends on how free energy and density of the material depend on composition and pressure. Nonideal solutions of low-molecular-weight species can have the sharp composition gradients in the field that are characteristic of solutions containing dense salts and colloids. Because each phase in the field is not homogeneous, but is stratified in pressure and composition, the number and composition of phases in a strong field can differ strikingly from those in earth's gravity. The phase rule does not apply to a system so stratified. Metastable states are possible in the field as well. All of these features are illustrated by the behavior of simple model nonideal solutions and, in two cases, by experiments. Implications for interpreting ultracentrifuge studies of phase behavior and fluid structure are discussed.

Sedimentation of Molecular Solutions in the Ultracentrifuge: II. Sedimentation Velocity, J. Colloid and Interface Science 113, 269 (1986). By W. R. Rossen, H. T. Davis, and L. E. Scriven.

Observed sedimentation velocities in solutions of unknown microstructure can be misleading. Sedimentation-velocity behavior is governed by the interplay of three factors: buoyant density, molecular weight or particle mass, and solution nonideality. As a result, nonideal molecular solutions near a plait point can sediment with fronts as sharp as those of ideal solutions of massive colloidal particles. In addition, because phenomenological transport coefficients increase without bound near a consolute point, or plait point, sedimentation velocities can be as high in near-critical molecular solutions as in colloidal mixtures. Sedimentation profiles computed for model nonideal, molecular solutions are reported here; these profiles resemble those of colloids, and micelle sizes computed in the usual way from these profiles appear deceptively reasonable. Hence caution is needed when inferring from sedimentation profiles the nature of microstructures present in solution.

Equilibrium Wetting on Rough Surfaces: A Simple Model for Wetting in Porous Media, J. Colloid and Interface Science (submitted). By J. B. Sweeney, J. A. N. Zasadzinski, H. T. Davis, and L. E. Scriven.

The structure and stability of perfectly wetting fluid menisci in axisymmetric pores have been investigated using the augmented Young-Laplace equation as solved by the Galerkin/finite element method. Both continuous and disconnected menisci geometries have been considered. The results of these calculations for single- and multiple-pore microscopic systems have been applied to macroscopic systems by the application of a statistical theory of multiphase transport in porous media. The results indicate the existence of two transport mechanisms: a capillary jump mechanism by which the non-wetting fluid invades pores and a film drainage mechanism by which wetting films and pendular structures, remaining after the

invasion of the non-wetting fluid, continue to drain. The difference between the two mechanisms is apparent at low-wetting-phase saturation in both the predictions of the statistical theory and in displacement experiments of perfectly wetting and intermediately wetting fluids in sintered teflon synthetic porous media.

Imaging Surfactant Dispersions by Electron Microscopy of Vitrified Specimens, Colloids and Surfaces 19, 166 (1986). By Y. Talmon.

Ultrafast cooling of thin, unsupported specimens of aqueous surfactant dispersions in liquid ethane causes them to vitrify. The ice matrix in these specimens is non-crystalline. Since no crystallization takes place, there is no phase segregation during cooling. Electron optical effects associated with a crystalline matrix, which obscure the inner structure of the dispersed aggregates in the ice, are also avoided. Contrast in these unstained specimens is very good when the correct defocus is applied. This paper presents the vitrification technique as applied to surfactant dispersions, gives several sample micrographs of natural and synthetic surfactant systems, and discusses further applications to more labile or complex systems, such as micellar solutions and microemulsions.

Statistical Mechanics of Rigid Particles in an External Field, J. Chem. Phys. 85, 6699 (1986). By T. K. Vanderlick, L. E. Scriven, and H. T. Davis.

A new density functional is employed which simplifies and unifies the generalized van der Waals (GVDW) theory and the exact one-dimensional theory of hard particles in the presence of an external potential or solid walls. Numerical solution of density profiles in planar systems is made easy by introduction of the density functional. Numerical results for one- and three-dimensional fluids reveal that the GVDW theory fails at high chemical potentials by admitting negative densities. We have some evidence that the cause of the failure is a negative eigenvalue of the weighting function defining the local mean density or excluded volume in the theory. Density profiles of the exact one-dimensional theory are compared to those of the GVDW theory, those of the former exhibiting similar but stronger oscillations and of course no regions of negative density.

Solution of Percus's Equation for the Density of Hard Rods in an External Field, Phys. Rev. A 34, 5130 (1986). By T. K. Vanderlick, L. E. Scriven, and H. T. Davis.

The theory of a one-dimensional fluid of hard rods has received quite a lot of attention because it often yields exact results which serve as a guide to understanding the properties of more complicated fluids. Of particular interest recently has been the density distribution of nonuniform fluids in external potentials or between solid walls. The purpose of this short paper is to report an explicit solution of the nonlinear integral equation derived by Percus for the density distribution of hard rods.

Toward an Understanding of Liposome Structure Through the Use of Computer Graphic Image Correlation, J. Electron Miscroscopy Technique 3, 385 (1986). By J. A. N. Zasadzinski, J. Kerins, H. T. Davis, and L. E. Scriven.

A computer-aided graphics approach to correlating transmission electron microscope images of freeze-fractured and thin-sectioned samples is outlined. Any three-dimensional model of the imaged structure can be mathematically sectioned to provide a two-dimensional representation of the model in the "fracture" plane. The method is used to demonstrate that the structure of lamellar liquid crystalline liposomes is based on a family of Dupin cyclides; closed parallel surfaces with a conjugate ellipse and hyperbola as curvature defects.

Polymerizable Surfactant Design for Transmission Electron Microscopy, J. Colloid and Interfacial Science 11, 347 (1986). By J. A. N. Zasadzinski, P. C. Vosejpka, and W. G. Miller.

Polymerized liposomes and vesicles are under close scrutiny as long-lived, stable substitutes for their natural and synthetic unpolymerized counterparts. The monomer surfactant, which contains one or more polymerizable groups, is dispersed in water at the proper temperature and concentration to form the lyotropic liquid crystalline phase of interest and polymerized while in the liquid crystalline state. In addition to their applications to slow-release and site-specific drug delivery, membrane-mediated chemistry, artifical photosynthesis, etc., polymerized surfactant liposomes and vesicles hold great promise as model systems for TEM investigations of lamellar liquid crystal structure. One such model polymerizable surfactant is DBPAI, or *N, N*-dimethyl-*N,N*-bis(1,3-pentadecadienyl-carbonyloxyethyl) ammonium iodide. Polarized light microscopy and differential scanning calorimetry (DSC) confirm that DBPAI forms lamellar liquid crystalline liposomes in water. The DBPAI liposomes were polymerized while in the liquid crystalline state by ultraviolet (UV) irradiation. The DBPAI liposomes were shown to be identical in structure before and after polymerization by a combination of X-ray diffraction and freeze-fracture TEM. However, turbidity measurements showed that the polymerized DBPAI liposomes were much more stable in acetone and ethanol than the monomer DBPAI liposomes, demonstrating that the chemical nature of the surfactant in the liposome had changed. The combination of structural preservation and enhanced chemical stability makes DBPAI a natural choice for TEM thin-sections. A method of preparing DBPAI liposomes for thin-section TEM is outlined and bilayer resolution images of the DBPAI liposomes are presented. Polymerized bilayers in thin-section TEM promise the enhanced resolution required to answer many important structural questions left unresolved by freeze-fracture TEM.

Finite Element Calculations of Fluid Menisci and Thin-Films in a Model Porous Media, J. Colloid and Interface Science (submitted). By J. A. N. Zasadinski, H. T. Davis, and L. E. Scriven.

Finite element solutions of the Augmented Young-Laplace (AYL)

equation are given for a number of axisymmetric menisci that correspond to idealized solid-solid contacts in a model porous medium. The influence of the disjoining pressure on the saturation of a non-polar wetting liquid is significant for porous media composed of particles with diameters of less than 100 microns; low interfacial tensions also caused more wetting liquid to be trapped in thin films. A method of predicting equilibrium wetting fluid saturation in a porous medium characterized only by the porosity, a characteristic length scale, the interfacial tension between the two fluids and the Hamaker constant of the solid-liquid-fluid system is proposed.

LIST OF PUBLICATIONS

1. Anderson, D. M., Studies in the Microstructure of Microemulsions, Ph.D. Thesis, University of Minnesota, June 1986.

2. Anderson, D. M., Davis, H. T., Evans, E. F., and Scriven, L. E., Bicontinuous Microemulsions and the Mean Curvature of the Oil-Water Interface, J. Phys. Chem. (to be submitted).

3. Anderson, D. M., Davis, H. T., Nitsche, J.C.C. and Scriven, L. E., "Periodic Surfaces of Prescribed Mean Curvature," Phil. Mag. (to be submitted).

4. Bellare, J. R., "A Controlled Environment System for Vitrification of Liquid TEM Samples," Proceedings of the 44th Annual EMSA Meeting, New Mexico, Aug. 11-16, 1986.

5. Bellare, J. R., Davis, H. T., Scriven, L. E., and Talmon, Y., "An Improved Controlled-Environment Vitrification System for Cryofixation of Hydrated TEM Samples," Proceedings of ICEM XIth International Congress on Electron Microscopy, Kyoto, Japan, Aug. 31-Sept. 7, 1986.

6. Bellare, J. R., Davis, H. T., Scriven, L. E., and Talmon, Y., "Microstructural Studies of Surfactant Aqueous Dispersions by a Vitrification Technique," Proceedings of ICEM XIth International Congress on Electron Microscopy, Kyoto, Japan, Aug. 31- Sept. 7, 1986.

7. Benner, R. E., Davis, H. T. and Scriven, L. E., "An Adaptive Finite Element Method for Steady and Transient Problems," SIAM (accepted).

8. Bodet, J. F., Davis, H. T., Scriven, L. E. and Miller, W. G., "Spin-Echo Pulsed- Gradient NMR Studies of Self-Diffusion in Hydrocarbon-Brine-Alcohol Solutions," J. Colloid and Interface Sci. (submitted).

9. Boyle, E. J., Scriven, L. E., and Davis, H. T., "Molecular Theory of the Ionic Double Layer at a Charged Wall," J. Chem. Phys. **86**, 2309 (1987).

10. Davis, H. T., "Completeness Theorem for a Product of Self-Adjoint Matrices," Chem. Eng. Commun. **41**, 267 (1986).

11. Davis, H. T., "On the Yvon-Born-Green Approach to the Density Distribution of Inhomogeneous Fluid," J. Chem. Phys. **85**, 6806 (1986).

12. Davis, H. T., "Some Recent Advances in Colloid and Interface Science: The Dynamics of Wetting and Fluids Confined between Solid Surfaces," Revista Mexicana de Fisica (Suplemento) **32** No. S1, S49-S99 (1986).

13. Heiba, A. A., "Porous Media: Fluid Distributions and Transport with Applications to Petroleum Recovery," Ph.D. Thesis, University of Minnesota, Dec. 1985.

14. Heiba, A. A., Davis, H. T., and Scriven, L. E., "Mechanism Based

Simulation of Oil Recovery Processes," SPE Reprint No. 15593, 61st Annual Technical Conference and Exhibition, New Orleans, LA, Oct. 5-8, 1986.

15. Kerins, J. ,Scriven, L. E., and Davis, H. T., "Stability and Sensitivity of Correlation Functions in a Single-Component Fluid," in *Supercomputer Applications*, R. W. Numrich ed., p. 117 (1985).

16. Kerins, J., Scriven, L.E., and Davis, H. T., "Correlation Functions in Subcritical Fluid," Adv. Chem. Phys. **65**, 215 (1986).

17. Kilpatrick, P. K., Davis, H. T., Scriven, L. E., and Miller, W. G., "Microstructure in n-Alkane-Water-Electrolyte Mixtures with Small Ethoxylated Alcohol Amphiphiles," J. Colloid and Interface Science (accepted).

18. Magda, J. J., Tirrell, M. V., and Davis, H. T., "Molecular Dynamics of Narrow Liquid-Filled Pores," J. Chem. Phys. **83**, 1888 (1985).

19. Miller, D. D., Bellare, J. R., Evans, D. F., Talmon, Y. and Ninham, B. W., "On the Meaning and Structure of Amphiphilic Phases: Inferences from Video Enhanced Microscopy and Cryo-Transmission Electron Microscopy," J. Phys. Chem. (submitted).

20. Puig, J. E., Hemker, D.L., Gupta, A., Davis, H. T. and Scriven, L. E., "Interfacial Tensions and Phase Behavior of Alcohol-Hydrocarbon-Water-Sodium Chloride Systems," J. Phys. Chem. **91**, 1137 (1986).

21. Puig, J. E., Seeto, Y., Pesheck, C. V. and Scriven, L. E., "Optical Analysis of the Spinning Drop," J. Colloid and Interface Science (submitted).

22. Rossen, W. R., Davis, H. T. and Scriven, L. E., "Sedimentation of Molecular Solutions in the Ultracentrifuge: I. Equilibrium Phase Behavior," J. Colloid and Interface Science **113**, 248 (1986).

23. Rossen, W. R., Davis, H. T. and Scriven, L. E., "Sedimentation of Molecular Solutions in the Ultracentrifuge: II. Sedimentation Velocity," J. Colloid and Interface Science **113**, 269 (1986).

24. Sweeney, J. B., Zasadzinski, J. A. N., Davis, H. T., and Scriven, L.E., "Equilibrium Wetting on Rough Surfaces: a Simple Model for Wetting in Porous Media," J. Colloid and Interface Sci. (submitted).

25. Talmon, Y., "Imaging Surfactant Dispersions by Electron Microscopy of Vitrified Specimens," Colloids and Surfaces **19**, 166 (1986).

26. Vanderlick, T. K., Scriven, L. E. and Davis, H. T., "Statistical Mechanics of Rigid Particles in an External Field," J. Chem. Phys. **85**, 6699 (1986).

27. Vanderlick, T. K., Scriven, L. E., and Davis, H. T., "Solution of Percus's Equation for the Density of Hard Rods in an External Field," Phys. Rev. A. **34**, 5130 (1986).

28. Zasadzinski, J. A. N., Kerins, J., Davis, H. T. and Scriven, L. E., "Toward an Understanding of Liposome Structure Through the Use of Computer Graphic Image Correlation," J. Electron Microscopy Technique **3**, 385 (1986).

29. Zasadzinski, J. A. N., Vosejpka, P.C., and Miller, W. G., "Polymerizable Surfactant Design for Transmission Electron Microscopy," J. Colloid and Interfacial Science **110**, 347 (1986).

30. Zasadzinski, J. A. N., Davis, H. T., and Scriven, L. E., "Finite Element Calculations of Thin Films and Fluid Menisci in a Model Porous Media," J. Colloid and Interface Science (submitted).

☆ U.S. GOVERNMENT PRINTING OFFICE:1987-761-030 / 60041